Optimization of laser damage detection and growth monitoring capabilities : application to the Laser MegaJoule facility

Guillaume Hallo

université PARIS-SACLAY

Optimization of laser damage detection and growth monitoring capabilities: application to the Laser MegaJoule facility

Optimisation des capacités de détection et de suivi de la croissance de l'endommagement laser pour l'installation laser MegaJoule

Thèse de doctorat de l'université Paris-Saclay

École doctorale n° 579, Sciences Mécaniques et Energétiques, Matériaux et Géosciences (SMEMaG)
Spécialité de doctorat : Mécanique des matériaux
Graduate School : Sciences de l'ingénierie et des systèmes. Référent : ENS Paris-Saclay

Thèse préparée dans l'unité de recherche **Laboratoire de Mécanique Paris-Saclay**,
sous la direction de **François HILD**, Directeur de Recherche,
le co-encadrement de **Chloé LACOMBE**, Ingénieur de Recherche,
le co-encadrement de **Jérôme NEAUPORT**, Directeur de Recherche

Thèse soutenue au Barp, le 9 janvier 2023, par

Guillaume HALLO

Composition du Jury

Membres du jury avec voix délibérative

Marc FERRARI Professeur, Université Aix-Marseille	Président
Fabien AMIOT Chargé de Recherche, CNRS	Rapporteur & Examinateur
Laurent GALLAIS Professeur, Ecole Centrale Marseille	Rapporteur & Examinateur
François GOUDAIL Professeur, IOGS	Examinateur

THESE DE DOCTORAT

NNT : 2023UPAST008

“Beauty is in the eye of the beholder – and what we see is scattered light.”
John C. Stover

Acknowledgement

I would like to start by thanking my thesis supervisors Chloé Lacombe and Jérôme Néauport who gave me valuable advice to carry out my thesis work. A big thank you to François Hild, very enthusiastic thesis director. You were always willing to help me whenever I needed it: as you told me at our first meeting, your PhD students are really your first priority!

I thank Pierre-Henri, Geneviève and Laurence for the opportunity to participate at La Fabrique Défense 2022. Thank you François G. and Olivier L. for your unfailing support.

I take the opportunity of this page to thank all those who helped me during the 3 years (and a little more) in the LMJ teams : Sébastien V., Vincent D., Martin S., Pierre-Marie D., Sandy C., Hervé C., Julien M., Kevin G., Céline C., Lydie B., Mélanie M., Stéphane B., Margaux C., Laurent H., Vincent B., Sylvain G., Nadja R., Martin C., Jean-François G., Charles B., Saaxewer D., Romain P., Thierry D., Florian G., Eric C.. Sylvain, Nadja, Romain, your good mood during the damage test days was very pleasant and you always answered present in spite of long experiments. I also thank Edouard B.: you have been an exceptional colleague. A big thank you for our discussions and your sharp analyses. I have a special thought for Marie T.: your strong experience in thermal imaging helped me a lot.

I thank Guillaume Maire for the tomography tests which finally did not find their place in this manuscript. I also met people who are passionate about their research work at the Fresnel Institute. Myriam Zerrad and Marin Fouchier, I thank you for spending time to perform the BSDF measurements on the SALSA bench. Particular thanks to Nicolas Bonod and Jean-Yves Natoli for the prolific exchanges on my thesis research. You helped me a lot to fully exploit the obtained results.

And thanks to all those with whom I shared good times after work hours. I had a great time playing tennis with Rock, Matthieu, Romain, Nathalie, Alexandre, Chloé and others. Yanis and Arthur, it's partly thanks to you that I climb walls despite a little vertigo. Arthur, thank you for windsurfing and wakeboarding sessions. Syl20, I think I will always remem-

ber this game of petanque at lunch time ! Khollégues, Mimi and Euge, thanks to you for the hikes in the Pyrenees, the skiing and of course the discovery of Guyana. They were very nice breaks during the 3 years of the thesis work. Léa, I think we can also thank the SNCF which, thanks to its legendary efficiency and its outstanding punctuality, allowed us to beat the record for the round trip between Bordeaux and Montpellier. Thank you Choubidou!

I warmly thank my parents who have always supported and encouraged me. It is really thanks to you that I have been able to achieve my goals so far.

Finally, I greatly thank the 2 reviewers of this manuscript Fabien Amiot and Laurent Gallais for having accepted to evaluate the work presented in this manuscript. I also thank Marc Ferrari for having chaired the thesis committee and François Goudail for having taken part in this committee.

Contents

Résumé en français

Depuis la création du LASER pour "Light Amplification by Stimulated Emission of Radiation" (Amplification de lumière par émission stimulée de radiation) en 1960 [1], cette avancée majeure n'a cessé d'être utilisée dans différents domaines à travers le monde : des premières opérations d'usinage [2] à la lecture de codes barres [3] en passant par les communications [4] et la médecine [5]. L'idée d'utiliser des faisceaux laser pour étudier des états de matière soumis à des températures et pressions jusqu'alors inaccessibles à l'échelle du laboratoire a été explorée dès 1960 avec un système laser à rubis composé de 12 faisceaux et dénommé "4 Pi" [6]. Depuis 1960, de nombreuses installations laser ont été construites pour réaliser des expériences de fusion. Les dernières installations laser de classe mégajoule imaginées et construites sont le National Ignition Facility (NIF) aux Etats-Unis [7], le Laser MégaJoule (LMJ) en France [8], le ShenGuang-III (SG-III) et le ShenGuang-IV (SG-IV) en Chine [9]. L'exploitation de telles installations est, dans une certaine mesure, limitée par le phénomène d'endommagement laser des composants optiques [10]. Un dommage laser est un cratère de diamètre allant de la dizaine de micromètres au millimètre avec une profondeur d'environ le tiers de son diamètre et présentant des fractures sous-surfaciques. L'endommagement laser, défini comme une modification irréversible de la matière des composants optiques induite par laser, impacte négativement les performances ainsi que l'exploitation de telles installations. La dynamique d'endommagement peut être décomposée en 2 phases : l'amorçage correspondant à l'apparition du dommage et la croissance du dommage lors d'une nouvelle exposition au flux laser [10]. Pour le NIF, le SG-III et le LMJ, l'endommagement se produit principalement sur les optiques en silice de fin de chaine traversées par un flux laser ultraviolet de quelques nanosecondes pour une énergie de l'ordre de la dizaine de kilojoules. Afin de repousser les difficultés liées à l'endommagement laser, de nombreux travaux ont été menés pour :

- Mesurer la capacité de résistance des composants optiques exposés

à des flux laser en fonction de différents paramètres [10, 11] ;

- Améliorer la tenue au flux des matériaux optiques [12–15] ;
- Améliorer les qualités spatiales et temporelle des faisceaux [16, 17] ;
- Développer des méthodes de réparation des dommages [18, 19] ;
- Augmenter la durée de vie des optiques sur chaines en diminuant localement l'énergie du faisceau laser pour arrêter la croissance des dommages [20, 21].

Les méthodes de réparation et d'augmentation de la durée de vie des optiques sont limitées à des tailles de dommages n'excédant pas $750\,\mu\mathrm{m}$. Il est donc nécessaire de pouvoir estimer la croissance des dommages avant qu'ils n'atteignent cette taille limite de $750\,\mu\mathrm{m}$. Des travaux ont donc été réalisés concernant l'observation et le contrôle des dommages laser directement sur les installations [20–23]. Ainsi, les grandes installations laser de classe mégajoule disposent d'un système d'imagerie sur chaine de l'endommagement de leurs dernières optiques en silice subissant l'endommagement lors du passage du faisceau laser ultraviolet : le FODI ("*Final Optics Damage Inspection*") pour le NIF [23] et le SG-III [24], le Module Diagnostic Centre Chambre (MDCC) pour le LMJ [25]. Ces systèmes optiques sont insérés après chaque tir laser au centre de la chambre d'expériences de l'installation. Les composants optiques observés sont éclairés par la tranche. Les systèmes d'imagerie collectent une partie du signal diffusé par les dommages éclairés. Les images d'endommagement sont à fond noir avec des pixels lumineux correspondant aux sites endommagés. La résolution spatiale des images obtenues ($\approx 100\,\mu\mathrm{m}$/pixel) étant de l'ordre de grandeur de la taille des dommages à suivre en croissance (de $10\,\mu\mathrm{m}$ à $750\,\mu\mathrm{m}$), l'estimation précise du diamètre des dommages est un défi. Des perturbations affectent les images acquises : déplacements apparents du système d'imagerie par rapport aux optiques observées, variations d'intensité lumineuse et de netteté entre des images d'un même hublot après chaque tir. Ces perturbations dégradent la qualité du suivi de la croissance des dommages sur chaine [25].

Les objectifs de recherche de cette thèse couvrent l'optimisation des capacités de détection et de suivi de la croissance de l'endommagement sur chaine avec un focus sur les installations laser de classe mégajoule. Les travaux menés ont pour objectif de participer à :

- L'amélioration de l'efficacité du processus de réparations des optiques;

- L'augmentation de la durée de vie des optiques sur chaine et donc la réduction du nombre de composants optiques neufs consommés par les installations chaque année.

Organisation du document

Ce document, organisé en 5 parties dont une première partie introductive (Partie I) et une dernière partie conclusive (Partie V), a pour objectif d'apporter des éléments de réponses concrets aux 3 questions suivantes :

1. **Comment mesurer la taille des dommages laser pour des diamètres inférieurs à la résolution spatiale des images ?**
   Le premier enjeu consiste à estimer la taille des dommages laser présents sur la face arrière des hublots de chambre du LMJ. La résolution spatiale des images ($\approx 100\,\mu\mathrm{m}$/pixel) n'étant pas suffisante pour décrire les dommages amorcés dont le diamètre est inférieur à $100\,\mu\mathrm{m}$, il convient de mesurer la taille des dommages autrement que par la méthode classique consistant à compter le nombre de pixels représentant un dommage. Cette question est abordée en Partie II.

   Le Chapitre 2 décrit le système d'éclairement et d'imagerie des dommages sur les hublots de chambre du LMJ. Ce chapitre traite de l'estimation du diamètre des dommages à partir de l'intensité lumineuse collectée par le système d'imagerie (méthode des niveaux de gris). Les performances de cette méthodes sont comparées à une méthode classique consistant à compter le nombre de pixels correspondant à l'image du dommage. L'estimation de diamètre basée sur les niveaux de gris implique un étalonnage de la mesure. Dans ce chapitre, il est décrit comment la modélisation optique du système d'acquisition peut se substituer à des étalonnages systématiques à partir d'un composant optique étalon composé de nombreux dommages.

   Le Chapitre 3 aborde le sujet de l'optimisation du système d'éclairement utilisé pour rendre visibles les dommages laser sur les hublots de chambre du Laser MégaJoule. L'objectif est de réduire les incertitudes de mesure des diamètres pour permettre un suivi fiable de la croissance de l'endommagement tout en améliorant la robustesse du système d'éclairement. Des évolutions sont proposées et détaillées dans le but d'améliorer la détection des dommages et la précision de mesures de leur taille.

2. **Comment corriger les perturbations affectant les images afin d'optimiser le suivi de la croissance des dommages sur chaine ?**

   Les perturbations (déplacements, variation d'éclairement et de focus) affectant les images impliquent une perte de précision sur le suivi de la croissance des dommages par la méthode de niveaux de gris des pixels. On s'intéresse donc à des méthodes pour contourner ces difficultés. Cette question est abordée en Partie III.

   Le Chapitre 4 décrit des méthodes de corrections des images basées sur les principes de Corrélation d'Images Numériques (CIN), mis en oeuvre avec succès dans le domaine de la mécanique des solides : correction de déplacements et de niveaux de gris. Ces méthodes sont validées sur un ensemble d'images de mouchetis, largement répandu et particulièrement favorable aux méthodes CIN, puis appliquées à une série d'images d'endommagement issues du LMJ.

   Les dommages présents sur les hublots de chambre sont rarement observés avec une haute résolution spatiale hors de la chaine laser. Le suivi de la croissance des dommages par la méthode des niveaux de gris ne peut donc pas être validé sur une série d'images d'endommagement acquises au LMJ. Le Chapitre 5 décrit une expérience de croissance de dommages réalisée sur un banc d'endommagement laser hautement instrumenté. Cette expérience a été réalisée dans le but de s'assurer de la possibilité de suivre la croissance des dommages laser à partir des mesures d'intensité des pixels. L'exploitation des données acquises lors de cette expérience à petite échelle apporte un éclairage sur l'efficacité et l'apport des méthodes de CIN pour le suivi de la croissance des dommages laser sur chaine LMJ.

   Afin d'améliorer la précision de suivi de la croissance des dommages par les intensités de pixels, la correction des niveaux de gris des images doit permettre de décrire le plus fidèlement possible les variations d'intensité des pixels d'une image à l'autre. Le Chapitre 6 décrit des travaux menés sur le développement d'une méthode de correction de Brillance/Contraste des images d'endommagement des hublots LMJ, basée sur la modélisation du système d'éclairement et sur des techniques d'Analyses en Composantes Principales (ACP).

3. **Les niveaux de gris, jusqu'à présent utilisés pour estimer le diamètres des dommages, peuvent-ils servir à décrire la morphologie volumique des dommages ?**

Cette question est abordée en Partie IV. Les résultats présentés au Chapitre 5 indiquent que les niveaux de gris ne décrivent pas uniquement la croissance en surface des dommages. Une deuxième expérience de croissance de dommages sur un banc d'endommagement laser hautement instrumenté a été réalisée. Le Chapitre 7 présente des travaux menés pour déterminer si l'analyse des intensités de pixels dans le cas d'une résolution spatiale suffisante des images en surface d'un dommage permet de décrire la morphologie volumique du dommage.

Conclusions générales

L'objectif principal de ce travail était l'optimisation de la détection et du suivi de la croissance de l'endommagement des dernières optiques du Laser MégaJoule en s'appuyant sur l'exemple des hublots de chambre. Cette optimisation concerne plusieurs aspects clés :

- **Estimation du diamètre des sites endommagés.** Dans le cas des hublots de chambre du Laser MégaJoule observés par le MDCC, le seuil de détection est de l'ordre de $30\,\mu\mathrm{m}$ soit $\frac{1}{3}$ de la résolution du système d'imagerie. Il a été confirmé dans le Chapitre 2 que la méthode basée sur l'intensité des pixels surpasse la technique de comptage de pixels en ce qui concerne l'estimation du diamètre des dommages. Ce résultat a été obtenu en effectuant l'étalonnage des niveaux de gris sur les diamètres de dommages à l'aide d'un hublot de chambre, monté sur une chaine laser et composé de 930 dommages dont les diamètres sont parfaitement connus. Cependant, cet étalonnage par mesure in-situ est long à mettre en place. Dans ce même Chapitre 2, une nouvelle méthode d'étalonnage, basée sur une modélisation optique, a été proposée. Ce modèle s'appuie d'une part sur une modélisation des systèmes d'éclairement et d'imagerie et d'autre part sur la mesure d'indicatrice de diffusion de dommages. Il a été démontré que l'étalonnage basée sur la modélisation optique est aussi efficace que l'étalonnage par mesure. Dans le cas du MDCC, il est possible d'obtenir le diamètre d'un dommage, D, en fonction de son intégrale des niveaux de gris, TIS.

- **Suivi de la croissance de l'endommagement tir après tir.** La mesure précise des diamètres des dommages est basée sur les intensités des pixels. Le suivi de la croissance des dommages repose donc sur une analyse fiable des variations de niveaux gris

d'une image à l'autre. Dans ce but, des corrections de déplacement et d'intensité lumineuse basées sur les principes de la Corrélation d'Images Numériques ont été développées et validées sur des images de type mouchetis puis des images d'endommagement acquises sur banc et sur l'installation LMJ (Chapitres 4 et 5). Les corrections de niveaux de gris proposées permettent de réduire l'impact des variations d'éclairement sur les mesures de diamètre. Les travaux présentés dans le Chapitre 6 permettent d'envisager une correction des niveaux de gris spécialement adaptée aux images des hublots du LMJ, s'appuyant sur les principes de l'ACP et sur la modélisation du système d'éclairement. Cette technique de correction des niveaux de gris permettrait une amélioration de la qualité de suivi de la croissance de l'endommagement. Cependant, le système d'éclairement à 2 LEDs est peu robuste et instable dans le temps. Les LEDs sont endommagées par les interactions électromagnétiques entre les faisceaux laser et la cible. Le modèle de simulation optique présenté au Chapitre 2 a été utilisé pour estimer numériquement l'impact de modifications potentielles du système d'éclairement des hublots LMJ sur les performances de suivi de la croissance de l'endommagement. Il a été montré que le remplacement du système actuel à 2 LEDs par un système à source fibrée avec insertion d'un réflecteur convexe permet d'améliorer la robustesse du système d'éclairement aux interactions électromagnétiques. De plus, le nouveau système d'éclairement apporterait un gain d'un facteur 4 sur l'homogénéité de l'éclairement par rapport à la solution actuellement en place sur LMJ.

- **Description de la morphologie volumique des dommages à partir des niveaux de gris.** L'apport des travaux menés ne concerne pas uniquement le suivi de l'endommagement sur les optiques des installations laser de classe mégajoule. Dans le chapitre 7, un modèle est proposé pour estimer la profondeur des dommages à partir des diamètres et des niveaux de gris mesurés en surface. Ce modèle peut être interprété comme une évolution de la relation de proportionnalité classique entre la profondeur et le diamètre. Le modèle proposé devrait permettre d'améliorer la compréhension des différentes phases de croissance des dommages sur les banc d'études de l'endommagement laser. Il convient toutefois de noter que la mesure quantitative de la profondeur à partir des niveaux de gris et du diamètre d'un dommage est valable dès lors qu'un étalonnage du système est réalisé. Sans étalonnage, il est néanmoins montré qu'une augmentation de profondeur sans évolution du diamètre est

décrite par une augmentation des niveaux de gris sans variation du diamètre mesuré.

D'un point de vue pratique pour l'installation, les méthodes et résultats présentés concourent à l'allongement de la durée de vie des hublots grâce à une estimation plus précise du diamètre et de la croissance des dommages. Ces méthodes, plus généralement appliquées aux bancs d'endommagement, permettent également un suivi plus précis de la croissance des dommages et donc une meilleure compréhension de la physique de l'endommagement laser.

En conclusion, les niveaux de gris après corrections des images sont un atout majeur pour l'étude de l'endommagement laser que ce soit sur les installations laser de classe mégajoule ou sur les bancs d'étude de l'endommagement laser.

References

[1] T. H. Maiman, "Stimulated Optical Radiation in Ruby,", vol. 187, no. 4736, pp. 493–494, Aug. 1960. doi: 10.1038/187493a0.

[2] A. K. Dubey and V. Yadava, "Laser beam machining—a review," *International Journal of Machine Tools and Manufacture*, vol. 48, no. 6, pp. 609–628, 2008, issn: 0890-6955. doi: https://doi.org/10.1016/j.ijmachtools.2007.10.017. [Online]. Available: https://www.sciencedirect.com/science/article/pii/S0890695507002325.

[3] E. Barkan and J. Swartz, "System Design Considerations In Bar-Code Laser Scanning," *Optical Engineering*, vol. 23, no. 4, pp. 413–420, 1984. doi: 10.1117/12.7973310. [Online]. Available: https://doi.org/10.1117/12.7973310.

[4] R. F. Kazarinov, "Physics and simulation of communication lasers," in *Physics and Simulation of Optoelectronic Devices II*, W. W. Chow and M. Osinski, Eds., International Society for Optics and Photonics, vol. 2146, SPIE, 1994, pp. 122–132. doi: 10.1117/12.178503. [Online]. Available: https://doi.org/10.1117/12.178503.

[5] R. Brancato, L. Giovannoni, R. Pratesi, and U. Vanni, "New Lasers For Ophthalmology: Retinal Photocoagulation With Pulsed Diode Lasers," in *1986 European Conf on Optics, Optical Systems and Applications*, S. Sottini and S. Trigari, Eds., International Society for Optics and Photonics, vol. 0701, SPIE, 1987, pp. 365–366. doi: 10.1117/12.937087. [Online]. Available: https://doi.org/10.1117/12.937087.

[6] llnl.gov. "The birth of the laser and icf." (2022), [Online]. Available: https://www.llnl.gov/archives/1960s/lasers (visited on 09/18/2022).

[7] LLNL. "What is the national ignition facility?" (2022), [Online]. Available: https://lasers.llnl.gov/about/what-is-nif (visited on 07/28/2022).

[8] CEA. "Laser mégajoule." (2022), [Online]. Available: http://www-lmj.cea.fr/ (visited on 07/28/2022).

[9] W. Zheng *et al.*, "Laser performance of the sg-iii laser facility," *High Power Laser Science and Engineering*, vol. 4, e21, 2016. doi: 10.1017/hpl.2016.20.

[10] K. Manes, M. Spaeth, J. Adams, and M. Bowers, "Damage mechanisms avoided or managed for nif large optics," *Fusion Science and Technology*, vol. 69, pp. 146–249, Feb. 2016. doi: 10.13182/FST15-139.

[11] S. G. Demos, M. Staggs, and M. R. Kozlowski, "Investigation of processes leading to damage growth in optical materials for large-aperture lasers," *Applied Optics*, vol. 41, no. 18, pp. 3628–3633, Jun. 2002. doi: 10.1364/AO.41.003628. [Online]. Available: http://ao.osa.org/abstract.cfm?URI=ao-41-18-3628.

[12] J. A. Menapace *et al.*, "Combined advanced finishing and uv-laser conditioning for producing uv-damage-resistant fused silica optics," in *Optical Fabrication and Testing*, Optica Publishing Group, 2002, OMB4. doi: 10.1364/OFT.2002.OMB4. [Online]. Available: http://opg.optica.org/abstract.cfm?URI=OFT-2002-OMB4.

[13] B. Bertussi, J.-Y. Natoli, and M. Commandre, "Effect of polishing process on silica surface laser-induced damage threshold at 355 nm," *Optics Communications*, vol. 242, no. 1, pp. 227–231, 2004, issn: 0030-4018. doi: https://doi.org/10.1016/j.optcom.2004.08.016. [Online]. Available: https://www.sciencedirect.com/science/article/pii/S0030401804008028.

[14] M. Trost, T. Herffurth, D. Schmitz, S. Schröder, A. Duparré, and A. Tünnermann, "Evaluation of subsurface damage by light scattering techniques," *Appl. Opt.*, vol. 52, no. 26, pp. 6579–6588, Sep. 2013. doi: 10.1364/AO.52.006579. [Online]. Available: http://ao.osa.org/abstract.cfm?URI=ao-52-26-6579.

[15] C. J. Stolz and F. Y. Génin, "Laser resistant coatings," in *Optical Interference Coatings*, N. Kaiser and H. K. Pulker, Eds. Berlin, Heidelberg: Springer Berlin Heidelberg, 2003, pp. 309–333, isbn: 978-3-540-36386-6. doi: 10.1007/978-3-540-36386-6_13. [Online]. Available: https://doi.org/10.1007/978-3-540-36386-6_13.

[16] V. Denis *et al.*, "The Laser Megajoule facility: laser performances and comparison with computational simulation," in *High-Power Laser Materials Processing: Applications, Diagnostics, and Systems VII*, S. Kaierle and S. W. Heinemann, Eds., International Society for Optics and Photonics, vol. 10525, SPIE, 2018, pp. 14–21. doi: 10.1117/12.2287342. [Online]. Available: https://doi.org/10.1117/12.2287342.

[17] D. Penninckx, S. Montant, J. Luce, É. Bordenave, É. Boursier, and C. Rouyer, "Impact of the kerr effect on fm-to-am conversion in high-power lasers," *Appl. Opt.*, vol. 60, no. 27, pp. 8277–8285, Nov. 2021. doi: 10.1364/AO.431738. [Online]. Available: https://opg.optica.org/ao/abstract.cfm?URI=ao-60-27-8277.

[18] J. Folta *et al.*, "Mitigation of laser damage on National Ignition Facility optics in volume production," in *Laser-Induced Damage in Optical Materials: 2013*, G. J. Exarhos, V. E. Gruzdev, J. A. Menapace, D. Ristau, and M. Soileau, Eds., International Society for Optics and Photonics, vol. 8885, SPIE, 2013, pp. 138–146. doi: 10.1117/12.2030475. [Online]. Available: https://doi.org/10.1117/12.2030475.

[19] T. Doualle *et al.*, "CO2 laser microprocessing for laser damage growth mitigation of fused silica optics," *Optical Engineering*, vol. 56, no. 1, pp. 1–9, 2016. doi: 10.1117/1.OE.56.1.011022.

[20] L. Mascio-Kegelmeyer, "Machine learning for managing damage on NIF optics," in *Laser-induced Damage in Optical Materials 2020*, C. W. Carr, V. E. Gruzdev, D. Ristau, and C. S. Menoni, Eds., International Society for Optics and Photonics, vol. 11514, SPIE, 2020. doi: 10.1117/12.2571016. [Online]. Available: https://doi.org/10.1117/12.2571016.

[21] C. Lacombe *et al.*, "Dealing with LMJ final optics damage: post-processing and models," in *Laser-induced Damage in Optical Materials 2020*, C. W. Carr, V. E. Gruzdev, D. Ristau, and C. S. Menoni, Eds., International Society for Optics and Photonics, vol. 11514, SPIE, 2020. doi: 10.1117/12.2571074. [Online]. Available: https://doi.org/10.1117/12.2571074.

[22] L. Kegelmeyer, P. Fong, S. Glenn, and J. Liebman, "Local area signal-to-noise ratio (lasnr) algorithm for image segmentation," *Proceedings of SPIE - The International Society for Optical Engineering*, vol. 6696, Oct. 2007. doi: 10.1117/12.732493.

[23] A. Conder, J. Chang, L. Kegelmeyer, M. Spaeth, and P. Whitman, "Final optics damage inspection (FODI) for the National Ignition Facility," in *Optics and Photonics for Information Processing IV*, A. A. S. Awwal, K. M. Iftekharuddin, and S. C. Burkhart, Eds., International Society for Optics and Photonics, vol. 7797, SPIE, 2010, pp. 167–178. doi: 10.1117/12.862596. [Online]. Available: https://doi.org/10.1117/12.862596.

[24] F. Wei *et al.*, "Automatic classification of true and false laser-induced damage in large aperture optics," *Optical Engineering*, vol. 57, no. 5, pp. 1–11, 2018. doi: 10.1117/1.OE.57.5.053112. [Online]. Available: https://doi.org/10.1117/1.OE.57.5.053112.

[25] G. Hallo, C. Lacombe, J. Néauport, and F. Hild, "Detection and Tracking of Laser Damage Sites on Fused Silica Components by Digital Image Correlation," *Optics and Lasers in Engineering*, vol. 146, p. 106 674, 2021.

Part I

Introduction

1

Introduction

1.1 Research objectives

Since its creation in 1960, the LASER (Light Amplification by Stimulated Emission of Radiation) has been used in many applications around the world: from the first machining operations [1] to bar code reading [2], not to mention communications [3] and medicine [4]. The idea of using lasers to study previously inaccessible states of matter at laboratory-scale was explored as from 1960 with a ruby laser system of 12 beams and named 4 PI [5, 6]. Since 1960, many laser facilties have been built to perform fusion experiments. The most recent megajoule-class laser facilities designed and built are the National Ignition Facility (NIF) [7] in the USA, the ShenGuang-III (SG-III) [8] in China and the Laser MegaJoule (LMJ) [9] in France. Such installations as well as petawatt class lasers are in some extent limited by the phenomenon called laser-induced damage of optical components [10]. Laser-induced damage, defined as a permanent change of optical components induced by laser beams, has a negative impact on laser performances and optimal operations of high power laser facilities [11]. In order to overcome the difficulties related to laser-induced damage, many works have been carried out to measure the damage laws of optical components as a function of laser parameters [10, 11], to increase the laser resistance of the optical components [12–14] and optical coatings [15], to improve the quality of laser beams [16], to develop methods of damage mitigation [17, 18] or even to extend life duration of optics on the beam lines [19, 20]. Other works have been conducted on the observation and monitoring of laser-induced damage directly on facilities [19–22].

The research objectives of the thesis cover the improvement of in-situ detection and monitoring of laser damage growth with focus on megajoule class laser facilities. The work carried out aims to be used to:

- limit the use of new optics by megajoule class laser facilities;
- improve the efficiency of the use of damage mitigation methods;
- increase the life span of optics.

1.1.1 Fusion scale laser facilities

The Comprehensive Nuclear-Test-Ban Treaty (CTBT) is a multilateral treaty that bans nuclear weapons test explosions and any other nuclear explosions, for both civilian and military purposes, in all environments [23]. Since 1996, 173 countries have ratified the CTBT, 13 have only signed it and 10 are in non-signatory status [24]. In order to ensure the operation of nuclear weapons while implementing the CTBT, France initiated the French Stockpile Stewardship program, namely, Simulation, based on three components [25]:

- the physics of weapons, defining all the physical phenomena involved in their operation;
- the numerical simulation of their performance;
- the experimental validation.

To validate the physical models, two large facilities, EPURE and the LMJ were defined. EPURE is dedicated to the non-nuclear phase of the weapon operation [26]. LMJ is used to reproduce on a very small scale the physical conditions of matter during the nuclear operation [27]. In the world, the 3 largest fusion scale laser facilities following similar objectives are:

- the National Ignition Facility (NIF) in the United States of America [28];
- the Laser MegaJoule (LMJ) in France [27];
- and the ShenGuang-III (SG-III) and ShenGuang-IV (SG-IV)in the People's Republic of China [8].

For each of the three facilities, an elementary nanosecond laser pulse is generated in an infrared wavelength ($1053\,\mathrm{nm}$). The energy of the pulse is amplified by passing through amplifying sections. Once amplified, the pulse is converted to an ultraviolet wavelength ($351\,\mathrm{nm}$) and focused on a millimeter-scale target placed in the center of an experimental chamber. The number of laser beams as well as some technological choices are the main differences between the 3 fusion class laser installations, but basically these laser systems are Nd:Phosphate flash pumped nanosecond frequency tripled lasers.

Laser MegaJoule (LMJ)

The Laser MegaJoule, a facility of $300\,\mathrm{m}$ length and $50\,\mathrm{m}$ high, was designed to deliver up to $1.4\,\mathrm{MJ}$ in a pulse duration from $1\,\mathrm{ns}$ to $20\,\mathrm{ns}$ (Figure 1.1). To reach this objective, this facility involves 176 laser beams, structured in quads (set of 4 beamlines) and bundles (set of 2 quads). One specific beam, so-called PETAL (PETawatt Aquitaine Laser), aims to reach petawatt experiments [29]. The maximum laser energy delivered by each LMJ beam is $7.5\,\mathrm{kJ}$ in the UV wavelength for a pulse duration of $3\,\mathrm{ns}$.

Figure 1.1: Laser MegaJoule facility in France [27].

The laser system is divided into 4 sections (Figure 1.2):

- Laser pulse generation. The initial laser pulse is generated by a main oscillator at $1053\,\mathrm{nm}$, so-called 1ω, at an energy of a few nanojoules. The energy of the pulse is then amplified from a few nanojoules up to $1\,\mathrm{J}$ in pre-amplifier modules. After this pre-amplification step, the beam size is about a $40\,\mathrm{mm}$ side square.
- Amplifying section. The pre-amplified pulse is then injected in the 4 pass with angular multiplexing amplifying section to reach an energy up to $20\,\mathrm{kJ}$. The laser beam is expanded to about $35\,\mathrm{cm}$ x $35\,\mathrm{cm}$. This section includes 16 glass plates doped with neodymium and pumped by flashes. The pulse passes 4 times through the amplifying section to reach the required energy and through spatial filters to filter out unwanted spatial frequencies.

- Transport section. The laser pulse at 1ω is then carried over approximately $40\,\mathrm{m}$ to the experiment chamber through a set of 5 to 6 mirrors.

- Frequency conversion and focusing section. The wavelength conversion from $1053\,\mathrm{nm}$ (1ω) to $351\,\mathrm{nm}$ (3ω) is performed by potassium dihydrogen phosphate (KH_2PO_4: KDP) and 70% deuterated potassium dihydrogen phosphate ($D_xKH_{2-x}PO_4$ with x the level of deuteration: DKDP) crystals. After the KDP component, the main pulse wavelength is $527\,\mathrm{nm}$, and $351\,\mathrm{nm}$ after the DKDP component. A grating is used to focus the 3ω laser beam at the center of the experiment chamber where there is a target. Before reaching the target, each laser beam propagates through a large fused silica optical component, so-called vacuum window. A vacuum window is a $425\mathrm{x}444\,\mathrm{mm}^2$ fused silica optics with $34\,\mathrm{mm}$ thickness that ensures the vacuum tightness between the experiment chamber and the other part of the facility.

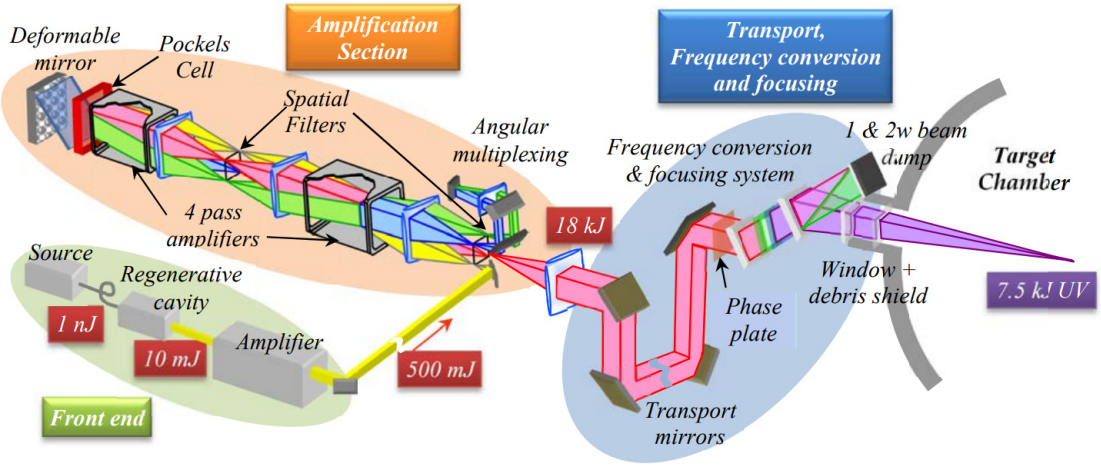

Figure 1.2: Schematic view of a Laser MegaJoule beam line [30].

The main characteristics about the Laser MegaJoule facility are gathered in Table 1.1.

National Iginition Facility (NIF)

The National Ignition Facility in the United States of America involves 192 laser beams in order to support among other programs the Stockpile Stewardship and the Inertial Confinement Fusion (ICF). It was designed to deliver more than $2\,\mathrm{MJ}$. The main differences with an LMJ beamline are

Features	Values
Building size	$300\,\mathrm{m}$ x $150\,\mathrm{m}$ x $40\,\mathrm{m}$
Number of laser beam	176
Final wavelength	$351\,\mathrm{nm}$
Ultraviolet laser energy on target	$1.4\,\mathrm{MJ}$
Laser beam size before focusing grating	$35\,\mathrm{cm}$ x $35\,\mathrm{cm}$
Pulse duration	From $1\,\mathrm{ns}$ to $20\,\mathrm{ns}$
Number of fused silica optics	2288
Number of KDP and DKDP crystal	528
Number of glass plates doped with neodymium	2816
Number of mirrors	1424

Table 1.1: Some features of the Laser MegaJoule facility.

the technical solutions to amplify and to focus the laser beam. At NIF, a focusing lens was chosen whereas a focusing grating is used at LMJ. The NIF is build since 2009 and in operation since then.

ShenGuang-III (SG-III)

The ShenGuang-III (SG-III) in the People's Republic of China is designed to reach a laser energy at 3ω of $200\,\mathrm{kJ}$ in a pulse duration of $3\,\mathrm{ns}$. This facility involves 48 laser beams. The design of a SG-III beamline is very similar to that of NIF.

1.1.2 Laser-induced damage

One of the phenomena limiting the operation of NIF, LMJ and SG-III is laser-induced damage of their optics [10]. Laser-induced damage is defined as a permanent degradation of a component due to the interaction between a laser beam and matter. It may be in the bulk or at the surface of the optics [31]. Many studies have been carried out to understand the influence of parameters on laser damage [11, 32–34]. These parameters concern the material properties of the optics or the characteristics of the laser beams. Laser-induced damage occurs in all optics [10], such as:

- the laser glass slabs doped with neodymium of the amplifying section;
- the optical glass with multilayer dielectric coatings in the transport section;
- the KDP/DKDP cristals finished with anti-reflective sol gel coatings in the frequency conversion section;

- the fused silica focusing gratings with anti-reflective coatings;
- the fused silica plates with anti-reflective coatings (vacuum windows and debris shields).

The laser-induced damage initation and growth mechanisms of fused silica components in ultraviolet and nanosecond range are described hereafter. The optics are more prone to damage by a UV beam than by an IR one [35]. The purpose of this thesis is limited to laser-induced damage of the LMJ fused silica vacuum windows and possibly to the gratings.

Vacuum window

At completion, 176 vacuum windows will be mounted on the LMJ facility. A vacuum window is a $40\,\mathrm{cm}$ x $40\,\mathrm{cm}$ fused silica component with $34\,\mathrm{mm}$ thickness (Figure 1.3). Fused silica is a glass that can be used to make large components with high resistance to UV laser damage [36].

Figure 1.3: A LMJ vacuum window [37].

Manufacturing of fused silica components consists of several steps:

- Silica synthesis - Vacuum windows are made of Suprasil S312 silica from Heraeus company by vapor phase oxidation reaction of $SiCl_4$, between $1300\,°\mathrm{C}$ and $1600\,°\mathrm{C}$ by Outside Vapor Deposition (OVD) [38]. Synthesized silica is then consolidated and vitrified at $2000\,°\mathrm{C}$. In order to obtain a laser wave front compatible with the experiments carried out at LMJ, the silica must be homogeneous and without inclusions.

- Shaping and polishing steps - The first step is to prepare the silica block to roughly obtain the shape of the vacuum windows. A grinding wheel is used to reduce the roughness and flatten the surface with a deviation from the requested shape of tens of micrometres. The next polishing step uses loose abrasive or fixed grinding to obtain a flatness of few micrometres. The final polishing step is based on loose abrasive and additionnal technics such as magnetorheological finishing. The flatness is hundreds of nanometres and the roughness is less than $1\,\mathrm{nm}$. After all polishing steps, the optical component is transparent.

- Anti-reflective coatings - In order to optimize 3ω transmission, anti-reflective coatings are applied by sol-gel process on the faces of the vacuum windows. The coating is composed of nanometre-scaled silica particles in ethanol. A thickness of $72\,\mathrm{nm}$ of this coating applied onto the vacuum window faces ensures a light transmission of 99.95% at 3ω wavelength.

Damage initiation

The polishing process can be described as the abrasion of silica by metal oxyde particles. This abrasion induces the formation of 2 distinct layers on the surface of the optical component [39, 40]:

- the so-called Beilby layer, a densified layer of silica (Figure 1.4) ;

- a layer that contains subsurface fractures, known as Sub-Surface Damage (SSD). Such SSD contain contaminants from the polishing process as well as structural defects induced by the fracturation of the silica network.

Without defects, silica used to create vacuum windows exhibits a very low absorption of 3ω photons. Sub-surface damage with contaminants are sources of 3ω photon absorption when they pass through the optical components [42]. When the 3ω laser beam reaches an SSD, the photons stimulate electrons by single and multi-photon absorption. This stimulation of electrons increases locally the temperature. When the temperature exceeds $10\,000\,\mathrm{K}$, the silica is locally ionized and a plasma is created. This plasma induces an increase in pressure and temperature. The plasma expansion generates a shock wave that locally fractures the matter. Damage sites initiated by a 3ω laser can be described as micrometric craters with subsurface cracks (Figure 1.5). The plasma expansion is greater on the

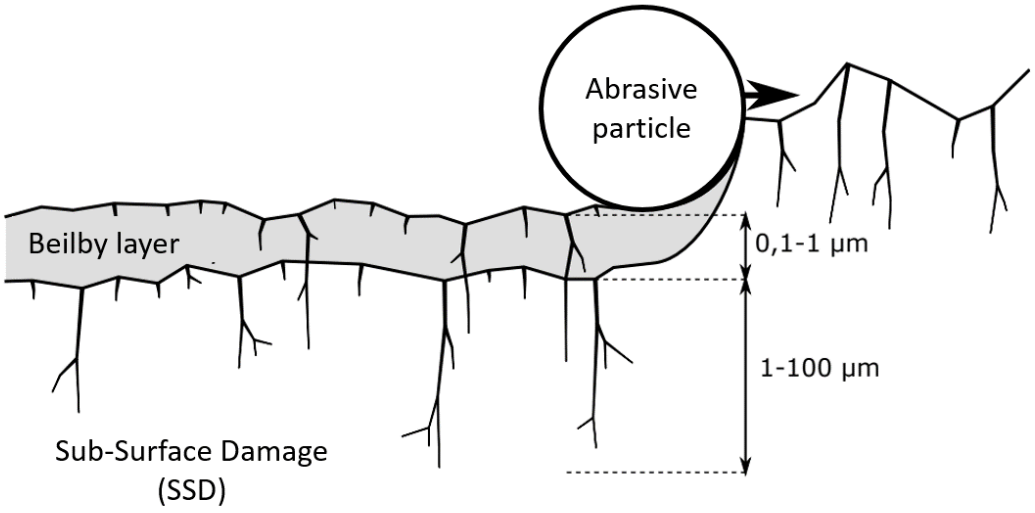

Figure 1.4: Schematic view of the Beilby and SSD layers on the fused silica optics induced by the polishing steps [41].

rear face, which makes it more susceptible to laser damage than the front face. Hence, SSD with contaminants are responsible for damage initiation on fused silica optics [43–45]. The density of initiated damage sites is a function of the laser fluence that reaches the optical component [10].

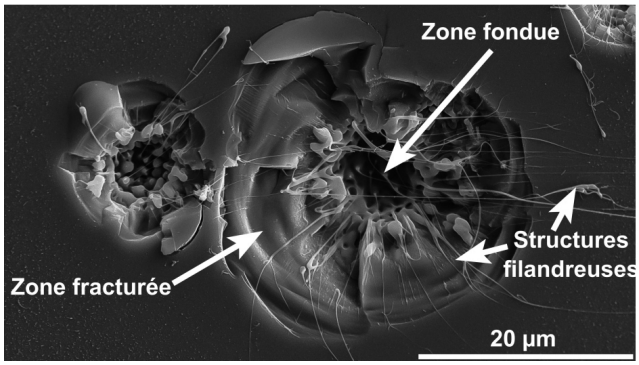

Figure 1.5: Scanning electron micrograph of damage sites induced by a 3ω ($351\,\mathrm{nm}$) laser beam at a fluence of $\approx 50\,\mathrm{J\,cm^{-2}}$ on the exit surface of a fused silica sample [41].

Damage growth

Each initiated damage site on a fused silica component is considered as a UV absorbing defect. When a damage site is exposed to a UV laser beam at sufficiently high fluence, a plasma is locally generated and same mechanisms as described for damage initiation apply. As a result, a damage site may grow when it is exposed to a laser shot (Figure 1.6).

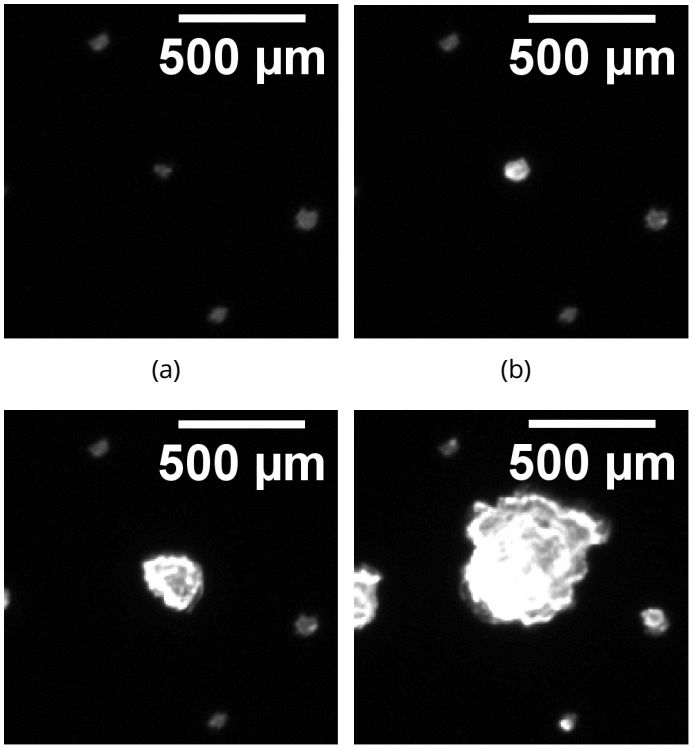

Figure 1.6: Example of a laser-induced damage growth sequence at 3ω on a fused silica sample for a pulse duration of $5\,\mathrm{ns}$ and a fluence of $\approx 8\,\mathrm{J\,cm^{-2}}$. Images acquired after (a) one laser shot, (b) 12 laser shots, (c) 20 laser shots and (d) 40 laser shots.

Laser-induced damage growth is a stochastic phenomenon [46, 47]. The damage growth probability is dependent on laser fluence, pulse duration, laser wavelength and damage size among others [33, 35, 48, 49]. Below $4\,\mathrm{J\,cm^{-2}}$, at 3ω for a pulse duration of $3\,\mathrm{ns}$, the damage growth probability is close to zero [33]. It was also demonstrated that multi-shot damage growth is exponential for pulse duration greater than $2\,\mathrm{ns}$ [33]

$$d_N = d_0 e^{\alpha(\phi)N} \tag{1.1}$$

where d_N is the site diameter measured after the N^{th} laser shot, N the number of shots at fluence ϕ, and α the exponential growth coefficient. Linear growth was observed for pulse duration ranging between $1\,\mathrm{ns}$ and $2\,\mathrm{ns}$ [33]

$$d_N = d_0 + g(\phi)N \tag{1.2}$$

where g denotes the linear growth coefficient.

As a result of efforts to reduce damage initiation density [45], damage growth is now considered, more than damage initiation, as one of the main difficulties in LMJ operation. Many large damage sites on a vacuum window may induce the failure of the component at the interface between the vacuum of the experiment chamber and the air of the rest of the facility. It is then necessary to monitor damage growth on the vacuum windows in order to improve LMJ optics lifetime. This is considered as a key objective of the thesis.

1.1.3 Project organization at LMJ for laser-induced damage

Laser-induced damage affects the LMJ operation in several ways:

- Safety of the facility. LMJ vacuum windows ensure the vacuum tightness of the experiment chamber. The thickness of the vacuum window is $34\,\mathrm{mm}$. The large growth of a damage site may lead to the failure of the vacuum window.

- Laser performance. When a laser beam illuminates a damage site, the latter absorbs and scatters part of the laser beam. Absorption by damage leads to a decrease in the vacuum window transmission and thus to a lower laser energy on the target. Light scattering by the sites induces a spread of the focal spot at the center of the experiment chamber. Thus, the decrease of laser performances due to laser damage influences the successful achievement of experiments.

In order to reduce the impact of laser damage on LMJ operation, scientific and operational teams work on laser-induced damage metrology and propose solutions to limit damage growth and to monitor damage.

Laser-induced damage metrology

In order to quantify influences of laser and material parameters on damage initiation and growth, many laser damage set-ups were developed. Most of these set-ups were first based on Gaussian beams with micrometer diameters [35, 50–54]. Such set-ups were used to better understand

optics damage. For instance, it was demonstrated that improving polishing process reduced the density of initiated damage sites [52]. The effect of laser pulse duration on laser damage in KDP and fused silica was also investigated [55]. It was demonstrated that combination of UV and IR wavelengths have an effect on initiation and growth in fused silica [35].

To go further, testing set-ups with large beams were then designed such as Optical Sciences Laser Upgrade (OSL upgrade) at the Lawrence Livermore National Laboratory [56] and MELBA (Moyen d'Endommagement Laser et Banc d'Analyse in French) at the CEA [57, 58]. Such large beam set-up were designed to be more representative of NIF and LMJ facilities [41]. The beam diameter of OSL is $\approx 11\,\mathrm{cm}$ with a shot rate of $60\,\mathrm{min}$. OSL Upgrade allows for damage investigation at high-fluence and large aperture.

For the thesis, dedicated experiments were performed on the MELBA laser testing set-up in order to validate the proposed methods (Chapters 5 and 7). MELBA testing set-up provides a smaller beam ($\approx 9\,\mathrm{mm}$) but a faster shot rate ($1\,\mathrm{min}$) than OSL Upgrade. A 3ω homogenous laser beam is produced every minute with tunable duration and temporal profile of the pulse (Figure 1.7). Many laser diagnostics give access to a precise metrology of the studied parameters. Imaging systems are used to acquire images of damage sites not only on the surface but also in the bulk of the tested component [59]. An automatic data processing software and a control system were developed to quickly generate test results with numerous laser shots. MELBA was used to study the impact of the temporel profile on laser damage of LMJ final fused silica optics [42].

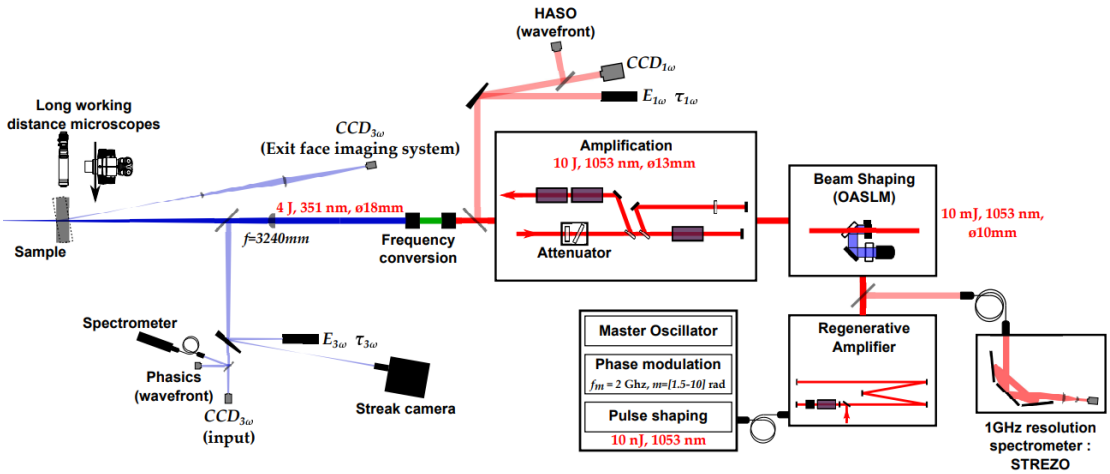

Figure 1.7: Schematic view of the MELBA laser damage testing set-up [57].

Solutions to increase lifetime of LMJ optics

Several methods were developed or are currently in development to increase liftime of LMJ fused silica optics.

Regarding new optics, the works are focused on decreasing the number of subsurface defects (SSD), scratch digs, contaminants and all possible sources of damage initiation. The main idea is to reduce contaminants in the Beilby layer. For instance, alternative polishing processes were developed such as MagnetoRheological Finishing (MRF) or Ion Beam Figuring (IBF) [60, 61].

Secondly, an optics recycle loop is currently being deployed [62, 63]. The aim is to increase lifetime of damaged optics before purchasing new optics. The recycle loop process is described in Figure 1.8. The strategy

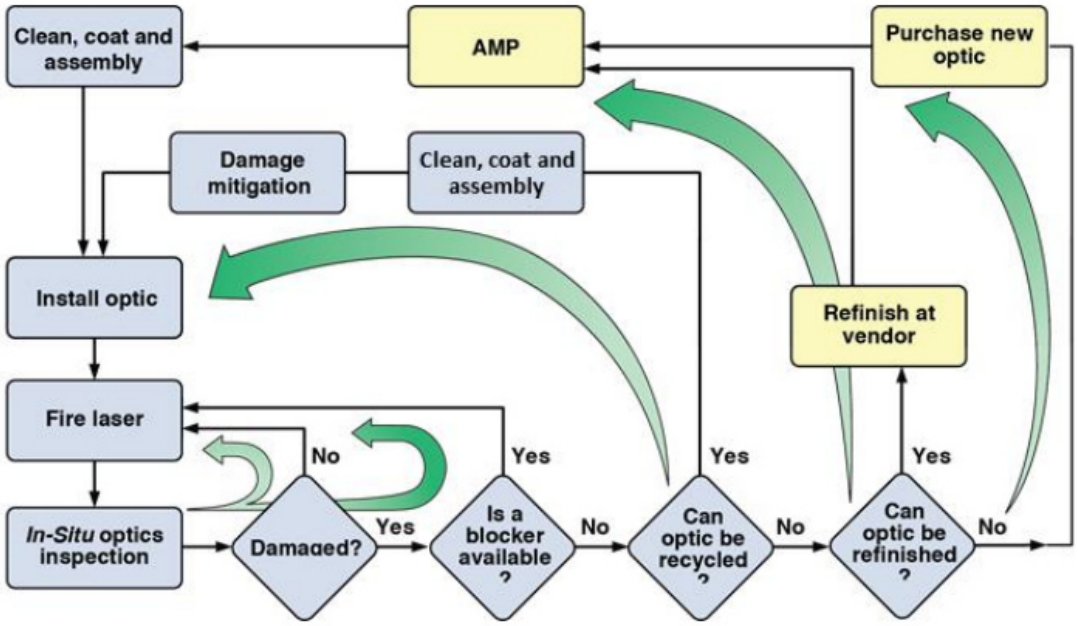

Figure 1.8: Optics recycle loop strategy for NIF [62]. The LMJ recycle loop is similar.

of the optics recycle loop relies on several steps:

- **In-Situ optics inspection** after each laser shot - This step is the main point of this thesis and the state of the art regarding in-situ inspection is described in Section 1.2.1. The aim is to detect and monitor damage initiation and growth of damage sites smaller than $750\,\mu\mathrm{m}$ in diameter.

- **Beam blockers** - Beam blockers consist in shadowing some damage sites to locally reduce the laser beam fluence less than the growth threshold. As a consequence, damage growth is inhibited at the position of each beam blocker [20]. However, the use of beam blockers reduces the laser beam energy. As a consequence, the number of beam blockers per beam is limited to between 10 and 20 at LMJ.

- **Damage mitigation** by CO_2 laser microprocessing - The method is based on fast microablation of silica. Conical craters are obtained by moving a CO_2 laser spot using a galvanometer beam scanner [18, 62]. Crack-free craters were designed to be more resistant to laser damage than initial damage sites. However, such method is limited to submillimetric damage sites ($750\,\mu m$ in diameter) and requires optics removals from the facility to be applied.

Optimal operation of fusion class laser facilities induces to limit the number of optics removals. Vacuum window removal is needed when the beam blockers are not sufficient to limit the size of damage sites less than $750\,\mu m$. Therefore, to optimize the vacuum window lifetime it is aimed to apply beam blockers to the fastest growing damage sites.

In summary, it is necessary:

- to measure precisely the size of each damage site on the vacuum window;

- to quantify damage growth of each site smaller than $750\,\mu m$ in diameter.

Both metrological requirements must be satisfied without removing the vacuum windows from the facility. Therefore in-situ damage observation and monitoring are necessary.

In-situ damage observation

At LMJ, several systems are used to observe damage on the optics along the beam path:

- The observation of damage sites of optics in the amplifying section is based on strioscopy principle [64];

- Damage sites in the amplifying, transport and final sections are observed using light diffraction by damage sites [22, 64];

- Images of final optics are acquired by an imaging sytem set at the center of the experiment chamber. This system is based on the acquisition of light scattering signals emitted by damage sites when the latters are lit by a dedicated LED-based system [20, 22].

The use of different observation systems according to the position of the components is due to constraints on the facility. The works carried out during this thesis are applied to damage monitoring on LMJ final optics and especially the vacuum windows. However, some methods may be applied to damage monitoring using others imaging systems. A state of the art regarding in-situ damage observation, detection and monitoring for vacuum windows is provided in Section 1.2.

1.2 State of the art

Efficient in-situ damage monitoring of LMJ vacuum windows involves good understanding and mastering of the following steps:

- Image acquisition;
- Corrections of the images;
- Detection of damage sites on the images;
- Estimation of damage diameters;
- Damage growth monitoring.

The state of the art for each step of damage monitoring of vacuum windows is described in the following sections. The identified limitations of each existing method and technical solutions are discussed.

1.2.1 Observation of laser-induced damage

The observation of laser-induced damage of vacuum windows is based on the acquisition of light scattering signals of the damage sites [22]. The observation system is divided into 2 devices:

- Lighting equipment;
- Image acquisition device.

Each vacuum window is located in a restricted environment, on the edge of the $8\,\mathrm{m}$ radius experiment chamber. There are many optics around the vacuum window: upstream the focusing grating, downstream the debris shield and the disposable debris shield. This space constraint was important for the design of the observation system.

Lighting section

The aim of the lighting system is to make visible damage sites on the vacuum window. It was chosen to take advantage of light scattering by laser-induced damage sites. When a damage site is lit, it scatters light in the whole space [14]. The lighting system is made up of:

- Two green Light-Emitting Diodes (LEDs) to lit the damage sites from one edge of each vacuum window;
- An aluminum alloy frame that maintains the vacuum window;
- The vacuum window.

The LEDs (Nischia NSPG500DS) provide a maximum emissivity at $525\,\mathrm{nm}$. These green LEDs are mounted on one edge of each vacuum window. The light provided by the LEDs enters into the optics and illuminates the rear and front sides of the vacuum window. The light that reaches the frame is reflected and scattered in the vacuum window. Light scattering by the frame contributes to homogenize the lighting of the rear face of the vacuum window.

Image acquisition section

The aim of the imaging system, the so-called MDCC (Module Diagnostic Centre Chambre in French), is to collect the light scattering signals emitted by potential damage sites and to generate images (Figure 1.9). In order to use only one system to acquire images of the 176 vacuum windows, the selected solution was to put the imaging system at the center of the experiment chamber after each laser shot. Thus, the acquisition system is attached on a motorized arm as shown in Figure 1.9. The latter inserts the system at the center of the experiment chamber and removes it.
The image acquisition solution, described in Figure 1.10, consists of:

- An optical lens that collects a part of the scattered light by damage sites to create an image of the observed vacuum window. The lens was optimized for 3 wavelengths ($525\,\mathrm{nm}$ for the observation of the

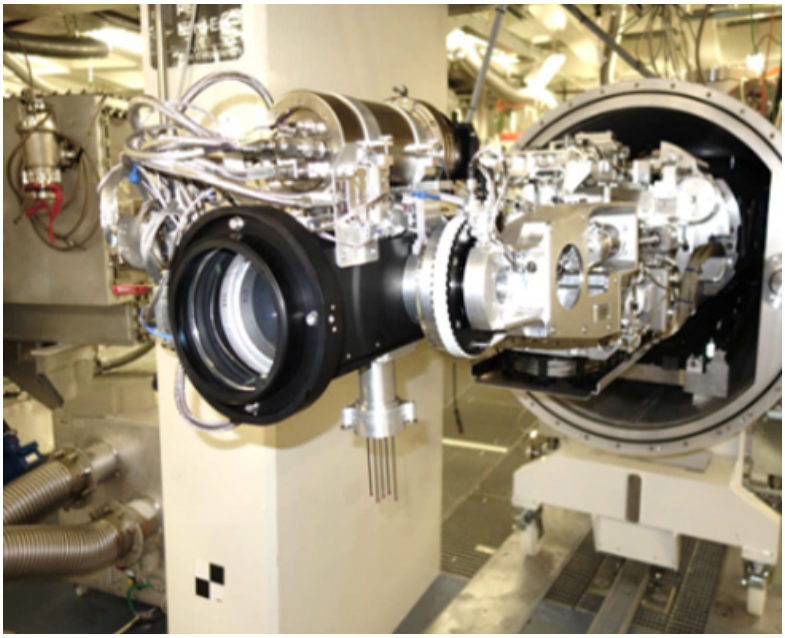

Figure 1.9: Image acquisition system of laser-induced damage on vacuum windows and the motorized arm [CEA].

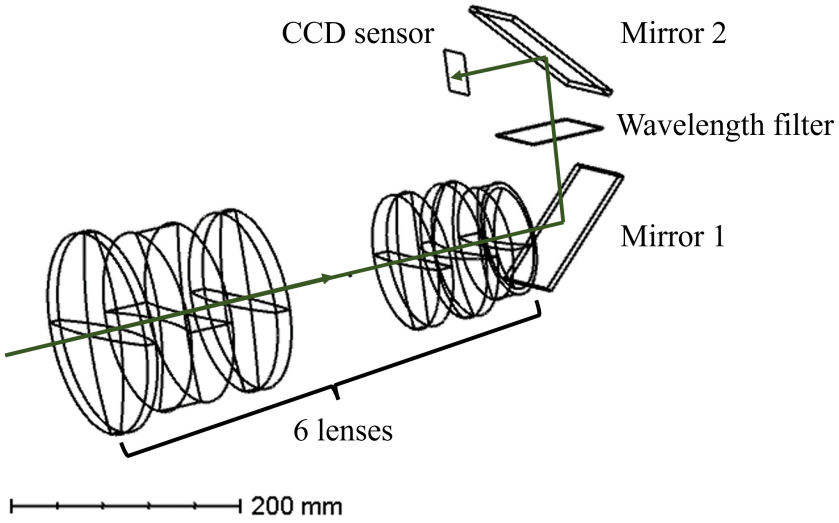

Figure 1.10: 3-dimensional representation generated with Zemax of the image acquisition system with 6 lens, two mirrors, one wavelength filter and a CCD sensor.

vacuum windows, $650\,\mathrm{nm}$ for the observation of the focusing grating and $351\,\mathrm{nm}$ for the acquisition of low energy laser beams). Such optimization led to an optical design with 6 lenses. In order to provide a compact system, 2 mirrors are used to fold the optical path.

- A wavelength filter with a band-pass at $525\,\mathrm{nm}$ to select the useful green light for damage observation on vacuum windows.
- A Coupled-Charge Device (CCD) that digitally records the resultant image. This sensor is a full frame CCD with 4096 x 4096 photo active pixels. The CCD sensor is cooled at $-25\,°\mathrm{C}$ in order to reduce thermal noise.

The resulting acquisitions are dark-field pictures on which damage sites are visible as bright spots (Figure 1.11). On this image, LEDs are on the right side. The background of the image is non-uniform due to lighting by LEDs and light reflections on other optics or mounted devices. The distance between the MDCC and the vacuum windows is about $8\,\mathrm{m}$. 88 vacuum windows are located at $780\,\mathrm{cm}$ from the MDCC (long-distance configuration) while 88 windows at $740\,\mathrm{cm}$ (short-distance configuration). Thus, the spatial resolution of the MDCC images when observing the vacuum windows is $102\,\mu\mathrm{m}$/pixel or $107\,\mu\mathrm{m}$/pixel depending on the configuration.

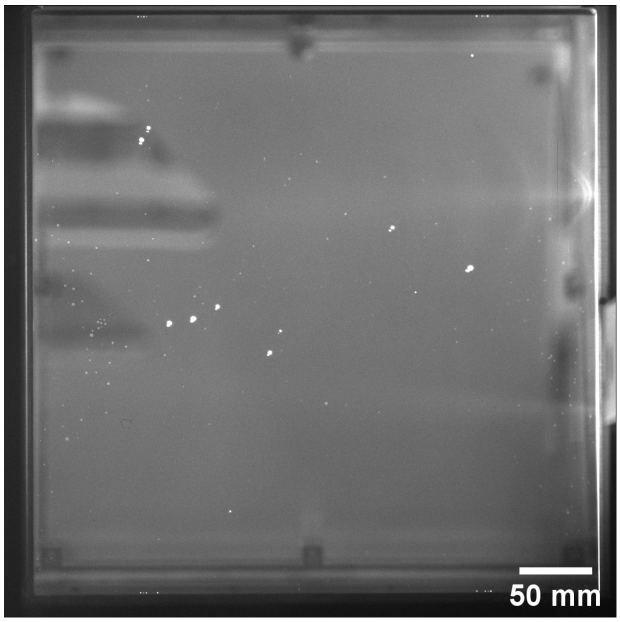

Figure 1.11: Acquired image of a vacuum window by the MDCC.

1.2.2 Laser-induced damage detection

An efficient algorithm for damage detection on vacuum window images is of major importance to accurately monitor damage growth, evaluate their impact on optics lifetime and to anticipate maintenance needs by predicting damage growth over the next laser shots. The main objectives of detection algorithm are:

- Detect damage sites as soon as possible at a sub-pixel resolution in order to evaluate damage growth on several shots before they reach $750\,\mu\mathrm{m}$ in diameter ;
- Give the position of each damage site in vacuum windows.

Different algorithms are used to detect damage sites such as simple thresholding, local thresholding or machine learning techniques. Such algorithms and their limits for vacuum window damage detection applications are described thereafter.

Simple thresholding

Thresholding techniques are widely used for separating an object considered as the target from the image background. For damage detection, the targets are damage sites and rest of the image is defined as the background. The aim of the thresholding technique is to identify pixels corresponding to damage sites and to set the corresponding pixel values to 1 while values of background pixels are set to 0. For simple thresholding, the same threshold is applied to all pixels of the image. Simple thresholding is described by

$$if \quad I(x,y) < T, \quad I(x,y) = 0 \qquad otherwise \quad I(x,y) = 1 \tag{1.3}$$

where (x, y) are pixel coordinates in an image I, and T the threshold level. Such value is chosen in order to obtain the required result.

It is possible to determine automatically the threshold value by numerous algorithms such as Otsu method [65]. A bimodal image is an image with two distinct groups of pixel values. The histogram of such image contains two peaks. With Otsu thresholding, the threshold is defined as the middle of both peaks.

This simple thresholding technique is efficient to detect damage sites when the background values are spatially homogeneous on the image and when pixel values of targets are always higher than global background intensity [66]. Such requirements are satisfied when damage sites are

detected on images with no disturbances such as images acquired on laser damage testing set-up. However, vacuum window images do not satisfy the present requirements since they suffer from disturbances due to the commissioning and operation of the facility. A constant thresholding method is not suitable for complex images such as vacuum window images.

Adaptive thresholding

Contrary to methods involving a constant threshold for all pixels, adaptive thresholding is based on a local threshold value that adapts itself to the background intensity. The threshold level is calculated for smaller regions.

A widely used adaptive thresholding technique is the so-called Local Area Signal-to-Noise Ratio (LASNR) [21]. This algorithm is based on a local analysis of the signal-to-noise ratio of an image, I. The local noise level is calculated at each pixel with respect to its neighboring pixels as follows

$$noise_I = \sqrt{G(I, \sigma_2)} \tag{1.4}$$

where σ_2 is selected according to the expected size of the neighborhood, and G a Gaussian function.

A signal image is defined as

$$signal_I = I - G(I, \sigma_1) \tag{1.5}$$

where σ_1 is a radius lower than the smallest damage sites, generally a fraction of a pixel to increase the intensity of small damage sites (smaller than one pixel).

From these two images ($noise_I$ and $signal_I$), an LASNR image is defined as

$$LASNR_I^2 = \frac{signal_I |signal_I|}{noise_I^2} \tag{1.6}$$

Then, damage sites are identified when a pixel satisfies the following condition

$$LASNR_I^2 > Threshold \tag{1.7}$$

For each cluster of pixels satisfying the previous inequality, the pixel location with maximum intensity is called a seed of a damage site.

Once seeds are identified, the extent of each damage site is determined from each seed by adaptive filling. The aim of such adaptive filling is to correctly label pixels around the seed as part of the damage site. Such method avoids to falsely label the background as part of damage. The image of a damage site is obtained iteratively from the seed pixel according

to a criterion on pixel intensity and ratio of added pixels at each step. If one of the following criteria is meet during a step, the adaptive filling procedure stops:

- Criterion of ratio of added pixels - The ratio of added pixels during a step to the number of pixels added during all previous steps is greater than a threshold in order to avoid to add pixels of noise or background to damage sites.
- Intensity criterion - The intensity of potential added pixels is less than a minimum fraction of the seed pixel intensity.

Another adaptive thresholding method, based on Local Area Signal Strength (LASS) algorithm and 2-D histograms, was applied to detect small defects in final optics damage in-situ inspection [66]. The LASS algorithm is applied to estimate the local area signal strength for each pixel of the image. The calculation of LASS values is almost identical to that of LASNR values described previously. Then an improved 2-D histogram is generated (see Figure 1.12). The vertical axis is the pixel intensity, while the abscissa axis corresponds to LASS (or LASNR) values. The points of the rightmost curve represent damage site edges or small damage sites while the leftmost curve indicate large defects.

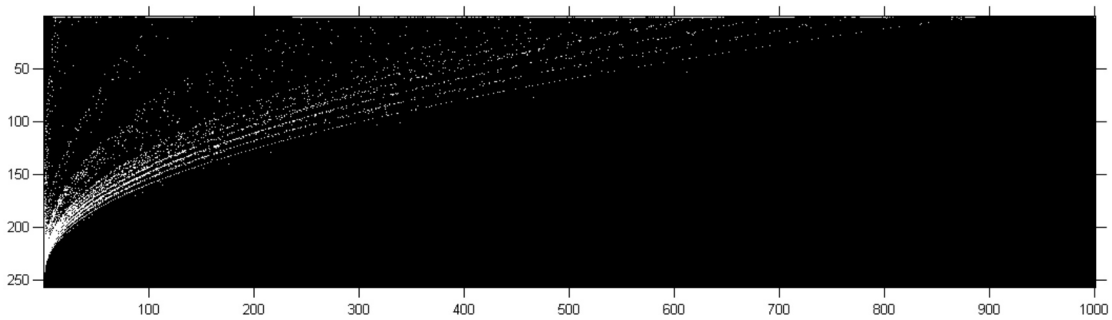

Figure 1.12: 2-D histogram with pixel intensity on the vertical axis and LASS value on the horizontal axis [66].

Damage segmentation performances of Otsu algorithm and LASS + 2D histogram were compared on an SG-III final optics image (Figure 1.13) [66]. The Otsu method works correctly since background values are spatially homogeneous. The LASS+2D histogram technique detects more damage sites than the Otsu method. However, more parameters are to be tuned for LASS+2D-histogram or LASNR algorithms. It is therefore necessary to be sure that the choice of parameters allows for the correct processing of the hundred images of damaged vacuum windows.

(a) (b) (c)

Figure 1.13: (a) Original image acquired by the image acquisition system of SG-III final optics. Segmentation results using (b) Otsu method and (c) LASS + 2D histogram [66].

1.2.3 Identification of true damage sites

In order to monitor damage growth, it is necessary to check if detected sites are damage sites. Several algorithms using machine learning techniques were used to identify true damage sites among all detected sites by simple or adaptive thresholding:

- Identifying optical reflections among potential damage sites [67]. Such algorithm is based on a decision tree with training on a very large number of damage sites labelled by human experts. Once the decision tree is trained, the correct identification of optical reflections among true damage sites is 99.8%.

- Identifying if a damage site is on the front or rear faces of the optical component with a precision of 95% whereas the success of analytical methods is less than 50% [68]. 27 attributes are associated with each damage site. The algorithm was trained on 1200 data points (about 60 damage sites with 20 laser shots on each site). A classification algorithm based on a sparse autoencoder and Extreme Learning Machine (ELM) was also developed to quickly identify damage sites on the input or exit face of the optics [69].

- Identifying true and false damage sites using a Kernel Extreme Learning Machine (K-ELM) model based on feature vectors consisting of 16 features [70]. Some features are the mean intensity, the image coordinates of the site, the LASNR value or the noise intensity. The

accuracy rate of the K-ELM classifier is 97% for the tested dataset. For this dataset, the size of damage sites varied between $50\,\mu\mathrm{m}$ and $1200\,\mu\mathrm{m}$.

Thresholding algorithms (simple or adaptive) are widely used to detect potential damage sites. Machine learning techniques were also developed to identify true damage sites among all potential damage sites. The training of such algorithms need a huge database created after numerous metrologies of damaged optics during maintenance process. Currently, only few maintenance activities are performed at LMJ and no set-up is dedicated to the precise and automatic observation of damaged optics while the NIF facility does [71].

1.2.4 Measurement of damage diameter

Once damage sites are detected and identified on images, the next step is damage diameter estimation. Two main methods are used to estimate the diameter of damage sites on final optics of fusion-class laser facilities:

- Direct diameter measurement;
- Diameter estimation by total integrated signal.

Direct diameter measurement by pixel-counting method

Direct diameter measurement refers to counting the number of pixels illuminated by the damage site

$$D = 2\sqrt{\frac{nb_{pixels}pixel_{field}}{\pi}} \tag{1.8}$$

where D is the estimated diameter, nb_{pixels} the number of illuminated pixels by a damage site, and $pixel_{field}$ the object field observed by a pixel of the imaging system.

High spatial resolution imaging systems are used to study damage growth on laser damage testing set-up. When the object field observed by a pixel is small compared to the size of damage sites and observed damage site are in the depth of field, a direct diameter measurement is efficient to estimate damage diameter, as shown in Figure 1.15. In case of observations out of depth of field, pixel-counting method overestimates measured diameters.

However, the spatial resolution of final optics imaging systems is about $100\,\mu\mathrm{m}$/pixel at NIF and LMJ and $200\,\mu\mathrm{m}$/pixel at SG-III for monitoring damage sites whose size ranges between $30\,\mu\mathrm{m}$ and $1\,\mathrm{mm}$. In order to visualize the difference between spatial resolution on a laser damage testing set-up (MELBA) and spatial resolution available at LMJ, an image of a damage site, whose diameter is $214\,\mu\mathrm{m}$, is shown in Figure 1.14. The discretization

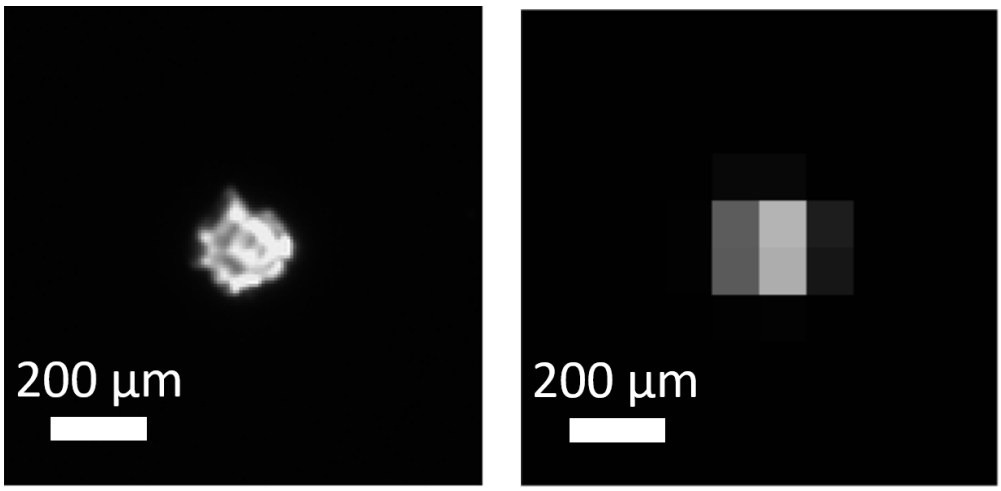

(a) (b)

Figure 1.14: (a) Image of a damage site whose diameter is $214\,\mu\mathrm{m}$ acquired on MELBA set-up with a pixel field of $6.5\,\mu\mathrm{m}$. (b) Image of the same damage site but with a pixel field of $100\,\mu\mathrm{m}$ corresponding the spatial resolution of images acquired on LMJ. To obtain the image with a pixel field of $100\,\mu\mathrm{m}$, a $15x15$ binning was applied to the MELBA image.

of diameter estimates based on pixel counting method is described in Figure 1.15. For instance at NIF and LMJ, the smallest measured diameter is $\approx 100\,\mu\mathrm{m}$ when a damage site lits only one pixel. Consequently, a variation of diameter is indistinguishable with direct measurement of diameter for damage sites smaller than $100\,\mu\mathrm{m}$ and poorly described for sites smaller than $300\,\mu\mathrm{m}$. For diameters less than $300\,\mu\mathrm{m}$, the discretization on measured diameters due to the spatial resolution prevents accurate measurements of damage size on LMJ vacuum windows. For damage sites larger than $300\,\mu\mathrm{m}$, the accuracy of damage size measurement by pixel counting at a spatial resolution of $100\,\mu\mathrm{m}$/pixel (LMJ and NIF) is almost equivalent to the accuracy with a resolution of $6.5\,\mu\mathrm{m}$/pixel (MELBA set-up) (Figure 1.15).

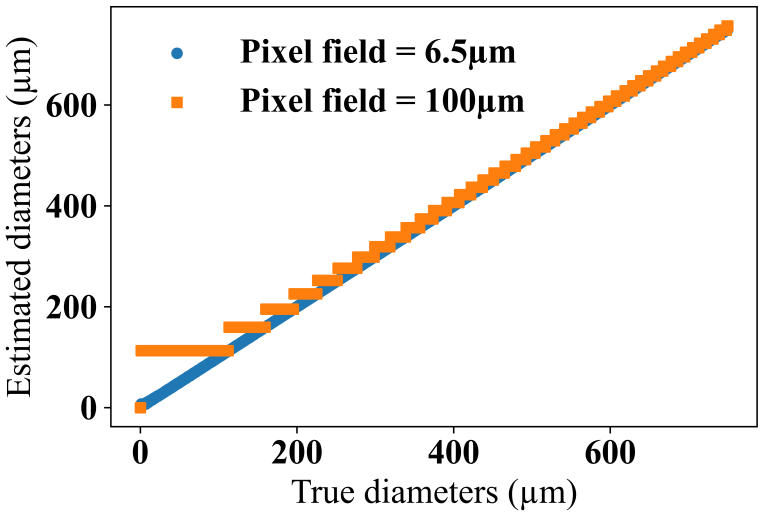

Figure 1.15: Diameter estimation by pixel counting method for a pixel field of $6.5\,\mu\mathrm{m}$ in blue and one of $100\,\mu\mathrm{m}$ in orange.

Diameter measurement from total integrated signal

Diameter measurement by pixel-counting method is not accurate for damage sites smaller than $300\,\mu\mathrm{m}$ while it is necessary to be able to estimate their size. In order to improve the resolution of in-situ diameter measurement, a method based on Total Integrated Signal (TIS) was proposed to estimate diameters of damage sites [22]. TIS is the gray level sum of pixels lit by a damage site. Such method relies on radiometry. Measured TIS values at NIF were calibrated on true diameters of damage sites (Figure 1.16). This calibration procedure was carried out by setting on a beamline an optic with a set of damage sites whose diameter was accurately measured using an optical microscope. From the measured TIS for each damage site and the corresponding true diameter, a calibration equation was generated

$$TIS = 2.86 D^{2.0841} \tag{1.9}$$

where D is the damage site diameter, and TIS the Total Integrated Signal collected from damage sites by the imaging system. Figure 1.16 indicates that it is possible to accurately size damage sites on final optics from $30\,\mu\mathrm{m}$ to $1\,\mathrm{mm}$ using TIS values provided by the imaging system while the spatial resolution of the imaging system is $\approx 100\,\mu\mathrm{m}$/pixel.

The growth behavior of laser-induced damage sites is of major importance for fusion-class laser facilities. Such phenomenon was largely described by measuring damage area or equivalent diameter in the litera-

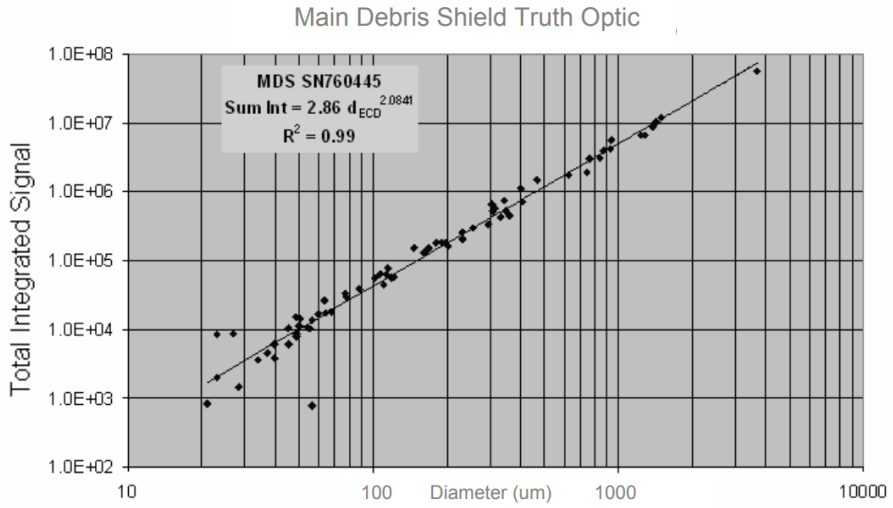

Figure 1.16: Calibration of TIS values on damage diameters from a true NIF optics [22].

ture[35, 72–74]. Pixel intensities are efficient to estimate damage size at a subpixel resolution from $30\,\mu\mathrm{m}$ to $1\,\mathrm{mm}$. To monitor damage growth using pixel intensities, it is necessary to ensure that intensity variations are only related to damage growth. However, disturbances during the acquisition process modify pixel intensities regardless of damage growth. Without image corrections, diameter estimations and damage growth monitoring are not accurate.

1.2.5 Digital Image Correlation - DIC

Pixel intensity in the acquired dark-field images appeared as relevant information for sizing damage sites. However, some disturbances affecting images during the acquisition process can make unusable the pixel intensity for damage monitoring. A method, so-called Digital Image Correlation (DIC), was developed in solid mechanics in order to monitor experiments from pixel intensity of a set of images [75]. DIC, in its simplest form, needs:

- an optical system to acquire images of the scene;
- a method for digitally recording images containing measurement data;
- algorithms to register the recorded digital images and extract the measurement data.

Before presenting the theoretical principles and some application cases of this method, we start with a brief review of the steps that led to DIC as it is known today.

A background overview

The first studies on optic date back to the writings of Euclid aroud 300 BCE. Leonardo da Vinci described perspective in 1492. In 1816, the photography was invented by Niepce. In 1839, Daguerre developed the daguerreotype, a process that uses iodine as a sensitive agent on a copper plate covered with a layer of silver to stabilize the acquired image over time.

With the invention of photography and its improvement, the first works on image correlation were led by Hobrough. In 1961, he tried to extract positional information from image matching processes. In the 1980s, digital images became available. Numerous works were carried out to extract shape information or to measure deformations from images in fields such as microscopy, medicine or object recognition.

In order to measure deformations, it is necessary to quantify object displacements between two images of the scene, *i.e.,* image registration. The first proposed DIC method to register images made use of the spatial intensity gradient of the images and a Newton-Raphson procedure [76]. In this case, Newton-Raphson procedure is used to iteratively minimize a cost function and estimate a displacement. The first DIC methods are based on the comparison of digital images for various small regions, so-called subsets [77]. The aim is to locate the positions of each subsets before and after deformation. Algorithms were applied to measure displacements on 2D images:

- Translations [78];
- Rigid body measurements (translations and planar rotations) [79];
- Deformation estimation in solids [80].

The subset (or local) methods only give displacement information for specific image points but they are quickly implemented. Global techniques were implemented to measure displacement fields on the whole image. Global approaches generally outperform local methods [81].

Digital Image Correlation principle

The following development of DIC principle is based on Ref. [82]. For DIC algorithms, it is assumed that the differences between a reference image

and a deformed one are due to the displacements of material points. Pixel intensity variations are considered as negligible. From these assumptions, the intensity conservation writes

$$I_0(\boldsymbol{x}) \approx I_n \circ \boldsymbol{\Phi}(\boldsymbol{x}) \quad ; \quad \boldsymbol{\Phi}(\boldsymbol{x}) = \boldsymbol{x} + \boldsymbol{U}(\boldsymbol{x}) \tag{1.10}$$

where I_0 (resp. I_n) is the scalar field of the light intensity collected by the camera sensor in the reference configuration (resp. deformed configuration), $\boldsymbol{x}$ the pixel coordinate in the reference configuration, $\boldsymbol{\Phi}$ a mapping function from reference to deformed configurations, $\boldsymbol{U}$ is the displacement field between both image configurations.

The first assumption describes the displacement field $\boldsymbol{U}$ and consequently the mapping function $\boldsymbol{\Phi}$ by a finite number of unknowns $\boldsymbol{a}$

$$\boldsymbol{U}(\boldsymbol{x}) \approx \boldsymbol{u}(\boldsymbol{x}, \boldsymbol{a}), \tag{1.11}$$

or equivalently

$$\boldsymbol{\Phi}(\boldsymbol{x}) \approx \boldsymbol{\phi}(\boldsymbol{x}, \boldsymbol{a}). \tag{1.12}$$

The vector $\boldsymbol{a}$ contains the amplitudes of the degrees of freedom of the displacement field parameterization: $\boldsymbol{a} = [a_1, a_2, ..., a_n]^T$.

The aim is to estimate the unknown amplitudes by iteratively minimizing a cost function, Ψ. At the iteration k, the cost function reads

$$\Psi(\boldsymbol{a}^k) = \frac{1}{2} \int_\Omega [I_0(\boldsymbol{x}) - I_n \circ \boldsymbol{\phi}(\boldsymbol{x}, \boldsymbol{a}^k)]^2 d\boldsymbol{x} \tag{1.13}$$

where the term $I_0(\boldsymbol{x}) - I_n \circ \boldsymbol{\phi}(\boldsymbol{x}, \boldsymbol{a}^k)$ is the so-called residual $r(\boldsymbol{x}, \boldsymbol{a}^k)$ [81]. Minimizing the cost function implies to find $\boldsymbol{a}^{opt}$ satisfying the following equation

$$\forall i \in [1, n], \Gamma(\boldsymbol{a}^{opt}) = \frac{\partial \Psi}{\partial a_i}(\boldsymbol{a}^{opt}) = 0. \tag{1.14}$$

The displacement unknowns at iteration $k+1$ are updated

$$\boldsymbol{a}^{k+1} = \boldsymbol{a}^k + \delta \boldsymbol{a} \tag{1.15}$$

where $\delta \boldsymbol{a}$ is the iterative displacement update. Such displacement update is considered as small thereafter.

The displacement unknowns are sought such that

$$\forall i \in [1, n], \Gamma_i(\boldsymbol{a}^{k+1}) = 0. \tag{1.16}$$

Since the displacement update is considered as small between two successive iterations, Equation (1.16) implies to solve the following linear system

$$\forall (i, j) \in [1, n]^2, \Gamma_i(\boldsymbol{a}^k) + \frac{\partial \Gamma_i}{\partial a_j}(\boldsymbol{a}^k) \delta \boldsymbol{a} = 0. \tag{1.17}$$

That is written as

$$[\boldsymbol{M}]\{\delta\boldsymbol{a}\} = \{\boldsymbol{b}\} \tag{1.18}$$

with

$$b_i = -\Gamma_i(\boldsymbol{a}^k) = -\frac{\partial\Psi}{\partial a_i}(\boldsymbol{a}^k), \tag{1.19}$$

$$M_{ij} = \frac{\partial\Gamma_i}{\partial a_j}(\boldsymbol{a}^k) = \frac{\partial^2\Psi}{\partial a_j\partial a_i}(\boldsymbol{a}^k). \tag{1.20}$$

The term b_i reads

$$b_i = -\frac{1}{2}\int_\Omega \frac{\partial r^2}{\partial a_i}(\boldsymbol{x},\boldsymbol{a}^k)d\boldsymbol{x} = -\int_\Omega \frac{\partial r}{\partial a_i}(\boldsymbol{x},\boldsymbol{a}^k)r(\boldsymbol{x},\boldsymbol{a}^k)d\boldsymbol{x}. \tag{1.21}$$

Hence

$$b_i = \int_\Omega \frac{\partial I_n\circ\boldsymbol{\phi}}{\partial a_i}(\boldsymbol{x},\boldsymbol{a}^k)r(\boldsymbol{x},\boldsymbol{a}^k)d\boldsymbol{x}. \tag{1.22}$$

After derivation of a composite function, the final form of b_i is

$$b_i = \int_\Omega \frac{\partial\boldsymbol{\phi}}{\partial a_i}\nabla I_n\circ\boldsymbol{\phi}(\boldsymbol{x},\boldsymbol{a}^k)r(\boldsymbol{x},\boldsymbol{a}^k)d\boldsymbol{x}. \tag{1.23}$$

The term M_{ij}, the Hessian matrix, reads

$$M_{ij} = \frac{1}{2}\int_\Omega \frac{\partial^2 r^2}{\partial a_i\partial a_j}(\boldsymbol{x},\boldsymbol{a}^k)d\boldsymbol{x}. \tag{1.24}$$

So,

$$M_{ij} = -\int_\Omega \frac{\partial}{\partial a_j}\left[\frac{\partial\boldsymbol{\phi}}{\partial a_i}(\boldsymbol{x},\boldsymbol{a}^k)\nabla I_n\circ\boldsymbol{\phi}(\boldsymbol{x},\boldsymbol{a}^k)r(\boldsymbol{x},\boldsymbol{a}^k)\right]d\boldsymbol{x}. \tag{1.25}$$

The term M_{ij} is written as a sum of three terms

$$M_{ij} = M_{ij}^a + M_{ij}^b + M_{ij}^c \tag{1.26}$$

with

$$M_{ij}^a = -\int_\Omega [\frac{\partial\boldsymbol{\phi}}{\partial a_i}(\boldsymbol{x},\boldsymbol{a}^k)\nabla I_n\circ\boldsymbol{\phi}(\boldsymbol{x},\boldsymbol{a}^k)][\nabla I_n\circ\boldsymbol{\phi}(\boldsymbol{x},\boldsymbol{a}^k)\frac{\partial\boldsymbol{\phi}}{\partial a_j}(\boldsymbol{x},\boldsymbol{a}^k)]d\boldsymbol{x} \tag{1.27}$$

and

$$M_{ij}^b = -\int_\Omega r(\boldsymbol{x},\boldsymbol{a}^k)\frac{\partial\boldsymbol{\phi}}{\partial a_i}(\boldsymbol{x},\boldsymbol{a}^k)\frac{\partial\boldsymbol{\phi}}{\partial a_j}(\boldsymbol{x},\boldsymbol{a}^k)\nabla\nabla I_n\circ\boldsymbol{\phi}(\boldsymbol{x},\boldsymbol{a}^k)d\boldsymbol{x} \tag{1.28}$$

and

$$M_{ij}^{c} = -\int_{\Omega} r(\boldsymbol{x}, \boldsymbol{a}^{k}) \frac{\partial^{2} \boldsymbol{\phi}}{\partial a_i a_j}(\boldsymbol{x}, \boldsymbol{a}^{k}) \nabla I_n \circ \boldsymbol{\phi}(\boldsymbol{x}, \boldsymbol{a}^{k}) d\boldsymbol{x}. \tag{1.29}$$

Several assumptions lead to a simplification of the Hessian matrix $[\boldsymbol{M}]$:

- $[\boldsymbol{M}^{b}]$ contains the second gradient of the image. Since the second gradient is highly sensitive to noise, it is chosen to omit this term, $[\boldsymbol{M}^{b}] \equiv 0$.
- The displacement basis is generally linearly independant, $[\boldsymbol{M}^{c}] \equiv 0$.

Hence,

$$[\boldsymbol{M}] \equiv [\boldsymbol{M}^{\boldsymbol{a}}] \tag{1.30}$$

Furthermore, $\nabla(I_n \circ \boldsymbol{\phi})$ is used instead of $\nabla I_n \circ \boldsymbol{\phi}$. The used gradient is computed on the reference image I_0 and not on the deformed image I_n.

The presented development leads to the common DIC formulation

- $[\boldsymbol{M}^{b}] \equiv 0$,
- $[\boldsymbol{M}^{c}] \equiv 0$,
- $\nabla(I_n \circ \boldsymbol{\phi}) \approx \nabla I_0$

DIC techniques are widely used in solid mechanics with for instance monitoring of mechanical experiments, detection and monitoring of damage phenomenon or study of crack propagation [75]. Such application cases are presented thereafter.

Monitoring of mechanical experiments

DIC is widely used to measure surface deformation during mechanical experiments. A uniaxial tensile loading of a planar specimen was performed to demonstrate the effectiveness of DIC methods for measurements of surface deformation [75]. Figure 1.17 illustrates the experimental setup for the uniaxial loading of a specimen. A dog-bone sample was maintained by hydraulic grips and loaded. An extensometer was set on a specimen to measure strains for comparison with DIC results. A camera acquired images of the specimen during the loading process. A halogen light was used to ensure a good contrast and uniform illumination.

Figure 1.18 shows the reference image acquired by the optical system. The observed face of the sample was painted to obtain a random black and white pattern. Such specific pattern is suitable for DIC algorithms [75]. In digital image correlation, it was shown that the standard displacement

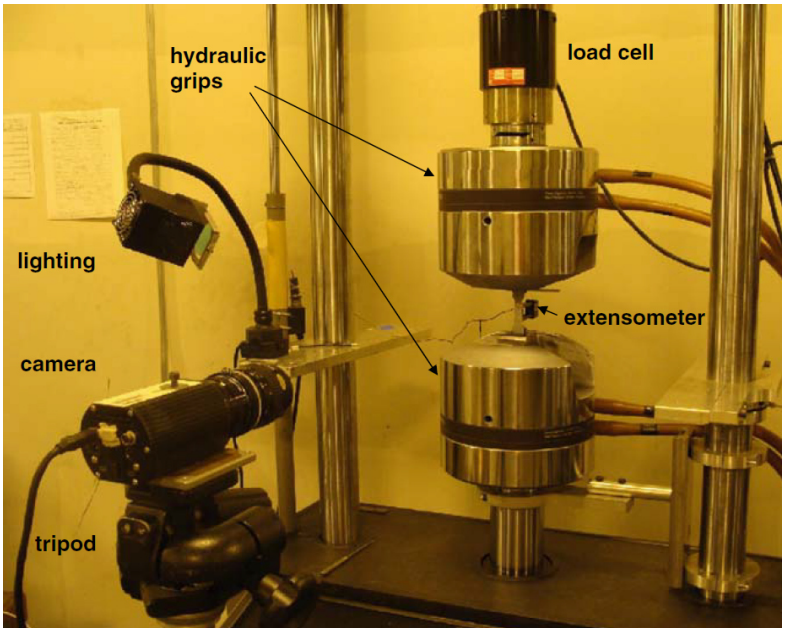

Figure 1.17: Experimental setup used for uniaxial loading of a dog-bone sample [75].

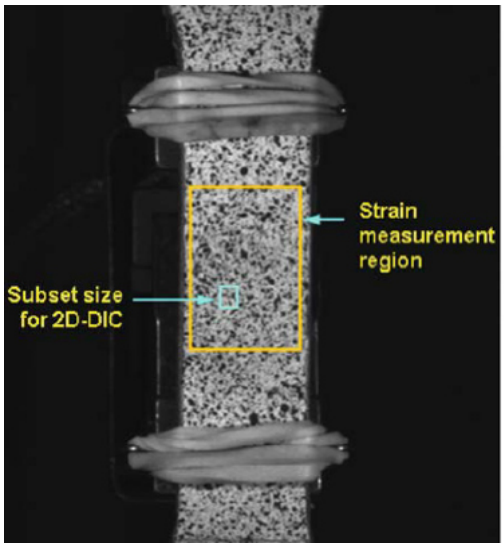

Figure 1.18: Reference image used in the DIC process. Strain measurement region is in the yellow rectangle. A subset area used for DIC purpose is the blue rectangle. The extensometer is behind the sample. [75].

uncertainties are inversely proportional to the mean contrast [81]. The intensity gradient, used in Hessian matrix, is well defined on the observed

area with the random pattern. Figure 1.18 indicates the strain measurement region in yellow and the subset size for DIC. The displacement data were measured by DIC for each subset.

Figure 1.19 compares the strain values obtained by DIC (red circles) and the given values by the extensometer (blue crosses). The values measured with both methods are in a agreement up to a strain of 3%. After this point, the sample locally failed. The difference is explained by a measurement averaged over the subsets for the DIC which gives higher strain values than the values provided by the extensometer. The three strain fields indicate that DIC gives access to local strain values. The analysis of the mechanical test can be described more accurately than using only the global extensometer values.

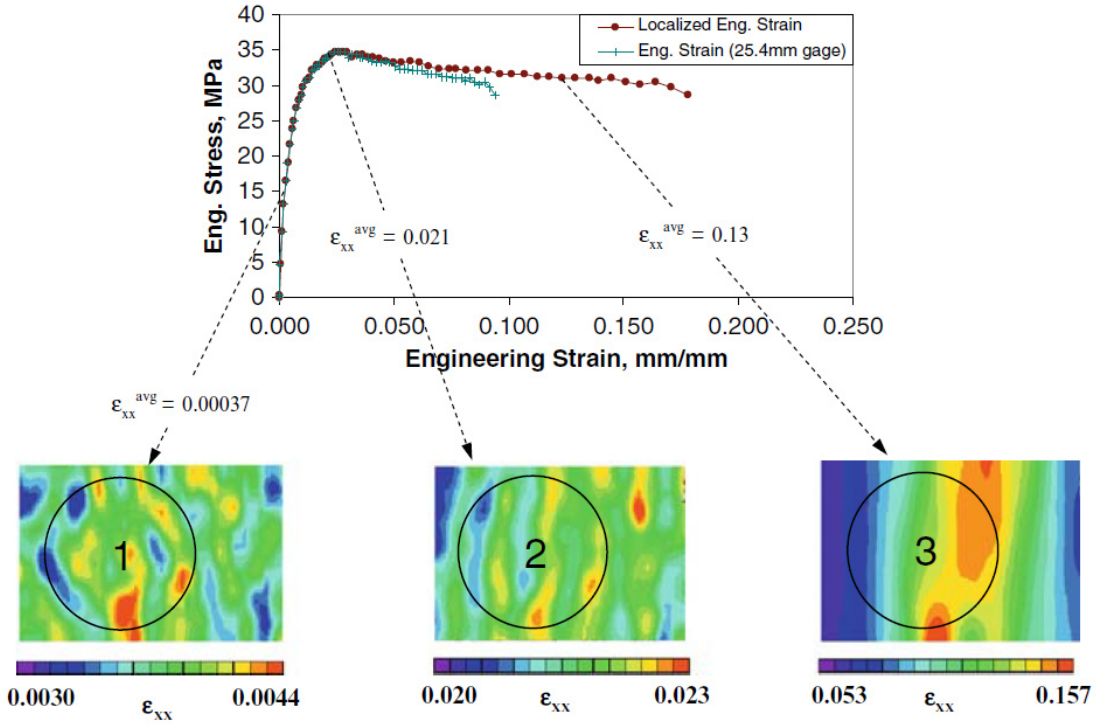

Figure 1.19: Comparison of strain values measured by DIC (red circles) and obtained with the extensometer (blue crosses). Three strain fields obtained by DIC are given at three load levels during the tensile test. The field of view is $14\,\mathrm{mm}$x$10\,\mathrm{mm}$. The circles on the fields represent the area on which the strain values are averaged to obtain the values reported in the graph [75].

The DIC method can accurately measure surface strains in tests on

planar samples. The main advantage of the method is the full-field aspect of the measurement which gives access to local behavior inaccessible with a standard extensometer.

Detection and monitoring of damage phenomena

Measurement of damage is needed for several reasons:

- Modeling the material response [83];
- Identification of parameters for prediction purpose and validation of damage laws [84];
- Evaluation of structure damage and its evolution [85–87].

DIC is also widely used to detect and monitor damage phenomena on loaded materials. Such method is suitable for different imaging systems such as among others visible or infrared cameras, scanning electron microscopes or electron backscatter diffraction (EBSD) acquisitions [88–91]. Cracks can be detected and monitored by DIC methods since displacement discontinuities across the crack are well defined. Different solutions are accurate to detect cracks and measure some of their characteristics such as location or orientation [83]:

- Discontinuity in measured displacement fields - At the location of a crack, a discontinuity in the displacement field appears. However, the resolution of the displacement field must be sufficient to make the discontinuity quantifiable [83].
- Increase of correlation residuals - In case of continuous displacement field assumption that do not describe crack discontinuities, large values of residuals appear at the location of the crack [92]. The main advantage of the residual field is that it can be computed at the pixel scale. However, the residual contains only data on intensity variation and not on displacements. For damage such as laser-induced damage sites on optics, pixel intensities are well correlated with their size [22]. So correlation residuals may be a good indicator to quantify laser-induced damage growth.
- Enrichment of the kinematic field to describe the crack - A coarse DIC analysis is applied without describing cracks in the displacement fields. The displacement field is then enriched by crack formulation if it allows for improving the description of the displacement [93].

Study of crack propagation

A 3-point bending test on a cementious specimen was performed in order to apply DIC methods for monitoring the propagation of a crack (Figure 1.20). The sample was painted to obtain a black and white random pattern on its face. The painted sample face was lit during the loading process in order to limit pixel intensity variations. A static visible camera acquired images of the loaded sample at periodic intervals. A vertical displacement was applied on the top of the specimen by the upper support point. The bending test was conducted until the crack initiates and propagates.

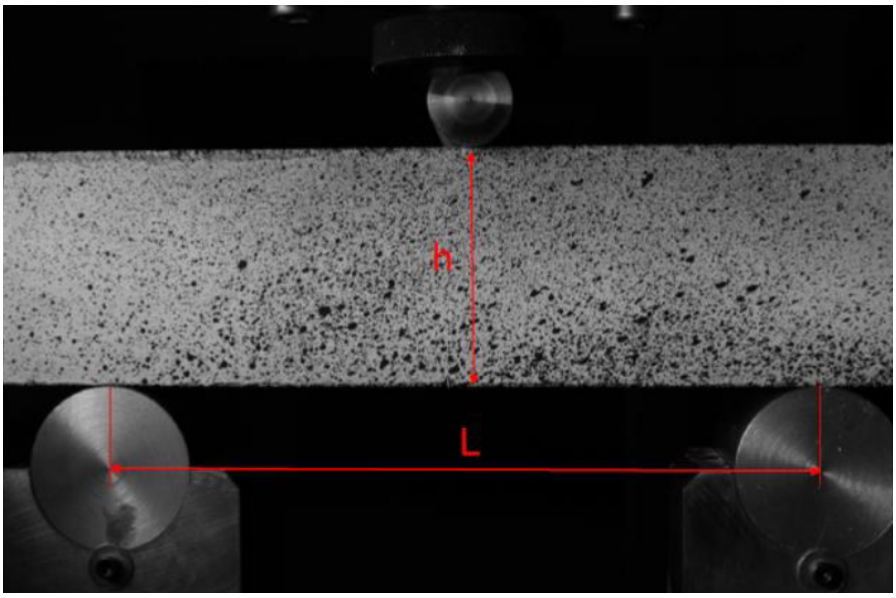

Figure 1.20: Image of the specimen before the beginning of the bending test.

The displacement fields were estimated using DIC. The set of images was corrected with the estimated displacement fields. Residual maps are obtained for each image of the set (two of them are presented in Figure 1.21). Before any loading, the normalised residual values varied between 1.7% and 2.9% of the image dynamic range. Such initial residual values could be due to acquisition noise, possible intensity variations of lighting or accuracy of displacement corrections. When the applied displacement is sufficient to reach specimen failure, a crack was clearly visible in the residual map while this crack was barely visible on the zoom in the corresponding image. The residual values on the crack were about 13%, 5 times

the initial residual values. In such case, a simple thresholding technique is sufficient to locate the crack in the residual map. It is noteworthy that the collapse of the specimen at the upper support point induced high residual values.

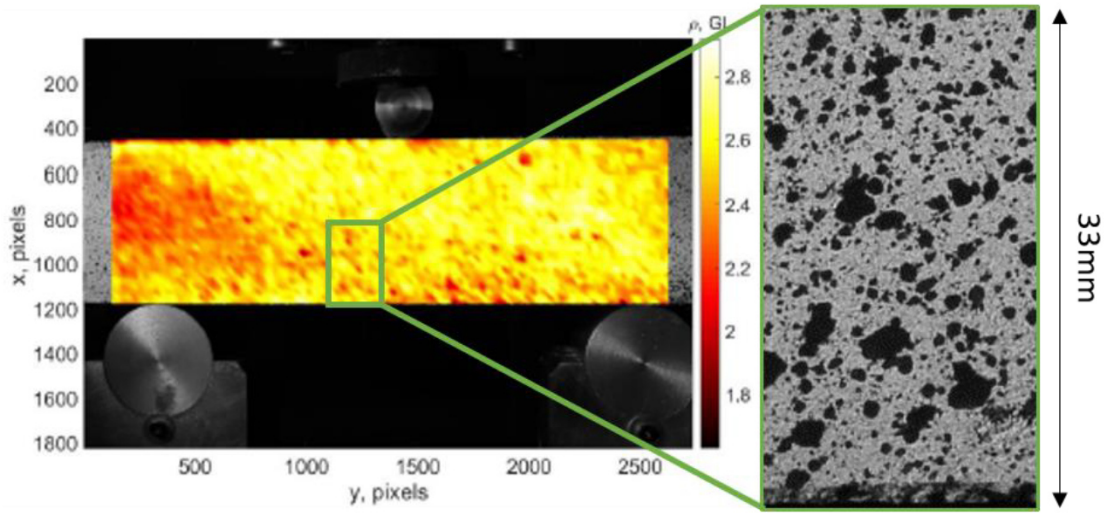

(a)

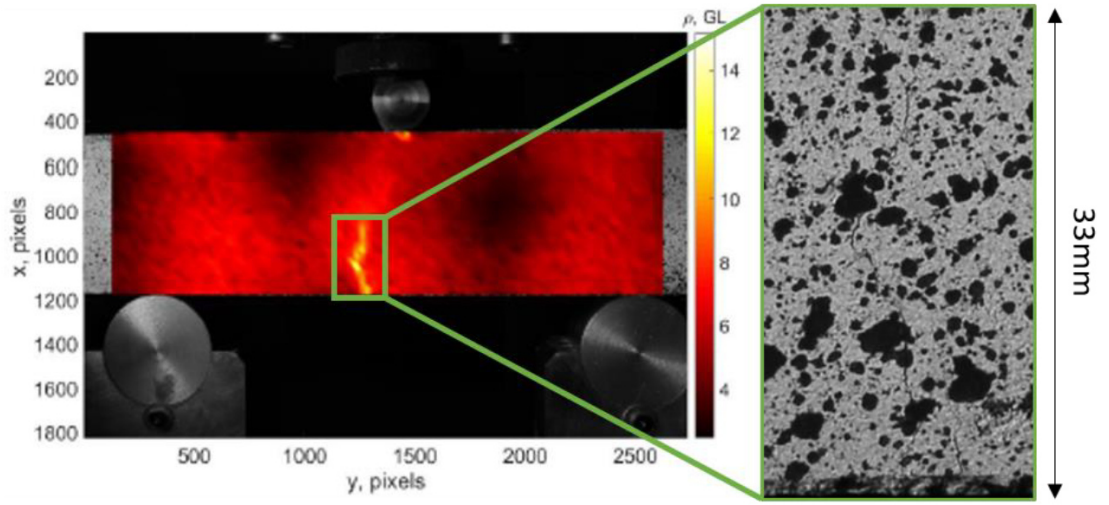

(b)

Figure 1.21: Gray level residual maps of the cementious specimen (a) before loading and (b) after crack initiation.

Digital Image Correlation methods are accurate to detect and monitor damage phenomena such as crack initiation and growth at sub-pixel res-

olution [83]. The images of LMJ final optics are significantly different from those commonly processed with DIC algorithms. For example, the optics are transparent in the visible range and it is not possible to paint a black and white pattern on such optics. Solutions to apply DIC methods on images of LMJ final optics will be presented in Part III.

1.2.6 Light scattering measurements

DIC methods are based on intensity gradient of the images. Detection of damage initiation relies on the residual values, correlated to pixel intensities. Monitoring laser damage initiation and growth by DIC methods therefore relies on the understanding of the process leading to the variation of pixel intensity due to damage sites in the images of the LMJ final optics, namely, light scattering. Such phenomenon is described by the so-called Bidirectional Scattering Disctribution Function (BSDF) [94]. The BSDF links the scattered radiance by a surface, L_s [$\mathrm{Wm^{-2}sr^{-1}}$], and the incident irradiance on the surface, E_i [$\mathrm{Wm^{-2}}$], for incident angles θ_i and ϕ_i, as well as the scattered angles θ_s and ϕ_s in spherical coordinate system

$$BSDF(\theta_i, \phi_i, \theta_s, \phi_s) = \frac{dL_s(\theta_i, \phi_i, \theta_s, \phi_s)}{dE_i(\theta_i, \phi_i, \theta_s, \phi_s)} \tag{1.31}$$

The BSDF of an object can be obtained by modeling [95]. Such methods are efficient to describe the BSDF from smooth to rough surface [96–101]. Modeling techniques were also used to estimate bulk scattering in optical multilayers [102]. Light scattering power by laser-induced shallow pits on silica was also described as a surface phenomenon [103]. Light scattering modeling of laser-induced damage sites is not considered in the rest of the document since damage sites involve coupled interactions between surface and bulk scattering that is a complex subject of research work for specialized teams.

The BSDF can also be measured by accurate tools [97, 104–109]. Such tools were designed to measure angular and spectral resolved scattering of complex optical coatings [108]. Scattering techniques were also used to evaluate subsurface damage [14]. Angle-resolved scatter of laser-damaged DKDP crystals were measured [110].

In the thesis, an instrument was used to measure the BSDF of several laser damage sites. It is the Spectral and Angular Light Scattering Apparatus in its 4$^{\text{th}}$ configuration (SALSA 4), as shown in Figure 1.22 [111]. The light source is a supercontinuum laser (WL-SC-400-8). The source beam is then split by a dichroic beam splitter into two channels: the first one between

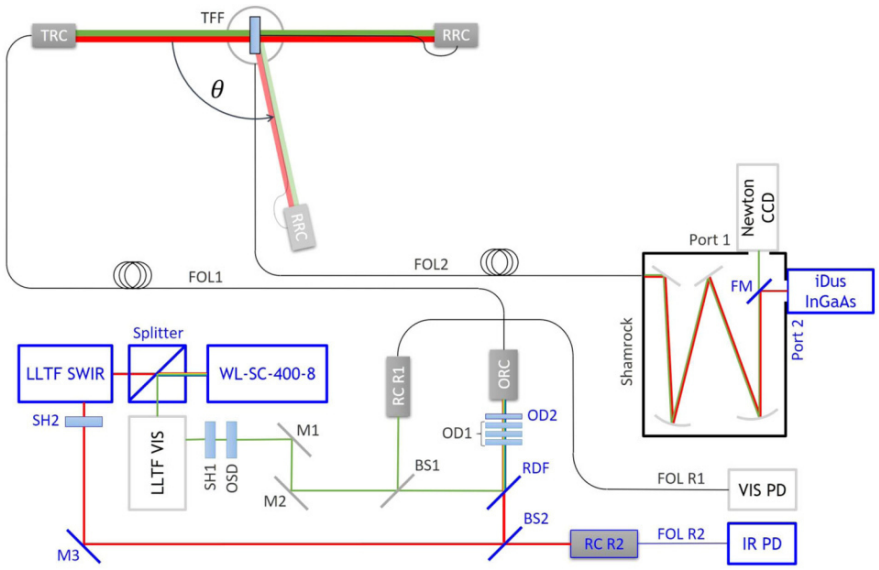

Figure 1.22: Schematic view of the SALSA 4 light scattering measurement set-up [111].

$400\,\mathrm{nm}$ and $975\,\mathrm{nm}$ and the second one between $975\,\mathrm{nm}$ and $2400\,\mathrm{nm}$. The optical components of the visible channel are as follows

- A tunable volume hologram filter (LLTF VIS) to select the wavelength between $400\,\mathrm{nm}$ and $1100\,\mathrm{nm}$ with a filter bandwith of about $2\,\mathrm{nm}$;
- An electro-mechanical shutter (SH1) to block the visible beam if it is not used;
- An order sorting device (OSD) to clean the spectral profile of the laser beam;
- A non-polarizing beam splitter (BS1) to reflect few % of the beam toward a reference optical fiber (FOL R1) using a reflective collimator (RC R1). The reference signal is collected by a silicon photoreceiver (VIS PD);
- The main part of the laser is oriented toward the measurement optical fiber (FOL1) by a parabolic off-axis reflective collimator (ORC);
- Optical densities (OD1 and OD2) are used to control the energy of the signal.

The infrared channel can be described in a similar way as the visible channel:

- A volume hologram filter (LLTF SWIR) to select the wavelength between $800\,\mathrm{nm}$ and $2300\,\mathrm{nm}$ with a spectral bandwith of about $3.5\,\mathrm{nm}$;
- An electro-mechanical shutter (SH2) to block the infrared beam if it is not used;
- A beam-splitter (BS2) to create the reference and measurement path directed toward FOL1 in the same way than the visible signal;
- A dichroic filter (RDF) is used to recombine the infrared and visible measurement beams;
- A reflective collimator (RC R2) and a InGaAs photoreceiver (IR PD) collect the reference signal.

The optical fiber (FOL1) is connected to a reflective collimator (TRC) to illuminate the sample (TFF) to be measured with the low-divergence measurement beam (visible or infrared). The central wavelength of the measurement beam is selected by opening one of the shutters (SH1 or 2) and tuning the corresponding volume hologram filter (LLTF VIS or SWIR). The diameter of the measurement beam is about $6\,\mathrm{mm}$. The scattered light by the sample is collected by a fiber collimator mounted on a rotating arm to select the scattered angle (θ). An optical fiber (FOL2) connects the RCC to a Czerny-Turner monochromator (Shamrock) coupled with a flip mirror (FM) to send the scattered (visible of infrared) signal to the adapted camera (Newton CCD for visible beam and iDus InGaAs sensor for infrared beam).

Such set-up was used to measure the BSDF for damage sites of different sizes. These input data are essential to develop an optical model of the acquisition process of vacuum window images. A model is proposed in Chapter 2.

1.3 Outline of research

The work carried out and described below is driven to meet the need to monitor the growth of laser damage sites at sub-pixel scale from spatially low-resolution images affected by perturbations in a constrained and inaccessible environment, namely, the vacuum windows of LMJ facility. Hence, the main objective of the thesis is to propose a sub-pixel and in-situ quantification of laser-induced damage sites on final optics of LMJ. The advances described are part of a set of activities carried out to optimize the optics use on the installation through the recycling loop. The presented

work is organized in 3 main parts, each answering one of the following questions:

- **Part II** - *How to develop and use an optical model in order to optimize the use of pixel intensities to size damage sites below the spatial resolution of the available images ?*

- **Part III** - *How to correct the perturbations affecting the images to optimize the in-situ damage growth monitoring?*

- **Part IV** - *Could the gray levels, so far used to estimate the diameter of damage sites, be used to describe damage volume morphology?*

In order to answer the previous three questions, the carried out work is at the meeting point between laser-induced damage phenomenon, the study of light scattering and some measurement methods used in solid mechanics.

1.3.1 From gray levels to damage size

"How to measure the size of damage sites below the spatial resolution of the available images?"

When damage size measurement at sub-pixel resolution is needed, pixel-counting is not sufficient. In Chapter 2, it is proposed to use a damage quantification method based on the sum of pixel intensities corresponding to damage sites. Such method implies to calibrate measured pixel intensities with damage diameters. The calibration is performed using two methods:

- A vacuum windows with 930 damage sites whose diameters are exactly known is used. This optical component is mounted on the facility and images of such calibration object are acquired.

- A calibration based on an optical model is proposed. It implies to model the lighting system using a ray tracing software, to measure light scattering by damage sites, and to numerically model the imaging system.

In Chapter 3, a new lighting system of vacuum windows is studied. The performance of damage size estimation by the new system is evaluated using the optical model described in Chapter 2.

1.3.2 Image corrections for damage growth monitoring

"How to correct the perturbations affecting the images to optimize the in-situ damage growth monitoring?"

In order to monitor damage growth from one laser shot to another using methods based on pixel intensities, it is necessary that the gray levels are comparable from one image to another. To that end, it is proposed in Chapter 4 to apply Digital Image Correlation on vacuum window images. Displacements and gray level correction methods are described and validated. After corrections, residual maps are only dependent of damage initiation and growth and acquisition noise. Thus, a new detection method of damage sites based on correlation residual maps is proposed in this chapter.

In Chapter 5, the proposed displacement correction method is applied to damage growth experiments on a dedicated laser damage set-up. The first aim is to validate the sub-pixel resolution of displacement estimations with high and low resolution images. The second objective is to experimentally verify if the intensity-based method is more efficient to detect damage growth than pixel-counting.

In Chapter 6, an original approach to correct for gray level variations based on Proper Orthogonal Decomposition and an optical model is described. The purpose is to propose a specific approach for images of vacuum windows rather than the general method described in Chapter 4.

1.3.3 From gray levels to damage morphology

"Could the gray levels, so far used to estimate the diameter of damage sites, be utilized to describe damage volume morphology?"

Parts II and III focused on the estimation of damage diameter and surface growth. Chapter 7 explores the possibility of describing the morphology of damage sites from surface images only. The development of this chapter is based on damage growth sequences performed on highly instrumented laser damage set-up.

References

[1] A. K. Dubey and V. Yadava, "Laser beam machining—a review," *International Journal of Machine Tools and Manufacture*, vol. 48, no. 6, pp. 609–628, 2008, issn: 0890-6955. doi: https://doi.org/10.1016/j.ijmachtools.2007.10.017. [Online]. Available: https://www.sciencedirect.com/science/article/pii/S0890695507002325.

[2] E. Barkan and J. Swartz, "System Design Considerations In Bar-Code Laser Scanning," *Optical Engineering*, vol. 23, no. 4, pp. 413–420, 1984. doi: 10.1117/12.7973310. [Online]. Available: https://doi.org/10.1117/12.7973310.

[3] R. F. Kazarinov, "Physics and simulation of communication lasers," in *Physics and Simulation of Optoelectronic Devices II*, W. W. Chow and M. Osinski, Eds., International Society for Optics and Photonics, vol. 2146, SPIE, 1994, pp. 122–132. doi: 10.1117/12.178503. [Online]. Available: https://doi.org/10.1117/12.178503.

[4] R. Brancato, L. Giovannoni, R. Pratesi, and U. Vanni, "New Lasers For Ophthalmology: Retinal Photocoagulation With Pulsed Diode Lasers," in *1986 European Conf on Optics, Optical Systems and Applications*, S. Sottini and S. Trigari, Eds., International Society for Optics and Photonics, vol. 0701, SPIE, 1987, pp. 365–366. doi: 10.1117/12.937087. [Online]. Available: https://doi.org/10.1117/12.937087.

[5] llnl.gov. "The birth of the laser and icf." (2022), [Online]. Available: https://www.llnl.gov/archives/1960s/lasers (visited on 09/18/2022).

[6] J. Nuckolls, L. Wood, A. Thiessen, and G. Zimmerman, "Laser Compression of Matter to Super-High Densities: Thermonuclear (CTR) Applications," *Nature*, vol. 239, no. 4, pp. 139–142, 1972. doi: 10.1038/239139a0. [Online]. Available: https://doi.org/10.1038/239139a0.

[7] J. A. Paisner, E. M. Campbell, and W. J. Hogan, "The national ignition facility project," *Fusion Technology*, vol. 26, no. 3, Nov. 1994.

[8] W. Zheng *et al.*, "Laser performance of the sg-iii laser facility," *High Power Laser Science and Engineering*, vol. 4, e21, 2016. doi: 10.1017/hpl.2016.20.

[9] M. L. Andre, "Status of the LMJ project," in *Solid State Lasers for Application to Inertial Confinement Fusion: Second Annual International Conference*, M. L. Andre, Ed., International Society for Optics and Photonics, vol. 3047, SPIE, 1997, pp. 38–42. doi: 10.1117/12.294307. [Online]. Available: https://doi.org/10.1117/12.294307.

[10] K. Manes, M. Spaeth, J. Adams, and M. Bowers, "Damage mechanisms avoided or managed for nif large optics," *Fusion Science and Technology*, vol. 69, pp. 146–249, Feb. 2016. doi: 10.13182/FST15-139.

[11] S. G. Demos, M. Staggs, and M. R. Kozlowski, "Investigation of processes leading to damage growth in optical materials for large-aperture lasers," *Applied Optics*, vol. 41, no. 18, pp. 3628–3633, Jun. 2002. doi: 10.1364/AO.41.003628. [Online]. Available: http://ao.osa.org/abstract.cfm?URI=ao-41-18-3628.

[12] J. A. Menapace *et al.*, "Combined advanced finishing and uv-laser conditioning for producing uv-damage-resistant fused silica optics," in *Optical Fabrication and Testing*, Optica Publishing Group, 2002, OMB4. doi: 10.1364/OFT.2002.OMB4. [Online]. Available: http://opg.optica.org/abstract.cfm?URI=OFT-2002-OMB4.

[13] B. Bertussi, J.-Y. Natoli, and M. Commandre, "Effect of polishing process on silica surface laser-induced damage threshold at 355 nm," *Optics Communications*, vol. 242, no. 1, pp. 227–231, 2004, issn: 0030-4018. doi: https://doi.org/10.1016/j.optcom.2004.08.016. [Online]. Available: https://www.sciencedirect.com/science/article/pii/S0030401804008028.

[14] M. Trost, T. Herffurth, D. Schmitz, S. Schröder, A. Duparré, and A. Tünnermann, "Evaluation of subsurface damage by light scattering techniques," *Appl. Opt.*, vol. 52, no. 26, pp. 6579–6588, Sep. 2013. doi: 10.1364/AO.52.006579. [Online]. Available: http://ao.osa.org/abstract.cfm?URI=ao-52-26-6579.

[15] C. J. Stolz and F. Y. Génin, "Laser resistant coatings," in *Optical Interference Coatings*, N. Kaiser and H. K. Pulker, Eds. Berlin, Heidelberg: Springer Berlin Heidelberg, 2003, pp. 309–333, isbn: 978-3-540-36386-6. doi: 10.1007/978-3-540-36386-6_13. [Online]. Available: https://doi.org/10.1007/978-3-540-36386-6_13.

[16] V. Denis *et al.*, "The Laser Megajoule facility: laser performances and comparison with computational simulation," in *High-Power Laser Materials Processing: Applications, Diagnostics, and Systems VII*, S. Kaierle and S. W. Heinemann, Eds., International Society for Optics and

Photonics, vol. 10525, SPIE, 2018, pp. 14–21. doi: 10.1117/12.2287342. [Online]. Available: https://doi.org/10.1117/12.2287342.

[17] J. Folta *et al.*, "Mitigation of laser damage on National Ignition Facility optics in volume production," in *Laser-Induced Damage in Optical Materials: 2013*, G. J. Exarhos, V. E. Gruzdev, J. A. Menapace, D. Ristau, and M. Soileau, Eds., International Society for Optics and Photonics, vol. 8885, SPIE, 2013, pp. 138–146. doi: 10.1117/12.2030475. [Online]. Available: https://doi.org/10.1117/12.2030475.

[18] T. Doualle *et al.*, "CO2 laser microprocessing for laser damage growth mitigation of fused silica optics," *Optical Engineering*, vol. 56, no. 1, pp. 1–9, 2016. doi: 10.1117/1.OE.56.1.011022.

[19] L. Mascio-Kegelmeyer, "Machine learning for managing damage on NIF optics," in *Laser-induced Damage in Optical Materials 2020*, C. W. Carr, V. E. Gruzdev, D. Ristau, and C. S. Menoni, Eds., International Society for Optics and Photonics, vol. 11514, SPIE, 2020. doi: 10.1117/12.2571016. [Online]. Available: https://doi.org/10.1117/12.2571016.

[20] C. Lacombe *et al.*, "Dealing with LMJ final optics damage: post-processing and models," in *Laser-induced Damage in Optical Materials 2020*, C. W. Carr, V. E. Gruzdev, D. Ristau, and C. S. Menoni, Eds., International Society for Optics and Photonics, vol. 11514, SPIE, 2020. doi: 10.1117/12.2571074. [Online]. Available: https://doi.org/10.1117/12.2571074.

[21] L. Kegelmeyer, P. Fong, S. Glenn, and J. Liebman, "Local area signal-to-noise ratio (lasnr) algorithm for image segmentation," *Proceedings of SPIE - The International Society for Optical Engineering*, vol. 6696, Oct. 2007. doi: 10.1117/12.732493.

[22] A. Conder, J. Chang, L. Kegelmeyer, M. Spaeth, and P. Whitman, "Final optics damage inspection (FODI) for the National Ignition Facility," in *Optics and Photonics for Information Processing IV*, A. A. S. Awwal, K. M. Iftekharuddin, and S. C. Burkhart, Eds., International Society for Optics and Photonics, vol. 7797, SPIE, 2010, pp. 167–178. doi: 10.1117/12.862596. [Online]. Available: https://doi.org/10.1117/12.862596.

[23] Ctbto.org. "Who we are: ctbto preparatory commission." (2022), [Online]. Available: https://www.ctbto.org/specials/who-we-are/ (visited on 07/28/2022).

[24] ——, "Status of signature and ratification: ctbto preparatory commission." (2022), [Online]. Available: https://www.ctbto.org/the-treaty/status-of-signature-and-ratification/ (visited on 07/28/2022).

[25] C. DAM, *Les 20 ans du programme Simulation : histoire d'un succès!* Commissariat À L'énergie Atomique, Direction Des Applications Militaires, Dl, 2016.

[26] CEA/DAM. "Installation epure." (2022), [Online]. Available: http://www-teutates.cea.fr/installation-epure.html (visited on 07/28/2022).

[27] CEA. "Laser mégajoule." (2022), [Online]. Available: http://www-lmj.cea.fr/ (visited on 07/28/2022).

[28] LLNL. "What is the national ignition facility?" (2022), [Online]. Available: https://lasers.llnl.gov/about/what-is-nif (visited on 07/28/2022).

[29] A. Casner *et al.*, "Lmj/petal laser facility: overview and opportunities for laboratory astrophysics," *High Energy Density Physics*, vol. 17, pp. 2–11, 2015, 10th International Conference on High Energy Density Laboratory Astrophysics, issn: 1574-1818. doi: https://doi.org/10.1016/j.hedp.2014.11.009. [Online]. Available: https://www.sciencedirect.com/science/article/pii/S1574181814000871.

[30] C. DAM, *LMJ-PETAL User Guide*. Commissariat À L'énergie Atomique, Direction Des Applications Militaires, Dl, 2015.

[31] A. V. Smith and B. T. Do, "Bulk and surface laser damage of silica by picosecond and nanosecond pulses at 1064 nm," *Appl. Opt.*, vol. 47, no. 26, pp. 4812–4832, Sep. 2008. doi: 10.1364/AO.47.004812. [Online]. Available: http://opg.optica.org/ao/abstract.cfm?URI=ao-47-26-4812.

[32] M. J. Soileau, N. Mansour, E. W. van Stryland, and W. E. Williams, "Laser-induced damage and the role of self-focusing," *Optical Engineering*, vol. 28, pp. 1133–1144, Oct. 1989. doi: 10.1117/12.7977098.

[33] R. A. Negres, M. A. Norton, D. A. Cross, and C. W. Carr, "Growth behavior of laser-induced damage on fused silica optics under uv, ns laser irradiation," *Optics Express*, vol. 18, no. 19, pp. 19 966–19 976, Sep. 2010. doi: 10.1364/OE.18.019966. [Online]. Available: http://www.opticsexpress.org/abstract.cfm?URI=oe-18-19-19966.

[34] M. Chambonneau and L. Lamaignère, "Multi-wavelength growth of nanosecond laser-induced surface damage on fused silica gratings," *Scientific Reports*, vol. 8, pp. 1–10, Jan. 2018. doi: 10.1038/s41598-017-18957-9.

[35] L. Lamaignere, S. Reyne, M. Loiseau, J.-C. Poncetta, and H. Bercegol, "Effects of wavelengths combination on initiation and growth of laser-induced surface damage in SiO2," in *Laser-Induced Damage in Optical Materials: 2007*, G. J. Exarhos, A. H. Guenther, K. L. Lewis, D. Ristau, M. J. Soileau, and C. J. Stolz, Eds., International Society for Optics and Photonics, vol. 6720, SPIE, 2007, pp. 150–158. doi: 10.1117/12.753057. [Online]. Available: https://doi.org/10.1117/12.753057.

[36] J. H. Campbell, "Damage resistant optical glasses for high power lasers: a continuing glass science and technology challenge," Aug. 2002. [Online]. Available: https://www.osti.gov/biblio/15003836.

[37] M. Pfiffer, "Amélioration de la tenue au flux laser des composants optiques du laser Mégajoules par traitement chimique," Theses, Université de Bordeaux, Oct. 2017. [Online]. Available: https://tel.archives-ouvertes.fr/tel-01671915.

[38] P. Schultz, "Fabrication of optical waveguides by the outside vapor deposition process," *Proceedings of the IEEE*, vol. 68, no. 10, pp. 1187–1190, 1980. doi: 10.1109/PROC.1980.11828.

[39] T. Suratwala *et al.*, "Sub-surface mechanical damage distributions during grinding of fused silica," *Journal of Non-Crystalline Solids*, vol. 352, no. 52, pp. 5601–5617, 2006, issn: 0022-3093. doi: https://doi.org/10.1016/j.jnoncrysol.2006.09.012. [Online]. Available: https://www.sciencedirect.com/science/article/pii/S0022309306011471.

[40] J. Neauport, P. Cormont, P. Legros, C. Ambard, and J. Destribats, "Imaging subsurface damage of grinded fused silica optics by confocal fluorescence microscopy," *Optics Express*, vol. 17, no. 5, pp. 3543–3554, Mar. 2009. doi: 10.1364/OE.17.003543. [Online]. Available: http://www.opticsexpress.org/abstract.cfm?URI=oe-17-5-3543.

[41] M. Veinhard, "Endommagement surfacique de la silice avec des faisceaux laser de type lmj," 2019AIXM0029, Ph.D. dissertation, 2019. [Online]. Available: http://www.theses.fr/2019AIXM0029/document.

[42] C. Bouyer, "Impact du profil temporel sur l'endommagement laser des composants de fin de chaîne en silice du lmj," Thèse de doctorat dirigée par Natoli, Jean-Yves, Ph.D. dissertation, 2022. [Online]. Available: http://www.theses.fr/s308491.

[43] J. Neauport, L. Lamaignere, H. Bercegol, F. Pilon, and J.-C. Birolleau, "Polishing-induced contamination of fused silica optics and laser induced damage density at 351 nm," *Opt. Express*, vol. 13, no. 25, pp. 10 163–10 171, Dec. 2005. doi: 10.1364/OPEX.13.010163. [Online].

Available: http://opg.optica.org/oe/abstract.cfm?URI=oe-13-25-10163.

[44] J. Neauport, P. Cormont, L. Lamaignère, C. Ambard, F. Pilon, and H. Bercegol, "Concerning the impact of polishing induced contamination of fused silica optics on the laser-induced damage density at 351nm," *Optics Communications*, vol. 281, no. 14, pp. 3802–3805, 2008, issn: 0030-4018. doi: https://doi.org/10.1016/j.optcom.2008.03.031. [Online]. Available: https://www.sciencedirect.com/science/article/pii/S0030401808002903.

[45] P. A. Baisden, L. J. Atherton, R. A. Hawley, *et al.*, "Large optics for the national ignition facility," *Fusion Science and Technology*, vol. 69, no. 1, pp. 295–351, 2016. doi: 10.13182/FST15-143. eprint: https://doi.org/10.13182/FST15-143. [Online]. Available: https://doi.org/10.13182/FST15-143.

[46] R. A. Negres, G. M. Abdulla, D. A. Cross, Z. M. Liao, and C. W. Carr, "Probability of growth of small damage sites on the exit surface of fused silica optics," *Opt. Express*, vol. 20, no. 12, pp. 13 030–13 039, Jun. 2012. doi: 10.1364/OE.20.013030. [Online]. Available: http://opg.optica.org/oe/abstract.cfm?URI=oe-20-12-13030.

[47] C. W. Carr, D. A. Cross, Z. M. Liao, M. A. Norton, and R. A. Negres, "The stochastic nature of growth of laser-induced damage," in *Pacific Rim Laser Damage 2015: Optical Materials for High-Power Lasers*, J. Shao, T. Jitsuno, W. Rudolph, and M. Zhu, Eds., International Society for Optics and Photonics, vol. 9532, SPIE, 2015, pp. 120–135. doi: 10.1117/12.2189861. [Online]. Available: https://doi.org/10.1117/12.2189861.

[48] R. Courchinoux *et al.*, "Laser-induced damage growth with small and large beams: comparison between laboratory experiments and large-scale laser data," in *Laser-Induced Damage in Optical Materials: 2003*, G. J. Exarhos, A. H. Guenther, N. Kaiser, K. L. Lewis, M. J. Soileau, and C. J. Stolz, Eds., International Society for Optics and Photonics, vol. 5273, SPIE, 2004, pp. 99–106. doi: 10.1117/12.524844. [Online]. Available: https://doi.org/10.1117/12.524844.

[49] M. A. Norton *et al.*, "Growth of laser-initiated damage in fused silica at 351 nm," in *Laser-Induced Damage in Optical Materials: 2000*, G. J. Exarhos, A. H. Guenther, M. R. Kozlowski, K. L. Lewis, and M. J. Soileau, Eds., International Society for Optics and Photonics, vol. 4347, SPIE, 2001, pp. 468–468. doi: 10.1117/12.425055. [Online]. Available: https://doi.org/10.1117/12.425055.

[50] R. M. Wood and R. J. Chad, "Laser-induced (1.064-μm) damage threshold measurement at the gec research laboratories, hirst research centre," *Appl. Opt.*, vol. 23, no. 21, pp. 3779–3781, Nov. 1984. doi: 10.1364/AO.23.003779. [Online]. Available: http://opg.optica.org/ao/abstract.cfm?URI=ao-23-21-3779.

[51] J.-Y. Natoli, P. Volto, M. Pommies, G. Albrand, and C. Amra, "Localized laser damage test facility at LOSCM: real-time optical observation and quantitative AFM study," in *Laser-Induced Damage in Optical Materials: 1997*, G. J. Exarhos, A. H. Guenther, M. R. Kozlowski, and M. J. Soileau, Eds., International Society for Optics and Photonics, vol. 3244, SPIE, 1998, pp. 76–85. doi: 10.1117/12.306969. [Online]. Available: https://doi.org/10.1117/12.306969.

[52] L. Gallais and J.-Y. Natoli, "Optimized metrology for laser-damage measurement: application to multiparameter study," *Appl. Opt.*, vol. 42, no. 6, pp. 960–971, Feb. 2003. doi: 10.1364/AO.42.000960. [Online]. Available: http://opg.optica.org/ao/abstract.cfm?URI=ao-42-6-960.

[53] M. A. Josse, R. Courchinoux, L. Lamaignere, J.-C. Poncetta, T. Donval, and H. Bercegol, "Computer-controlled measurements of laser-induced damage statistics on large optics," in *Laser-Induced Damage in Optical Materials: 2004*, G. J. Exarhos, A. H. Guenther, N. Kaiser, K. L. Lewis, M. J. Soileau, and C. J. Stolz, Eds., International Society for Optics and Photonics, vol. 5647, SPIE, 2005, pp. 365–372. doi: 10.1117/12.585272. [Online]. Available: https://doi.org/10.1117/12.585272.

[54] C. Gouldieff, F. Wagner, and J.-Y. Natoli, "Nanosecond uv laser-induced fatigue effects in the bulk of synthetic fused silica: a multi-parameter study," *Opt. Express*, vol. 23, no. 3, pp. 2962–2972, Feb. 2015. doi: 10.1364/OE.23.002962. [Online]. Available: http://www.osapublishing.org/oe/abstract.cfm?URI=oe-23-3-2962.

[55] C. W. Carr, M. J. Matthews, J. D. Bude, and M. L. Spaeth, "The effect of laser pulse duration on laser-induced damage in KDP and SiO2," in *Laser-Induced Damage in Optical Materials: 2006*, G. J. Exarhos, A. H. Guenther, K. L. Lewis, D. Ristau, M. J. Soileau, and C. J. Stolz, Eds., International Society for Optics and Photonics, vol. 6403, SPIE, 2007, 64030K. doi: 10.1117/12.696079. [Online]. Available: https://doi.org/10.1117/12.696079.

[56] M. C. Nostrand *et al.*, "A large-aperture high-energy laser system for optics and optical component testing," in *Laser-Induced Damage in Optical Materials: 2003*, G. J. Exarhos, A. H. Guenther, N. Kaiser, K. L. Lewis, M. J. Soileau, and C. J. Stolz, Eds., International Society for Optics and Photonics, vol. 5273, SPIE, 2004, pp. 325–333. doi: 10.1117/12.528327. [Online]. Available: https://doi.org/10.1117/12.528327.

[57] M. Veinhard, O. Bonville, R. Courchinoux, R. Parreault, J.-Y. Natoli, and L. Lamaignère, "MELBA: a fully customizable laser for damage experiments," in *Laser-Induced Damage in Optical Materials 2017*, G. J. Exarhos, V. E. Gruzdev, J. A. Menapace, D. Ristau, and M. Soileau, Eds., International Society for Optics and Photonics, vol. 10447, SPIE, 2017, pp. 151–157. [Online]. Available: https://doi.org/10.1117/12.2281125.

[58] L. Lamaignère *et al.*, "A powerful tool for comparing different test procedures to measure the probability and density of laser induced damage on optical materials," *Review of Scientific Instruments*, vol. 90, no. 12, 125102, p. 125 102, Dec. 2019. doi: 10.1063/1.5122274.

[59] M. Veinhard, O. Bonville, R. Courchinoux, R. Parreault, J.-Y. Natoli, and L. Lamaignère, "Parametric study of laser-induced damage growth in fused silica optics with large beams at 351nm. part 2: fractal analysis," *Appl. Opt.*, vol. 59, no. 31, pp. 9652–9659, Nov. 2020. doi: 10.1364/AO.400696. [Online]. Available: http://opg.optica.org/ao/abstract.cfm?URI=ao-59-31-9652.

[60] J. A. Menapace, "Developing magnetorheological finishing (MRF) technology for the manufacture of large-aperture optics in megajoule class laser systems," in *Laser-Induced Damage in Optical Materials: 2010*, G. J. Exarhos, V. E. Gruzdev, J. A. Menapace, D. Ristau, and M. J. Soileau, Eds., International Society for Optics and Photonics, vol. 7842, SPIE, 2010, 78421W. doi: 10.1117/12.855603. [Online]. Available: https://doi.org/10.1117/12.855603.

[61] W. Liao, Y. Dai, Z. Liu, X. Xie, X. Nie, and M. Xu, "Detailed subsurface damage measurement and efficient damage-free fabrication of fused silica optics assisted by ion beam sputtering," *Opt. Express*, vol. 24, no. 4, pp. 4247–4257, Feb. 2016. doi: 10.1364/OE.24.004247. [Online]. Available: http://opg.optica.org/oe/abstract.cfm?URI=oe-24-4-4247.

[62] M. L. Spaeth *et al.*, "Optics recycle loop strategy for nif operations above uv laser-induced damage threshold," *Fusion Science and Technology*, vol. 69, no. 1, pp. 265–294, 2016. doi: 10.13182/FST15-119. eprint: https://doi.org/10.13182/FST15-119. [Online]. Available: https://doi.org/10.13182/FST15-119.

[63] P. Cormont, C. Houee, B. D. C. Fernandes, M. Pfiffer, and D. Taroux, "Recycle loop deployed for the large optical components of megajoule laser," in *Optical Design and Fabrication 2019 (Freeform, OFT)*, Optica Publishing Group, 2019, JT5A.9. doi: 10.1364/FREEFORM.2019.JT5A.9. [Online]. Available: http://opg.optica.org/abstract.cfm?URI=Freeform-2019-JT5A.9.

[64] C. E. Thompson, "Optics damage inspection for the nif," Jun. 1998. [Online]. Available: https://www.osti.gov/biblio/289272.

[65] N. Otsu, "A threshold selection method from gray-level histograms," *IEEE Transactions on Systems, Man, and Cybernetics*, vol. 9, no. 1, pp. 62–66, 1979. doi: 10.1109/TSMC.1979.4310076.

[66] F. Bo, C. Fengdong, L. Bingguo, and L. Guodong, "Segmentation of small defects in Final Optics Damage Online Inspection images," in *2012 International Conference on Image Analysis and Signal Processing*, Nov. 2012, pp. 1–4. doi: 10.1109/IASP.2012.6425003.

[67] G. M. Abdulla, L. M. Kegelmeyer, Z. M. Liao, and W. Carr, "Effective and efficient optics inspection approach using machine learning algorithms," in *Laser-Induced Damage in Optical Materials: 2010*, G. J. Exarhos, V. E. Gruzdev, J. A. Menapace, D. Ristau, and M. J. Soileau, Eds., International Society for Optics and Photonics, vol. 7842, SPIE, 2010, pp. 386–393. doi: 10.1117/12.867648. [Online]. Available: https://doi.org/10.1117/12.867648.

[68] A. Carr *et al.*, "Defect classification using machine learning," in *Laser-Induced Damage in Optical Materials: 2008*, G. J. Exarhos, D. Ristau, M. J. Soileau, and C. J. Stolz, Eds., International Society for Optics and Photonics, vol. 7132, SPIE, 2008, pp. 322–327. doi: 10.1117/12.817418. [Online]. Available: https://doi.org/10.1117/12.817418.

[69] G. Liu *et al.*, "Fast automatic classification of input and exit surface laser-induced damage in large-aperture final optics," in *2018 IEEE 3rd Advanced Information Technology, Electronic and Automation Control Conference (IAEAC)*, 2018, pp. 782–790. doi: 10.1109/IAEAC.2018.8577501.

[70] F. Wei *et al.*, "Automatic classification of true and false laser-induced damage in large aperture optics," *Optical Engineering*, vol. 57, no. 5, pp. 1–11, 2018. doi: 10.1117/1.OE.57.5.053112. [Online]. Available: https://doi.org/10.1117/1.OE.57.5.053112.

[71] C. F. Miller *et al.*, "Characterization and repair of small damage sites and their impact on the lifetime of fused silica optics on the National Ignition Facility," in *Laser-Induced Damage in Optical Materials 2018: 50th Anniversary Conference*, C. W. Carr, G. J. Exarhos, V. E. Gruzdev, D. Ristau, and M. Soileau, Eds., International Society for Optics and Photonics, vol. 10805, SPIE, 2018, p. 108051D. doi: 10.1117/12.2501839. [Online]. Available: https://doi.org/10.1117/12.2501839.

[72] M. A. Norton *et al.*, "Growth of laser damage in SiO2 under multiple wavelength irradiation," in *Laser-Induced Damage in Optical Materials: 2005*, G. J. Exarhos, A. H. Guenther, K. L. Lewis, D. Ristau, M. Soileau, and C. J. Stolz, Eds., International Society for Optics and Photonics, vol. 5991, SPIE, 2006, pp. 91–102. doi: 10.1117/12.638833. [Online]. Available: https://doi.org/10.1117/12.638833.

[73] R. A. Negres, D. A. Cross, Z. M. Liao, M. J. Matthews, and C. W. Carr, "Growth model for laser-induced damage on the exit surface of fused silica under uv, ns laser irradiation," *Optics Express*, vol. 22, no. 4, pp. 3824–3844, Feb. 2014. doi: 10.1364/OE.22.003824. [Online]. Available: http://www.opticsexpress.org/abstract.cfm?URI=oe-22-4-3824.

[74] M. Veinhard *et al.*, "Parametric study of laser-induced damage growth in fused silica optics with large beams at 351nm. Part 1: stochastic approach," *Appl. Opt.*, vol. 59, no. 31, pp. 9643–9651, Nov. 2020. doi: 10.1364/AO.400691. [Online]. Available: http://ao.osa.org/abstract.cfm?URI=ao-59-31-9643.

[75] M. A. Sutton, J.-J. Orteu, and H. W. Schreier, *Image Correlation for Shape, Motion and Deformation Measurements - Basic Concepts, Theory and Applications*. Springer Science, 2009, isbn: 978-0-387-78746-6. doi: 10.1007/978-0-387-78747.

[76] B. D. Lucas and T. Kanade, "An Iterative Image Registration Technique with an Application to Stereo Vision," in *IJCAI'81: 7th international joint conference on Artificial intelligence*, vol. 2, Vancouver, Canada, Aug. 1981, pp. 674–679. [Online]. Available: https://hal.archives-ouvertes.fr/hal-03697340.

[77] W. H. Peters and W. F. Ranson, "Digital imaging techniques in experimental stress analysis," *Optical Engineering*, vol. 21, pp. 427–431, 1982.

[78] M. Sutton, W. Wolters, W. Peters, W. Ranson, and S. McNeill, "Determination of displacements using an improved digital correlation method," *Image and Vision Computing*, vol. 1, no. 3, pp. 133–139, 1983, issn: 0262-8856. doi: https://doi.org/10.1016/0262-8856(83)90064-1. [Online]. Available: https://www.sciencedirect.com/science/article/pii/0262885683900641.

[79] W. H. Peters, W. F. Ranson, M. A. Sutton, T. C. Chu, and J. Anderson, "Application Of Digital Correlation Methods To Rigid Body Mechanics," *Optical Engineering*, vol. 22, no. 6, p. 738, Dec. 1983. doi: 10.1117/12.7973231.

[80] T. Chu, W. Ranson, and M. Sutton, "Applications of digital-image-correlation techniques to experimental mechanics," *Experimental Mechanics*, vol. 25, pp. 232–244, Sep. 1985. doi: 10.1007/BF02325092.

[81] F. Hild and S. Roux, "Comparison of local and global approaches to digital image correlation," *Experimental Mechanics*, vol. 52, no. 9, pp. 1503–1519, 2012.

[82] J. Neggers, B. Blaysat, J. P. M. Hoefnagels, and M. G. D. Geers, "On image gradients in digital image correlation," *International Journal for Numerical Methods in Biomedical Engineering*, vol. 105, no. 4, pp. 243–260, 2016. doi: 10.1002/nme.4971. [Online]. Available: https://hal.archives-ouvertes.fr/hal-03261191.

[83] F. Hild and S. Roux, "Handbook of damage mechanics," in Springer, 2015, ch. Evaluating Damage with Digital Image Correlation: A. Introductory Remarks and Detection of Physical Damage, pp. 1255–1275.

[84] F. Hild and S. Roux, "Evaluating damage with digital image correlation: b. from physical to mechanical damage," in *Handbook of Damage Mechanics: Nano to Macro Scale for Materials and Structures*, G. Z. Voyiadjis, Ed. New York, NY: Springer New York, 2013, pp. 1–20, isbn: 978-1-4614-8968-9. doi: 10.1007/978-1-4614-8968-9_25-1. [Online]. Available: https://doi.org/10.1007/978-1-4614-8968-9_25-1.

[85] M. Caminero, S. Pavlopoulou, M. López-Pedrosa, B. Nicolaisson, C. Pinna, and C. Soutis, "Using digital image correlation techniques for damage detection on adhesively bonded composite repairs," *Advanced Composites Letters*, vol. 21, no. 2, p. 096 369 351 202 100 203,

2012. doi: 10.1177/096369351202100203. eprint: https://doi.org/10.1177/096369351202100203. [Online]. Available: https://doi.org/10.1177/096369351202100203.

[86] T. Ramos *et al.*, "2d and 3d digital image correlation in civil engineering – measurements in a masonry wall," *Procedia Engineering*, vol. 114, pp. 215–222, 2015, ICSI 2015 The 1st International Conference on Structural Integrity Funchal, Madeira, Portugal 1st to 4th September, 2015, issn: 1877-7058. doi: https://doi.org/10.1016/j.proeng.2015.08.061. [Online]. Available: https://www.sciencedirect.com/science/article/pii/S1877705815017002.

[87] J. Curt, M. Capaldo, F. Hild, and S. Roux, "Modal analysis of a wind turbine tower by digital image correlation," *Journal of Physics: Conference Series*, vol. 1618, no. 2, p. 022 002, Nov. 2020. doi: 10.1088/1742-6596/1618/2/022002. [Online]. Available: https://doi.org/10.1088/1742-6596/1618/2/022002.

[88] T. M. Grabois, J. Neggers, L. Ponson, F. Hild, and R. D. Toledo Filho, "On the validation of integrated dic with tapered double cantilever beam tests," *Engineering Fracture Mechanics*, vol. 191, pp. 311–323, 2018, issn: 0013-7944. doi: https://doi.org/10.1016/j.engfracmech.2017.12.015. [Online]. Available: https://www.sciencedirect.com/science/article/pii/S0013794417309232.

[89] A. Charbal *et al.*, "Integrated digital image correlation considering gray level and blur variations: application to distortion measurements of ir camera," *Optics and Lasers in Engineering*, vol. 78, pp. 75–85, Mar. 2016. doi: 10.1016/j.optlaseng.2015.09.011.

[90] A. Guery, F. Latourte, F. Hild, and S. Roux, "Characterization of sem speckle pattern marking and imaging distortion by digital image correlation," *Measurement Science and Technology*, vol. 25, pp. 5401–, Jan. 2014. doi: 10.1088/0957-0233/25/1/015401.

[91] Q. Shi *et al.*, "Calibration of Crystal Orientation and Pattern Center of EBSD using Integrated Digital Image Correlation," *Materials Characterization*, Jun. 2021. doi: 10.1016/j.matchar.2021.111206. [Online]. Available: https://hal.archives-ouvertes.fr/hal-03652308.

[92] V. Sciuti, R. Canto, J. Neggers, and F. Hild, "On the benefits of correcting brightness and contrast in global digital image correlation: monitoring cracks during curing and drying of a refractory castable," *Optics and Lasers in Engineering*, vol. 136, p. 106 316, 2021, issn: 0143-8166. doi: https://doi.org/10.1016/j.optlaseng.2020.106316. [On-

line]. Available: http://www.sciencedirect.com/science/article/pii/S0143816620305686.

[93] J. Rupil, S. Roux, F. Hild, and L. Vincent, "Fatigue microcrack detection with digital image correlation," *The Journal of Strain Analysis for Engineering Design*, vol. 46, no. 6, pp. 492–509, 2011. doi: 10.1177/0309324711402764. eprint: https://doi.org/10.1177/0309324711402764. [Online]. Available: https://doi.org/10.1177/0309324711402764.

[94] F. E. Nicodemus, J. C. Richmond, J. J. Hsia, *et al.*, "Geometrical considerations and nomenclature for reflectance," in *Radiometry*. USA: Jones and Bartlett Publishers, Inc., 1992, pp. 94–145, isbn: 0867202947.

[95] J. Stover, *Optical Scattering: Measurement and Analysis*, ser. Press Monographs. SPIE Press, 2012, isbn: 9780819492517. [Online]. Available: https://books.google.fr/books?id=tDtpLwEACAAJ.

[96] E. L. Church, P. Z. Takacs, and T. A. Leonard, "The Prediction Of BRDFs From Surface Profile Measurements," in *Scatter from Optical Components*, J. C. Stover, Ed., International Society for Optics and Photonics, vol. 1165, SPIE, 1990, pp. 136–150. doi: 10.1117/12.962842. [Online]. Available: https://doi.org/10.1117/12.962842.

[97] C. L. Vernold and J. E. Harvey, "Comparison of Harvey-Shack scatter theory with experimental measurements," in *Scattering and Surface Roughness*, Z.-H. Gu and A. A. Maradudin, Eds., International Society for Optics and Photonics, vol. 3141, SPIE, 1997, pp. 128–138. doi: 10.1117/12.287792. [Online]. Available: https://doi.org/10.1117/12.287792.

[98] M. G. Dittman, "K-correlation power spectral density and surface scatter model," in *Optical Systems Degradation, Contamination, and Stray Light: Effects, Measurements, and Control II*, O. M. Uy, J. C. Fleming, and M. G. Dittman, Eds., International Society for Optics and Photonics, vol. 6291, SPIE, 2006, pp. 226–237. doi: 10.1117/12.678320. [Online]. Available: https://doi.org/10.1117/12.678320.

[99] J. E. Harvey, A. Krywonos, and J. C. Stover, "Unified scatter model for rough surfaces at large incident and scatter angles," in *Advanced Characterization Techniques for Optics, Semiconductors, and Nanotechnologies III*, A. Duparré, B. Singh, and Z.-H. Gu, Eds., International Society for Optics and Photonics, vol. 6672, SPIE, 2007, pp. 103–110. doi: 10.1117/12.739139. [Online]. Available: https://doi.org/10.1117/12.739139.

[100] S. Schröder, A. Duparré, L. Coriand, A. Tünnermann, D. H. Penalver, and J. E. Harvey, "Modeling of light scattering in different regimes of surface roughness," *Opt. Express*, vol. 19, no. 10, pp. 9820–9835, May 2011. doi: 10.1364/OE.19.009820. [Online]. Available: http://www.opticsexpress.org/abstract.cfm?URI=oe-19-10-9820.

[101] J. C. Stover, V. Lopushenko, K. Tayabaly, and E. Church, "Calculating BTDF from window surface roughness," in *Optical Manufacturing and Testing X*, O. W. Fähnle, R. Williamson, and D. W. Kim, Eds., International Society for Optics and Photonics, vol. 8838, SPIE, 2013, pp. 16–21. doi: 10.1117/12.2024599. [Online]. Available: https://doi.org/10.1117/12.2024599.

[102] C. Amra, "First-order vector theory of bulk scattering in optical multilayers," *J. Opt. Soc. Am. A*, vol. 10, no. 2, pp. 365–374, Feb. 1993. doi: 10.1364/JOSAA.10.000365. [Online]. Available: http://josaa.osa.org/abstract.cfm?URI=josaa-10-2-365.

[103] E. Feigenbaum, N. Nielsen, and M. J. Matthews, "Measurement of optical scattered power from laser-induced shallow pits on silica," *Appl. Opt.*, vol. 54, no. 28, pp. 8554–8560, Oct. 2015. doi: 10.1364/AO.54.008554. [Online]. Available: http://ao.osa.org/abstract.cfm?URI=ao-54-28-8554.

[104] M. Lequime, M. Zerrad, C. deumié, and C. Amra, "A goniometric light scattering instrument with high-resolution imaging," *Optics Communications*, vol. 282, Apr. 2009. doi: 10.1016/j.optcom.2008.12.053.

[105] M. Zerrad, M. Lequime, C. Deumié, and C. Amra, "CCD-ARS set-up: a comprehensive and fast high-sensitivity characterisation tool for optical components," in *Optical Micro- and Nanometrology III*, C. Gorecki, A. K. Asundi, and W. Osten, Eds., International Society for Optics and Photonics, vol. 7718, SPIE, 2010, pp. 52–62. doi: 10.1117/12.854059. [Online]. Available: https://doi.org/10.1117/12.854059.

[106] R. Ceolato, N. Riviere, and L. Hespel, "Reflectances from a supercontinuum laser-based instrument: hyperspectral, polarimetric and angular measurements," *Opt. Express*, vol. 20, no. 28, pp. 29 413–29 425, Dec. 2012. doi: 10.1364/OE.20.029413. [Online]. Available: http://www.opticsexpress.org/abstract.cfm?URI=oe-20-28-29413.

[107] F. Leloup, W. Ketelaere, J. Audenaert, and P. Hanselaer, "Rapid determination of the photometric bidirectional scatter distribution function by use of a near-field goniophotometer," *Proceedings of SPIE - The International Society for Optical Engineering*, vol. 9018, Jan. 2014. doi: 10.1117/12.2035958.

[108] S. Liukaityte, M. Zerrad, M. Lequime, T. Bégou, and C. Amra, "Measurements of angular and spectral resolved scattering on complex optical coatings," in *Optical Systems Design 2015: Advances in Optical Thin Films V*, M. Lequime, H. A. Macleod, and D. Ristau, Eds., International Society for Optics and Photonics, vol. 9627, SPIE, 2015, pp. 229–235. doi: 10.1117/12.2191227. [Online]. Available: https://doi.org/10.1117/12.2191227.

[109] D. J. Griffith, "Measurement and modelling of the directional scattering of light.," Ph.D. dissertation, 2015.

[110] R. Fluck, P. J. Wegner, L. M. Sheehan, and L. A. Hackel, "Angle-resolved scatter measurements of laser-damaged DKDP crystals using a bidirectional scatter diagnostics," in *Laser-Induced Damage in Optical Materials: 2000*, G. J. Exarhos, A. H. Guenther, M. R. Kozlowski, K. L. Lewis, and M. J. Soileau, Eds., International Society for Optics and Photonics, vol. 4347, SPIE, 2001, pp. 423–431. doi: 10.1117/12.425048. [Online]. Available: https://doi.org/10.1117/12.425048.

[111] M. Fouchier, M. Zerrad, M. Lequime, and C. Amra, "Wide-range wavelength and angle resolved light scattering measurement setup," *Opt. Lett.*, vol. 45, no. 9, pp. 2506–2509, May 2020. doi: 10.1364/OL.392000. [Online]. Available: http://opg.optica.org/ol/abstract.cfm?URI=ol-45-9-2506.

Part II

From gray levels to damage size

Accurate damage size measurement at subpixel resolution is of major importance in order to optimize the LMJ optics recycle loop. The aim is to be able to measure damage sizes from $30\,\mu\mathrm{m}$ to $300\,\mu\mathrm{m}$. Since the spatial resolution of acquired images is $\approx 100\,\mu\mathrm{m}$/pixel, diameter estimations by pixel-counting methods are not sufficient. Another method based on pixel intensities was proposed at NIF to measure damage diameter [1]. The pixel intensity method needs a time-consuming calibration process, performed most of the time using dedicated optics with damage sites. This part is organized in 2 chapters.

In Chapter 2, an optical model-based calibration is proposed to measure damage sizes from pixel intensities. The model involves lighting system simulations, measurements of light scattering by damage sites and simulation of the imaging system. The optical-model based calibration is compared to an in-situ calibration performed with a dedicated vacuum window with more than 900 damage sites.

The current LMJ lighting system is based on 2 LEDs for each vacuum window. Such system is limited in robustness and lighting homogeneity on the exit surface of vacuum windows. A new lighting system was proposed by a student during his internship in order to overcome these limitations. The proposed system involves a fiber source and a reflector integrated in the frame of vacuum windows. In Chapter 3, the performances of the proposed lighting system are simulated using the model described in Chapter 2 and compared to those obtained for the twin LED system in nominal (2 LEDs on) and degraded (1 LED on) configurations.

2

Optical model-based calibration of gray levels for damage size assessment

Fused silica is prone to damage under ultraviolet laser irradiation. Because they are key components to achieve fusion on high energy laser facilities, final fused silica optics are analyzed after each laser shot. Due to limited image resolution, the accurate quantification of damage sites smaller than $300\,\mu\mathrm{m}$ is based on light scattering measurements aiming for sub-pixel detection after calibration. The calibration is usually conducted by time-consuming measurements for laser facilities. It is proven herein that modeling a laser damage size monitoring process based on light scattering is efficient to link gray levels to damage diameters avoiding any experimental calibration based on a reference optics on the facility.

Extended version from:
G. Hallo, C. Lacombe, M. Fouchier, M. Zerrad, J. Néauport and F. Hild.
Optical model-based calibration of gray levels for damage size assessment.
Submitted paper.

2.1 Introduction

High power laser facilities such as the National Ignition Facility (NIF), the ShenGuang-III (SG-III) and the Laser MegaJoule (LMJ) were designed to achieve fusion by inertial confinement [1–3]. For each laser beam, multi-kilojoule ultraviolet (UV) laser energy with nanosecond pulse duration is required. Under such extreme laser conditions, optical components made of fused silica are prone to exhibiting laser-induced damage [4]. Once a damage site has initiated, it grows after each UV laser shot since the laser energy is greater than the growth threshold, which is usually the case for fusion scale laser facilities [5]. To some extent, the performances of such large installations are therefore limited by laser-induced damage of final optics [6]. To partially overcome this issue, two complementary methods have been developed, namely, Carbon Dioxide (CO_2) laser optics mitigation and local laser shadowing [7]. CO_2 laser optics mitigation is possible as long as the damage size is less than $750\,\mu\mathrm{m}$. However, the mitigation requires the optics to be removed from the facility. Small parts of the laser beam may be shaded to stop the growth of critical damage sites and, therefore manage the number of optics removals. Hence, it is necessary to detect damage sites and quantify their growth before they reach the mitigation limit. In order to be sure that no damage site reaches the mitigation limit ($750\,\mu\mathrm{m}$ in diameter), a corresponding safety margin of a factor 2 on the estimated damage diameter is taken, so that the limit used at LMJ is $300\,\mu\mathrm{m}$. This margin takes into account the measurement error on the diameter as well as the possibility for a damage site to exceed $750\,\mu\mathrm{m}$ in diameter after one supplementary laser shot with high fluence. Images of the final optics are acquired after each laser shot using similar imaging systems at NIF, SG-III and LMJ [7–9]. The optics are illuminated from the edge. Light is internally trapped in the optics until it reaches a damage site that scatters it. A part of the scattered light from damage sites is collected by the imaging system at a distance of $8\,\mathrm{m}$. The acquired images are dark-fields with bright spots corresponding to damage sites. The image resolution ($\approx 100\,\mu\mathrm{m}$/pixel) is not sufficient to accurately measure the diameter of damage sites less than $300\,\mu\mathrm{m}$ by counting the number of pixels corresponding to the image of damage sites (so-called pixel-counting method). This low accuracy on diameter measurement is not compatible with damage growth quantification required for an efficient mitigation.

Light scattering methods were widely used to estimate the size of proteins [10]. To measure damage growth with sub-pixel resolution without modifying the imaging and acquisition systems, one proposed solution was

to use the gray levels of acquired images due to damage light scattering [7]. However, images may suffer from some disturbances [11]. Techniques based on Digital Image Correlation (DIC) principles were proposed to correct these acquired images. After corrections, the pixel intensity variations were only affected by damage growth and acquisition noise [11]. Since light scattering from molecules allows their radius of gyration and weight to be estimated, the signals emitted by light scattering from laser damage may provide information about their diameter, depth and possibly their growth. Thanks to an image calibration process, it was shown that integrated gray levels were positively correlated to damage sizes [7]. This calibration process requires an optic to be prepared with numerous laser damage sites with different sizes, to be mounted on the installation, and images of the damaged optic to be acquired. In the busy operational schedule of a large fusion-scale laser facility, this method is time-consuming, especially since this calibration must be performed for each of the laser beams due to possible variations in lighting conditions.

In the following, an optical model-based calibration is proposed to estimate damage diameters from gray levels instead of using a reference optics mounted on the facility. The optical model of the image acquisition process makes gray level simulations possible. The model may be used after revision or potential structural modification of the acquisition system to avoid a new online time-consuming calibration. It is based on damage light scattering measurements, optical simulation of the lighting system, and a numerical model of the image acquisition system.

The image acquisition system of laser-induced damage on LMJ final optics is described in Section 2.2. Each step of the modeling process is presented, namely, lighting system, light scattering by damage sites, and imaging system. An image of a final optics with 930 damage sites was acquired on the LMJ facility to be used as reference for the simulations. The results are presented and compared to the reference image (Section 2.3).

2.2 Material and methods

The monitored 176 final optics at LMJ, among which the so-called vacuum windows, are distributed all around the $8\,\mathrm{m}$ in radius experiment chamber. A vacuum window is a $40\,\mathrm{cm}$ large optical component. To make damage sites visible, each vacuum window is illuminated by 2 green Light-Emitting Diodes (LEDs) mounted on one edge of the components. Such LEDs have a maximum emissivity at $525\,\mathrm{nm}$. Light provided by the LEDs enters into the optics and illuminates the rear and front sides of the vacuum windows.

Aluminum alloy frames maintain the optical components. The light that reaches the frame is reflected in the vacuum window. Laser damage sites, mainly located on the front face, scatter light. A part of this scattered light is collected by an objective lens, that images vacuum windows on a Charge Coupled Device (CCD) sensor. It converts the collected light energy into gray levels. The image acquisition configuration and an example of acquired image are shown in Figure 2.1.

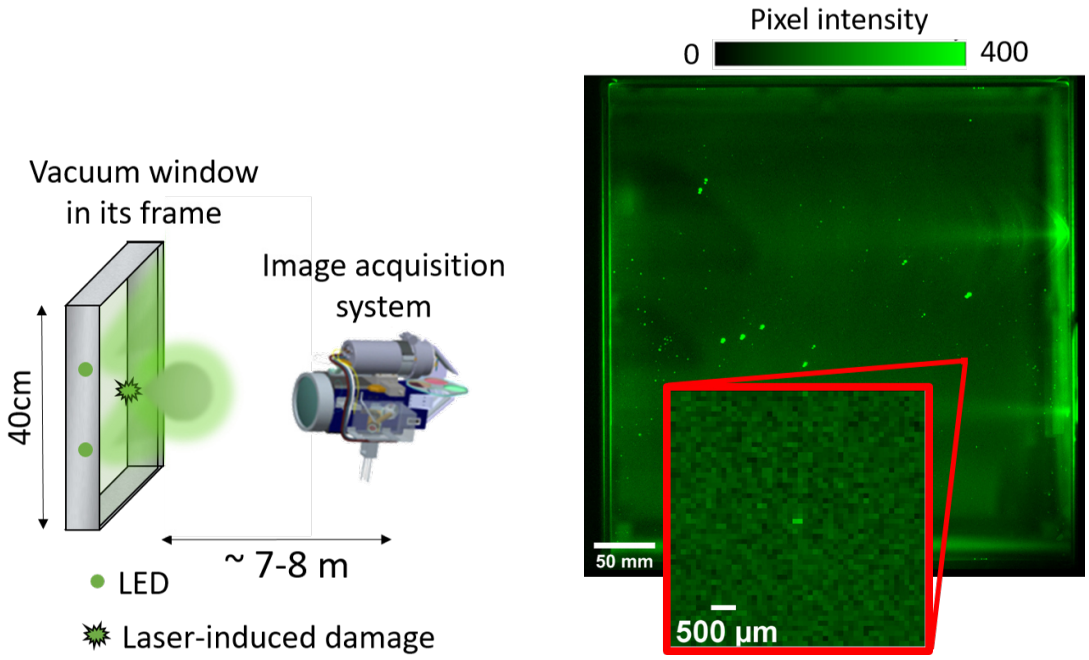

Figure 2.1: (a) Schematic view of image acquisition for an LMJ vacuum window. (b) Example of acquired image of a damaged vacuum window. A damage site with a diameter of less than $300\,\mu\mathrm{m}$ is shown in the red box.

The optical model presented in this chapter is divided into several parts (lighting system, light scattering by damage sites and imaging system) as shown in Figure 2.2. Using the proposed model, the integrated pixel intensity of a damage site is expressed as a function of damage site size and lighting parameters. Each part is fully described in the following section.

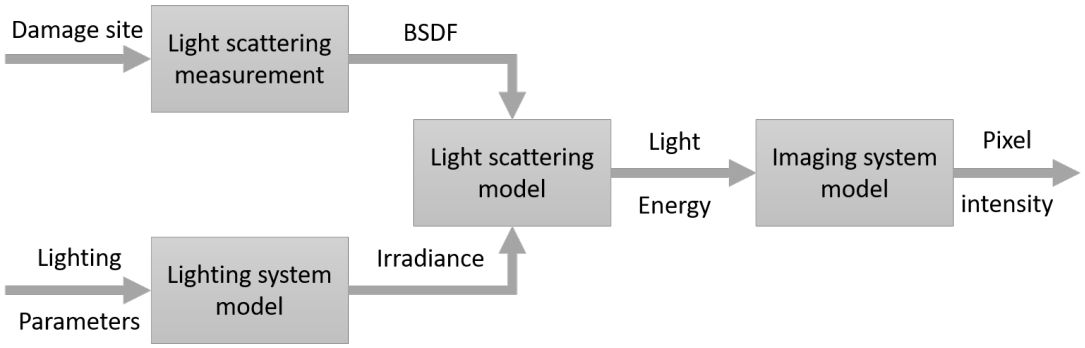

Figure 2.2: Block diagram of the optical model starting from a damage site and lighting system parameters to pixel intensity in the image.

2.2.1 Lighting system model

The two LEDs, the fused silica vacuum window and its aluminum alloy frame are considered as the lighting system. The following simplifying assumptions are made:

- Reflections on the frame are considered as specular;
- Screws and other small mounting devices of the frame have been removed from the model for ray tracing considerations;
- Optical coating anti-reflection in the ultraviolet wavelength of the vacuum window is not modeled.

Under these assumptions, the input data of the lighting system model are:

- The LED wavelength emissivity ($525\,\mathrm{nm}$);
- The angular distribution of LED emission (Nichia NSPG500DS);
- The light intensity of the LEDs ($37.7\,\mathrm{cd}$);
- The geometry of a vacuum window with beveled corners made of fused silica (Heraeus Suprasil);
- The simplified geometry of the optical frame in aluminum alloy and its 90% reflectivity at $525\,\mathrm{nm}$.

These input data were implemented in the ray tracing software Zemax OpticStudio in a non-sequential mode [12]. A square matrix of 100 rectangular detectors collects the incident radiance [$\mathrm{W\,m^{-2}\,sr^{-1}}$] on the front face of the vacuum window for several positions on the surface as shown as orange squares in Figure 2.3.

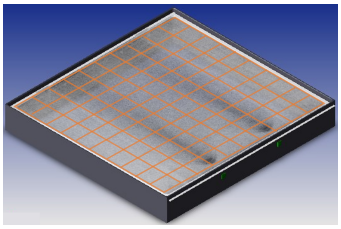

Figure 2.3: Result of OpticStudio (Zemax) simulation with the described lighting system model. The square matrix of detectors is shown as orange squares. The distribution of simulated incident light energy on the face of the window is displayed in gray levels.

2.2.2 Lighting scattering measurements

Once the (previously simulated) incident light reaches a damage site, the latter scatters it according to a function known as the Bidirectional Scattering Distribution Function (BSDF) [13]. The BSDF links the scattered radiance by a surface, L_s [$\mathrm{W\,m^{-2}\,sr^{-1}}$], and the incident irradiance on the surface, E_i [$\mathrm{W\,m^{-2}}$], for the incident angles θ_i and ϕ_i, and the scattered angles θ_s and ϕ_s (spherical coordinates)

$$BSDF(\theta_i, \phi_i, \theta_s, \phi_s) = \frac{dL_s(\theta_i, \phi_i, \theta_s, \phi_s)}{dE_i(\theta_i, \phi_i, \theta_s, \phi_s)} \tag{2.1}$$

To simulate the amount of scattered light toward the imaging system, the BSDF function needs to be known. It may be modeled or directly measured [14]. Beckmann and Spizzichino proposed to measure the scatter as a function of angle, and to relate it to surface statistics [15]. Since then, many other works have linked the surface roughness to the scattering function from smooth to rough surfaces [16–20]. However, the validity of these models is limited to surface scattering. A damage site can be seen as a crater in hundreds of micrometers with sub-surface cracks [21]. Scattering surface models do not take into account the interaction between crater scattering (surface) and sub-surface crack scattering (volume).

It is also possible to measure directly the BSDF of a sample in reflection and transmission [14, 22]. In this paper, it was chosen to measure the BSDF of 12 damage sites whose diameters ranged from $100\,\mu\mathrm{m}$ to $700\,\mu\mathrm{m}$. The 12 damage sites were initiated with a $1064\,\mathrm{nm}$ wavelength laser at $8\,\mathrm{ns}$ pulse duration on fused silica wafers with no optical coating. The wafers were circular with a $1\,\mathrm{mm}$ thickness and a $10\,\mathrm{cm}$ diameter. Two sites were initiated on each wafer, spaced by $5\,\mathrm{cm}$ between them, and $2.5\,\mathrm{cm}$ from the wafer edge. For larger sites, multilaser shots were performed

to grow the sites to the specified size. Despite the damage mechanisms being different between ultraviolet and infrared wavelengths, the damage morphology obtained at infrared wavelength for diameters greater than $200\,\mu\mathrm{m}$ was representative of damage sites initiated and grown at ultraviolet wavelength [23]. However, smaller damage sites (with diameters less than $200\,\mu\mathrm{m}$) induced by infrared laser were not considered representative of ultraviolet laser-induced damage sites [23]. This is the reason why the diameters used for the simulation begin at $230\,\mu\mathrm{m}$. Seven measured damage sites are shown in Figure 2.4.

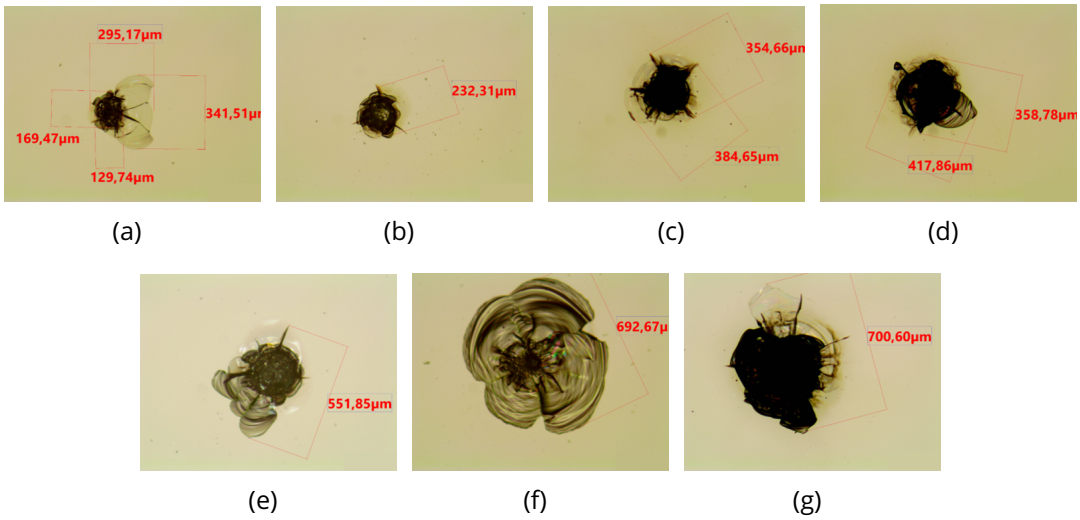

(a) (b) (c) (d)

(e) (f) (g)

Figure 2.4: Images of 7 laser damage sites whose BSDF was measured. The different shapes of the sites are considered as representative of the sites observed on a dedicated LMJ vacuum window.

The scattering measurements were performed with the Spectral and Angular Light Scattering Apparatus in its 4$^{\text{th}}$ configuration (SALSA 4) [22]. A supercontinuum laser and spectrally tunable filters allow the illumination wavelength to be chosen in the range $[400\,\mathrm{nm};\ 1650\,\mathrm{nm}]$. The measured quantity with SALSA 4 is the Angle Resolved Scattering (ARS)

$$ARS(\theta_i, \phi_i, \theta_s, \phi_s) = BSDF(\theta_i, \phi_i, \theta_s, \phi_s)\cos(\theta_i) \tag{2.2}$$

The BSDFs were measured for all damage sites at $525\,\mathrm{nm}$ wavelength, which matched the maximum emissivity of LMJ lighting systems. Measurements at $650\,\mathrm{nm}$, $800\,\mathrm{nm}$ and $1600\,\mathrm{nm}$ for site (b) in Figure 2.4 were carried out to eventually find a wavelength that maximized the scattering signal

of damage sites. No variation in light scattering was measured between the different wavelengths.

Based on ARS measurements, it is possible to compute the energy of light collected by the objective lens of the LMJ imaging system. The scattered radiance of a damage site toward the objective of the imaging system reads

$$L_s = \int_{\theta_i} \int_{\phi_i} \int_{\theta_s} \int_{\phi_s} BSDF(\theta_i, \phi_i, \theta_s, \phi_s) E_i(\theta_i, \phi_i) d\theta_i d\phi_i d\theta_s d\phi_s \tag{2.3}$$

for $\theta_i \in [0; \frac{\pi}{2}]$; $\phi_i \in [0; 2\pi]$; $\theta_s \in [\pi - \alpha, \pi]$ and $\phi_s \in [0, 2\pi]$, where α is the object aperture angle of the objective lens. Thus, the scattered radiance becomes

$$L_s = 4\pi^2 \int_{\theta_i} \int_{\phi_i} \int_{\theta_s} ARS(\theta_i, \phi_i, \theta_s) L_i(\theta_i, \phi_i) d\theta_i d\phi_i d\theta_s \tag{2.4}$$

The scattered flux toward the objective lens Φ_s [W] reads

$$\Phi_s = L_s \cos(\theta_{obj}) A_d 2\pi (1 - \cos(\alpha)) \tag{2.5}$$

where L_s [$\mathrm{W\,m^{-2}\,sr^{-1}}$] is the scattered radiance toward the objective, A_d [$\mathrm{m^2}$] the area of the damage site, α the objective aperture angle, and θ_{obj} the angle between the normal axis to the face of the vacuum window and the optical axis of the camera.

The scattered flux to the objective lens is considered as constant over the acquisition time of the camera, Δ_t [s]. Thus, the scattered light energy, E_s [J] toward the objective lens reduces to

$$E_s = \Phi_s \Delta_t \tag{2.6}$$

2.2.3 Imaging system model

Once the scattered energy toward the objective lens is computed, the integrated signal of gray levels is obtained by modeling the CCD sensor whose model is summarized in Figure 2.5.

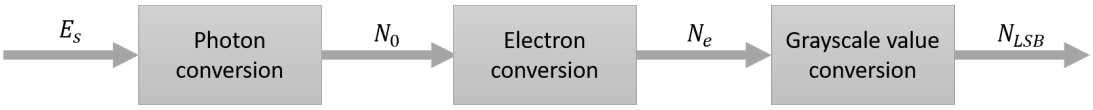

Figure 2.5: Several steps to create the imaging system model.

Several conversions are performed:

- Photon conversion – $N_0 = \frac{E_s}{h\nu}$, where N_0 is the number of photons collected by the CCD sensor for a light energy E_s at the associated frequency ν, and h Planck's constant;

- Electron conversion – $N_e = QE(\lambda)N_0$, where N_e is the number of electrons generated by the CCD sensor for a given number of photons, $QE(\lambda)$ the Quantum Efficiency of the CCD sensor at a given wavelength λ;

- Gray level conversion – $\mathrm{TIS} = \frac{N_e}{F_c}$, where TIS is the Total Integrated Signal level on the CCD sensor pixels that are illuminated by the image of a damage site. F_c is the conversion factor of the CCD sensor to estimate the pixel intensities from the number of electrons generated by the pixels. Experimentally, the TIS is the sum of the intensity of pixels that describes the image of a damage site.

Finally, the Total Integrated Signal (TIS) reads

$$\mathrm{TIS} = w\frac{E_s QE}{h\nu F_c} \tag{2.7}$$

where the coefficient w is a constant weight used to calibrate the model on measurements. The purpose of this coefficient is to compensate for errors due to the lack of exact knowledge of some system parameters.

2.2.4 Validation with a vacuum window image

To validate the results of simulations using the proposed model, 930 damage sites were initiated on a new vacuum window. A Neodymium-Doped Yttrium Aluminium Garnet (Nd:YAG) laser set-up was used to initiate damage sites [24]. True damage site diameters were measured with an optical microscope before the component was mounted on the facility. The diameters of these sites ranged between $50\,\mu\mathrm{m}$ and $270\,\mu\mathrm{m}$, and they are referred to as true diameters. An image of this optical component illuminated by the lighting system was acquired by the imaging device once the component was mounted on the LMJ beam. The acquired image is shown Figure 2.6 (b). A mitigation process of laser damage sites with a CO_2 laser was applied on the red areas in Figure 2.6 (a). The damage mitigation testing sites are beyond the scope of this chapter.

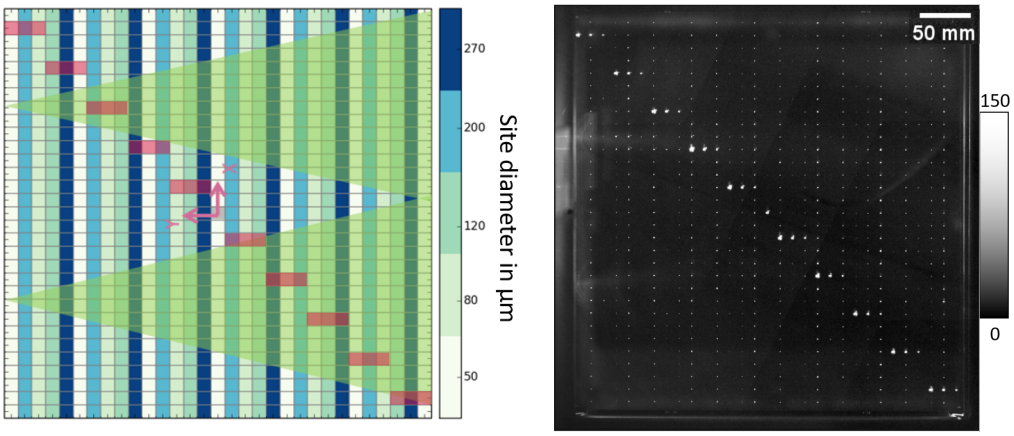

(a) (b)

Figure 2.6: (a) Draft of the damaged vacuum window with $50\,\mu\mathrm{m}$, $80\,\mu\mathrm{m}$, $120\,\mu\mathrm{m}$, $200\,\mu\mathrm{m}$ and $270\,\mu\mathrm{m}$ damage diameters. (b) Acquired image of the vacuum window (16-bit digitization).

2.3 Results

The TIS was measured for each damage site of the acquired image shown in Figure 2.6(b), and it is plotted as a function of the true damage site diameter in Figure 2.7. The measured TIS values are the sum of pixel values considered to describe each calibrated damage sites of the vacuum window.

The incident light is collected by the area of each damage site. As shown in Equation (2.5), the flux scattered by a damage site is proportional to its surface area. Hence, it was chosen to interpolate the measured TIS with a square power law in diameter (*i.e.,* linear in area)

$$\mathrm{TIS}_m = \kappa \left(\frac{D}{D_0}\right)^2 \tag{2.8}$$

where D denotes the diameter of the damaged site, D_0 the physical size of one pixel ($100\,\mu\mathrm{m}$), and κ the scale parameter equal to $3.5\ 10^3$ gray levels. Thus, the diameter of a damage site reads

$$D = D_0\sqrt{\frac{\mathrm{TIS}}{\kappa}} \tag{2.9}$$

The TISs of 5 damage sites (a, b, c, d, e in Figure 2.4) were simulated for the 100 positions on the vacuum window corresponding to the 100

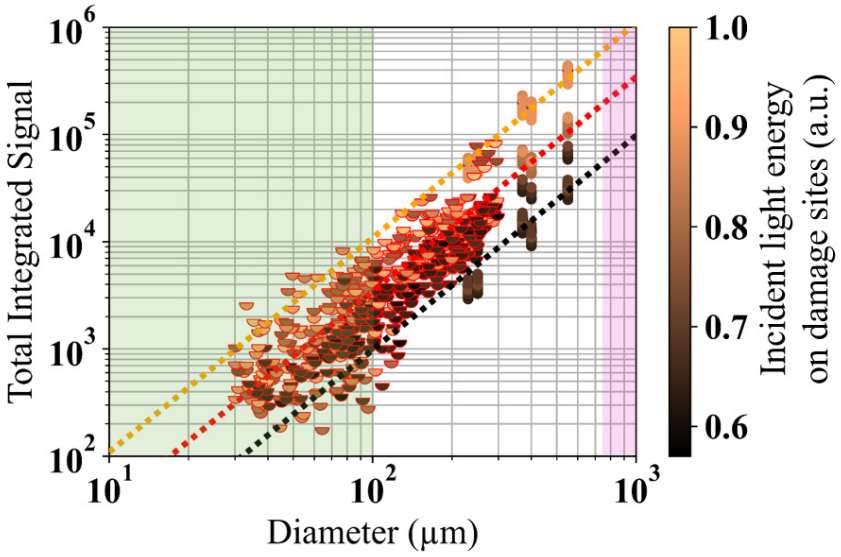

Figure 2.7: Measured TIS_m on the acquired image for each damage site as a function of its diameter (half circle markers with red edge). The color bar indicates the incident light energy on each damage site in arbitrary units. The measured results are interpolated by Equation (2.8) (red dotted line). Simulated TIS_s for 5 damage sites as a function of their diameters (full circle markers). The orange (resp. dark) dashed line indicates the interpolation of the TIS_s for the 10% brightest (resp. the 10% least illuminated) areas on the vacuum window with $\kappa = 10^4$ (resp. $\kappa = 10^3$). The pink rectangle corresponds to damage sites that could not be mitigated using the CO_2 laser method while it is possible for green and white domains. The green area corresponds to damage sites whose diameters were less than the available image resolution.

rectangular detectors used to collect the incident radiance. The damage diameters for the simulation varied from $230\,\mu\mathrm{m}$ and $550\,\mu\mathrm{m}$, corresponding to about the largest size where damage mitigation was possible (white area in Figure 2.7). The simulated TIS_s for these 5 damage sites are plotted with circled markers in Figure 2.7 as functions of damage diameter. The simulated TIS_s was also interpolated by the same diameter squared law. The scale parameter was equal to $3.5\ 10^3$ gray levels.

As shown in Figure 2.7, for any size of the damage sites, all TISs obtained by simulation or acquisition are in agreement with Equation (2.9). The proposed optical model is deemed efficient to simulate damage TIS measured by the LMJ acquisition system. For most damage sites, the higher

the incident light energy, the higher the TIS. However, some exceptions are observed. They are likely to be due to the approximations of modeling and differences in morphology between sites.

Figure 2.8 compares the results of diameter estimation using two different methods (*i.e.,* pixel-counting method and TIS-based method) for damage diameters ranging between $30\,\mu\mathrm{m}$ and $300\,\mu\mathrm{m}$. These diameters correspond to sizes where a decision about damage mitigation has to be made. Measuring the diameter by pixel-counting induces an overestimation by a factor varying between 2.2 and 3.4 compared to the true damage sizes while measuring diameters by TIS leads to a correct estimation of the true size of damage. It is worth noting that the 95% prediction interval is almost 3 times narrower for TIS diameters ($\pm\ 68\,\mu\mathrm{m}$ corresponding to green area) than for directly measured diameters ($\pm \approx 180\,\mu\mathrm{m}$ corresponding to blue area). The 95% prediction interval is an estimate of an interval in which diameter estimation for a new damage site will fall with a 0.95 probability.

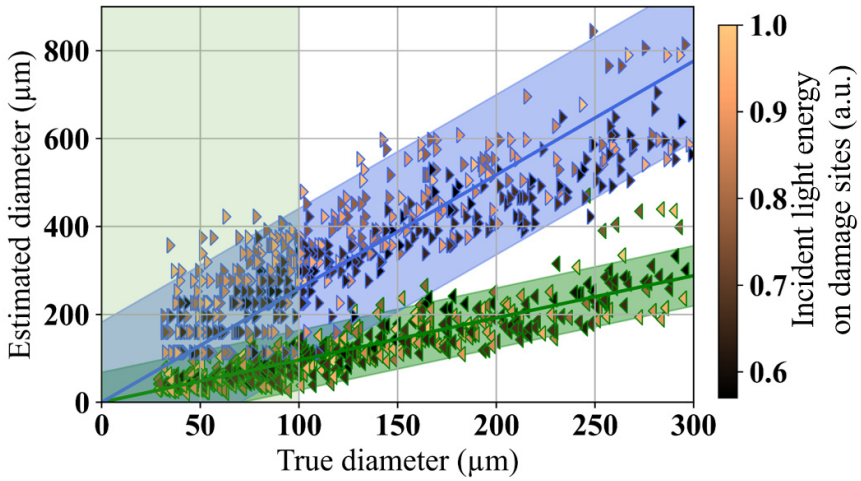

Figure 2.8: Measured diameters of each damage sites by pixel-counting method on the acquired image as a function of the true diameter (right triangle with blue edge). The blue line indicates a linear interpolation of measured diameters. The blue area shows the 95% prediction interval of the measured diameters. Estimated diameters of each damage sites from TIS using Equation (2.9) (left triangle with green edge). The green line indicates the linear interpolation of the estimated diameters. The green area shows the 95% prediction interval of the estimated diameters.

Table 2.1 summarizes the prediction intervals on diameter estimations

based on pixel-counting method and TIS measurements for 4 true diameter intervals. The slopes of the linear interpolation between estimated and true diameters are given for both methods. It is noteworthy that the TIS-based method is efficient to estimate damage size for damage sites less than the image resolution (*i.e.,* [30; 100] μm), which is not the case for pixel-counting measurements. Furthermore, the slope for the TIS diameter is constant over all true diameter intervals from $30\,\mu m$ to $300\,\mu m$. It is not possible to state the same for the measured diameter by pixel-counting method. The relationship between true damage size and measured size on the images is nonlinear. However, as damage sites become larger, the prediction interval of the TIS diameter widens. Diameter estimations by TIS are accurate up to damage sizes of $200\,\mu m$, which indicates that it is a convenient way of monitoring damage initiation and early growth.

Table 2.1: Diameter estimation based on pixel-counting measurements on the acquired image, and on TIS measurements for 4 true diameter intervals. The so-called prediction interval is an estimate of an interval in which a future diameter estimation will fall with a 0.95 probability. The slope is the coefficient of the linear interpolation between the true and estimated diameters for each method (direct measurement and TIS).

True diameters	Pixel-counting diameter		TIS diameter	
	Slope	Prediction interval	Slope	Prediction interval
[30; 100] μm	3.44	$\pm$ 144 μm	0.94	$\pm$ 41 μm
[100; 200] μm	2.74	$\pm$ 155 μm	0.95	$\pm$ 67 μm
[200; 300] μm	2.28	$\pm$ 167 μm	0.97	$\pm$ 120 μm
[30; 300] μm	2.59	$\pm$ 182 μm	0.96	$\pm$ 68 μm

2.4 Discussion

A large scatter of TIS over one decade is observed for identical damage sizes in the current LMJ configuration of lighting and acquisition systems, either by measurement or by simulation. This scatter is related to the light energy received by the damage sites depending on their position on the vacuum window (Figure 2.7). This large scatter is mainly due to nonuniform light distribution on the damaged face of the vacuum window induced by the twin LED system (Figure 2.3). These results indicate that the current lighting system itself is not sufficient to provide an invariant TIS measurement according to the damage site position on the vacuum

window. However, it was possible to measure accurately the damage diameter by coupling measured TIS for a damage site and its position on the optical component using the proposed model and simulations. Despite taking into account the TIS and the position of the damage sites, differences in light scattering between 2 sites of same size induced an uncertainty on the size measurement ($\pm$ $68\,\mu\mathrm{m}$ for true diameters between $30\,\mu\mathrm{m}$ and $300\,\mu\mathrm{m}$). The uncertainty is sufficiently low to provide a significant gain on diameter estimation compared to pixel-counting measurements. The scatter of diameter estimation for identical true diameters may also be due to differences in damage morphology.

In the case of damage monitoring on LMJ windows, it was possible to detect damage sites of the order of $10\,\mu\mathrm{m}$ in the best lighting configuration, while $30\,\mu\mathrm{m}$ damage sites were barely visible in the worst configuration. These values are given in the case when the scattered light by a damage site is collected only by a single pixel, which is not always true.

As a comparison, the calibration of TIS_m was performed at NIF by acquiring images on the facility [25]. The TIS_m were measured for several damage sites that were allowed to grow up to $4\,\mathrm{mm}$. The TIS was given as a function of diameter raised to the power 2.08. The square power law measured and proposed in this chapter appears to be a simpler result to interpret and use than NIF's law in order to estimate damage sizes from TIS data. However, NIF results did not give any information about TIS scatter for damage sites with same size as well as diameter measurement dispersal for damage sites of identical sizes.

Beyond the current system modeling, the proposed approach should allow to virtually test and evaluate modifications of lighting or image acquisition systems, be it at LMJ, NIF, or SG-III facilities, or any other installation interested in accurately monitoring damage growth by acquiring light scattering signals.

2.5 Conclusion

An optical model was proposed to simulate the Total Integrated Signal (TIS) used to quantify the size of laser-induced damage sites on fused silica optics of high energy laser facilities. The model was based on three steps, namely, (i) lighting system modeling using a ray tracing software, (ii) measurements of light scattering by damage sites, and (iii) numerical imaging system modeling. The provided TIS simulations using the proposed model were calibrated and validated on an acquired image that contained 930 damage sites whose size was precisely measured using an optical

microscope before the component was mounted on the facility.

The measured TIS on the acquired image demonstrated that the LMJ lighting system itself was not sufficient to measure accurately damage sizes with the TIS alone. However, it was possible to determine the damage size by using both the proposed model and raw TIS measurements.

The model may also be used to virtually propose and test system modifications in order to improve damage size measurements if necessary. Although the chapter focused on the damage monitoring system of LMJ, the proposed approach may be utilized to model and simulate the performance of other systems based on the measurement of light scattering signals. Using such model, it was possible to avoid time-consuming online measurements to calibrate TIS levels with the size of scattering objects (damage sites in the present case).

References

[1] G. H. Miller, E. Moses, and C. Wuest, "The national ignition facility," *Optical Engineering*, vol. 43, no. 12, pp. 2841–2853, 2004.

[2] X. He and W. Zhang, "Advances in the national inertial fusion program of china," *EPJ Web of Conferences*, vol. 59, pp. 01 009–, Nov. 2013. doi: 10.1051/epjconf/20135901009.

[3] J. Ebrardt and J. M. Chaput, "LMJ project status," *Journal of Physics: Conference Series*, vol. 112, no. 3, p. 032 005, May 2008. doi: 10.1088/1742-6596/112/3/032005. [Online]. Available: https://doi.org/10.1088/1742-6596/112/3/032005.

[4] L. Lamaignère, G. Dupuy, A. Bourgeade, A. Benoist, A. Roques, and R. Courchinoux, "Damage growth in fused silica optics at 351 nm: refined modeling of large-beam experiments," *Applied Physics B: Lasers and Optics*, vol. 114, no. 4, pp. 517–526, Mar. 2014. doi: 10.1007/s00340-013-5555-6.

[5] K. Manes, M. Spaeth, J. Adams, and M. Bowers, "Damage mechanisms avoided or managed for nif large optics," *Fusion Science and Technology*, vol. 69, pp. 146–249, Feb. 2016. doi: 10.13182/FST15-139.

[6] P. A. Baisden, L. J. Atherton, R. A. Hawley, *et al.*, "Large optics for the national ignition facility," *Fusion Science and Technology*, vol. 69, no. 1, pp. 295–351, 2016. doi: 10.13182/FST15-143. eprint: https://doi.org/10.13182/FST15-143. [Online]. Available: https://doi.org/10.13182/FST15-143.

[7] M. L. Spaeth *et al.*, "Optics recycle loop strategy for nif operations above uv laser-induced damage threshold," *Fusion Science and Technology*, vol. 69, no. 1, pp. 265–294, 2016. doi: 10.13182/FST15-119. eprint: https://doi.org/10.13182/FST15-119. [Online]. Available: https://doi.org/10.13182/FST15-119.

[8] F. Wei *et al.*, "Automatic classification of true and false laser-induced damage in large aperture optics," *Optical Engineering*, vol. 57, no. 5, pp. 1–11, 2018. doi: 10.1117/1.OE.57.5.053112. [Online]. Available: https://doi.org/10.1117/1.OE.57.5.053112.

[9] G. Hallo, C. Lacombe, R. Parreault, *et al.*, "Sub-pixel detection of laser-induced damage and its growth on fused silica optics using registration residuals," *Opt. Express*, vol. 29, no. 22, pp. 35 820–35 836, Nov. 2021. doi: 10.1364/OE.433862. [Online]. Available: http://opg.optica.org/oe/abstract.cfm?URI=oe-29-22-35820.

[10] K. Takeuchi, Y. Nakatani, and O. Hisatomi, "Accuracy of protein size estimates based on light scattering measurements," *Open Journal of Biophysics*, vol. 4, Nov. 2013. doi: 10.4236/ojbiphy.2014.42009.

[11] G. Hallo, C. Lacombe, J. Néauport, and F. Hild, "Detection and Tracking of Laser Damage Sites on Fused Silica Components by Digital Image Correlation," *Optics and Lasers in Engineering*, vol. 146, p. 106 674, 2021.

[12] Zemax LLC, *Opticstudio*, version 15.5, 2015. [Online]. Available: https://www.zemax.com/pages/opticstudio.

[13] F. E. Nicodemus, J. C. Richmond, J. J. Hsia, *et al.*, "Geometrical considerations and nomenclature for reflectance," in *Radiometry*. USA: Jones and Bartlett Publishers, Inc., 1992, pp. 94–145, isbn: 0867202947.

[14] J. Stover, *Optical Scattering: Measurement and Analysis*, ser. Press Monographs. SPIE Press, 2012, isbn: 9780819492517. [Online]. Available: https://books.google.fr/books?id=tDtpLwEACAAJ.

[15] P. Beckmann and A. Spizzichino, *The scattering of electromagnetic waves from rough surfaces*. Oxford: Pergamon, 1963.

[16] E. L. Church, P. Z. Takacs, and T. A. Leonard, "The Prediction Of BRDFs From Surface Profile Measurements," in *Scatter from Optical Components*, J. C. Stover, Ed., International Society for Optics and Photonics, vol. 1165, SPIE, 1990, pp. 136–150. doi: 10.1117/12.962842. [Online]. Available: https://doi.org/10.1117/12.962842.

[17] M. G. Dittman, "K-correlation power spectral density and surface scatter model," in *Optical Systems Degradation, Contamination, and Stray Light: Effects, Measurements, and Control II*, O. M. Uy, J. C. Fleming, and M. G. Dittman, Eds., International Society for Optics and Photonics, vol. 6291, SPIE, 2006, pp. 226–237. doi: 10.1117/12.678320. [Online]. Available: https://doi.org/10.1117/12.678320.

[18] J. E. Harvey, A. Krywonos, and J. C. Stover, "Unified scatter model for rough surfaces at large incident and scatter angles," in *Advanced Characterization Techniques for Optics, Semiconductors, and Nanotechnologies III*, A. Duparré, B. Singh, and Z.-H. Gu, Eds., International Society for Optics and Photonics, vol. 6672, SPIE, 2007, pp. 103–110. doi: 10.1117/12.739139. [Online]. Available: https://doi.org/10.1117/12.739139.

[19] J. E. Harvey, N. Choi, A. Krywonos, and J. G. Marcen, "Calculating BRDFs from surface PSDs for moderately rough optical surfaces," in *Optical Manufacturing and Testing VIII*, J. H. Burge, O. W. Fähnle, and R. Williamson, Eds., International Society for Optics and Photonics, vol. 7426, SPIE, 2009, pp. 141–149. doi: 10.1117/12.831302. [Online]. Available: https://doi.org/10.1117/12.831302.

[20] D. B. H. Juan Irizar, "Brdf prediction using surface micro-roughness measurements," *ICSOS*, 2012.

[21] M. Veinhard, O. Bonville, R. Courchinoux, R. Parreault, J.-Y. Natoli, and L. Lamaignère, "Quantification of laser-induced damage growth using fractal analysis," *Opt. Lett.*, vol. 42, no. 24, pp. 5078–5081, Dec. 2017. doi: 10.1364/OL.42.005078. [Online]. Available: http://ol.osa.org/abstract.cfm?URI=ol-42-24-5078.

[22] M. Fouchier, M. Zerrad, M. Lequime, and C. Amra, "Wide-range wavelength and angle resolved light scattering measurement setup," *Opt. Lett.*, vol. 45, no. 9, pp. 2506–2509, May 2020. doi: 10.1364/OL.392000. [Online]. Available: http://opg.optica.org/ol/abstract.cfm?URI=ol-45-9-2506.

[23] M. Chambonneau and L. Lamaignère, "Multi-wavelength growth of nanosecond laser-induced surface damage on fused silica gratings," *Scientific Reports*, vol. 8, pp. 1–10, Jan. 2018. doi: 10.1038/s41598-017-18957-9.

[24] H. Bercegol, R. Courchinoux, M. A. Josse, and J. L. Rullier, "Observation of laser-induced damage on fused silica initiated by scratches," in *Laser-Induced Damage in Optical Materials: 2004*, G. J. Exarhos,

A. H. Guenther, N. Kaiser, K. L. Lewis, M. J. Soileau, and C. J. Stolz, Eds., International Society for Optics and Photonics, vol. 5647, SPIE, 2005, pp. 78–85. doi: 10.1117/12.585290. [Online]. Available: https://doi.org/10.1117/12.585290.

[25] A. Conder, J. Chang, L. Kegelmeyer, M. Spaeth, and P. Whitman, "Final optics damage inspection (FODI) for the National Ignition Facility," in *Optics and Photonics for Information Processing IV*, A. A. S. Awwal, K. M. Iftekharuddin, and S. C. Burkhart, Eds., International Society for Optics and Photonics, vol. 7797, SPIE, 2010, pp. 167–178. doi: 10.1117/12.862596. [Online]. Available: https://doi.org/10.1117/12.862596.

Toward a new lighting system

Robust and precise diameter estimation is of major importance for an efficient operation of megajoule class laser facilities such as the LMJ. The estimation of damage diameters based on pixel intensity values reaches sub-pixel resolution (from $\approx 30\,\mu\mathrm{m}$ to $300\,\mu\mathrm{m}$). However, lighting systems based on LEDs may show limitations in robustness, resulting in a critical loss of accuracy in diameter estimation over time. In the sequel, a new lighting system, which is based on a fiber source and a reflector integrated in the maintaining frame, is studied to check if the needed criteria of accuracy and robustness over time are reached. The performances of the proposed system are numerically estimated through an optical model. These performances are compared to those of the current lighting system in nominal and degraded configurations. It is shown that the proposed lighting system reduces the uncertainty on diameter estimation by a pixel intensity method by a factor of 3 compared to the nominal configuration.

The proposed new lighting system was designed by Benjamin Roy during its apprenticeship between September 2019 and August 2021 at the CEA CESTA, under the supervision of Gérard Razé.

3.1 Introduction

The operating cost and laser performances of megajoule-class laser facilities are in part related to laser-induced damage of their final optical components [1, 2]. Damage initiation and growth are experienced almost daily on high energy laser facilities [3, 4]. To partially overcome the influence of laser-induced damage on such installations, a recycle loop of damaged optics is currently in development and described in Section 1.1.3 of the introduction. To optimize techniques operated during the recycle loop such as mitigation process and local laser shadowing, it is essential to detect damage sites and quantify their growth before they reach a size of $300\,\mu\mathrm{m}$ in diameter. The spatial resolution of acquired images on a daily basis is typically $100\,\mu\mathrm{m}$ [4, 5]. Measuring a damage site by counting the number of activated pixels by the site is inaccurate due to large discretization and prediction interval for small diameters (Chapter 2).

It was proposed to use the Total Integrated Signal (TIS) of activated pixels to estimate the diameter of damage sites [6]. Diameter estimates by TIS gave access to sub-pixel resolution on diameter unlike pixel counting methods (Chapter 2). The prediction interval using TIS-based measurement is smaller than that obtained by a pixel-counting method. TIS-based diameter estimation requires gray level calibration on real diameters. This calibration, performed by measurement or by modeling, must be valid from one image to another. Efficiency of model-based calibration has been demonstrated for the acquisition system of LMJ made up of a lighting system by two LEDs and an imaging system (Chapter 2). However, the induced inhomogeneity by twin LED lighting reduces the accuracy of diameter measurement by TIS (Chapter 2). Furthermore, LEDs are highly sensitive to electromagnetic interaction between laser beams and the target. Therefore, the LEDs are susceptible to degradation and they may not light on when needed (degraded configuration). The lighting inhomogeneity then increases.

A robust lighting system that illuminates the optical component more homogeneously than the twin LEDs was designed by an apprentice engineer. The proposed new lighting system is presented in Section 3.2. This lighting solution is modeled using the principles described in Chapter 2. Performances of the proposed lighting system are evaluated by using the model (Section 3.3) and compared with the performances of the currently used twin LED system in a nominal (2 LEDs) and in a degraded (1 LED) configuration (Section 3.4).

3.2 New lighting system

The two LEDs, the fused silica vacuum window and its aluminium alloy frame are considered as the current lighting system, shown in Figure 3.1. The current system with 2 LEDs provides an inhomogeneous lighting on the exit surface of vacuum windows. A new system was proposed by Benjamin Roy during his internship in order to improve 2 weaknesses of the twin LED system:

- The resistance to electromagnetic pulse sometimes generated after the interaction of target and laser beams during experiments;
- The homogeneity of illumination on the damaged face.

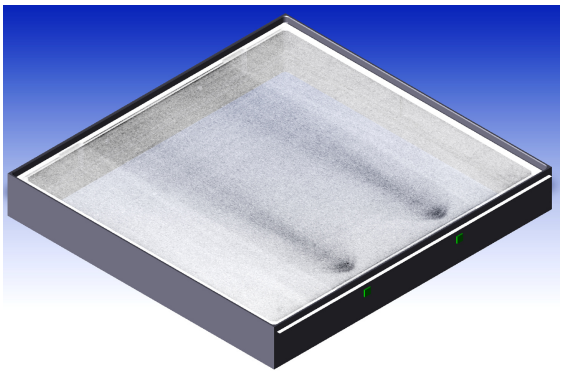

Figure 3.1: 3D image of the current lighting system with the vacuum window in its frame and the 2 LEDs.

The proposed new lighting solution takes into account the following constraints:

- Modification of the optical component is not allowed;
- Space around the frame of the optical component is limited;
- The proposed modifications must ensure that the structure of the frame does not deform over time. Thus, the width of the area that can be changed without affecting the performance and functionality of the frame is limited to the space between the 2 LED slots (represented in green in Figure 3.1).

Under these constraints, the studied solution introduces 2 modifications of the lighting system (Figure 3.2):

- The twin LEDs are replaced by a fiber source and a lens to adapt the divergence of light. The fiber source has the advantage of not suffering from electromagnetic interactions between the laser beams and the target;
- A convex aluminum alloy reflector is integrated into the frame in front of the fiber source to scatter incident light over the entire optical component.

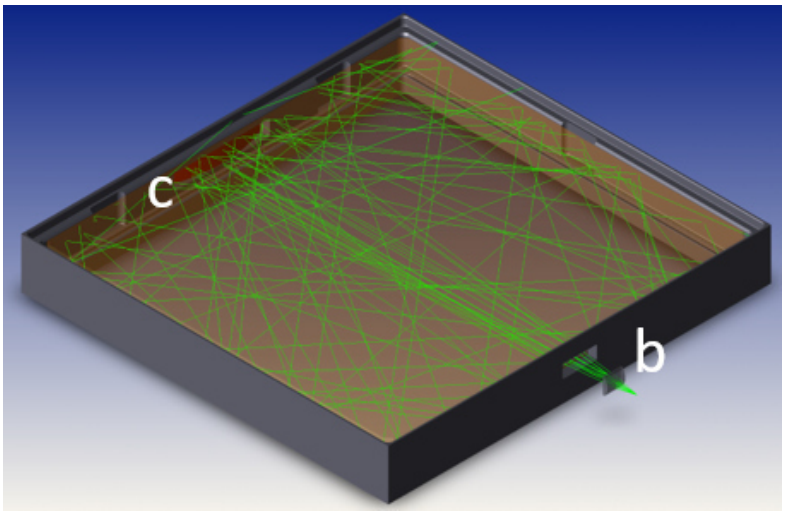

(a)

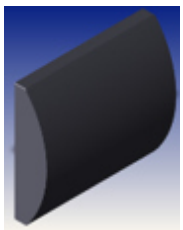

(b)

(c)

Figure 3.2: (a) 3D image of the proposed lighting system with the vacuum window (clear orange), the frame (grey), the fiber source that emits rays in green. A lens (b) is used to adapt the divergence of light and thus enhance the light homogeneity of the exit surface of the vacuum window. A convex aluminum reflector (c) is added in front of the fiber source to scatter incident light over the whole exit surface. 3D images generated with OpticStudio Zemax.

The proposed lighting system was implemented in the optical model

presented in Chapter 2 to simulate the TIS values according to the positions of the damage sites on the vacuum window. Such model is based on optical simulation of the lighting system, measurements of light scattering of damage sites using the set-up SALSA4 and numerical simulation of the image acquisition system. Measured diameters are estimated from TIS by Equation (2.9). These diameter estimations are used to quantify the improvements on in-situ damage sizing provided by the new system based on fiber source.

3.3 Results

The chosen criteria to quantify the performance of the systems are the detection threshold of damage sites (in micrometre) and the error on diameter estimations. Indeed, the detection threshold and the diameter estimation are highly relevant to in-situ monitor damage initiation and growth. The performances of three lighting system configurations are estimated with the model described in Chapter 2: the current system with 2 LEDs (Figure 3.3 (a)), the current system with only 1 LED on (Figure 3.3 (b)) and the proposed system with the fiber source and the reflector (Figure 3.3 (c)). The obtained performance levels for each configuration are given in Table 3.1.

Table 3.1: Performances (detection threshold and error on diameter estimation) estimated by model for three lighting system configurations.

Lighting systems	Detection threshold	Error on diameter
Twin LEDs (nominal)	$30\,\mu\mathrm{m}$	$\pm$ 34%
Twin LEDs (degraded)	$80\,\mu\mathrm{m}$	from -75% to -17%
Fiber source and reflector	$30\,\mu\mathrm{m}$	$\pm 10\%$

3.4 Discussion

Damage diameters measured with the degraded lighting system (1 LED over two switched on) are clearly under-estimated (from -75% to -17%) compared to true damage diameters. Hence, damage monitoring with only one LED is not reliable. Given that such lighting condition occurs due to electromagnetic interactions between laser beams and the target or improper maintenance operations, it appears necessary to set up a more robust lighting system.

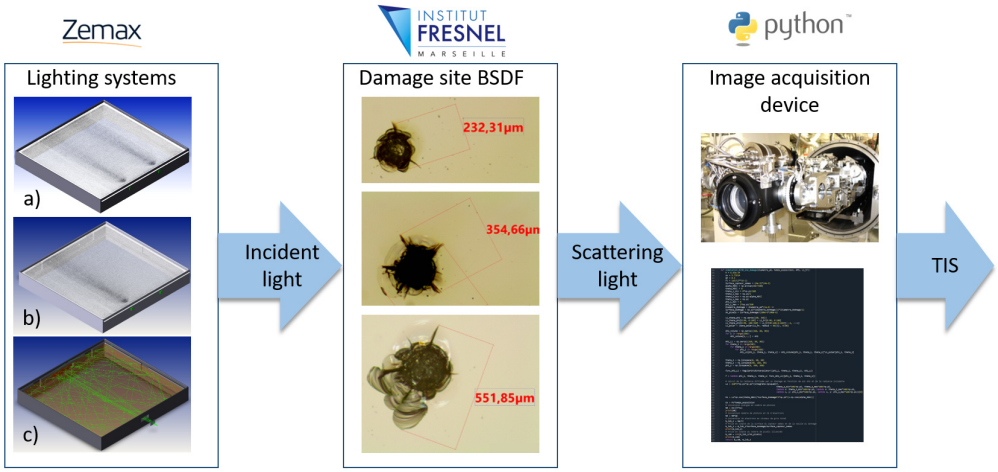

Figure 3.3: Model framework used to simulate the performance of damage diameter estimation from TIS with (a) the current lighting system with 2 LEDs, (b) the current lighting system with only 1 LED on and (c) the proposed lighting system with the fiber source and the reflector. The incident light on the damaged face of a vacuum window was simulated by modeling the lighting system with the ray tracing software Zemax. The scattered light by a damage site was estimated using the BSDF measured at the Institut Fresnel. The Total Integrated Signal was numerically computed by modeling the image acquisition system with Python.

The proposed lighting system is robust to electromagnetic interactions. Furthermore, the uncertainties on diameter estimation with the fiber source and the reflector are estimated to be 3 times lower than those obtained with the dual LED system in nominal operation.

Given these positive results obtained by simulation, it is necessary to perform measurements to validate the obtained results. To implement such system at LMJ, it would be necessary to remove the 176 optical frames, make modifications to the frames, install the new lighting systems and then mount the frames on the facility. Optics cost saving induced by a better estimation of damage diameters would be a good reason to promote these lighting system modifications on LMJ facility.

3.5 Conclusion

It was demonstrated numerically that the impact of degraded lighting conditions with only one LED on is disastrous for in-situ damage growth

monitoring. Such degraded configuration induces a large underestimation of damage diameters measured by the TIS method and a damage detection threshold that is not compatible with the requirements related to the lifetime increase of the optics by damage mitigation and laser shadowing techniques. Basically, such degraded situation induces an early and unnecessary maintenance of vacuum windows.

A new lighting system based on a fiber source and a reflector integrated in the maintaining frame was proposed. The performances of such system were numerically simulated by using the developed optical model. The detection threshold of damage sites was the same as that obtained with the twin LED system. However, the uncertainties on the estimated diameters by the TIS-based method were 3 times smaller than that with the twin LED system in its nominal configuration. The potential improvements induced by the proposed lighting system are very promising. Optical measurements should be performed to confirm the gains estimated by modeling.

Even with the proposed modifications of the lighting system, it is necessary to find solutions to limit the impact of disturbances affecting the measured pixel intensities. For this purpose, image correction techniques are presented in Part III.

References

[1] S. G. Demos, M. Staggs, and M. R. Kozlowski, "Investigation of processes leading to damage growth in optical materials for large-aperture lasers," *Applied Optics*, vol. 41, no. 18, pp. 3628–3633, Jun. 2002. doi: 10.1364/AO.41.003628. [Online]. Available: http://ao.osa.org/abstract.cfm?URI=ao-41-18-3628.

[2] K. Manes, M. Spaeth, J. Adams, and M. Bowers, "Damage mechanisms avoided or managed for nif large optics," *Fusion Science and Technology*, vol. 69, pp. 146–249, Feb. 2016. doi: 10.13182/FST15-139.

[3] L. Mascio-Kegelmeyer, "Machine learning for managing damage on NIF optics," in *Laser-induced Damage in Optical Materials 2020*, C. W. Carr, V. E. Gruzdev, D. Ristau, and C. S. Menoni, Eds., International Society for Optics and Photonics, vol. 11514, SPIE, 2020. doi: 10.1117/12.2571016. [Online]. Available: https://doi.org/10.1117/12.2571016.

[4] C. Lacombe *et al.*, "Dealing with LMJ final optics damage: post-processing and models," in *Laser-induced Damage in Optical Materials 2020*, C. W. Carr, V. E. Gruzdev, D. Ristau, and C. S. Menoni, Eds., International Society for Optics and Photonics, vol. 11514, SPIE, 2020. doi: 10.1117/12.2571074. [Online]. Available: https://doi.org/10.1117/12.2571074.

[5] L. Kegelmeyer, P. Fong, S. Glenn, and J. Liebman, "Local area signal-to-noise ratio (lasnr) algorithm for image segmentation," *Proceedings of SPIE - The International Society for Optical Engineering*, vol. 6696, Oct. 2007. doi: 10.1117/12.732493.

[6] A. Conder, J. Chang, L. Kegelmeyer, M. Spaeth, and P. Whitman, "Final optics damage inspection (FODI) for the National Ignition Facility," in *Optics and Photonics for Information Processing IV*, A. A. S. Awwal, K. M. Iftekharuddin, and S. C. Burkhart, Eds., International Society for Optics and Photonics, vol. 7797, SPIE, 2010, pp. 167–178. doi: 10.1117/12.862596. [Online]. Available: https://doi.org/10.1117/12.862596.

Part III

Image corrections for damage growth monitoring

In Part II, it was demonstrated that in-situ measurements of damage size by a pixel intensity method are efficient to reach sub-pixel resolution. However, new images are not acquired with the same conditions due to small repositioning errors of the imaging device, background modifications and lighting variations that may arise. Such disturbances affect the measured pixel intensities and in this way estimated damage diameters. It is thus necessary to limit the impact of such disturbances in order to be able to accurately measure damage diameters. This objective is addressed in the 3 chapters of Part III.

In Chapter 4, a method based on DIC principles is proposed to spatially register images with sub-pixel resolution and to correct for pixel intensity variations due to background and lighting modifications. The procedure was validated on dedicated images and then applied to a set of vacuum window images.

In order to demonstrate the sub-pixel resolution of the proposed registration method (Chapter 4) and to validate the ability to in-situ monitor damage growth by measuring pixel intensities, a damage growth experiment was performed on the MELBA damage testing set-up equipped to provide high resolution images of damage sites (Chapter 5).

Generic brightness and contrast corrections, proposed in Chapter 4, were designed to correct for only low frequency spatial variations in order to preserve pixel intensities of damage sites. Thus, such generic techniques are not efficient to correct for high frequency spatial intensity variations. In Chapter 6, brightness and contrast corrections based on Proper Orthogonal Decomposition (POD) and an optical model is proposed to specifically correct for high and low spatial frequency intensity variations while preserving damage intensity.

4

Detection and tracking of laser damage sites on fused silica components by Digital Image Correlation

Final optics of high energy laser facilities are susceptible to laser-induced damage that reduces the quality of laser beams. In such facilities, images of vacuum windows are acquired on a daily basis. However, some motions may occur in addition to illumination changes. A method based on registration principles is developed to correct for disturbances between succesive images, which leads to sub-pixel resolution and corrects for brightness and contrast variations. The procedure is applied to a set of actual images of a fused silica vacuum window. The proposed approach is efficient to ensure reliable monitoring of damage initiation and growth.

Reproduced from:
G. Hallo, C. Lacombe, J. Néauport and F. Hild.
Detection and tracking of laser damage sites on fused silica components by Digital Image Correlation.
Optics and Lasers in Engineering. 146, 106674, 2021

4.1 Introduction

The “Laser MegaJoule” (LMJ) is a high energy laser facility involving 176 beams. It is developed to deliver about $1.4\,\mathrm{MJ}$ of ultraviolet laser energy in a few nanoseconds on targets placed in the center of its vacuum chamber [1]. High energy laser installations such as the National Ignition Facility (NIF) in the US [2, 3], the SG-III in China [4] and LMJ in France are designed to achieve fusion ignition experiments [5]. In order to reach the required energy level, each LMJ beamline is designed to deliver a laser shot of $7.5\,\mathrm{kJ}$ at $351\,\mathrm{nm}$ wavelength for $3\,\mathrm{ns}$. Each laser beam is amplified at $1053\,\mathrm{nm}$ wavelength by an amplifying section to reach $20\,\mathrm{kJ}$. During amplification, the section of the square laser beam is about $35\,\mathrm{cm}$. Once the laser beam is amplified, it is carried toward the target chamber by 6 mirrors over about $40\,\mathrm{m}$. Each beam propagates through KDP and DKDP crystals in order to be converted into ultraviolet radiation. Then, the beam is focused on the target with a UV focusing diffraction grating. After the grating, the focused laser beam at $351\,\mathrm{nm}$ wavelength traverses the fused silica final optics.

These facilities use a complex set of large optical components, with a side length of about $40\,\mathrm{cm}$, which are crossed by a high-energy UV laser beam. The first final optics is the vacuum window that lies on the interface between the vacuum chamber and the other parts of the facility operating at atmospheric pressure. Away from the fused silica optics are the debris shield and the disposable debris shield whose aim is to protect vacuum windows from target debris.

Fused silica components are susceptible to laser-induced damage [6], which is defined as a permanent change of the optical component induced by laser beams. For a UV nanosecond laser pulse at high energy, the laser damage morphology is a crater with subsurface fractures [6, 7]. Laser damage initiation is due to a combination of loading induced by the UV laser beam [8] and random defects [9, 10] or self-focusing [11] or even particulate contamination [12, 13] on the optics surface. LMJ, NIF and SG-III facilities were designed to operate at twice the fluence known to cause damage growth on fused silica components [1, 2, 4] such as vacuum windows. Damage growth is defined as the increase of damage area and depth for successive laser shots. Physical mechanisms of damage initiation and growth are well known and modeled [6]. The main laser parameters affecting damage growth on the exit surface of fused silica components are the fluence [7], the wavelength [6, 14] and the pulse time duration [6]. The stochastic behavior of laser-induced damage growth has to be taken

into account [6, 15, 16].

Since such windows ensure air tightness of the vacuum chamber, it is required to monitor these optical components. Monitoring laser damage growth on vacuum windows is essential to control the quality of laser beams and to limit the operating costs using optics mitigation [17–19]. Thus, observation systems have been developed to track laser damage sites without removing fused silica components after each laser shot. NIF, SG-III and LMJ facilities use similar observation systems that are called Final Optics Damage Inspection (FODI) [20, 21] for NIF and SG-III, and Chamber Center Diagnostic Module (or MDCC) for LMJ [22]. FODI and MDCC were both designed to image each UV final optics from the center of the experiment chamber after each laser shot. These optics are illuminated through the edge of the component [20–22] resulting in dark-field pictures on which damage sites are visible as bright spots. After each laser shot, new laser damage sites may initiate on the optical component and already existing damage sites may grow. Initiation and growth of damage sites modify the gray levels of pixels where the damage site is located.

The analysis focuses herein on dark-field images for laser damage detection and tracking on final fused silica optics. Monitoring and predicting laser damage growth by processing dark field images of optical components acquired by different diagnostics is a challenge for high energy laser facilities [21, 22]. During the last fifteen years, NIF has developed algorithms, such as the so-called Local Area Signal-To-Noise Ratio (LASNR) procedure [23], to detect potential laser damage sites as soon as they initiate on the last optical components. Machine learning techniques and decision trees were used to automatically spot and track these sites with a small amount of false alarms [21, 24] for diameters greater than $50\,\mu\mathrm{m}$. Detection of laser damage sites at LMJ is also based on the LASNR algorithm [22]. This method allows for a basic non-destructive control of vacuum windows after each shot. However, the positioning of the observation system is not perfect and illumination conditions may vary between successive acquisitions. Therefore, up to now, damage tracking over time has been highly dependent on the conditions of image acquisition.

Image registration and gray level corrections are possible using Digital Image Correlation (DIC) [25, 26]. DIC needs one camera only to acquire images of the scene and a computer to register images and extract displacement fields. This technique is widely used in solid mechanics in order to follow mechanical tests [25–27], extract useful data for damage detection and quantification [28] or study crack propagation [29]. DIC offers sufficient resolution to track crack initiation and growth at micro-structural

levels [30] and to quantify cracks in carbon fiber composites [31].

In this study, a novel method based on DIC principles is developed to detect and quantify laser damage sites by processing acquired images. This method involves sub-pixel registration of dark field images and corrections of gray level variations induced by variable lighting conditions. With these corrections, laser damage sites are detected on residual maps as soon as they appear on the optical component. One key element of the proposed procedure lies in the fact that image registration and corrections of illumination variations cannot be performed over the same region of interest. Image registration is performed using less than 1% of the image area due to the absence of reliable markers in the laser illuminated area. This situation does not allow standard DIC solutions to be used. The procedure was applied to an image series of LMJ vacuum window. It is shown that image registration and gray level corrections are essential to ensure an efficient tracking of laser damage sites. The chapter is organized as follows. The MDCC system is first described. General concepts of image registration and gray level corrections using DIC are then introduced. The efficiency of the proposed methods is validated on computer generated images, and on LMJ vacuum window images acquired by MDCC.

4.2 Lighting and observation system

The experiment chamber of the LMJ facility is an $8\,\mathrm{m}$ in radius sphere. Eventually, 176 fused silica vacuum windows, distributed in quads over the sphere surface, will be analyzed after each laser shot. The MDCC imaging system is placed at the center by a motorized arm. This arm orients the MDCC toward each window. The image is formed on the sensor by a 6-lens objective optimized for the $525\,\mathrm{nm}$ wavelength. The pixel size of the MDCC projected onto the window plane is about $100\,\mu\mathrm{m}$. The definition of the MDCC camera is 16 Mpixels. The CCD sensor is cooled at $-25\,°\mathrm{C}$ in order to reduce thermal noise. The configuration of the MDCC system is presented in Figure 4.1.

To make laser damage sites visible, two green LEDs, with a maximum emissivity at $525\,\mathrm{nm}$, are placed near one edge of each vacuum window. Light provided by LEDs enters into the optics and illuminates rear and front sides of the component. Laser damage sites, which are distributed on the front side of windows, scatter light. A part of the scattered light from damage sites is collected by the MDCC camera, which is focused on the front side of the vacuum window. The depth of field in the object space, which is equal to $15\,\mathrm{mm}$, is sufficiently small to image only the

front side of the window so that damage sites are sharp. Imaging of the vacuum window is possible through the debris shield and disposable debris shield but any damage on these optics may generate background noise and make detection of damage sites in vacuum windows more difficult.

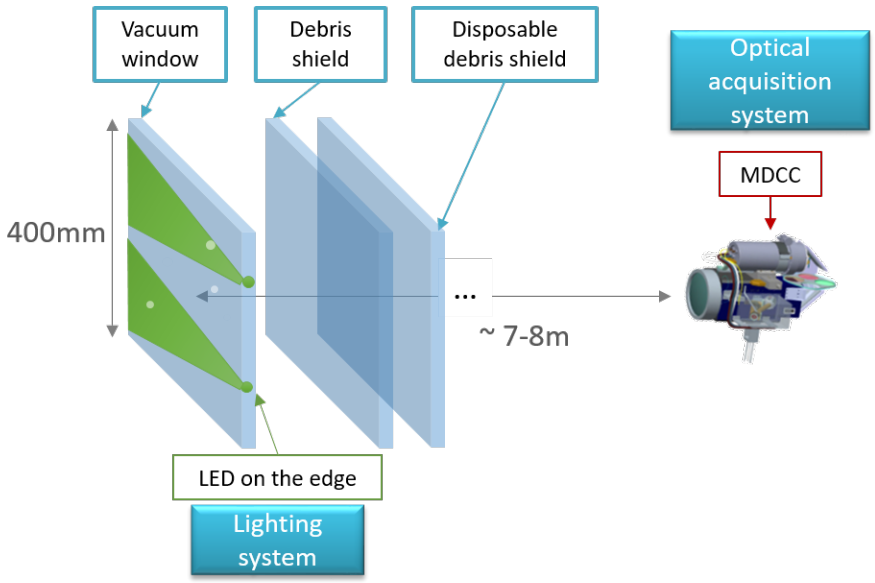

Figure 4.1: Configuration of the final optics assembly of the LMJ facility and position of MDCC when it is used to acquire images of a vacuum window from the chamber center.

An example of a window image acquired by the MDCC camera is shown in Figure 4.2. Laser damage sites are observed as well as light beams emitted by green LEDs, and reflections from mechanical objects around the window. However, the positioning of the MDCC is not perfect and illumination conditions may vary from one acquisition to another. To follow damage growth in series of acquisitions, it is necessary to correct small motions and intensity variations in image series.

Any image of a vacuum window (Figure 4.3) is divided into different areas. Each area has specific features. The central area of vacuum windows, corresponding to the zone where the beam propagates through the window, is referred to as *laser beam area*. In that area, there are features such as laser damage sites that are likely to grow from shot to shot. The regular situation corresponds to vacuum windows free of any damage sites (Figure 4.3). Successive shots will induce gradually more numerous damage sites in the *laser beam area*. Data from the *laser beam area* are therefore not sufficiently stable over time to be used for image

registration. This zone represents more than 75% of the imaged area.

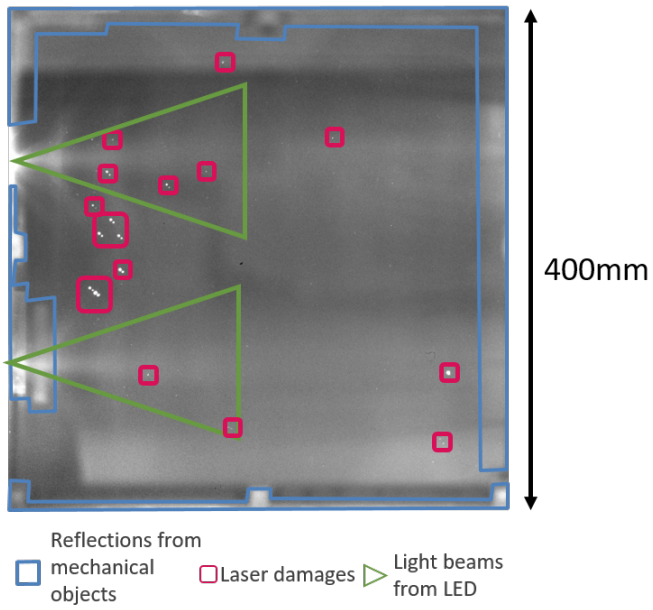

Figure 4.2: Window image acquired by the MDCC. The two green LEDs near the left edge of the window illuminate the inside of the optical component. Laser-induced damage sites are revealed as small bright spots. Some reflections from mechanical objects and light sources located outside the experiment chamber are also visible.

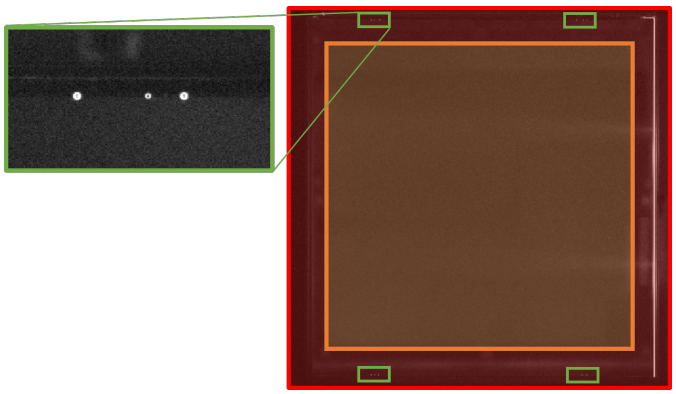

Figure 4.3: Different areas in a window image. The green box shows the four *fiducial areas* used for image registration. The red *edge area* contains the four *fiducial areas*. The orange *laser beam area* shows the region where the laser beam traverses the vacuum window.

Ideally, image registration should mainly use the remaining area, defined as *edge area*. The *edge area* contains *fiducial areas*, divided into four zones located near each corner. Four reference "points," designated as *fiducials*, are located in each *fiducial area*. They are used as spatial markers to check the focusing plane of the MDCC on optics mostly free of any scratches, defects or damage sites. A *fiducial* is a crater made by ablation with a CO_2 laser after optical polishing and before anti-reflective coating. *Fiducial areas* are also to used as reliable spots for image registration purposes. When a window is illuminated by the two LEDs located near one edge, each *fiducial* scatters sufficiently light toward the MDCC camera for being visible on images. Due to their position outside the *laser beam area*, the *fiducials* are stable contrary to objects located inside the *laser beam area*. Gray levels of pixels belonging to *edge areas* are modified by light reflections from mechanical objects such as the aluminum alloy frame maintaining the vacuum window. Variations of the lighting system induce gray level changes near image edges.

Kinematic measurements cannot be performed securely in the *laser beam area* for two main reasons:

(i) In some situations, damage sites are not observed in the *laser beam area*. It is particularly true for new optics that have just been installed (Figure 4.3). Consequently, no contrast is available for image registration.

(ii) After each laser shot, damage sites may initiate and others grow. Consequently, the assumption of gray level conservation is not satisfied even if background corrections are performed. Such effects make displacement estimations less secure.

Standard DIC codes are generally applied to images of speckled sample surfaces [25]. This speckle pattern provides sufficient contrast over the region of interest to ensure convergence of these codes. However, vacuum windows cannot be painted for obvious optical considerations. For all these reasons, displacement estimations by DIC were only performed on the *fiducial areas* and then extrapolated over the *laser beam area* thanks to the use of a reduced basis. It is worth noting that the *fiducial areas* used for registration purposes only represent about 0.7% of the total image area and surround the *laser beam area*.

Despite the fact that the location of vacuum windows is fixed, apparent "motions" between successive LMJ vacuum window image acquisitions possess the following features:

- Translations up to tens of pixels.

- Rotations from some degrees up to $180°$. Large rotations are due to the *ad-hoc* maintenance of the observation system that may lead to inversion of the camera frame.
- Limited scale changes close to one.

Such small displacement levels are due to small errors in repositioning of the MDCC system between successive image acquisitions. They occur between each acquisition of the same window. On the contrary, large rotations are (very) occasional. They are due to the maintenance of the observation system for example. From one acquisition to another, lighting conditions may change. The gray level variations are due to two phenomena:

- illumination variations of LEDs. They may slightly move and/or their intensity vary from one day to another. This phenomenon induces contrast changes between successive images. In the worst case, one LED can even be turned off.
- variations of other lighting sources near the experiment chamber. This phenomenon essentially induces non-uniform and unstable brightness variations.

These modifications lead to gray level variations and avoid an efficient comparison of images of the same window shot after shot.

Therefore damage tracking over time is highly dependent on the conditions associated with image acquisition. To be able to track efficiently damage sites, it is proposed to correct variations between successive images of the same optics.

4.3 Image registration and gray level correction

An algorithm is proposed to spatially register window images and correct for illumination variations. The algorithm begins with image registration using a DIC algorithm initialized by a first estimation of rigid body translations and rotation, in addition to scale changes. Once the registration is performed, gray level variations are corrected. DIC consists in estimating the displacement field by registering a reference image, I_0, and a deformed image of the scene, I_n. Pixel coordinates in the image are denoted by $\boldsymbol{x}$. The initial global residual τ_{init} calculated over the considered Region Of Interest (ROI) reads

$$\tau_{init}^2 = \sum_{\boldsymbol{x}\in \mathrm{ROI}} \rho_{init}^2(\boldsymbol{x}) \qquad \text{with} \qquad \rho_{init}(\boldsymbol{x}) = I_0(\boldsymbol{x}) - I_n(\boldsymbol{x}) \tag{4.1}$$

where ρ is the residual evaluated at each pixel position in the ROI. Considering window images, "disturbances" such as displacements ($\boldsymbol{u}$), illumination variations (brightness b and contrast c), damage initiation and growth (d) and acquisition noise (η) have an effect on the initial residual

$$\rho_{init}(\boldsymbol{x}) = \rho_{init}[\boldsymbol{u}(\boldsymbol{x}), b(\boldsymbol{x}), c(\boldsymbol{x}), d(\boldsymbol{x})] + \eta(\boldsymbol{x}). \tag{4.2}$$

The aim of this section is to describe a method that leads to a final residual value, ρ_{final}, that only depends on gray level variations due to damage sites and acquisition noise

$$\rho_{final}(\boldsymbol{x}) = \rho_{final}(d(\boldsymbol{x})) + \eta(\boldsymbol{x}) \tag{4.3}$$

4.3.1 Image registration

The first step of the method is to spatially register images. The hypothesis of local gray level conservation [25] reads

$$I_0(\boldsymbol{x}) = I_n(\boldsymbol{x} + \boldsymbol{u}(\boldsymbol{x})) \tag{4.4}$$

where $\boldsymbol{u}$ is the displacement field between the reference image I_0 and the deformed image I_n. For final optics images, this hypothesis is not exactly true due to illumination variations. Because of the stability of *fiducials* over time, it is assumed that the gray level variation is small enough in *fiducial areas* between successive images to consider the hypothesis of local gray level conservation valid at the registration step. Consequently, the DIC residual reads

$$\rho_{DIC}(\boldsymbol{x}) = I_0(\boldsymbol{x}) - I_n(\boldsymbol{x} + \boldsymbol{u}(\boldsymbol{x})) \tag{4.5}$$

For vacuum window images, the displacement field is written as a linear combination of horizontal translation ($p = 1$), vertical translation ($p = 2$), rotation about the optical axis ($p = 3$) and scaling ($p = 4$)

$$\boldsymbol{u}(\boldsymbol{x}) = \sum_{p=1}^{4} \boldsymbol{\Phi}_p(\boldsymbol{x}, \upsilon_p) \tag{4.6}$$

where the four fields $\boldsymbol{\phi}_p$ are detailed in Table 4.1. The four degrees of freedom correspond to those of similarity transformations, which are a specific case of homography transformations [32]. Three of these fields (*i.e.,* $p = 1, 2, 4$) are linear with respect to the sought amplitudes υ_p (*i.e.,* $\boldsymbol{\Phi}_p(\boldsymbol{x}, \upsilon_p) = \upsilon_p \boldsymbol{\phi}_p(\boldsymbol{x})$). The third field (*i.e.,* $p = 3$) associated with possibly large rotations is nonlinear in terms of the angular amplitude $\upsilon_3 = \theta$

$$\boldsymbol{\Phi}_3(\boldsymbol{x}, \theta) = ([\mathbf{R}(\theta)] - [\mathbf{I}])\boldsymbol{x} \tag{4.7}$$

Table 4.1: Considered kinematic basis used to estimate displacement fields induced by MDCC motions.

Elementary displacement	Field
Horizontal translation	$\boldsymbol{\phi}_1(\boldsymbol{x}) = \mathbf{e}_x$
Vertical translation	$\boldsymbol{\phi}_2(\boldsymbol{x}) = \mathbf{e}_y$
Rotation about optical axis	$\boldsymbol{\Phi}_3(\boldsymbol{x}, \upsilon_3) = ([\mathbf{R}(\upsilon_3)] - [\mathbf{I}])\boldsymbol{x}$
Scaling	$\boldsymbol{\phi}_4(\boldsymbol{x}) = \boldsymbol{x}$

where $[\mathbf{R}(\theta)]$ denotes the rotation matrix.

The registration residual, τ_{DIC}, is defined as

$$\tau_{DIC}^2(\{\boldsymbol{\upsilon}\}) = \sum_{\boldsymbol{x} \in \mathrm{ROI_{DIC}}} \rho_{DIC}^2(\boldsymbol{x}, \{\boldsymbol{\upsilon}\}) \tag{4.8}$$

where $\mathrm{ROI_{DIC}}$ defines the area used to estimate the displacement field $\mathbf{u}$ (*i.e., fiducial area*, see Figure 4.3). The aim of the registration algorithm is to find the four amplitudes υ_i that minimize τ_{DIC}^2 over $\mathrm{ROI_{DIC}}$. This minimization follows an iterative Gauss-Newton scheme [33]. A cubic interpolation scheme is used to create the corrected images. The iterative scheme of the minimization procedure ends when the norm of the iterative corrections is less than a determined threshold (*i.e.,* 10^{-3} px in the present case). At convergence, a registered image $I_{n[DIC]}$ is created.

The registration is *simultaneously* performed over the four *fiducial areas* (Figure 4.3). As such, this is a global approach to DIC. Further, the selected kinematic basis only consists of four fields that were tailored to the present situation. It thus is an integrated DIC approach that does not require any additional post-processing once the four degrees of freedom were measured. In particular, they are easily extrapolated over the *laser beam area*.

It is necessary to choose initial values for the four amplitudes in order to initialize the first iteration of the minimization scheme. One of the classical initializations, namely, starting with zero amplitudes, is not sufficient for window images because images may suffer from very large displacements due to large rotations as explained in Section 4.2. An efficient initialization is essential to ensure the convergence of the registration algorithm [34,

35]. Cross-correlation methods via Fast Fourier Transforms (FFT) are used to find these initial displacements, rotations and scale changes [36–40]. Each step of the initialization procedure is described in Figure 4.4.

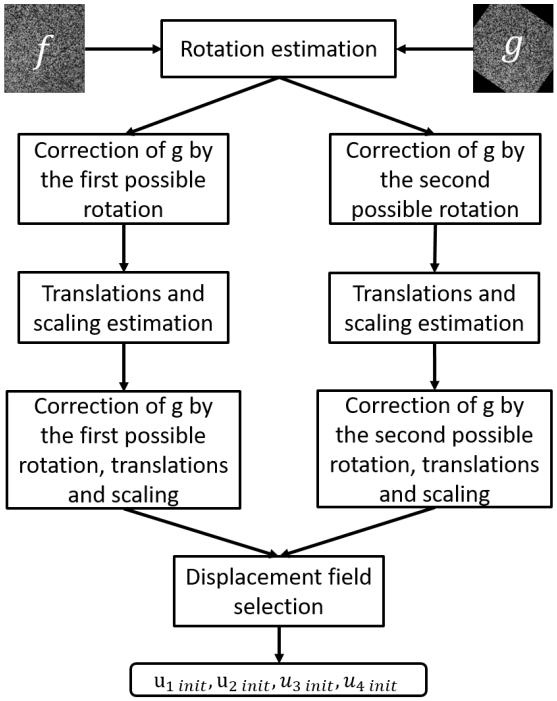

Figure 4.4: Different initialization steps of the registration.

The first step consists in estimating the rotation of the deformed image g with respect to the reference image f. Initially, images are encoded with Cartesian coordinates. Encoding Fourier transform images from Cartesian space to polar coordinates converts rotations into translations. A global correlation product is applied between the Fourier transforms of images f and g encoded in polar coordinates. This correlation product is translation invariant. The position of the peak of the correlation product gives the rotation angle between g and f [39]. However, the Fourier spectra of the images are centro-symmetric. The result of the correlation product is composed of two twin-peaks having the same maximum levels (Figure 4.5). This phenomenon induces a 180-degree ambiguity [41]. After the estimation of the rotation, two angles are possible, θ_1 and θ_2. This ambiguity is solved by the *Displacement field selection* step.

After the estimation of the rotation angle, the image g is corrected with the two estimated angles, θ_1 and θ_2. Scaling and translations are estimated using a correlation product in Cartesian frame between image f and the

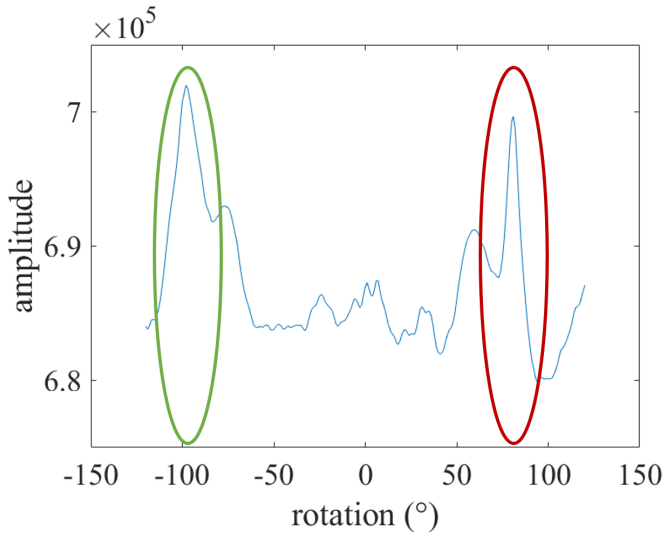

Figure 4.5: Cross-section of the correlation product of the Fourier spectrum encoded in polar space for a $-100°$ angle. The green peak corresponds to the $-100°$ angle and the red peak corresponds to the $80°$ angle (*i.e.,* $80 \equiv -100° \mod [180°]$).

images corrected by the two angles. The two images are separated in four quadrants corresponding to the four *fiducial areas*. The cross-correlation product is calculated on each quadrant of images encoded in Cartesian coordinates. A displacement vector is obtained for each quadrant, from which overall translations and scaling are deduced. The last step of the initialization procedure is the selection of the appropriate displacement field among the two options. The criterion consists in choosing the smallest residual between τ_1 and τ_2 computed over $\mathrm{ROI}_{\mathrm{GL}}$ corresponding to the whole image except the edges.

The gray level residual after registration depends on gray level variations, damage growth and noise

$$\rho_{DIC}(\boldsymbol{x}) = \rho_{DIC}[b(\boldsymbol{x}), c(\boldsymbol{x}), d(\boldsymbol{x})] + \eta(\boldsymbol{x}) \tag{4.9}$$

Once the deformed image is corrected by the measured displacement field, the next step is to correct for gray level variations.

4.3.2 Brightness and Contrast Corrections

The gray level correction is estimated between the reference image f and the corrected image g_{DIC}. Gray level variations between f and g_{DIC} are

accounted for by performing brightness and contrast corrections [33]

$$I_0(\boldsymbol{x}) = b(\boldsymbol{x}) + (1 + c(\boldsymbol{x}))I_{n[DIC]}(\boldsymbol{x}) \tag{4.10}$$

where b is the brightness field, and c the contrast field. Consequently, the associated residual becomes

$$\rho_{GL}(\boldsymbol{x}) = I_0(\boldsymbol{x}) - b(\boldsymbol{x}) - (1 + c(\boldsymbol{x}))I_{n[DIC]}(\boldsymbol{x}) \tag{4.11}$$

The brightness and contrast fields are written as linear combinations of new scalar fields ψ_k

$$b(\boldsymbol{x}) = \sum_{k=1}^{N} b_k \psi_k(\boldsymbol{x}) \qquad \text{and} \quad c(\boldsymbol{x}) = \sum_{k=1}^{N} c_k \psi_k(\boldsymbol{x}) \tag{4.12}$$

where b_k and c_k are the amplitudes to be determined. Contrary to the existing corrections for local DIC, which are uniform over each considered subset [25], the brightness and contrast corrections are *fields* made up of low order polynomials since the *laser beam area* covers a large part of the image (see Table 4.2). The low order polynomials do not remove the damage data.

Table 4.2: Interpolation fields, ψ_k, used for brightness and contrast corrections. The fields are expressed in dimensionless coordinates (X, Y) whose origin is the top left corner.

Order	Interpolation fields
Constant	$\psi_1(\boldsymbol{x}) = 1$
Linear	$\psi_2(\boldsymbol{x}) = X \quad \psi_3(\boldsymbol{x}) = Y$
Bi-linear	$\psi_4(\boldsymbol{x}) = XY$
Order 2	$\psi_5(\boldsymbol{x}) = X^2 \quad \psi_6(\boldsymbol{x}) = Y^2$
$\vdots$	$\vdots$

Such corrections consist in solving a linear system in order to minimize the residual τ_{GL}

$$\tau_{GL}(\{\mathbf{b}\}, \{\mathbf{c}\}) = \sum_{\boldsymbol{x} \in \mathrm{ROI_{GL}}} \rho_{GL}^2(\boldsymbol{x}, \{\mathbf{b}\}, \{\mathbf{c}\}) \tag{4.13}$$

with respect to the amplitudes $\{\mathbf{b}\}, \{\mathbf{c}\}$ of b and c fields, where $\mathrm{ROI}_{\mathrm{GL}}$ is defined as the *beam area* enlarged by 100 pixels on each edge (Figure 4.3).

After solving the linear system, brightness and contrast fields are applied to image $I_{n[DIC]}$ in order to get a registered image corrected for gray level variations $I_{n[DIC+GL]}$. The local residual after registration and gray level corrections, ρ_D, then only depends on damage variations and acquisition noise

$$\rho_D(\boldsymbol{x}) = \rho_D(d(\boldsymbol{x})) + \eta(\boldsymbol{x}). \tag{4.14}$$

4.4 Validation of proposed algorithm

An artificial image set was created in order to validate the previous algorithm.

4.4.1 Registration scheme

The reference image, f, is a black and white speckle pattern of a biaxial experiment on a low-cost composite [42]. To create the validation image set, displacements were applied to the reference image, f. The applied displacements correspond to typical motions that can be seen on vacuum window images. Images belonging to the validation set are shown in Figure 4.6.

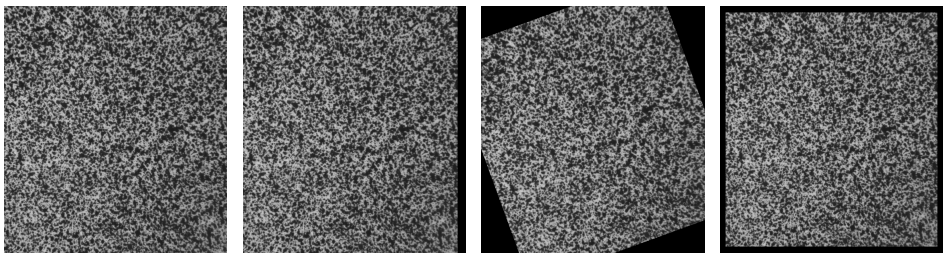

(a) (b) (c) (d)

Figure 4.6: Computer generated images used to validate the registration algorithm. (a) reference image. (b) -20.33 pixel horizontal translation. (c) $-20°$ rotation. (d) Scaling with 0.95 factor.

The validation image set of the registration algorithm is organized as follows:

- Image 1: reference image

- Images 2 to 10: small rotations ranging from $-3°$ to $5°$ by $1°$ step
- Images 11 to 18: translations along $\mathbf{e}_x$ from -10 to -40 pixels by 5-pixel step
- Images 19 to 25: scaling from 0.85 to 1.15 by 0.05 step
- Images 26 to 35: translations along $\mathbf{e}_y$ varying between 14.7 and -22.3 pixels by random steps
- Images 36 to 54: large rotations from $5°$ to $180°$.

Figure 4.7 shows the efficiency of image registration for all the images belonging to the validation set. Before registration, the mean RMS residual is 31% of the dynamic range of the reference image f. After registration, the mean RMS residual reaches 1.1%. If the displacement corrections were perfect, the residual should be exactly 0. The remaining difference comes from the cubic interpolation used for the creation of the validation images and the correction of the deformed images. The residual is exactly 0 for images 11 to 18. For these images, no interpolation was needed since translations were integer-valued. This observation also applies for a $180°$ rotation and unitary scaling.

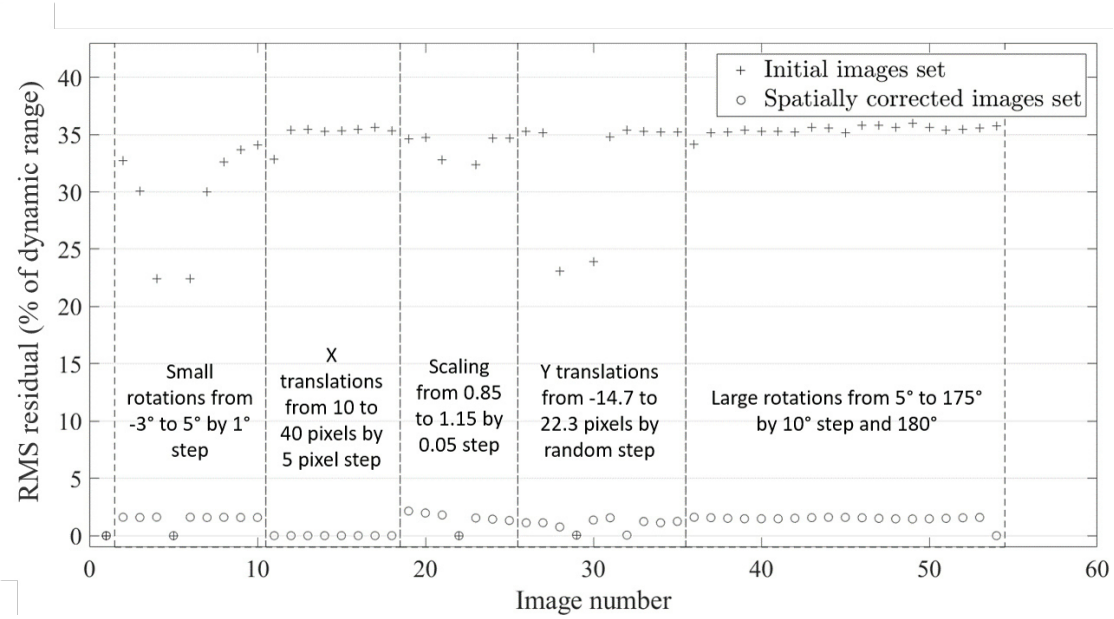

Figure 4.7: Dimensionless RMS residual before and after registration of the images belonging to the validation image set.

4.4.2 Gray level correction

For gray level correction, a validation image g_{test} is created from a brightness and contrast variation applied to the reference image f (with no additional motions)

$$g_{test}(\mathbf{x}) = b_{test}(\mathbf{x}) + c_{test}(\mathbf{x}) f(\mathbf{x}) \tag{4.15}$$

with

$$b_{test}(\mathbf{x}) = 10 \sin\left(\frac{2\pi \mathbf{x}}{400}\right) \quad \text{and} \quad c_{test}(\mathbf{x}) = 1 + 0.2 \sin\left(\frac{2\pi \mathbf{x}}{400}\right) \tag{4.16}$$

The chosen brightness and contrast fields represent an approximation of an intensity increase of the two LEDs used to illuminate a vacuum window. It is worth noting that the selected fields do not belong to the assumed basis (see Table 4.2). Images f and g_{test} and the gray level corrected image (8 bit digitization) are shown in Figure 4.8. The initial RMS residual between f and g_{test} is equal to 11%. After gray level correction, the RMS residual decreases to 2%.

If the order of the chosen basis is sufficiently high, the gray level correction is effective for the correction of the validation image. One can notice in Figure 4.8 a slight edge effect on g_{test} after gray level correction. In this example, the ROI used for the correction corresponds to the whole image. To avoid this edge effect on the *beam area* of window images, $\mathrm{ROI}_{\mathrm{GL}}$ is the *beam area* enlarged by 100 pixels on each edge.

In Figure 4.9, the influence of the order to correct gray level variations is investigated. If the field order is not sufficient, the RMS residual does not decrease and the gray level correction is not efficient. From order 4 on, the correction becomes useful. A satisfying correction is obtained from order 6 on and the gain becomes negligible for higher orders.

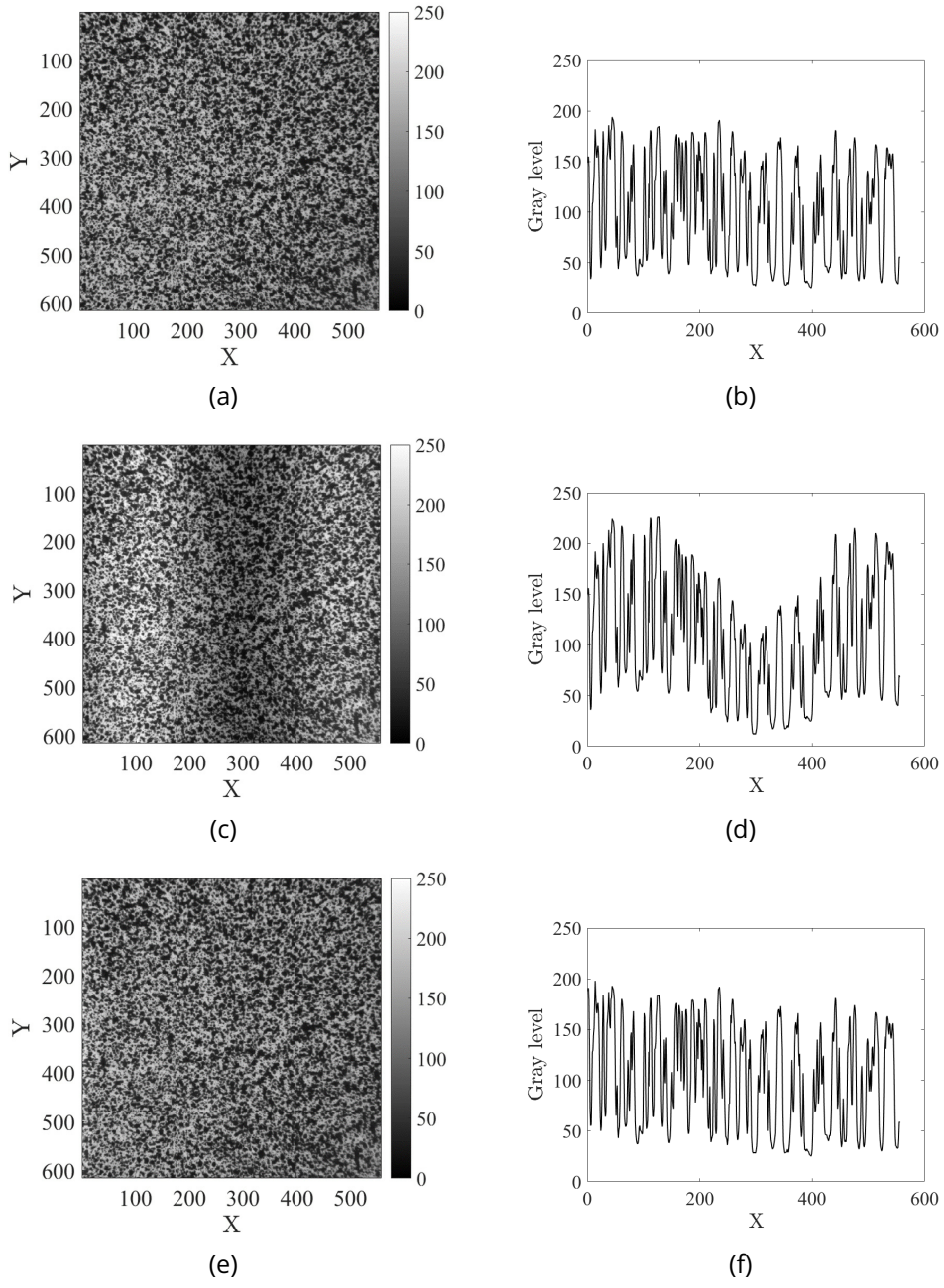

Figure 4.8: (a) Reference image f, (b) validation image g_{test}, (c) corrected image g_{GL}, and associated profiles for each image.

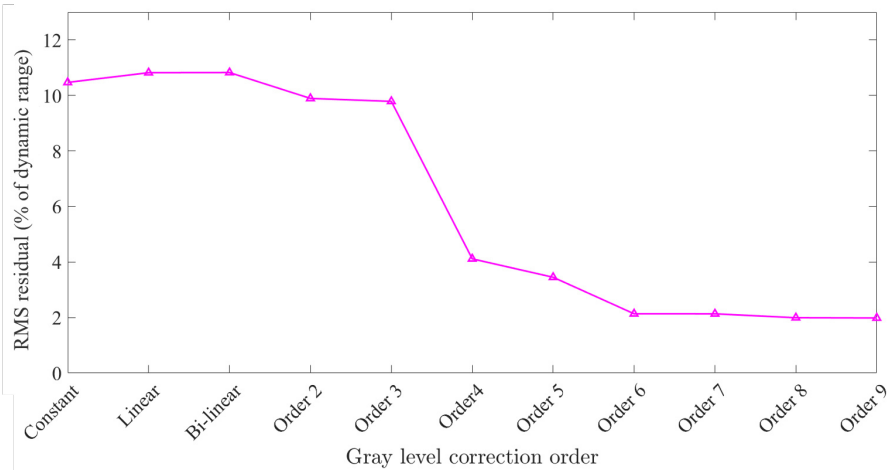

Figure 4.9: Influence of the scalar field order on the efficiency of the gray level correction for the selected fields.

4.5 Application to window images

The algorithm of image registration and gray level correction was validated on a set of computer-generated images. In this section, it is proposed to apply the developed procedure to an LMJ series of 18 vacuum window images acquired after laser shots. The main challenge lies in the "disturbances" between window images. They are mainly made of light reflections and noise that are not stable over time contrary to the speckle pattern of the computer generated images. As explained in Section 4.2, *fiducials* located at each corner of vacuum windows were designed to help image registration. It will be shown that the four *fiducial areas* are sufficient to register vacuum window images and that gray level corrections applied to registered images is efficient. The effectiveness of the corrections is evaluated with the change of the RMS residual calculated over the ROI corresponding to the *laser beam area*, and on residual maps focus on a randomly selected laser damage located on the *laser beam area*.

Due to acquisition noise, the minimum residual level is 0.04% of the dynamic range of the reference image. The standard deviation of the noise was estimated on a 100×100-pixel (undamaged) area of the image over which the average gray level was stable. The standard deviation of acquisition noise is equal 10 gray levels, and the root mean square corresponds to 0.04% of the dynamic range of the reference image. If the RMS residual level is greater than this threshold, one can state that something has changed between reference and deformed images. Initially,

it could be small motions, gray level variations due to lighting conditions, or damage as described in Equation (4.2).

4.5.1 DIC registration

Results of the registration residuals are shown in Figure 4.10. The initial residual levels are not stable over time due to all possible disturbances that can vary from an image to another. All RMS residuals are greater than the 0.04% threshold. The residual maps obtained before image registration show that motions actually occur. Image registration reduces the residual levels for images acquired after each laser shot. Residual maps obtained after image registration confirm that the registration is efficient as laser damage in the reference image is superimposed with the same laser damage on the registered image. Laser damage is still observable on the residual maps because its gray levels have changed between the reference configuration and the following acquisitions. Only residual maps after shots 2 and 18 are shown but the same results are observed over time.

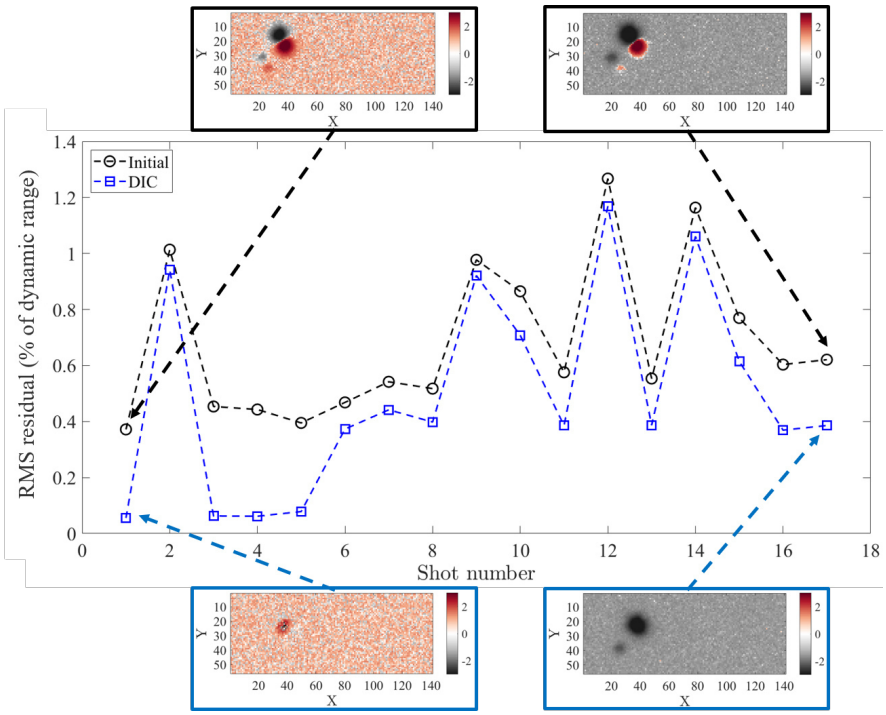

Figure 4.10: Dimensionless RMS residuals before registration of MDCC images (dashed black line) are always higher than those obtained after image registration (dashed blue line). Residual maps corresponding to a damaged area are shown to confirm that image registration was efficient.

The RMS residuals are still greater than the 0.04% threshold due to acquisition noise. These levels could be due to variable lighting conditions and/or damage growth.

4.5.2 Gray level correction

The residual field after image registration mainly contains gray level variations due to illumination changes, damage growth and noise (Figure 4.10). In this section, the proposed gray level correction is performed. It is essential that the gray level correction preserve damage data contained in residual maps. Results of the gray level correction are shown in Figure 4.11. The chosen order for brightness and contrast fields is $N = 3$.

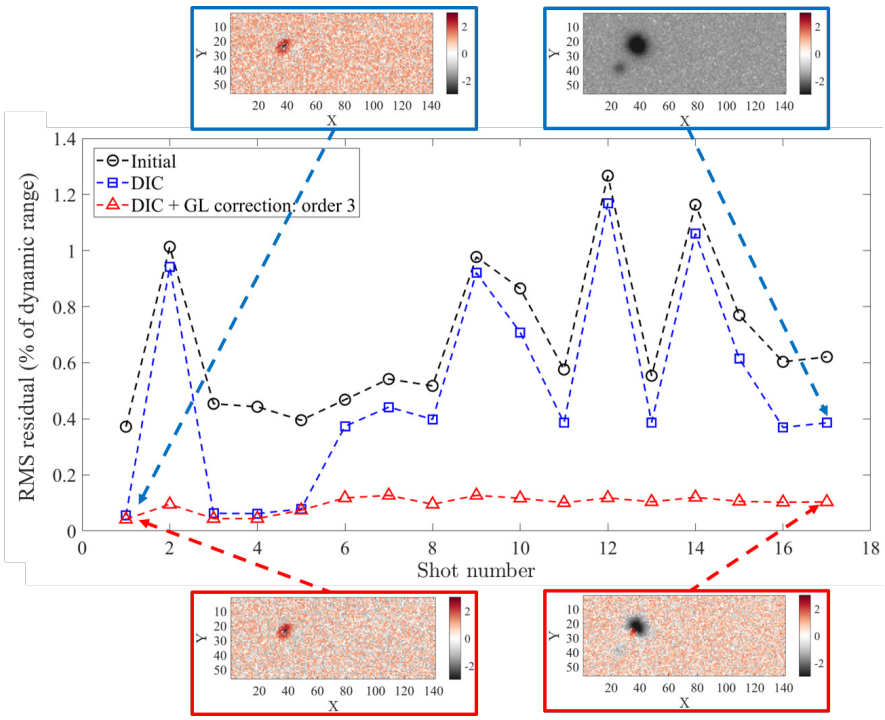

Figure 4.11: Comparison of initial residual (dashed black line), residual after image registration (dashed blue line) and gray level variation (dashed red line) for the raw window images. The final residuals are significantly lower than their initial levels. Residual maps corresponding to a damage area are plotted in this figure in order to visually confirm that the corrections were efficient.

The RMS residual before and after gray level correction is a good indicator of the effectiveness of the proposed correction. The final residual

levels after both corrections oscillate between 0.05% and 0.13% of the dynamic range. This residual is very close to the 0.04% threshold due to acquisition noise, more stable and lower than those obtained after image registration alone. The residual maps in Figure 4.11 show that the gray level correction is effective to correct for variations due to variable illumination conditions.

In Figure 4.12, the influence of the scalar field order is studied for the gray level corrections. Constant brightness and contrast corrections over the *laser beam area*, which are equivalent to the so-called zero-mean normalized correction [25, 43], are not sufficient to take into account gray level variations on vacuum window images. Corrections of order 3 are a good compromise between correcting variations and keeping damage data (Figure 4.13). More local variations may lead to even lower residuals. Finite element discretizations [44] or principal component analyses [45] may be investigated. For the feasibility study performed herein, it is believed that the 3^{rd} order corrections were sufficient.

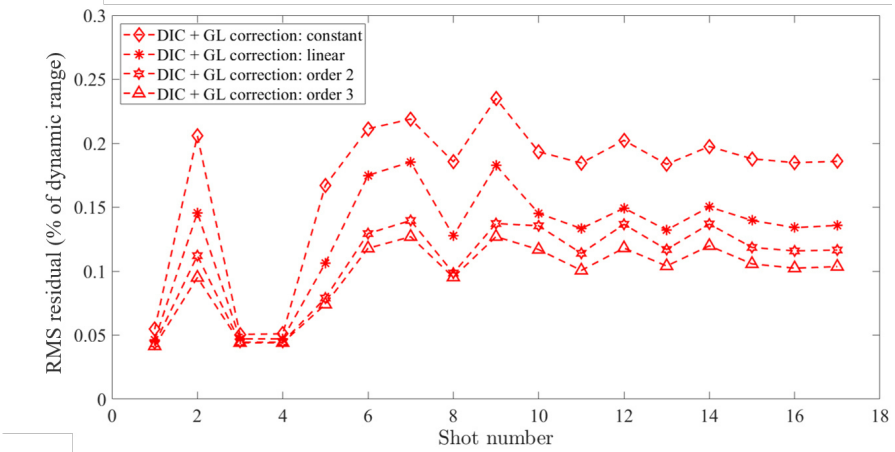

Figure 4.12: Influence of the order of the scalar fields on the RMS residual.

Figure 4.13 shows the effectiveness of the gray level correction applied to the window image set. After brightness and contrast corrections, the profile of image 3 follows nearly that of the reference image without erasing the damage site. The brightness and contrast corrections significantly reduced the effect of illumination variations. However, the proposed method is not perfect. For instance, between Y coordinates 2500 and 3000 pixels of Figure 4.13, there is still a difference between both profiles. One can notice that in this section, the variation is less than 50 gray levels, close to acquisition noise.

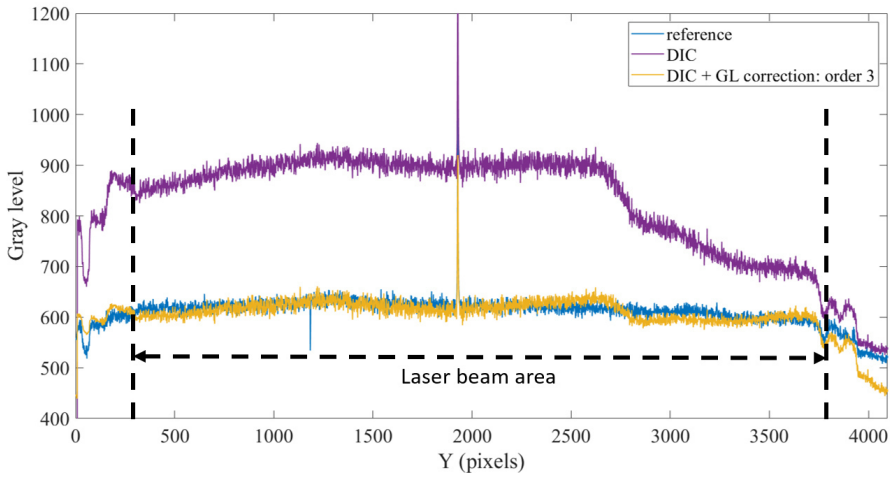

Figure 4.13: Profile comparison of image 3 after registration, after brightness and contrast corrections, and reference image. The narrow peak corresponds to a damage site that is preserved by the various corrections.

4.5.3 Preliminary brightness correction

Up to now, the brightness and contrast corrections were performed after spatial registrations on raw dark-field images. In order to enhance the effectiveness of the gray level corrections, a preliminary correction is proposed. After each shot, two different images of a vacuum window are acquired:

- A window image with LEDs turned on. In this image, scattering objects located on the window are visible. An illumination variation caused by the LEDs induces contrast variations from one image to another.
- A window image with LEDs turned off. The aim of this acquisition is to get all the illumination effects coming from all other sources than LEDs. Such sources, which are not stable from one acquisition to another, lead to brightness variations.

The difference between these two images makes it possible to create pre-corrected images that may have the same brightness level from one acquisition to another. This pre-correction slightly enhances the brightness and contrast corrections as shown in Figure 4.14. Thanks to this operation, the hypothesis of gray level conservation, which is used for image registration, is more valid and image registration is likely to be more stable.

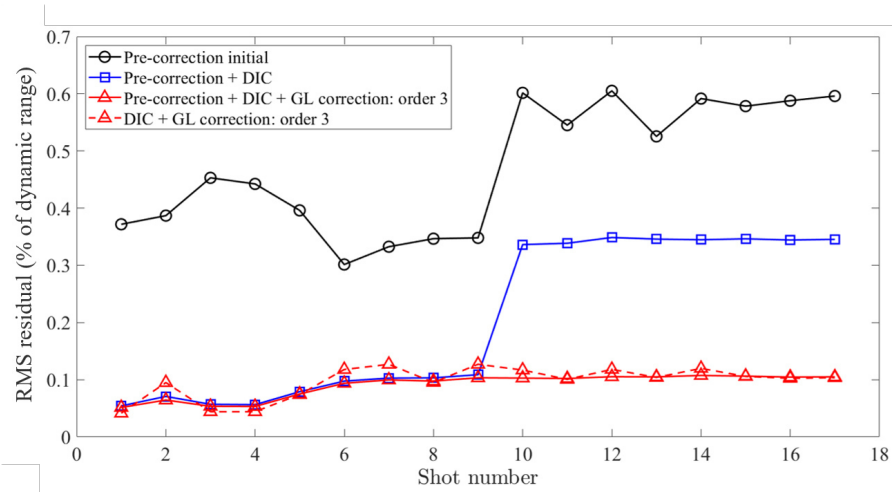

Figure 4.14: Comparison of initial residual, after image registration, residual, after brightness and contrast corrections for raw images and pre-corrected images.

An increase of the RMS residuals for pre-corrected images between shot 9 and 10 before gray level correction may be due to illumination issues. An analysis of the contrast field for images from shots 9 and 10 (Figure 4.15) proves that the sudden increase before gray level corrections is due to the bottom LED. In that area, the contrast level is close to one for image from shot 9 and tends to zero for image from shot 10. It is possible to state that the bottom LED was turned off before image from shot 10. This conclusion is confirmed by the observation of registered images from shots 9 and 10, in Figure 4.15. In that area, the gray levels increased between images from shots 9 and 10.

The brightness and contrast corrections make comparisons between corrected images after each shot possible. The detection of abnormal illumination variations (*e.g.,*turning on and off LEDs) is also possible thanks to an analysis of the contrast field. When an LED is switched off during image acquisition, the luminance near that LED is too weak to make damage sites in this area visible. It is essential to check that the LEDs are turned on to be able to detect and follow damage growth from one shot to another. Brightness and contrast corrections account for illumination variations but they cannot find missing information (in too dark zones).

Except for an exceptional issue related to LEDs, the proposed algorithms make Lagrangian comparisons of successive images possible. After image registration and gray level corrections, the residual only depends on damage initiation and growth, as well as acquisition noise.

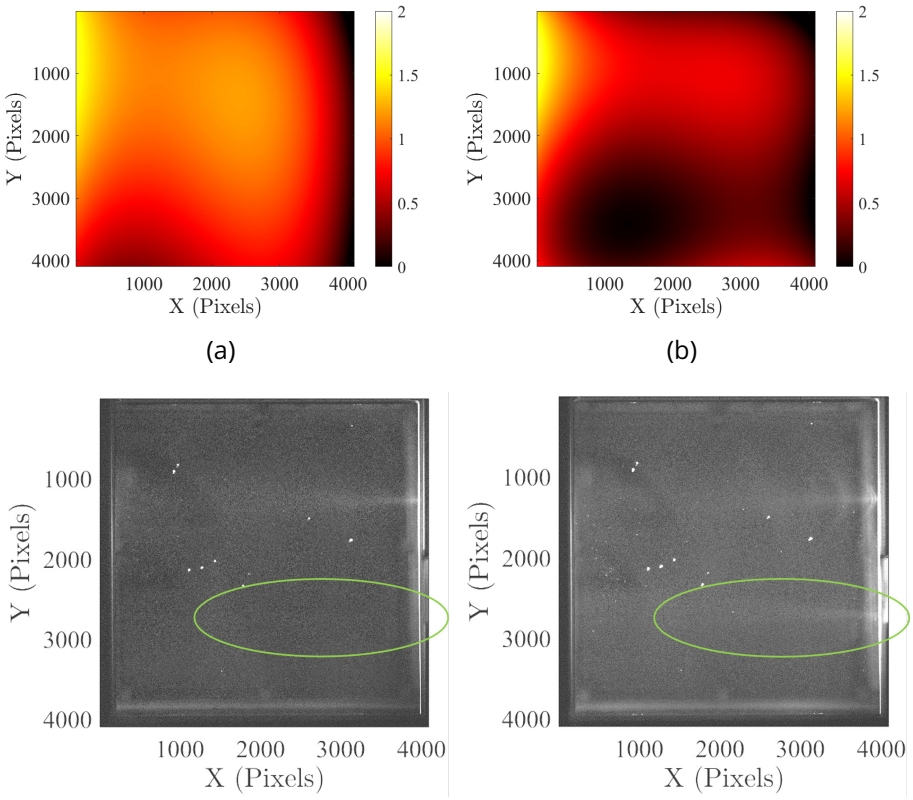

Figure 4.15: Effect of turning on an LED on the estimated contrast field (see green ellipses). (a,b) Estimated contrast field for image from shots 9 (a) and 10 (b) subtracted by the image from shots 9 and 10 respectively acquired with LED off. (c,d) Registered image from shots 9 (c) and 10 (d) subtracted by the image from shots 9 and 10 respectively acquired with LED off.

4.6 Laser damage detection and quantification

Once the window images are corrected thanks to the presented algorithms, it is possible to compare directly gray levels of successive images. In these conditions, each gray level variation that is more important than noise can be considered as a potential damage site. Based on this observation, an efficient way to detect potential damage sites and to quantify damage growth is presented.

4.6.1 Detection of potential damage sites

To detect damage sites, it is proposed to threshold absolute values of residual maps ρ^n_{DIC+GL} between the reference image and the corrected image acquired after laser shot n, $I_{n[DIC+GL]}$. This thresholding method is designated as DIC thresholding in the following part of this section. The detection threshold has to be small enough to capture all damage sites as soon as they initiate. However, the selected threshold has to be higher than acquisition noise to avoid numerous false alarms. Experimentally, acquisition noise was estimated to have a standard deviation of 10 gray levels.

The present approach is compared to LASNR that does not take into account the evolution of gray levels over time, contrary to the present method. The detection principle of the LASNR method is based on the comparison of the grey level of each pixel with its surrounding neighbors [23].

Figure 4.16 shows all detected sites on the same image with both analyses. The DIC threshold is defined at the acquisition noise limit. The LASNR parameters are the same as those used on LMJ. With these parameters, DIC is more efficient than LASNR to detect potential damage sites. The former detects twice the number of objects than the latter for the treated example.

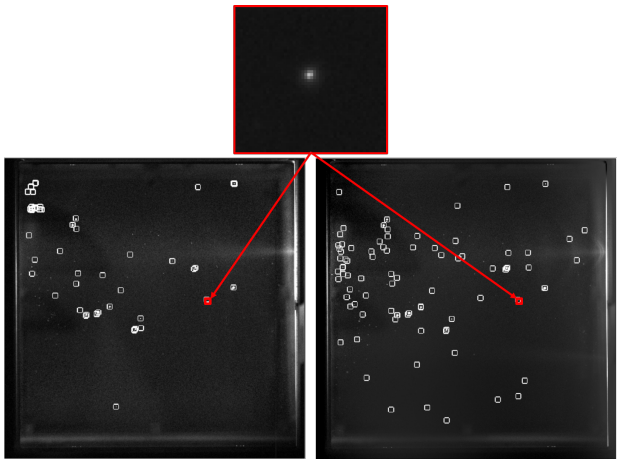

Figure 4.16: Results of two different detection methods. On the left, detected sites by LASNR. On the right, sites determined *via* DIC. The detected damage sites are represented by white boxes. The selected area used to illustrate damage growth is depicted as the red box.

Undetected sites by LASNR are isolated pixels that have a varying gray

level near acquisition noise of the observation system. The proposed approach can be considered as more efficient than LASNR as it detects objects that initiate and grow from one shot to another. If the reference image were acquired on an undamaged window, all initiated damage sites would possibly be detected by DIC as soon as their gray levels are higher than that corresponding to acquisition noise of the camera.

4.6.2 Damage growth

It is necessary to know if detected objects are truly laser-induced damage sites or any other object. The labeling of detected sites as damaged is possible by following the change of the residual ρ_D of an area around them. An example corresponding to a detected site (red box in Figure 4.16) is chosen to illustrate this section. The aim is to be sure that detected zones by DIC are actually damage sites, and to quantify damage growth after each shot.

An estimation of the maximum diameter of damage sites is approximately equal to one millimeter. This size is equivalent to tens of pixels on images. Therefore, an analysis area of 50-pixel side centered about each detected site is defined. In order to identify laser damage sites among all detected areas, an analysis of the RMS residual for each of them is performed. Dust and other particles are not bonded on the window. They may disappear or move from an acquisition to another. This phenomenon leads to a brief increase of the RMS residual, and then a decrease to initial levels. Objects associated with this feature are not damage sites.

The quantification of damage growth is carried out with the analysis of the variation of the RMS residual on the selected area. Figure 4.17 shows the change of the residual map from the first to the last image for the area under study. The size and gray level of the damaged zone increase after each shot. However, damage growth is not constant.

The increase of RMS residual after each shot is compared to the energy level of the corresponding shot in Figure 4.18. It is observed that:

- The increase of RMS residual is linked with the growth of the damaged area. These gray levels are directly connected with the way damage sites scatter light.

- The variation of RMS residual is potentially related to the energy at 3ω of the corresponding shot [6]. In the studied example, the RMS level does not change when the energy of the shot is less than $2\,\mathrm{kJ}$. Conversely, it increases when the energy is of the order of $3\,\mathrm{kJ}$. It

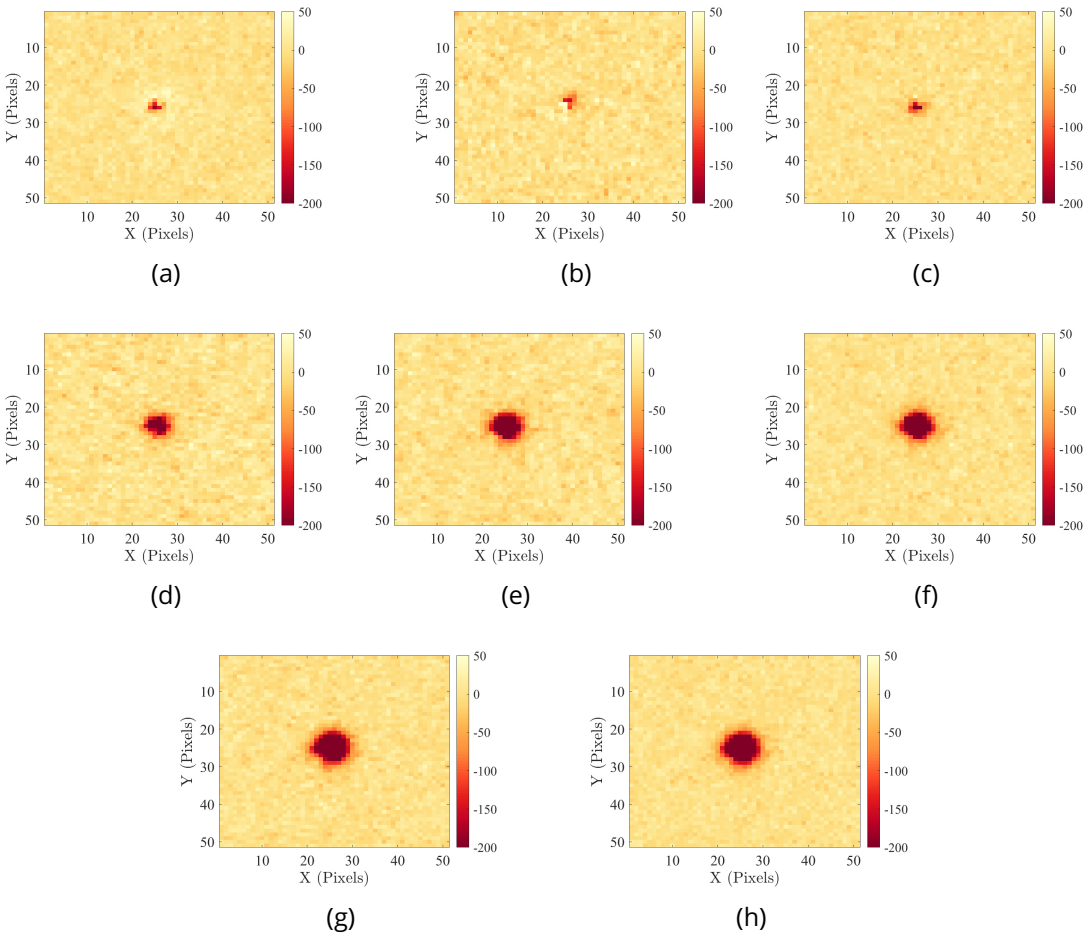

Figure 4.17: Variation of gray level residual maps after each shot on the analysis area selected for a detected damage site (red box in Figure 4.16) with DIC for shots 1 (a), 2 (b), 4 (c), 6 (d), 8 (e), 12 (f), 14 (g), 16 (h). The image is encoded over 16 bits.

is worth noting that the residual estimated for the damaged area is local in comparison to the shot energy that is global, namely, calculated for the whole beam. Furthermore, other parameters, such as pulse duration, may have an influence on damage growth on vacuum windows [6]. A statistical analysis on more damage sites and shots is necessary to analyze such correlations.

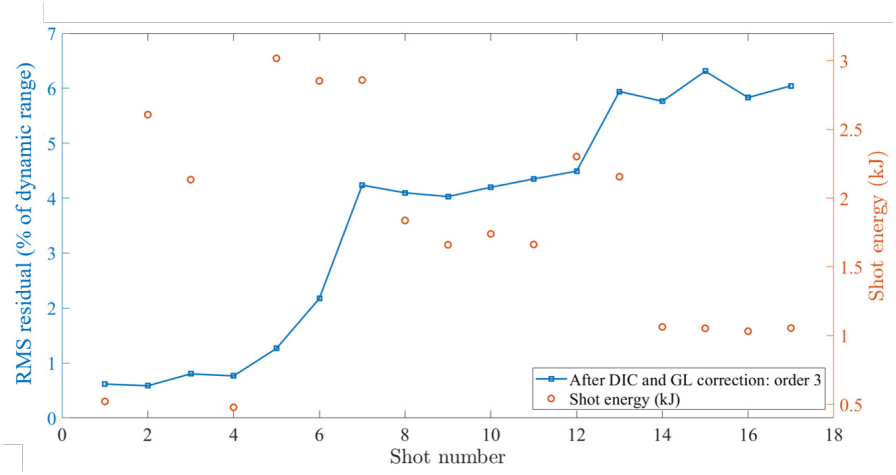

Figure 4.18: Variation of RMS residual for the analyzed area (displayed in Figure 4.17) after each shot. Comparison with the global energy of each shot.

4.7 Conclusion

In this chapter, a solution for spatial registration and correction of illumination variations was presented for the detection of damage on LMJ vacuum windows. Special implementations were required since the area over which DIC was performed was not identical to that where brightness/contrast corrections were carried out. A reduced kinematic basis was selected to extrapolate the measured displacement fields. The proposed algorithms were first validated on computer-simulated images using a standard speckle pattern for DIC analyses. Then, they were applied to a set of real images of an LMJ vacuum window where fiducials were used for registration purposes, and the beam illuminated area for brightness and contrast corrections.

The proposed correction methods can be used in high energy laser facilities where it is necessary to follow damage growth in which small motions and illumination variations may occur. The new method of laser-induced damage detection is based on the analysis of the final residual fields. Detection and quantification of laser-induced damage led to very low residual levels as functions of laser shots. These residual maps are independent of the displacements between acquisitions and are no longer affected by gray level variations that are not induced by damage growth. The present implementation was compared to the widely-used LASNR algorithm and provided better results. The advantage of this method is to

be based on the overall increase of light scattering with damage growth.

A study, which is based on BSDF (Bidirectional Scattering Distribution Function) measurements [46], is in progress with the aim of identifying factors modifying the scattering level of damage sites. The gray levels of damage sites may then be linked with their size as well as the fracture mechanism or with the morphology of the crater.

References

[1] M. L. Andre, "Status of the LMJ project," in *Solid State Lasers for Application to Inertial Confinement Fusion: Second Annual International Conference*, M. L. Andre, Ed., International Society for Optics and Photonics, vol. 3047, SPIE, 1997, pp. 38–42. doi: 10.1117/12.294307. [Online]. Available: https://doi.org/10.1117/12.294307.

[2] J. A. Paisner, E. M. Campbell, and W. J. Hogan, "The national ignition facility project," *Fusion Technology*, vol. 26, no. 3, Nov. 1994.

[3] W. Hogan, E. Moses, B. Warner, M. Sorem, and J. Soures, "The national ignition facility," *Nuclear Fusion*, vol. 41, p. 567, May 2002. doi: 10.1088/0029-5515/41/5/309.

[4] W. Zheng *et al.*, "Laser performance of the sg-iii laser facility," *High Power Laser Science and Engineering*, vol. 4, e21, 2016. doi: 10.1017/hpl.2016.20.

[5] H. Schwoerer, J. Magill, and B. Beleites, *Lasers and Nuclei*. Springer, 2006. doi: 10.1007/b11559214.

[6] K. Manes, M. Spaeth, J. Adams, and M. Bowers, "Damage mechanisms avoided or managed for nif large optics," *Fusion Science and Technology*, vol. 69, pp. 146–249, Feb. 2016. doi: 10.13182/FST15-139.

[7] S. G. Demos, M. Staggs, and M. R. Kozlowski, "Investigation of processes leading to damage growth in optical materials for large-aperture lasers," *Applied Optics*, vol. 41, no. 18, pp. 3628–3633, Jun. 2002. doi: 10.1364/AO.41.003628. [Online]. Available: http://ao.osa.org/abstract.cfm?URI=ao-41-18-3628.

[8] M. Veinhard *et al.*, "Effect of non-linear amplification of phase and amplitude modulations on laser-induced damage of thick fused silica optics with large beams at 351 nm," *Journal of Applied Physics*, vol. 124, no. 16, p. 163106, Oct. 2018. doi: 10.1063/1.5049864.

[9] N. Bloembergen, "Role of cracks, pores, and absorbing inclusions on laser induced damage threshold at surfaces of transparent dielectrics," *Applied Optics*, vol. 12, no. 4, pp. 661–664, Apr. 1973. doi: 10.1364/AO.12.000661. [Online]. Available: http://ao.osa.org/abstract.cfm?URI=ao-12-4-661.

[10] J. Neauport, P. Cormont, P. Legros, C. Ambard, and J. Destribats, "Imaging subsurface damage of grinded fused silica optics by confocal fluorescence microscopy," *Optics Express*, vol. 17, no. 5, pp. 3543–3554, Mar. 2009. doi: 10.1364/OE.17.003543. [Online]. Available: http://www.opticsexpress.org/abstract.cfm?URI=oe-17-5-3543.

[11] M. J. Soileau, N. Mansour, E. W. van Stryland, and W. E. Williams, "Laser-induced damage and the role of self-focusing," *Optical Engineering*, vol. 28, pp. 1133–1144, Oct. 1989. doi: 10.1117/12.7977098.

[12] D. M. Kane and D. R. Halfpenny, "Reduced threshold ultraviolet laser ablation of glass substrates with surface particle coverage: a mechanism for systematic surface laser damage," *Journal of Applied Physics*, vol. 87, no. 9, pp. 4548–4552, 2000. doi: 10.1063/1.373100. eprint: https://doi.org/10.1063/1.373100. [Online]. Available: https://doi.org/10.1063/1.373100.

[13] S. Palmier *et al.*, "Surface particulate contamination of the LIL optical components and their evolution under laser irradiation," in *Laser-Induced Damage in Optical Materials: 2006*, G. J. Exarhos, A. H. Guenther, K. L. Lewis, D. Ristau, M. J. Soileau, and C. J. Stolz, Eds., International Society for Optics and Photonics, vol. 6403, SPIE, 2007, pp. 301–310. doi: 10.1117/12.695442. [Online]. Available: https://doi.org/10.1117/12.695442.

[14] M. Chambonneau and L. Lamaignère, "Multi-wavelength growth of nanosecond laser-induced surface damage on fused silica gratings," *Scientific Reports*, vol. 8, pp. 1–10, Jan. 2018. doi: 10.1038/s41598-017-18957-9.

[15] R. A. Negres, D. A. Cross, Z. M. Liao, M. J. Matthews, and C. W. Carr, "Growth model for laser-induced damage on the exit surface of fused silica under uv, ns laser irradiation," *Optics Express*, vol. 22, no. 4, pp. 3824–3844, Feb. 2014. doi: 10.1364/OE.22.003824. [Online]. Available: http://www.opticsexpress.org/abstract.cfm?URI=oe-22-4-3824.

[16] R. A. Negres, M. A. Norton, D. A. Cross, and C. W. Carr, "Growth behavior of laser-induced damage on fused silica optics under uv, ns laser irradiation," *Optics Express*, vol. 18, no. 19, pp. 19 966–19 976, Sep. 2010. doi: 10.1364/OE.18.019966. [Online]. Available: http://www.opticsexpress.org/abstract.cfm?URI=oe-18-19-19966.

[17] P. Cormont, P. Combis, L. Gallais, C. Hecquet, L. Lamaignère, and J. L. Rullier, "Removal of scratches on fused silica optics by using a co2 laser," *Optics Express*, vol. 21, no. 23, pp. 28 272–28 289, Nov. 2013. doi: 10.1364/OE.21.028272. [Online]. Available: http://www.opticsexpress.org/abstract.cfm?URI=oe-21-23-28272.

[18] J. Folta *et al.*, "Mitigation of laser damage on National Ignition Facility optics in volume production," in *Laser-Induced Damage in Optical Materials: 2013*, G. J. Exarhos, V. E. Gruzdev, J. A. Menapace, D. Ristau, and M. Soileau, Eds., International Society for Optics and Photonics, vol. 8885, SPIE, 2013, pp. 138–146. doi: 10.1117/12.2030475. [Online]. Available: https://doi.org/10.1117/12.2030475.

[19] T. Doualle *et al.*, "CO2 laser microprocessing for laser damage growth mitigation of fused silica optics," *Optical Engineering*, vol. 56, no. 1, pp. 1–9, 2016. doi: 10.1117/1.OE.56.1.011022.

[20] F. Wei *et al.*, "Automatic classification of true and false laser-induced damage in large aperture optics," *Optical Engineering*, vol. 57, no. 5, pp. 1–11, 2018. doi: 10.1117/1.OE.57.5.053112. [Online]. Available: https://doi.org/10.1117/1.OE.57.5.053112.

[21] L. Mascio-Kegelmeyer, "Machine learning for managing damage on NIF optics," in *Laser-induced Damage in Optical Materials 2020*, C. W. Carr, V. E. Gruzdev, D. Ristau, and C. S. Menoni, Eds., International Society for Optics and Photonics, vol. 11514, SPIE, 2020. doi: 10.1117/12.2571016. [Online]. Available: https://doi.org/10.1117/12.2571016.

[22] C. Lacombe *et al.*, "Dealing with LMJ final optics damage: post-processing and models," in *Laser-induced Damage in Optical Materials 2020*, C. W. Carr, V. E. Gruzdev, D. Ristau, and C. S. Menoni, Eds., International Society for Optics and Photonics, vol. 11514, SPIE, 2020. doi: 10.1117/12.2571074. [Online]. Available: https://doi.org/10.1117/12.2571074.

[23] L. Kegelmeyer, P. Fong, S. Glenn, and J. Liebman, "Local area signal-to-noise ratio (lasnr) algorithm for image segmentation," *Proceedings of SPIE - The International Society for Optical Engineering*, vol. 6696, Oct. 2007. doi: 10.1117/12.732493.

[24] C. Amorin, L. Kegelmeyer, and W. Kegelmeyer, "A hybrid deep learning architecture for classification of microscopic damage on national ignition facility laser optics," *Statistical Analysis and Data Mining: The ASA Data Science Journal*, vol. 12, Sep. 2019. doi: 10.1002/sam.11437.

[25] M. A. Sutton, J.-J. Orteu, and H. W. Schreier, *Image Correlation for Shape, Motion and Deformation Measurements - Basic Concepts, Theory and Applications*. Springer Science, 2009, isbn: 978-0-387-78746-6. doi: 10.1007/978-0-387-78747.

[26] P. Rastogi and E. Hack, *Optical Methods for Solid Mechanics: A Full-Field Approach*. Weinheim Wiley-VCH-Verl. 2012, Jun. 2012, isbn: 978-3-527-41111-5.

[27] M. A. Sutton, "Computer Vision-Based, Noncontacting Deformation Measurements in Mechanics: A Generational Transformation," *Applied Mechanics Reviews*, vol. 65, no. 5, Aug. 2013, issn: 0003-6900. doi: 10.1115/1.4024984. eprint: https://asmedigitalcollection.asme.org/appliedmechanicsreviews/article-pdf/65/5/050802/6073861/amr_65_05_050802.pdf. [Online]. Available: https://doi.org/10.1115/1.4024984.

[28] G. Z. Voyiadis, *Handook of Damage Mechanics*. Springer Science, 2015.

[29] F. Hild and S. Roux, "Handbook of damage mechanics," in Springer, 2015, ch. Evaluating Damage with Digital Image Correlation: A. Introductory Remarks and Detection of Physical Damage, pp. 1255–1275.

[30] E. Schwartz *et al.*, "The use of digital image correlation for non-destructive and multi-scale damage quantification," in *Sensors and Smart Structures Technologies for Civil, Mechanical, and Aerospace Systems 2013*, J. P. Lynch, C.-B. Yun, and K.-W. Wang, Eds., International Society for Optics and Photonics, vol. 8692, SPIE, 2013, pp. 706–720. doi: 10.1117/12.2012277. [Online]. Available: https://doi.org/10.1117/12.2012277.

[31] M. Mehdikhani, E. Steensels, A. Standaert, K. Vallons, L. Gorbatikh, and S. Lomov, "Multi-scale digital image correlation for detection and quantification of matrix cracks in carbon fiber composite laminates in the absence and presence of voids controlled by the cure cycle," *Composites Part B: Engineering*, vol. 154, pp. 138–147, Dec. 2018. doi: 10.1016/j.compositesb.2018.07.006.

[32] R. I. Hartley and A. Zisserman, *Multiple View Geometry in Computer Vision*, Second. Cambridge University Press, ISBN: 0521540518, 2004.

[33] F. Hild and S. Roux, "Digital image correlation," in *Optical Methods for Solid Mechanics. A Full-Field Approach*, P. Rastogi and E. Hack, Eds., Weinheim (Germany): Wiley-VCH, 2012, pp. 183–228.

[34] G. Besnard, F. Hild, and S. Roux, ""Finite-element" displacement fields analysis from digital images: Application to Portevin-Le Chatelier bands," *Experimental Mechanics*, vol. 46, pp. 789–803, 2006.

[35] Z. Jiang, Q. Kemao, H. Miao, J. Yang, and L. Tang, "Path-independent digital image correlation with high accuracy, speed and robustness," *Optics and Lasers in Engineering*, vol. 65, pp. 93–102, 2015, Special Issue on Digital Image Correlation, issn: 0143-8166. doi: https://doi.org/10.1016/j.optlaseng.2014.06.011. [Online]. Available: https://www.sciencedirect.com/science/article/pii/S0143816614001560.

[36] D. Barker and M. Fourney, "Measuring fluid velocities with speckle patterns," *Optics Lett.*, vol. 1, pp. 135–137, 1977.

[37] T. Dudderar and P. Simpkins, "Laser speckle photography in a fluid medium," *Nature*, vol. 270, pp. 45–47, 1977.

[38] R. Grousson and S. Mallick, "Study of flow pattern in a fluid by scattered laser light," *Applied Optics*, vol. 16, pp. 2334–2336, 1977.

[39] B. S. Reddy and B. N. Chatterji, "An fft-based technique for translation, rotation, and scale-invariant image registration," *IEEE Transactions on Image Processing*, vol. 5, no. 8, pp. 1266–1271, Aug. 1996, issn: 1941-0042. doi: 10.1109/83.506761.

[40] Z. Fang *et al.*, "Efficient and automated initial value estimation in digital image correlation for large displacement, rotation, and scaling," *Appl. Opt.*, vol. 59, no. 33, pp. 10 523–10 531, Nov. 2020. doi: 10.1364/AO.405551. [Online]. Available: http://ao.osa.org/abstract.cfm?URI=ao-59-33-10523.

[41] J. N. Sarvaiya, S. Patnaik, and S. Bombaywala, "Image registration using log-polar transform and phase correlation," in *TENCON 2009 - 2009 IEEE Region 10 Conference*, Jan. 2009, pp. 1–5. doi: 10.1109/TENCON.2009.5396234.

[42] D. Claire, F. Hild, and S. Roux, "Identification of damage fields using kinematic measurements," *Comptes Rendus Mécanique*, vol. 330, pp. 729–734, 2002. doi: 10.1016/S1631-0721(02)01524-3. [Online]. Available: https://hal.archives-ouvertes.fr/hal-00002902.

[43] B. Wang, B. Pan, and G. Lubineau, "Some practical considerations in finite element-based digital image correlation," *Optics and Lasers in Engineering*, vol. 73, pp. 22–32, 2015, issn: 0143-8166. doi: https://doi.org/10.1016/j.optlaseng.2015.03.010. [Online]. Available: https://www.sciencedirect.com/science/article/pii/S0143816615000494.

[44] V. Sciuti, R. Canto, J. Neggers, and F. Hild, "On the benefits of correcting brightness and contrast in global digital image correlation: monitoring cracks during curing and drying of a refractory castable," *Optics and Lasers in Engineering*, vol. 136, p. 106 316, 2021, issn: 0143-8166. doi: https://doi.org/10.1016/j.optlaseng.2020.106316. [Online]. Available: http://www.sciencedirect.com/science/article/pii/S0143816620305686.

[45] C. Jailin and S. Roux, "Modal decomposition from partial measurements," *Comptes Rendus Mécanique*, vol. 347, no. 11, pp. 863–872, 2019, issn: 1631-0721. doi: https://doi.org/10.1016/j.crme.2019.11.011. [Online]. Available: http://www.sciencedirect.com/science/article/pii/S1631072119301822.

[46] S. Liukaityte, M. Zerrad, M. Lequime, T. Bégou, and C. Amra, "Measurements of angular and spectral resolved scattering on complex optical coatings," in *Optical Systems Design 2015: Advances in Optical Thin Films V*, M. Lequime, H. A. Macleod, and D. Ristau, Eds., International Society for Optics and Photonics, vol. 9627, SPIE, 2015, pp. 229–235. doi: 10.1117/12.2191227. [Online]. Available: https://doi.org/10.1117/12.2191227.

5

Sub-pixel detection of laser-induced damage and its growth on fused silica optics using registration residuals

Fused silica optics are key components to manipulate high energy Inertial Confinement Fusion (ICF) laser beams but their optical properties may be degraded by laser-induced damage. The detection of laser damage sites is of major importance. The challenge is to monitor damage initiation and growth at sub-pixel scale with highly sensitive measurements. The damage diameter is a widely used indicator to quantify damage growth but its accuracy is strongly dependent on the available image resolution. In Chapter 4, it was shown that registration residual maps (i.e., gray level differences between two registered images) could also be used to monitor laser-induced damage. In this chapter, the performance of both indicators are compared to detect laser damage initiation and growth at high and low image resolutions thanks to a highly instrumented laser setup. The results prove that registration residual maps are more efficient to detect sub-pixel laser damage growth than diameter measurements at a given image resolution. The registration residual maps are therefore a powerful indicator for monitoring laser-induced damage initiation and growth at sub-pixel scale either for laser damage metrology setups, for high energy laser facilities, or other situations where damage is suspected to occur. The accuracy of (laser-induced) damage laws may also be improved thanks to this tool.

Reproduced from:
G. Hallo, C. Lacombe, R. Parreault, N. Roquin, T. Donval, L. Lamaignère, J. Néauport and F. Hild
Sub-pixel detection of laser-induced damage and its growth on fused silica optics using registration residuals.
Optics Express 29, 35820-35836, 2021.

5.1 Introduction

The optics of high energy Inertial Confinement Fusion (ICF) laser facilities suffer from laser-induced damage. Once a damage site initiates, it grows after each ultraviolet laser shot since the ultraviolet energy is greater than the growth threshold [1]. Due to the presence of damage sites on final fused silica components, the available laser energy is limited for each experiment. Some techniques have been developed to limit damage growth such as locally reducing the laser energy under the growth threshold by shadowing [2] or using CO_2 laser optics mitigation [3, 4]. However, optics mitigation at the Laser MegaJoule (LMJ) facility is effective only if the damage site diameter is less than $700\,\mu\mathrm{m}$, and if early damage growth is measurable. Hence, the objective is to detect laser damage sites before they reach sizes of about $100\,\mu\mathrm{m}$ [2, 5]. This physical size represents about one pixel for observation systems of high energy laser installations such as Final Optics Damage Inspection (FODI) at the National Ignition Facility (NIF) [6] and ShenGuang-III (SG-III) [7], or the Chamber Center Diagnostic Module (MDCC [2, 8]) of the LMJ facility [8]. Consequently, sub-pixel damage detection is needed on such final optics. The observed final optics at NIF are the vacuum windows, the second and third harmonic generator crystals, the final focusing lens and the main debris shield [6] whereas only the vacuum windows and the focusing gratings are observed at LMJ [2].

In order to monitor laser damage, different methods have been developed to detect its growth as soon as possible without removing the component. It was proposed to detect potential damage sites using an algorithm based on the analysis of the Local Area Signal-to-Noise Ratio (LASNR) for each pixel of each image [9]. This algorithm is widely used at NIF and LMJ to detect damage sites on final optics. An algorithm based on local area signal strength and 2D histogram was then applied to damage detection [10]. These algorithms are deemed efficient for early detection of damage sites. NIF announced the detection of sites whose diameter was at least $30\,\mu\mathrm{m}$, which is three tenth of the resolution of FODI images by using the integrated signal captured from a laser-induced damage site to calculate the area and size of small sites [6].

However, due to apparent motions and lighting and background variations from one image to another, it is difficult to perform an efficient metrology of damage growth. These fluctuations modify the gray levels (*i.e.,* image intensity) of each pixel between successive acquisitions. Before any image correction, the registration residual map, which is the gray level

difference between a reference image and an image of the same optics acquired after some laser shots, is a function of apparent motions, lighting and background variations, damage growth and acquisition noise. A method to correct for motions as well as lighting and background variations was recently developed [8]. The corrections, which consist in spatial image registrations based on Digital Image Correlation principles [11] coupled with brightness and contrast corrections [12], make it possible to compare gray level variations of each pixel from one image to another. This technique is widely used in solid mechanics in order to monitor mechanical tests [11, 13, 14], to extract useful data for damage detection and quantification [15, 16]. In the present case, the first step is the measurement of the displacement field between a reference image and a set of images acquired after each laser shot. The second step consists in correcting for low order gray level variations that are due to lighting and background variations. After these corrections are carried out, the registration residual map becomes a function of damage growth and acquisition noise only. Pixels in the registration residual map that have higher gray levels than the noise level may be attributed to damage initiation or growth. This method may enable for earlier detection of potential damage sites than using the so-called LASNR algorithm.

The first aim of this chapter is to demonstrate the effectiveness of image registration with sub-pixel resolution performing registrations on images typical of final optics. The second objective is to estimate the smallest damage diameter variation that is noticeable and detectable on images with a $100\,\mu\mathrm{m}$/pixel resolution *via* two indicators: the measured diameter of a damage site and the registration residual map. It is proposed to use high resolution images (*i.e.,* $6.5\,\mu\mathrm{m}$/pixel) of a fused silica component that can be down-sampled to obtain similar low resolution images (*i.e.,* $100\,\mu\mathrm{m}$/pixel) of optics acquired at LMJ, NIF and SG-III. These high resolution images were acquired on a highly instrumented experimental laser setup (*i.e.,* MELBA [17–21]) designed to reproduce LMJ conditions of laser shots at the wavelength of $351\,\mathrm{nm}$ followed by image acquisitions.

The MELBA setup is described in Section 5.2. The noise level was estimated with and without displacements between acquisitions at high and low resolutions in Section 5.3. Sample and camera motions were applied in order to validate the registration algorithm based on digital image correlation principles on high and low resolution images (Section 5.4). Laser damage sites were initiated on the sample to estimate the smallest damage site visible at both resolutions (Section 5.5.1). One hundred laser shots were used to grow initiated laser damage sites. Detection

thresholds of damage growth were then estimated at both resolutions in Section 5.5.2. The present chapter is based on LMJ-like data but it is believed that the advantages of the method are valid for detecting and monitoring laser damage growth for laser damage metrology setup, for high energy laser facilities with needs of sub-pixel resolution, and possibly other configurations in which damage is suspected to occur.

5.2 Experimental setup

At the LMJ facility, images of optics are acquired by a camera, with the so-called MDCC system [2, 8], after each laser shot. The observation system is composed of two green LEDs placed near one edge of a vacuum window. Lighting provided by LEDs enters into the optics and illuminates rear and front sides of the component. Laser damage sites scatter light. A part of the scattered light from damage is collected by the MDCC camera focused on the front side of the vacuum window. A vacuum window is a $40\,\mathrm{cm}$x$40\,\mathrm{cm}$ fused silica optics with $34\,\mathrm{mm}$ thickness. The MDCC setup is shown in Figure 5.1 (a). The operating sequence is composed of three parts:

- The 35x$35\,\mathrm{cm}$ ultraviolet nanosecond laser beam irradiates the vacuum window with fluences ranging from 1 to $8\,\mathrm{J\,cm^{-2}}$. At these fluences, damage initiation and growth may occur [1].
- The MDCC module is placed at the center of the experiment chamber and oriented toward the vacuum window. The lighting system is switched on. Laser damage sites are visible. Images of the optics are acquired at $100\,\mu\mathrm{m}$/pixel resolution.
- The lighting system is switched off. Background images are acquired and subtracted from images of the optics. The MDCC module is removed from the experiment chamber.

The characterization optical (MELBA) setup has been widely used to study laser damage initiation and growth in order to understand and quantify laser-induced damage as functions of laser parameters [18, 20, 21]. This highly instrumented setup was used herein to reproduce the MDCC operating sequence but with high resolution images (*i.e.,* $6.5\,\mu\mathrm{m}$/pixel). MELBA is composed of a lighting system integrated to the sample holder, a high resolution camera that can be translated, and a nanosecond ultraviolet laser beam (Figure 5.1 (b)). The sample used for this experiment is a 10x$10\,\mathrm{cm}$ fused silica component with $34\,\mathrm{mm}$ thickness.

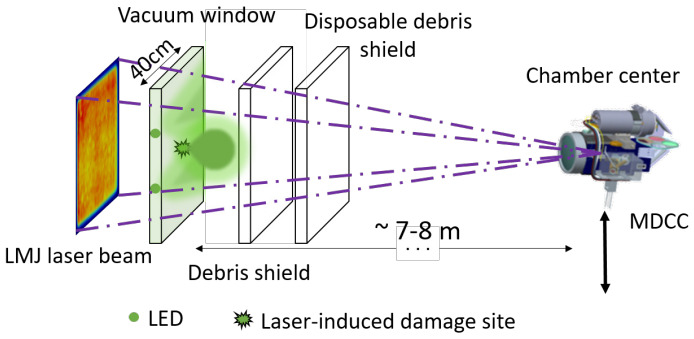

(a)

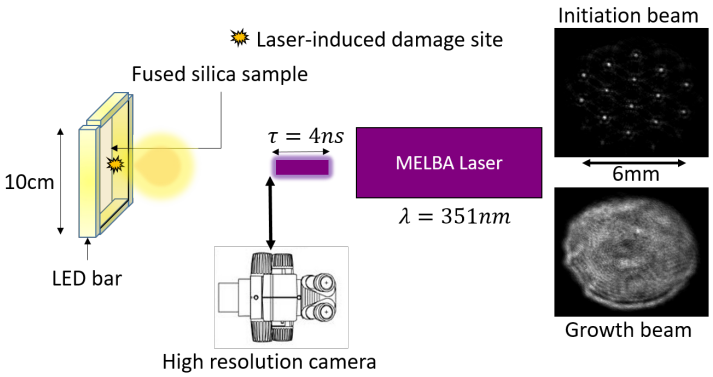

(b)

Figure 5.1: (a) MDCC image acquisition setup at LMJ with the path of the laser beam shown in purple dash-dotted line. (b) MELBA experimental setup with the spatial shape of two available nanosecond ultraviolet laser beams.

Table 5.1 compares the characteristics of the MDCC acquisition setup with those obtained with the MELBA setup. Both setups provide dark field images of a fused silica component. The MELBA camera can be moved horizontally. The position of the focal plane can also be adjusted. The sample holder allows for the following displacements: translations (vertical and horizontal directions), and rotation about the vertical axis. The spatial resolution of the MELBA camera is 15 times higher than that of the MDCC camera. This high resolution allows damage site diameters to be assessed very accurately.

In order to make LMJ vacuum window image registration possible, four fiducials were laser etched on each corner of the optics (in green boxes in Figure 5.2 (a)). These fiducials are craters made by ablation with a CO_2

Table 5.1: Characteristics of MDCC and MELBA setups.

Set-up	MDCC	MELBA
Lighting system	2 green LEDs	4 LED bars
Camera definition	4096×4096 pixels	1392×1040 pixels
Pixel depth	16 bits	8 bits
Image resolution	$100\,\mu m$/pixel	$6.5\,\mu m$/pixel
Imaged area	409x$409\,mm$	9x$6.8\,mm$

laser on the front face of the optics. They are used by the registration algorithm to perform displacement corrections between successive image acquisitions [8]. To mimic fiducials on the MELBA silica sample, laser damage sites were initiated in each corner of the imaged area (Figure 5.2 (b)). Four different patterns make it possible to distinguish each corner of the image. The intensity of the lighting system and the camera exposure time were chosen so that the markers did not saturate the sensor. These markers have a similar purpose as the random black and white speckle (Figure 5.2 (c)) widely used in digital image correlation [11].

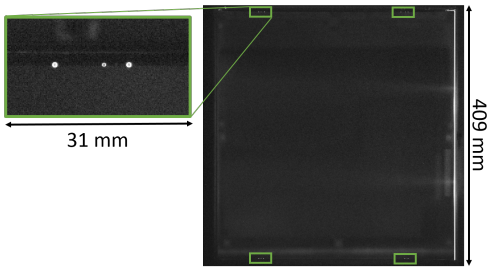

(a)

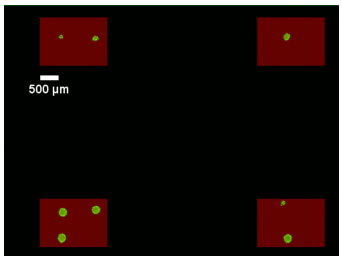

(b)

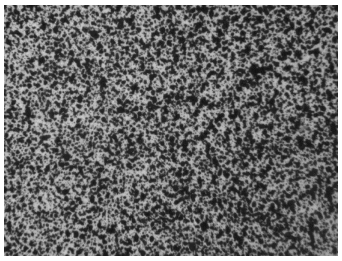

(c)

Figure 5.2: (a) MDCC vaccum window image with fiducials in green boxes. (b) MELBA image of the silica sample with markers in green color inside red boxes. (c) Random black and white pattern.

Two properties of the areas used for image registration purposes are summarized in Table 5.2. The mean image contrast is defined by

$$\sqrt{\langle \|\boldsymbol{\nabla} I_0\|_2^2} = \sqrt{\frac{1}{N_{pix}} \sum_{\boldsymbol{x}} \|\boldsymbol{\nabla} I_0(\boldsymbol{x})\|_2^2} \ , \tag{5.1}$$

where N_{pix} is the number of pixels in the region of interest, $\mathbf{x}$ the vector position of each considered pixel, and $\| \bullet \|_2$ the L_2-norm. In digital image correlation, it was shown that the standard displacement uncertainties are inversely proportional to the mean contrast [22]. Random (speckle) patterns are "image correlation friendly" as they usually cover the whole region of interest of the images to be registered, and provide high contrasts (Figure 5.2(c)). On the contrary, the areas used for spatial registrations of the optics images cover a much smaller part of the images, and do not correspond to the analysis area for damage detection and quantification. They also provide a lower contrast. The MELBA markers have similar properties as LMJ fiducials. The effectiveness of sub-pixel registration for MDCC images was evaluated using MELBA images as both configurations were similar. Despite these degraded situations, it will be shown that image registration of such images was possible and effective (Section 5.4).

Table 5.2: Characteristics of areas and mean contrast used for image registration purposes: random black and white pattern, MELBA markers and LMJ fiducials (Figure 5.2).

	Random pattern	**MELBA markers**	**LMJ fiducials**
Image area (%)	$100\ \%$	$15\ \%$	$1\ \%$
$\sqrt{\langle \|\boldsymbol{\nabla} I_0\|_2^2}$ *(gray level)*	28	2.8	6.9

In order to compare the effectiveness of measured diameters and registration residuals to detect small damage growth at high and low image resolutions, nanosecond ultraviolet laser shots were performed on the fused silica component using the MELBA setup. Two configurations were used:

- Damage initiation configuration (in magenta in Figure 5.3) – Before reaching the fused silica sample, the laser beam traversed an optical component composed of 19 phase rings in a hexagonal array that changes the fluence shape of the laser beam [19]. On the fused silica plane, the laser beam featured intense spots where fluences were

locally about $30\,\mathrm{J\,cm^{-2}}$. At these fluences, the probability of damage initiation tends toward unity [1, 21, 23].

- Damage growth configuration (in blue in Figure 5.3) – The fluence shape of the laser beam was more uniform than in the previous configuration since phase rings were removed from the laser path. The mean fluences ranged from 1 to $9\,\mathrm{J\,cm^{-2}}$ during the growth step. The growth threshold fluence was measured at about $5\,\mathrm{J\,cm^{-2}}$ for a pulse duration of $4\,\mathrm{ns}$ [24]. The damage growth threshold was overcome using the MELBA damage growth configuration.

In both configurations, the pulse duration was $4\,\mathrm{ns}$.

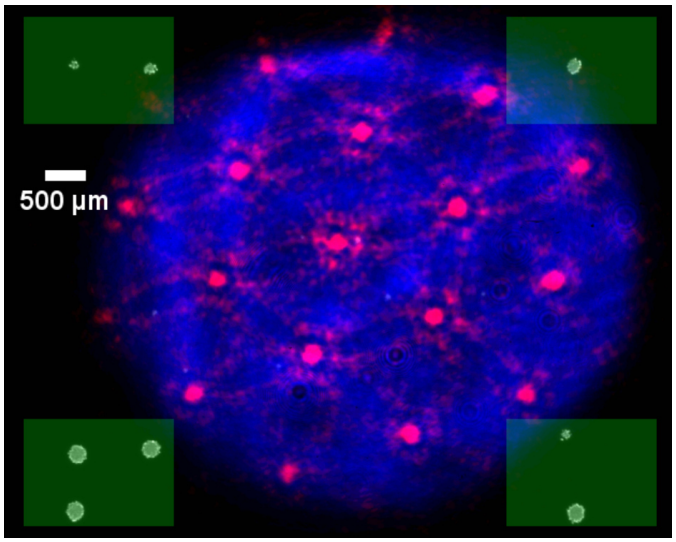

Figure 5.3: Composite image depicting the observed area of the fused silica sample by the high resolution camera. Initiated laser markers are displayed in light green. The area used for image registration purposes is represented as green boxes. The damage initiation beam is shown in magenta. The damage growth beam is shown in blue.

The results that will be reported in Sections 5.3 and 5.4 were obtained with no laser shot. The image of the fused silica sample contained only the registration markers. The results that will be reported in Section 5.5.1 were obtained by initiating laser damage sites with 3 laser shots in the MELBA damage initiation configuration. The objective was to estimate the smallest damage site detectable at $100\,\mu\mathrm{m}$/pixel resolution. The results that will be reported in Section 5.5.2 were obtained with one hundred laser shots in the damage growth configuration. The aim was to estimate the ability of the indicators to detect damage growth.

5.3 Uncertainty quantification

Since the MDCC is removed from the experiment chamber before each laser shot, it was necessary to quantify MELBA acquisition uncertainties with applied displacements between acquisitions. In order to estimate the minimum reachable registration residual level in the MELBA configuration, 100 images were acquired with no laser shot; 20 among them with no applied displacement. Consequently, the Root Mean Square (RMS) residual should be at the noise level if the positions of the camera and the sample holder were perfectly stable. This acquisition sequence with no displacement corresponds to images 0 to 19. Image 0 was considered as the reference. 80 images were acquired after a prescribed displacement and automatic return to the reference position of the camera between each acquisition. This second configuration with camera translations between acquisitions mimics the acquisition process at LMJ. If the mechanical return were perfect, the RMS residual should also be at the noise level. This sequence corresponds to images 20 to 99.

The image registration algorithm used herein is based on the gray level conservation hypothesis [11]

$$I_0(\boldsymbol{x}) = I_n(\boldsymbol{x} + \boldsymbol{u}(\boldsymbol{x})), \tag{5.2}$$

where I_0 is the reference image, I_n the "deformed" image, $\boldsymbol{x}$ the pixel position, and $\boldsymbol{u}$ the sought displacement vector between the reference and deformed configurations. The aim of the registration procedure is to estimate the displacement field $\boldsymbol{u}(\boldsymbol{x})$ that minimizes, over the four marker areas (green zones in Figure 5.3), the L_2 norm of the registration residual ρ defined as

$$\rho(\boldsymbol{x}) = I_0(\boldsymbol{x}) - I_n(\boldsymbol{x} + \boldsymbol{u}(\boldsymbol{x})). \tag{5.3}$$

The measured displacement field $\boldsymbol{u}$ is written as a linear combination of in-plane horizontal and vertical translations, rotation about the optical axis and scaling. The four degrees of freedom correspond to those of a similarity transformation, which is a particular case of homography transformations [25]. The image registration procedure follows two steps.

- First, an initialization is used to coarsely estimate large displacements. A correlation product in log-polar coordinates between the Fourier transforms of the reference image and a deformed image provides the rotation angle and the scaling factor [26]. The horizontal and vertical translations are estimated using a correlation product in Cartesian coordinates. This coarse displacement estimation ensures the convergence of the next step.

- Second, a registration residual minimization is performed to measure with sub-pixel resolution the displacement amplitudes that minimize the L_2-norm of the registration residual over the fiducial/marker areas. This minimization follows an iterative scheme where a linear system is solved at each iteration. After each iteration, a new picture of the corrected image is generated by using the current estimation of the displacement field. Thanks to gray level interpolation schemes, sub-pixel resolutions are achieved [22]. The iterative procedure ends when the norm of the displacement amplitude corrections become less than 10^{-3} pixel in the present case. At convergence, a registered image $I_n(\boldsymbol{x} + \boldsymbol{u}(\boldsymbol{x}))$ is obtained.

More details on the implemented image registration algorithm can be found in Refs. [8, 27]. This registration algorithm was chosen because it provided sub-pixel resolution on the displacement field estimation. In the present case, neither brightness nor contrast corrections were performed.

The image registration algorithm was applied to the whole image set described above. RMS residuals without any correction (*i.e.,* $\rho(\boldsymbol{x}) = I_0(\boldsymbol{x}) - I_n(\boldsymbol{x})$) and after image registration (*i.e.,* $\rho(\boldsymbol{x}) = I_0(\boldsymbol{x}) - I_n(\boldsymbol{x} + \boldsymbol{u}(\boldsymbol{x}))$) are shown as functions of image number in Figure 5.4 (a). The initial residual between images 0 to 19 was about 0.1 % of the dynamic range of the reference picture. After image registration, the RMS residual was very close to this level. In the case with no prescribed displacement, the benefits of image registration were small (as expected). This result confirms that acquisition noise is about 0.1 % of the dynamic range.

When there were camera motions and automatic return between each acquisition (from images 20 to 99), the initial RMS residuals increased to reach a level up to 0.4 % of the dynamic range. This RMS change indicated that there was a difference between the reference image and the following ones. After spatial image registration, the RMS residual returned to the minimum level for images 1 to 99, thereby indicating that spatial registration was successful. The measured translations, rotation and scaling are plotted as functions of image number in Figure 5.4 (b-d). It is worth noting that non-zero displacement amplitudes were found not only for images 20 to 99 but also for images 1 to 19 for which no camera translations were prescribed. The measured displacements between each acquisition gave access to the measurement uncertainties associated with the whole optical setup and registration algorithm. The observed displacements were mainly due to translations since the rotation angle was equal to 0 on average with a standard deviation of 0.001°, and the scaling factor was equal to 1 with a negligible standard deviation. The

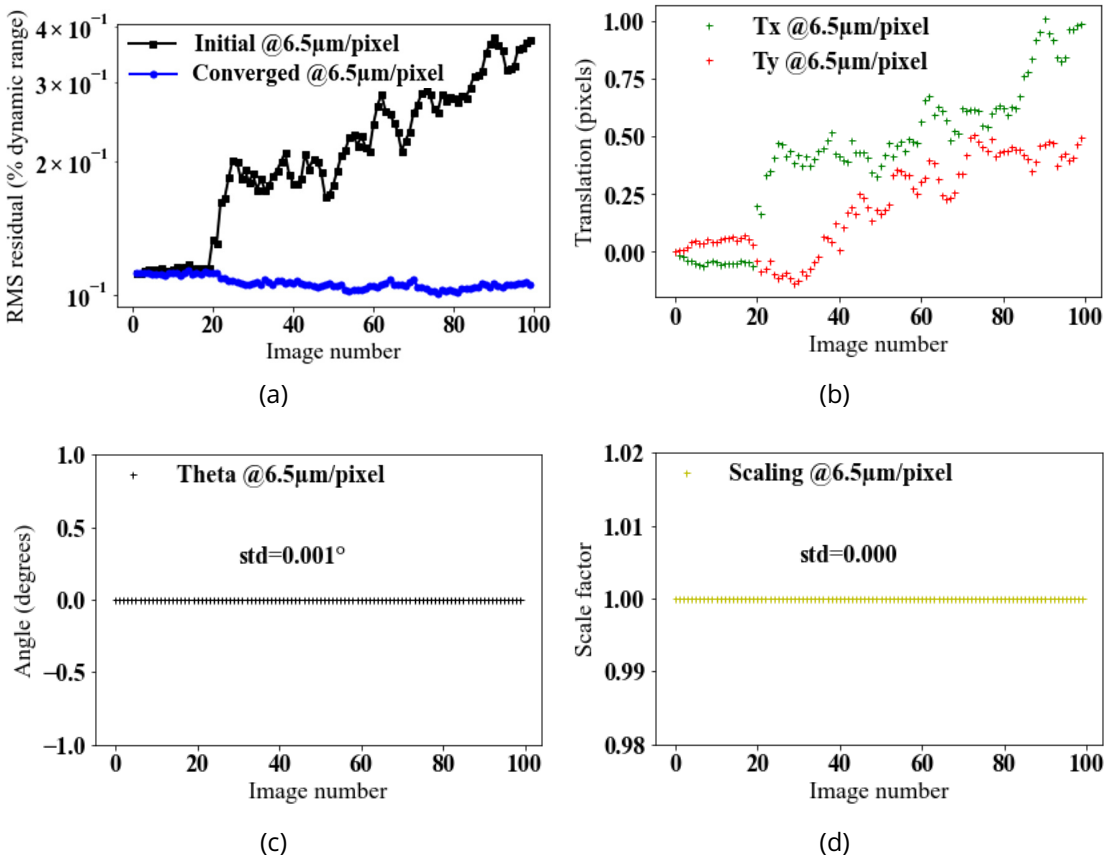

Figure 5.4: Measurement results for the image set at high resolution ($6.5\,\mu\mathrm{m}$/pixel) to estimate uncertainties. (a) RMS residual between the reference image 0 and all images of the set before correction and after image registration. Measured translations (b), rotations (c) and scale factor (d) as functions of image number.

measured translation amplitudes indicated that a drift occurred between the silica sample and the camera throughout the acquisition sequence. Image registration using digital image correlation principles made it possible to correct such displacement drift even if its amplitude was less than one pixel.

All these measurements indicate that the lowest RMS residual in this configuration was about 0.1 % of the dynamic range. Image changes that induce RMS residuals less than this threshold cannot be detected. It was also shown that the automatic return to the reference position corresponding to images 20 to 99 was not perfect. After 70 acquisitions

without image registration, the displacement amplitude was greater than 1 pixel. To detect accurately damage initiation and growth in this configuration of the MELBA setup and consequently with the MDCC system, an efficient sub-pixel image registration method was needed to account for such small kinematic drifts [8].

In order to estimate the minimum reachable RMS residual at MDCC resolution ($100\,\mu\mathrm{m}$/pixel), a binning with a factor 15 was applied to the image set acquired at high resolution. Low resolution images were registered using the same registration code. At this resolution, the lowest RMS residual was ca. $0.02\ \%$ of the dynamic range (Figure 5.5 (a)). For images 20 to 99, the registrations lowered the residuals but their level did not reach that of acquisition noise. This difference was due to the pixel displacement amplitudes that became 15 times smaller for low resolution images than for high resolution images.

The measured displacements on low resolution images were in agreement with those obtained on high resolution images. Despite low resolution images, the translation and scale levels between acquisitions were well estimated (Figure 5.5 (b,d)). However, the measured rotation fluctuation at low resolution (Figure 5.5 (c)) was twice that at high resolution (Figure 5.4 (c)).

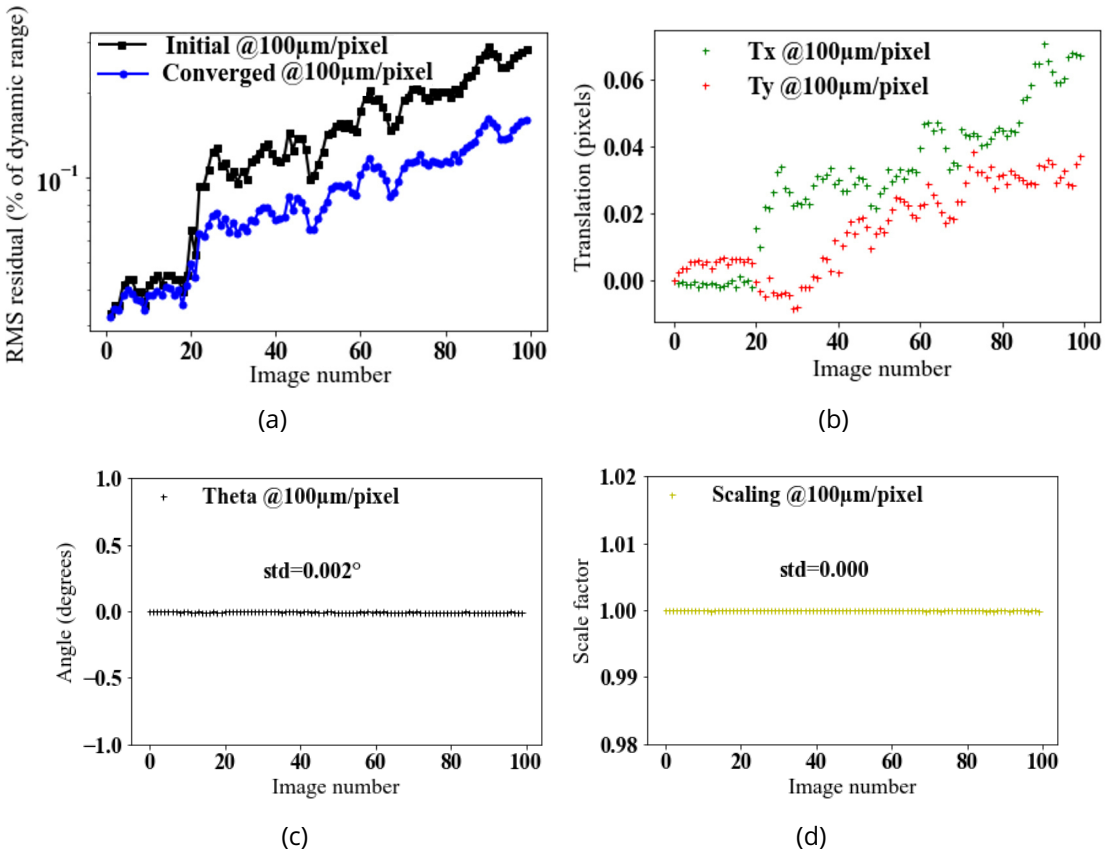

Figure 5.5: Measurement results for the image set at low resolution ($100\,\mu\mathrm{m}$/pixel) to estimate uncertainties. (a) RMS residual between the reference image 0 and all images of the set before correction and after image registration. Measured translations (b), rotations (c) and scale factor (d) as functions of image number.

5.4 Displacement corrections

In order to further check the effectiveness of the sub-pixel resolution of the registration algorithm, another image set was acquired with prescribed translations along the horizontal, vertical and longitudinal axis. Displacements between images were selected as follows:

- Images 0 to 9: Horizontal translation of $30\,\mu\mathrm{m}$.
- Images 10 to 19: Vertical translation of $40\,\mu\mathrm{m}$.
- Images 20 to 99: Longitudinal translation every 10 images. This

displacement blurs images when longitudinal translations are greater than the depth of field.

The results of high resolution image registration are shown in Figure 5.6. For this image set, the initial RMS residuals were greater than $1\ \%$ of the dynamic range. After registration of the first 30 images, the RMS residual was very close to the minimum level. For these images, the displacements were very well corrected and the registered images were nearly identical to the reference (up to acquisition noise). For the following images, the RMS residuals after registration were lower than their initial levels, but greater than the baseline. After each longitudinal displacement step, the residuals increased. The longitudinal displacement step was chosen to be about one half of the camera depth of field. As a consequence, the markers began to be blurred after image 30 when the depth of field was reached.

The measured translations for images 0 to 19 were consistent with the prescribed displacements. As rotations about the optical axis were not performed, the measured rotation angle was equal to 0 with a standard deviation of $0.002°$ (Figure 5.6 (c)), which is twice that reported earlier (Figure 5.4 (c)) for the same image resolution. This higher uncertainty in the rotation measurement appears to stem from the fact that the images used for the present study began to be blurred from image number 30 on. As the images became less sharp, the contrast of the markers used for image registration decreased. As a result, the accuracy of rotation measurements was reduced but was still low.

The measured scaling factor was equal to 1 before image 20 and increased every 10 images from images 20 to 99 (Figure 5.6 (d)). A consequence of prescribing longitudinal displacements was the measurement of horizontal and vertical translations (Figure 5.6 (b)). These motions were due to misalignment between the optical axis of the camera and the normal to the sample surface.

Displacements on low resolution images of this set were also measured. The estimated translations at high resolution are plotted as functions of those at low resolution in Figure 5.7. The expected factor 15 between the two resolutions was nearly obtained (*i.e.,* $6.5\,\mu\mathrm{m}$/pixel and $100\,\mu\mathrm{m}$/pixel). Higher uncertainties were observed for y translations than for x translations between high and low resolutions due to smaller amplitudes in the y-direction. These results confirmed that the registration algorithm was effective to correct for displacements between images with sub-pixel resolution by performing the residual minimization on the four corners that contained markers.

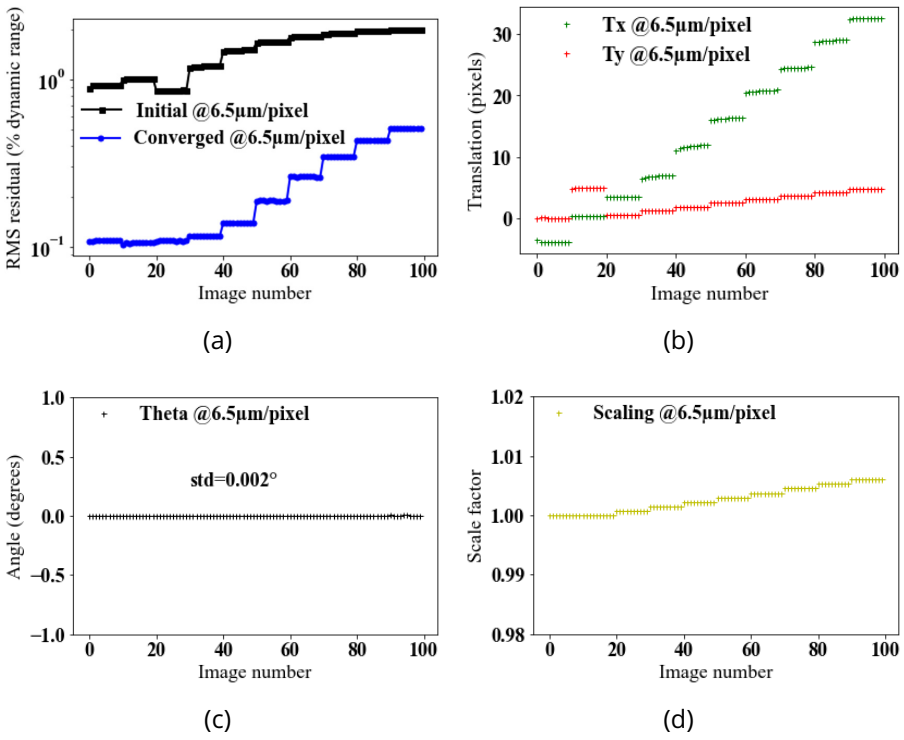

Figure 5.6: Displacement measurements for an image set with a resolution of $6.5\,\mu\mathrm{m}$/pixel. (a) RMS residuals before correction and after image registration. Measured translations (b), rotations (c) and scale factor (d).

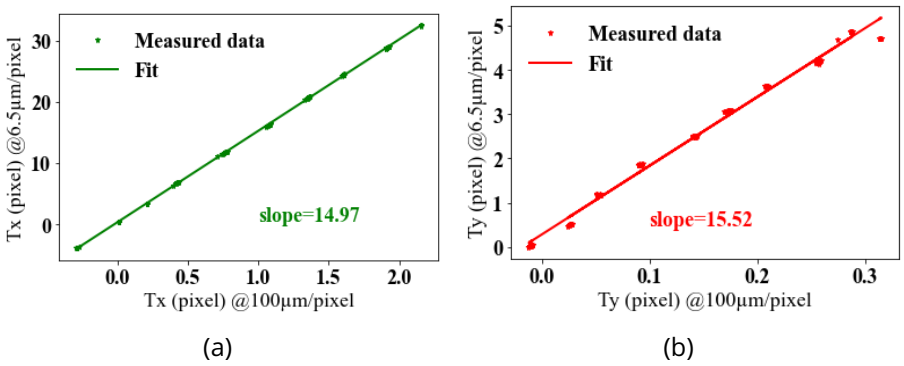

Figure 5.7: Measured x (a) and y (b) translations at high resolution as functions of measured translations at low resolution. The measured slopes are about 15 as expected from the resolution change.

5.5 Damage detection and quantification

In order to estimate the minimum diameter of damage sites that can be detected, a series of ultraviolet laser shots was performed on the fused silica sample. Images of the sample surface were acquired after each laser shot. Lighting conditions were the same as those used for the quantification of uncertainties. The reference image was that of the sample before the initiation shot. The acquisition procedure was the same as the sequence described previously (images 20 to 99), namely, an image of the sample surface was acquired, then the camera was moved to allow the laser to irradiate the sample. After each laser shot, an automatic return to the initial position was applied to the camera. A new image of the sample was acquired.

Between images 0 and 1, three (initiation) laser shots were performed to initiate 29 laser-induced damage sites. The damage diameter was estimated on high resolution (thresholded) images. The threshold was chosen to be slightly higher than the acquisition noise level (*i.e.,* 2 gray levels). The acquisition noise level is defined as the intensity fluctuation due to the acquisition system. The noise level for the high resolution images was estimated on a 100×100-pixel undamaged area in the reference image. The mean value was 0.95 gray level and its standard deviation 0.21 gray level. The equivalent diameter is that of a disk that has the same area as the damage site. Sixteen damage sites had an equivalent diameter less than $50\,\mu\mathrm{m}$, 10 sites an equivalent diameter ranging from $50\,\mu\mathrm{m}$ to $100\,\mu\mathrm{m}$, and 3 sites an equivalent diameter greater than $100\,\mu\mathrm{m}$. After image 1, the laser beam was used for the growth sequence. The corresponding mean fluences are reported in Figure 5.8. The fluence level was gradually increased to reach a maximum mean of about $8\,\mathrm{J\,cm^{-2}}$, which is representative of fluences that may hit the final optics of high energy laser facilities [28].

5.5.1 Damage initiation

The RMS residuals at high and low image resolutions are shown in Figure 5.8. The initial levels depended on displacement, damage initiation and growth, as well as acquisition noise. After image registration, the corresponding residual was no longer due to displacements but only to damage and acquisition noise. At the resolution of $6.5\,\mu\mathrm{m}$/pixel, the RMS residual corresponding to acquisition noise was $0.1\ \%$ of the dynamic range. After image registration, the RMS residual corresponding to the

initially damaged sample was about $0.25\ \%$ of dynamic range at high and low resolutions. This value was greater than the threshold corresponding to acquisition noise. The global residual indicated that the initiation sequence was detected at both resolutions.

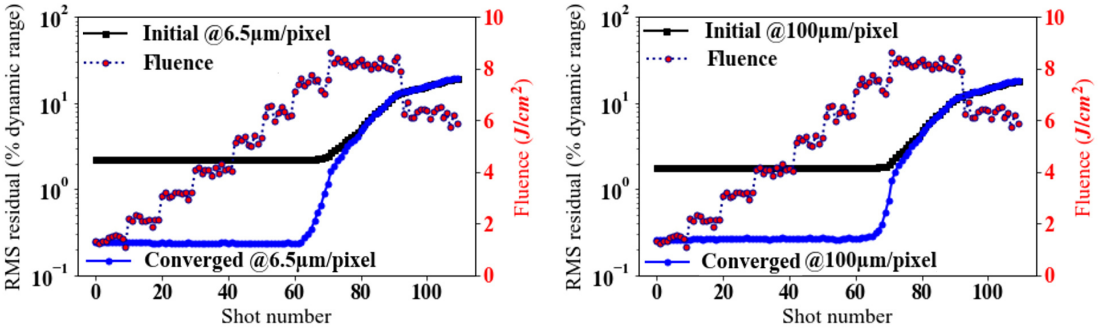

(a) (b)

Figure 5.8: Mean fluence of the shots inducing damage initiation and growth. RMS residuals obtained before and after image registration and laser beam fluence (a) at high resolution ($6.5\,\mu$m/pixel) and (b) low resolution ($100\,\mu$m/pixel).

Figure 5.9 (a) shows the cumulative number of detected damage sites after initiation at high and low resolutions. The number at high resolution was considered as the reference. The smallest detected damage site at low resolution had an equivalent diameter of $53\,\mu$m. When the diameter of a damage site was greater than $100\,\mu$m, all initiated damage sites were detected at low resolution, whereas no damage site out of 16 was detected when its diameter was less than $50\,\mu$m. When the diameter varied from $50\,\mu$m to $100\,\mu$m, 8 sites out of 10 were detected (Figure 5.9 (b)). The smallest diameter detectable at low resolution was about $50\,\mu$m. This value is close to the detection performance announced to be at least $30\,\mu$m for FODI [6].

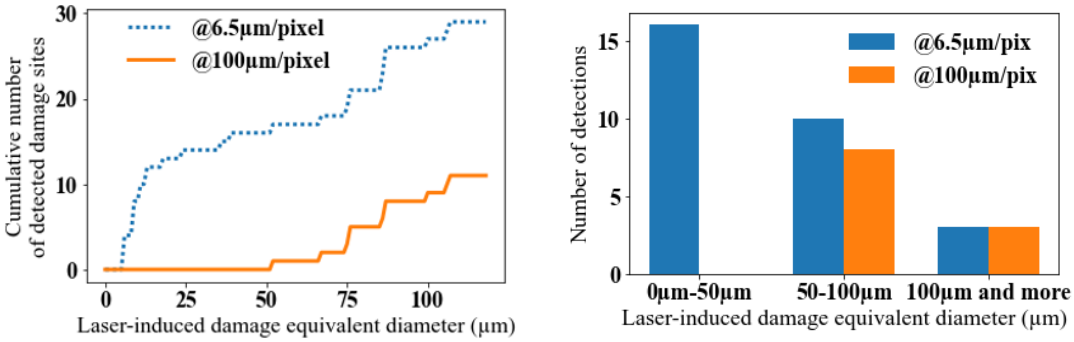

(a) (b)

Figure 5.9: (a) Cumulative number of initiated damage sites detected at high and low resolutions as function of damage site diameter. (b) Number of initiated damage sites detected at high and low resolutions as functions of damage site diameter.

5.5.2 Damage growth

Among the 29 initiated damage sites, 4 sites grew during the growth sequence (Figure 5.10).

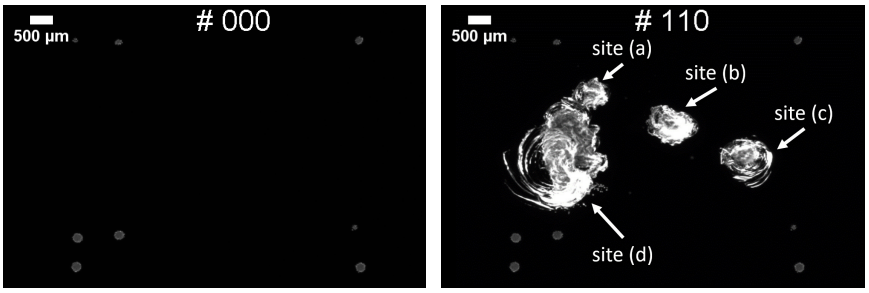

(a) (b)

Figure 5.10: Acquired images of the sample at high resolution (a) before damage growth (# 000) and (b) after the last laser shot (# 110). Four damage sites grew during the growth sequence.

The equivalent diameters of each growing site at low and high resolutions were measured (Figure 5.11). The four damage sites grew after a different number of laser shots. It was observed that the diameters at high resolution related to damage growth before those at low resolution. The average delay of damage growth detection at high and low resolutions was about 1 laser shot for fluences varying between 6 and $8\,\mathrm{J\,cm^{-2}}$.

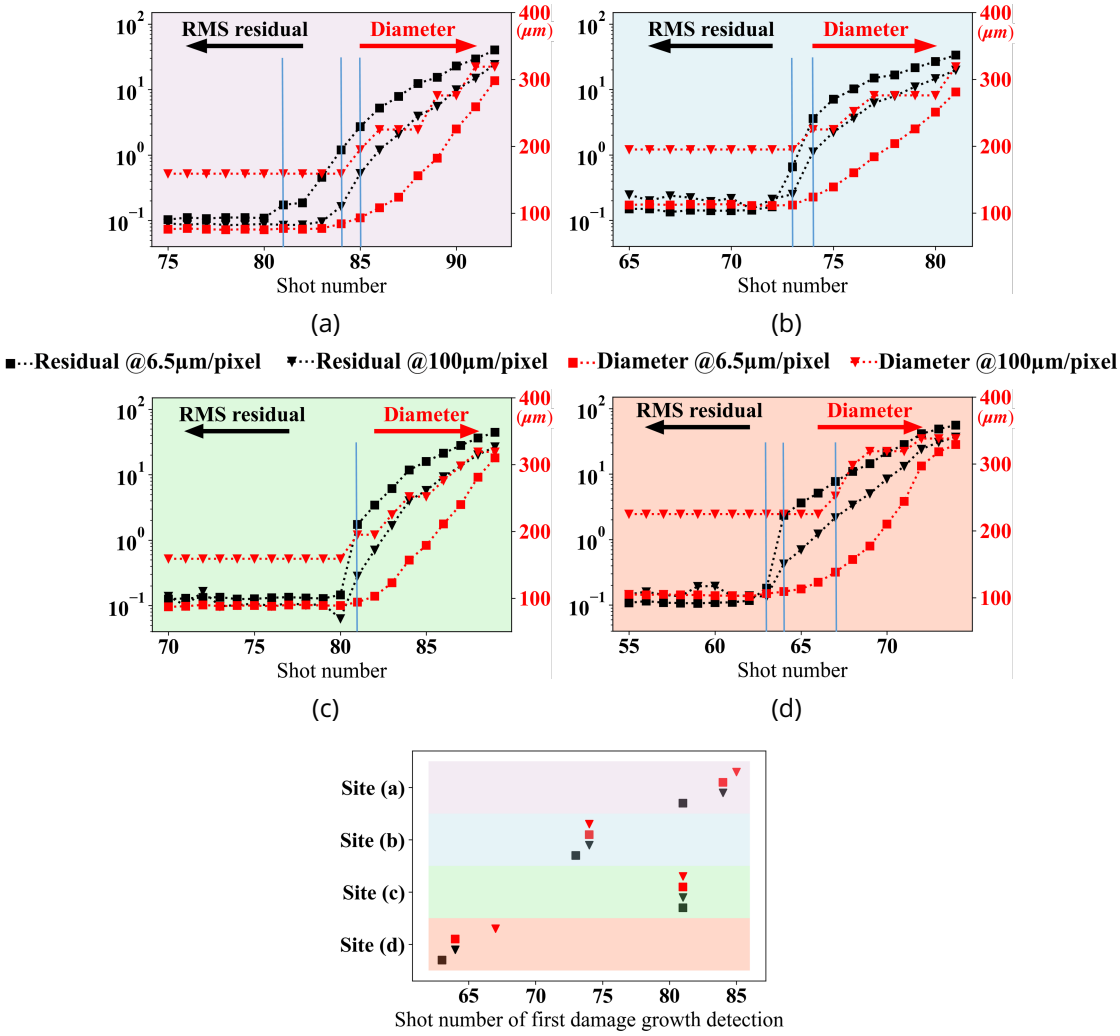

Figure 5.11: RMS registration residual (% of dynamic range) measured on 45×45-pixel areas centered about the four growing damage sites (a-d) at high resolution (dotted black line with black square markers) and on the corresponding area at low resolution (dotted black line with black triangles) as functions of shot number. Changes of equivalent diameters (in $\mu\mathrm{m}$) of damage sites at high resolution (red dotted line with red crosses) and at low resolution (red dotted line with red diamonds). The blue vertical lines indicate the first laser shot where damage growth was detected using each criterion. (e) Shot numbers of first damage growth detection for the four sites and for each growth indicator. The detection threshold for the measured diameters was a variation between two successive acquisitions greater than $6\,\mu\mathrm{m}$. For the RMS registration residuals, the detection threshold was a variation between two successive acquisitions greater than 0.1 % of dynamic range corresponding to acquisition noise.

In addition to this delay, the measured diameter at low resolution was overestimated compared to high resolution results for diameters less than $300\,\mu\mathrm{m}$. The growth rate at low resolution was different from that at high resolution since some false plateaus occurred.

The Pearson coefficient measures the correlation between two data sets [29, 30]. This coefficient was assessed between the four growth indicators (*i.e.,* diameter at high and low image resolutions and registration residual at both resolutions) for the four growing damage sites. The correlation coefficient between the growth indicators was measured on the laser shot intervals shown in Figure 5.11. These intervals were chosen to include the onset of damage growth. The Pearson correlation coefficient between low and high resolution diameters was equal to 0.927 on average for the four growing sites (Table 5.3). Thus the diameter at low resolution was not a perfect indicator for damage growth when the damage site was smaller than $300\,\mu\mathrm{m}$ in diameter.

Table 5.3: Pearson correlation coefficients measured between different indicators used to detect laser damage growth. The strongest correlation is between the measured damage diameter at $6.5\,\mu\mathrm{m}$/pixel and RMS residual at the same resolution. The lowest correlation is between measured damage diameters at $6.5\,\mu\mathrm{m}$/pixel and $100\,\mu\mathrm{m}$/pixel resolutions.

Correlated quantities	**Site (a)**	**Site (b)**	**Site (c)**	**Site (d)**	**Mean**
Diameter @$6.5\,\mu$m/pixel and diameter @$100\,\mu$m/pixel	0.873	0.933	0.967	0.933	$\mathbf{0.927}$
Diameter @$6.5\,\mu$m/pixel and RMS residual @$6.5\,\mu$m/pixel	0.995	0.997	0.998	0.995	$\mathbf{0.996}$
Diameter @$6.5\,\mu$m/pixel and RMS residual @$100\,\mu$m/pixel	0.959	0.989	0.976	0.968	$\mathbf{0.973}$
RMS residual @$6.5\,\mu$m/pixel and RMS residual @$100\,\mu$m/pixel	0.980	0.988	0.987	0.986	$\mathbf{0.985}$

As images were registered, it was possible to analyze gray level variations of each pixel between each laser shot. The RMS residuals were measured on 45×45-pixel areas centered about each damage site at high resolution and on the corresponding 3×3-pixel areas at low resolution (Figure 5.11). The Pearson correlation coefficient between measured diameters and RMS residuals at high resolution was equal to 0.996 on average (Table 5.3). This high level establishes a strong link between damage growth and high resolution RMS residuals. This value was not exactly one because RMS residuals contained not only damage information but also gray level

variations of pixels belonging to a damage site. As shown in Figure 5.11, damage growth was detected on RMS residuals at high resolution "1.25 laser shot" (on average) prior to similar detection at low resolution.

The Pearson coefficient between measured diameters at high resolution and RMS residuals at low resolution was about 0.973 (Table 5.3). This correlation level validates the link between damage growth and low resolution RMS residuals. The Pearson coefficient between low resolution RMS residuals and high resolution damage diameters was higher than that between low and high resolution damage diameters. It thus is better to use low resolution RMS residuals than low resolution damage diameters to detect efficiently damage growth. It is worth noting that there was no delay between the onset of damage growth observed on the measured diameters at high resolution and on the RMS residuals at low resolution. Hence, damage growth measurement via RMS residuals at low resolution was at least as effective as damage diameter measurement at high resolution.

The best indicator for damage growth between the four presented cases was the RMS residual at high resolution. With that indicator, it was possible to detect variations of damage diameters less than $9\,\mu\mathrm{m}$ (Table 5.4). The smallest variations of damage diameter were provided for each growth indicator by calculating the damage variation measured with high resolution images at the laser shot where damage growth was observed with each indicator. The worst indicator was the measured diameter with the resolution of $100\,\mu\mathrm{m}$/pixel. The smallest damage variation observable with this indicator was $18\,\mu\mathrm{m}$. The measured diameters at $6.5\,\mu\mathrm{m}$/pixel resolution were as efficient as the RMS residuals at $100\,\mu\mathrm{m}$/pixel with the smallest detectable damage diameter variation of $9\,\mu\mathrm{m}$.

Table 5.4: Smallest diameter variation observed for each damage site with the measured diameter at $6.5\,\mu\mathrm{m}$/pixel and $100\,\mu\mathrm{m}$/pixel, the RMS residual at $6.5\,\mu\mathrm{m}$/pixel and $100\,\mu\mathrm{m}$/pixel.

Damage growth indicator	**Site (a)**	**Site (b)**	**Site (c)**	**Site (d)**	**Mean**
Diameter @6.5 µm/pixel	$8\,\mu\mathrm{m}$	$11\,\mu\mathrm{m}$	$7\,\mu\mathrm{m}$	$8\,\mu\mathrm{m}$	$9\,\mu\mathrm{m}$
Diameter @100 µm/pixel	$8\,\mu\mathrm{m}$	$11\,\mu\mathrm{m}$	$7\,\mu\mathrm{m}$	$34\,\mu\mathrm{m}$	$15\,\mu\mathrm{m}$
RMS residual @6.5 µm/pixel	$< 8\,\mu\mathrm{m}$	$< 11\,\mu\mathrm{m}$	$< 7\,\mu\mathrm{m}$	$< 8\,\mu\mathrm{m}$	$< 9\,\mu\mathrm{m}$
RMS residual @100 µm/pixel	$8\,\mu\mathrm{m}$	$11\,\mu\mathrm{m}$	$7\,\mu\mathrm{m}$	$8\,\mu\mathrm{m}$	$9\,\mu\mathrm{m}$

5.6 Conclusion

For the first time, a highly instrumented laser setup was used to quantify the effectiveness of a new damage growth indicator based on registration residual fields. This indicator probes the quality of sub-pixel image registration (*i.e.,* offsets to the gray level conservation). The displacement estimation used for this registration was sufficiently robust by using no more than 15% of the full image surface and a rather low contrast, which were well below what is classically encountered in digital image correlation applications.

Two image resolutions were compared to detect damage initiation and growth. High resolution images were used as ground truth. The low image resolution corresponded to those of imaging systems used in high energy laser facilities such as NIF, SG-III and LMJ. At low image resolution, it was shown that the smallest initiated damage site that could be detected using the RMS registration residual was about $50\,\mu\mathrm{m}$ (*i.e.,* half of the image resolution). This value is close to the detection performance reported for FODI (at NIF).

Further, it was shown that the registration residual could be used as an efficient laser damage growth indicator since it outperformed the widely used diameter measurement at both resolutions. After image registration and using the registration residual as damage growth indicator, it was possible to detect $9\,\mu\mathrm{m}$ damage diameter variations at the resolution of $100\,\mu\mathrm{m}$/pixel. This damage diameter variation was validated with the measurements at $6.5\,\mu\mathrm{m}$/pixel resolution, and with the RMS registration residuals at $100\,\mu\mathrm{m}$/pixel resolution. Yet, it was not detectable when measuring diameters at $100\,\mu\mathrm{m}$/pixel resolution.

These results pave the way toward a novel and more sensitive approach for detecting the initiation and growth of laser damage sites. The registration residuals were a powerful tool to capture the onset of damage growth in accordance with the needs of fusion scale high energy laser systems. The registration residual also provided improved resolution and allowed damage sites to be detected when smaller than the size of a single pixel of the imaging system. Even though applied to the monitoring of laser-induced damage, the proposed indicator may be utilized in other situations in which damage is suspected to occur.

References

[1] K. Manes, M. Spaeth, J. Adams, and M. Bowers, "Damage mechanisms avoided or managed for nif large optics," *Fusion Science and Technology*, vol. 69, pp. 146–249, Feb. 2016. doi: 10.13182/FST15-139.

[2] C. Lacombe *et al.*, "Dealing with LMJ final optics damage: post-processing and models," in *Laser-induced Damage in Optical Materials 2020*, C. W. Carr, V. E. Gruzdev, D. Ristau, and C. S. Menoni, Eds., International Society for Optics and Photonics, vol. 11514, SPIE, 2020. doi: 10.1117/12.2571074. [Online]. Available: https://doi.org/10.1117/12.2571074.

[3] P. Cormont *et al.*, "Relevance of Carbon Dioxide Laser to Remove Scratches on Large Fused Silica Polished Optics," *Advanced Engineering Materials*, 2014.

[4] T. Doualle *et al.*, "CO2 laser microprocessing for laser damage growth mitigation of fused silica optics," *Optical Engineering*, vol. 56, no. 1, pp. 1–9, 2016. doi: 10.1117/1.OE.56.1.011022.

[5] L. Mascio-Kegelmeyer, "Machine learning for managing damage on NIF optics," in *Laser-induced Damage in Optical Materials 2020*, C. W. Carr, V. E. Gruzdev, D. Ristau, and C. S. Menoni, Eds., International Society for Optics and Photonics, vol. 11514, SPIE, 2020. doi: 10.1117/12.2571016. [Online]. Available: https://doi.org/10.1117/12.2571016.

[6] A. Conder, J. Chang, L. Kegelmeyer, M. Spaeth, and P. Whitman, "Final optics damage inspection (FODI) for the National Ignition Facility," in *Optics and Photonics for Information Processing IV*, A. A. S. Awwal, K. M. Iftekharuddin, and S. C. Burkhart, Eds., International Society for Optics and Photonics, vol. 7797, SPIE, 2010, pp. 167–178. doi: 10.1117/12.862596. [Online]. Available: https://doi.org/10.1117/12.862596.

[7] F. Wei *et al.*, "Automatic classification of true and false laser-induced damage in large aperture optics," *Optical Engineering*, vol. 57, no. 5, pp. 1–11, 2018. doi: 10.1117/1.OE.57.5.053112. [Online]. Available: https://doi.org/10.1117/1.OE.57.5.053112.

[8] G. Hallo, C. Lacombe, J. Néauport, and F. Hild, "Detection and Tracking of Laser Damage Sites on Fused Silica Components by Digital Image Correlation," *Optics and Lasers in Engineering*, vol. 146, p. 106 674, 2021.

[9] L. Kegelmeyer, P. Fong, S. Glenn, and J. Liebman, "Local area signal-to-noise ratio (lasnr) algorithm for image segmentation," *Proceedings of SPIE - The International Society for Optical Engineering*, vol. 6696, Oct. 2007. doi: 10.1117/12.732493.

[10] F. Bo, C. Fengdong, L. Bingguo, and L. Guodong, "Segmentation of small defects in Final Optics Damage Online Inspection images," in *2012 International Conference on Image Analysis and Signal Processing*, Nov. 2012, pp. 1–4. doi: 10.1109/IASP.2012.6425003.

[11] M. A. Sutton, J.-J. Orteu, and H. W. Schreier, *Image Correlation for Shape, Motion and Deformation Measurements - Basic Concepts, Theory and Applications*. Springer Science, 2009, isbn: 978-0-387-78746-6. doi: 10.1007/978-0-387-78747.

[12] F. Hild and S. Roux, "Digital image correlation," in *Optical Methods for Solid Mechanics. A Full-Field Approach*, P. Rastogi and E. Hack, Eds., Weinheim (Germany): Wiley-VCH, 2012, pp. 183–228.

[13] P. Rastogi and E. Hack, *Optical Methods for Solid Mechanics: A Full-Field Approach*. Weinheim Wiley-VCH-Verl. 2012, Jun. 2012, isbn: 978-3-527-41111-5.

[14] M. A. Sutton, "Computer Vision-Based, Noncontacting Deformation Measurements in Mechanics: A Generational Transformation," *Applied Mechanics Reviews*, vol. 65, no. 5, Aug. 2013, issn: 0003-6900. doi: 10.1115/1.4024984. eprint: https://asmedigitalcollection.asme.org/appliedmechanicsreviews/article-pdf/65/5/050802/6073861/amr_65_05_050802.pdf. [Online]. Available: https://doi.org/10.1115/1.4024984.

[15] F. Hild and S. Roux, "Handbook of damage mechanics," in Springer, 2015, ch. Evaluating Damage with Digital Image Correlation: A. Introductory Remarks and Detection of Physical Damage, pp. 1255–1275.

[16] G. Z. Voyiadis, *Handook of Damage Mechanics*. Springer Science, 2015.

[17] M. Veinhard, O. Bonville, R. Courchinoux, R. Parreault, J.-Y. Natoli, and L. Lamaignère, "MELBA: a fully customizable laser for damage experiments," in *Laser-Induced Damage in Optical Materials 2017*, G. J. Exarhos, V. E. Gruzdev, J. A. Menapace, D. Ristau, and M. Soileau, Eds., International Society for Optics and Photonics, vol. 10447, SPIE, 2017, pp. 151–157. [Online]. Available: https://doi.org/10.1117/12.2281125.

[18] M. Chambonneau and L. Lamaignère, "Multi-wavelength growth of nanosecond laser-induced surface damage on fused silica gratings," *Scientific Reports*, vol. 8, pp. 1–10, Jan. 2018. doi: 10.1038/s41598-017-18957-9.

[19] L. Lamaignère *et al.*, "A powerful tool for comparing different test procedures to measure the probability and density of laser induced damage on optical materials," *Review of Scientific Instruments*, vol. 90, no. 12, 125102, p. 125 102, Dec. 2019. doi: 10.1063/1.5122274.

[20] L. Lamaignère *et al.*, "Damage probability versus damage density: analysis from tests using small beams versus large beams," in *Laser-induced Damage in Optical Materials 2020*, C. W. Carr, V. E. Gruzdev, D. Ristau, and C. S. Menoni, Eds., International Society for Optics and Photonics, vol. 11514, SPIE, 2020, pp. 1–15. doi: 10.1117/12.2571834. [Online]. Available: https://doi.org/10.1117/12.2571834.

[21] M. Veinhard *et al.*, "Parametric study of laser-induced damage growth in fused silica optics with large beams at 351nm. Part 1: stochastic approach," *Appl. Opt.*, vol. 59, no. 31, pp. 9643–9651, Nov. 2020. doi: 10.1364/AO.400691. [Online]. Available: http://ao.osa.org/abstract.cfm?URI=ao-59-31-9643.

[22] F. Hild and S. Roux, "Comparison of local and global approaches to digital image correlation," *Experimental Mechanics*, vol. 52, no. 9, pp. 1503–1519, 2012.

[23] L. Lamaignère, G. Dupuy, A. Bourgeade, A. Benoist, A. Roques, and R. Courchinoux, "Damage growth in fused silica optics at 351 nm: refined modeling of large-beam experiments," *Applied Physics B: Lasers and Optics*, vol. 114, no. 4, pp. 517–526, Mar. 2014. doi: 10.1007/s00340-013-5555-6.

[24] R. A. Negres, M. A. Norton, D. A. Cross, and C. W. Carr, "Growth behavior of laser-induced damage on fused silica optics under uv, ns laser irradiation," *Optics Express*, vol. 18, no. 19, pp. 19 966–19 976, Sep. 2010. doi: 10.1364/OE.18.019966. [Online]. Available: http://www.opticsexpress.org/abstract.cfm?URI=oe-18-19-19966.

[25] R. I. Hartley and A. Zisserman, *Multiple View Geometry in Computer Vision*, Second. Cambridge University Press, ISBN: 0521540518, 2004.

[26] B. S. Reddy and B. N. Chatterji, "An fft-based technique for translation, rotation, and scale-invariant image registration," *IEEE Transactions on Image Processing*, vol. 5, no. 8, pp. 1266–1271, Aug. 1996, issn: 1941-0042. doi: 10.1109/83.506761.

[27] G. Hallo, C. Lacombe, J. Néauport, and F. Hild, "Detection and tracking of laser damage on LMJ vacuum windows by digital image correlation," in *Dimensional Optical Metrology and Inspection for Practical Applications X*, K. G. Harding, S. Zhang, and B. Li, Eds., International Society for Optics and Photonics, vol. 11732, SPIE, 2021, pp. 87–95. [Online]. Available: https://doi.org/10.1117/12.2587171.

[28] M. Nicolaizeau and J.-L. Miquel, "LMJ status: fifth bundle commissioning and PW class laser coupling," in *High Power Lasers for Fusion Research V*, A. A. S. Awwal and C. L. Haefner, Eds., International Society for Optics and Photonics, vol. 10898, SPIE, 2019, pp. 1–10. doi: 10.1117/12.2507193. [Online]. Available: https://doi.org/10.1117/12.2507193.

[29] K. Pearson, "Notes on regression and inheritance in the case of two parents," *Proceedings of the Royal Society of London*, vol. 58, pp. 240–242, 1895.

[30] M. Nefzger and J. Drasgow, "The needless assumption of normality in pearson's r.," *American Psychologist*, vol. 12, pp. 623–625, 1957.

6

Toward advanced brightness and contrast corrections

Gray level analysis is efficient to reach sub-pixel resolution on the estimation of damage diameters. Thus, to monitor damage growth under spatial image resolution, it is essential to be able to compare pixel intensities after each laser shot. Low-order polynomial brightness and contrast corrections were proposed in Chapter 4. However, by construction, such method is not efficient to correct for high frequency spatial intensity variations. In this Chapter, original brightness and contract corrections, based on Proper Orthogonal Decomposition and optical model, are proposed to correct for intensity variations at high and low spatial frequencies, without altering gray levels describing damage sites. These corrections were applied to a set of vacuum window images and compared to low-order polynomial corrections.

6.1 Introduction

Large efforts on image processing were put in order to improve online detection and quantification of damage sites and their growth [1–7]. Since the more accurate method to estimate damage diameters was based on the analysis of pixel intensities (Chapter 2), it was essential to be able to compare pixel intensities from one image to another [8]. For this purpose, a robust lighting system over time was proposed in Chapter 3 and image correction techniques based on Digital Image Correction (DIC) techniques were developed (Chapter 4). Gray level corrections were based on low-order polynomial brightness and contrast corrections. This kind of generic correction was suitable to correct intensity variations that can be spatially described by low order polynomial functions. They were proposed to preserve the high frequency spatial variations to damage sites. Thus, by construction such generic methods were not sufficient to correct for high frequency spatial intensity variations.

Several methods were proposed to correct for variations of pixel intensities. First, gray levels of images were corrected by applying an offset value on the whole image, corresponding to uniform brightness correction [9]. It was also proposed to apply an uniform intensity scale factor on images to correct for contrast corrections [10, 11]. Uniform offset and scale corrections were also combine, leading to brightness and contrast corrections such as the Zero-mean Normalised Sum of Squared Difference (ZNSSD) or the Zero-mean Normalized Cross-Correlation (ZNCC) [10, 12]. Since brightness and contrast modifications were not always uniform over the whole images, non uniform corrections were proposed [13]. Brightness and contrast fields were described using Finite Element (FE) and low-order polynomial fields [14, 15]. Low-order polynomial fields without FE were also used to correct for brightness and contrast variations (Chapter 4) [7]. However, uniform and low-order polynomial descriptions were limited to low-frequency spatial variations. To overcome this limitation, image background removal, *i.e.,* brightness correction, based on Proper Orthogonal Decomposition (POD) was used in the field of particle image velocimetry [16]. To be efficient, such method requires a set of images that contain sufficient number of possible background modifications.

In this chapter, it is proposed to develop brightness and contrast corrections specifically adapted to images of final optics (Section 6.2). The brightness correction was based on POD of a set of true background images while contrast corrections made use of the optical model presented in Chapter 2. The results of the proposed gray level corrections

are presented and compared to generic corrections in Section 6.3.

6.2 Methods

The principle of pixel intensity correction is based on the modified hypothesis of pixel intensity conservation

$$I_0(\boldsymbol{x}) = b(\boldsymbol{x}) + (1 + c(\boldsymbol{x}))I_n(\boldsymbol{x}) \tag{6.1}$$

where I_0 is the reference image, $\boldsymbol{x}$ pixel coordinates in the image, I_n the image to be corrected, b and c are respectively the brightness and contrast fields. In the generic formulation (Section 4.3.2), brightness and contrast fields were written as a linear combination of low order polynomial fields

$$b(\boldsymbol{x}) = \sum_{k=1}^{N} b_k \psi_k(\boldsymbol{x}) \qquad \text{and} \quad c(\boldsymbol{x}) = \sum_{k=1}^{N} c_k \psi_k(\boldsymbol{x}) \tag{6.2}$$

where ψ_k was the polynomial field of order k. The amplitude of the polynomial field of order k for brightness (resp. contrast) was b_k (resp. c_k).

Figure 6.1 shows one case where the generic configuration was sufficient to correct for gray level variations between images and another residual map where the generic method was not adapted. In the second residual map, high frequency intensity variations corresponding to local discontinuities were not described by the generic method. These discontinuities may be due to edges of the grating behind the vacuum window.

In order to correct for such variations, it is proposed to construct a brightness and contrast basis that specifically takes into account of vacuum window background variations and LED intensity changes. Background modes were extracted from window images by Proper Orthogonal Decomposition (POD). Contrast modes describing LED shapes were simulated using a ray tracing software (Zemax OpticStudio [17]) and the model of the lighting system discussed in Chapter 2.

6.2.1 Background corrections by POD

The polynomial brightness correction was efficient to correct for low order variations but not sufficiently effective when high frequency spatial corrections were needed, as shown in Figure 6.1. The proposed background correction was based on the extraction of spatial modes by POD on a

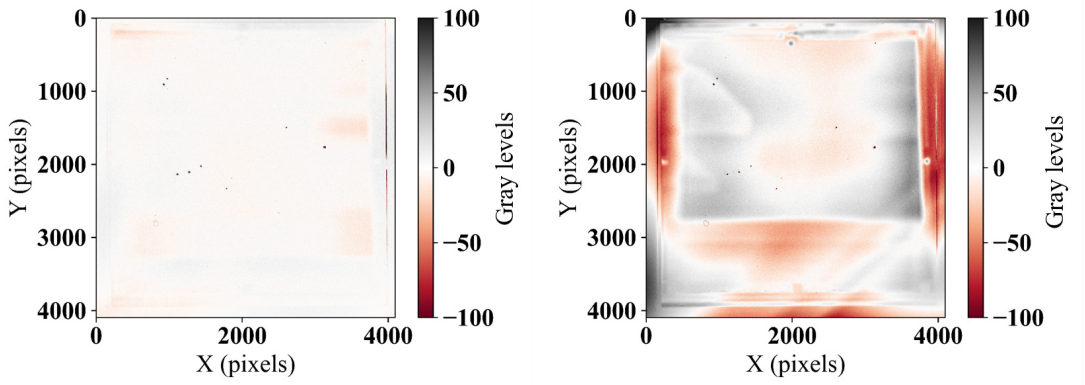

(a) (b)

Figure 6.1: Gray level residual maps of two vacuum window images after image registration and generic gray level corrections. (a) The correction was sufficient, the RMS residual was 0.05% of the image dynamic range. (b) The correction was not sufficient, high spatial frequency variations are visible in the residual map. The RMS residual was 0.1% of the image dynamic range.

sufficient number of background acquisitions. If all possible background disturbances are acquired in the set of images, then the extracted modes by POD define a good basis. Each background image, bg, is written as a linear combination of background modes, B_i

$$bg(\mathbf{x}) = \sum_{i=1}^{N_{modes}} \beta_i B_i(\mathbf{x}) \tag{6.3}$$

To estimate the background modes, B_i, the snapchot method was used [18]. An acquired background image after the laser shot number i is b_i. The snapshot correlation matrix, $\mathbf{C}$, is defined as

$$\mathbf{C}_{ij} = b_i^{\top} \cdot b_j \tag{6.4}$$

Singular Value Decomposition (SVD) was applied to the snapshot correlation matrix. This decomposition is written as

$$[\mathbf{C}] = [\mathbf{U}][\mathbf{S}][\mathbf{V}] \tag{6.5}$$

where $[\mathbf{U}]$ is the left singular matrix, $[\mathbf{S}]$ contains the singular values and $[\mathbf{V}]$ is the right singular matrix.

Each background spatial mode B_i is written as

$$B_i(\mathbf{x}) = \sum_{j=1}^{N} \mathbf{V}_{ij} b_j(\mathbf{x}) \tag{6.6}$$

The first 15 background images of a set of 18 images were selected ($N_{modes} = 15$). The snapshot correlation matrix of these 15 background images was decomposed using the SVD method. The eigen values of each mode and the cumulative modal energy are displayed in Figure 6.2. The first background mode (mode number = 1) described more than 99.7% of background variations in the selected snapshot set. The spatial and temporal variations of the first three modes are given inf Figure 6.3. The temporal variation of the first mode was positive for all snapshots. The following modes represented more local variations and their amplitudes were centered about zero. It is worth noting that the representations of the first three spatial modes described different perturbations that occurred (or not) in the snapshots. Some modes did not describe all snapshots. For instance, the amplitude of the third mode was zero for snapshots 4, 5, 11 and 13 (Figure 6.3 (f)).

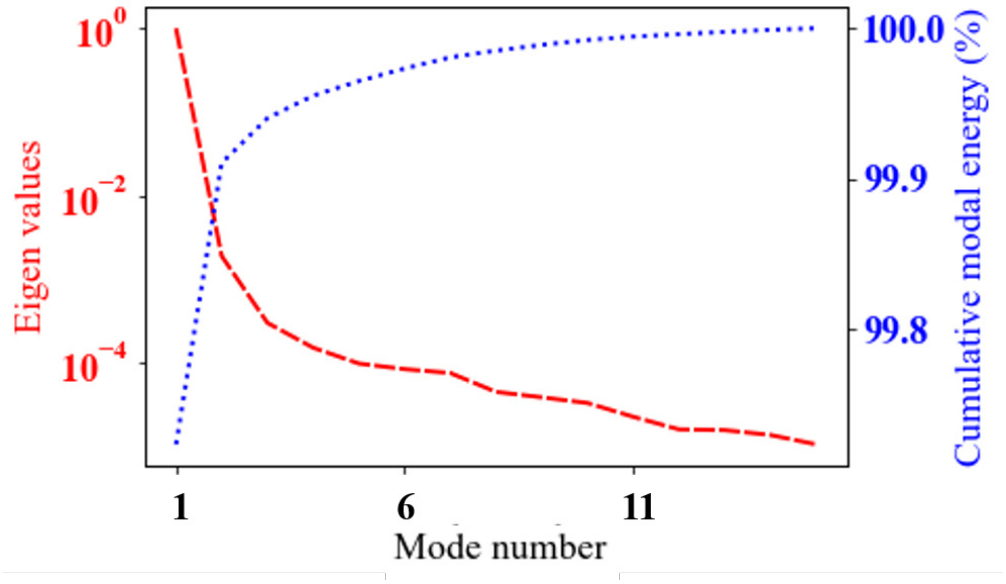

Figure 6.2: (Red) Eigen values from the singular value decomposition of the snapshot correlation matrix. (Blue) Cumulative modal energy contained in the n-th first modes. As an example, the first two modes contain more than 99.9% of the total modal energy.

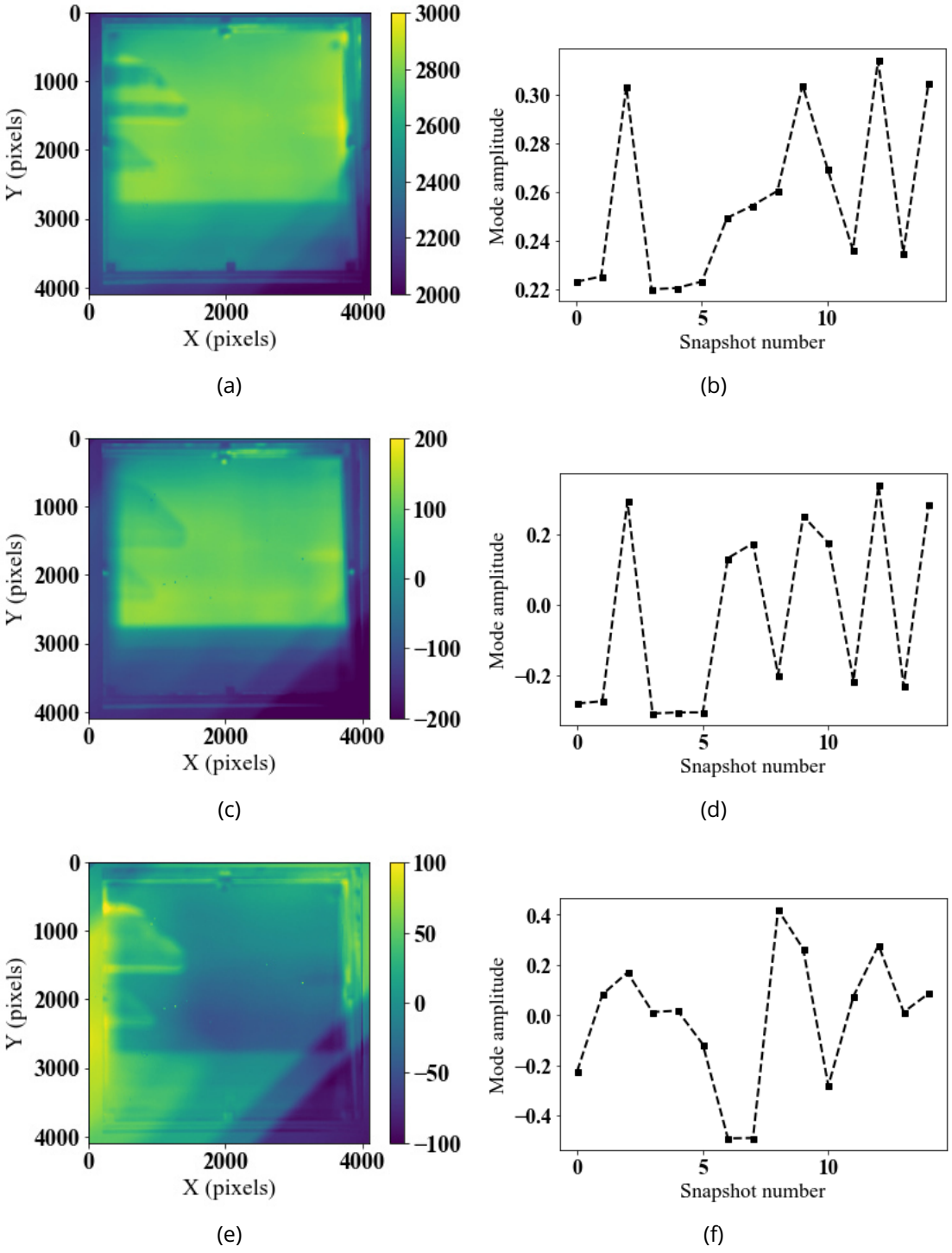

Figure 6.3: First three modes and the spatial (left) and temporal (right) variations. (a, b) First background mode. (c, d) Second background mode. (e, f) Third background mode.

6.2.2 Correction of lighting variations using a ray tracing model

The estimation of specific spatial modes for contrast corrections was based on the lighting system model presented in Chapter 2. The proposed contrast field, c_{LED} was written as a linear combination of two spatial modes, C_1 (resp. C_2), corresponding to the influence of the first (resp. second) LED

$$c_{LED}(\mathbf{x}) = \sum_{i=1}^{2} \gamma_i C_i(\mathbf{x}) \tag{6.7}$$

where γ_i was the amplitude of the corresponding spatial mode. Such description of the contrast field assumed that the contrast variations were only due to variations of LED intensity.

Both spatial contrast modes, C_1 and C_2, generated by the ray tracing model of the lighting system are shown in Figure 6.4.

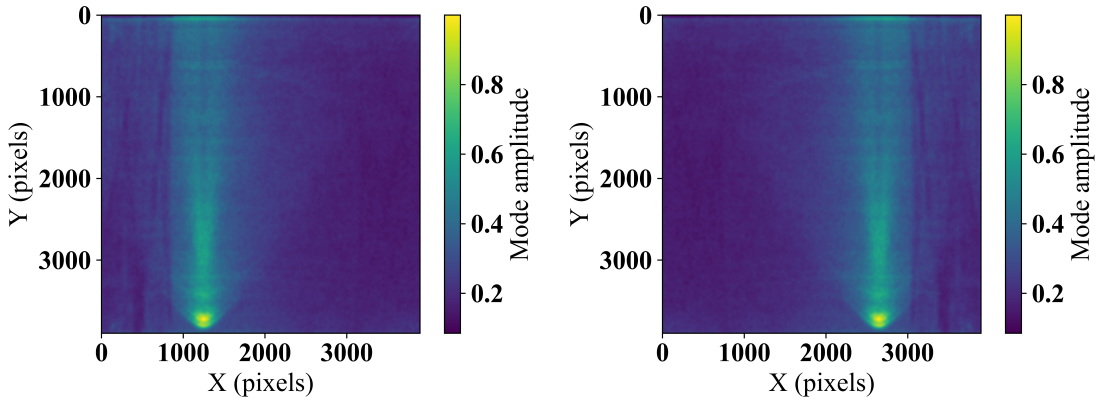

Figure 6.4: Generated spatial modes for specific contrast corrections, corresponding to the left (a) and right (b) LEDs.

6.3 Results

Background and contrast corrections using the proposed method were applied to the set of vacuum window images used in Chapter 4.

6.3.1 Background correction

15 background images were used to estimate the background spatial modes. Images 16, 17 and 18 were used for validation puroposes of the background correction method. The validation step of the background correction based on POD principles consisted in the reconstruction of background images that were not used to estimate the 15 background modes. Figure 6.5 shows the RMS residual between the reconstructed background images and the corresponding true background images for each of the 18 images of the set. For images that were used to create the background modes (image number 1 to 15), the RMS residual was exactly 0. No background information was lost in the POD process. For the 3 images that were not used to create the background modes, the RMS residual was close to the estimated acquisition noise ($\approx 0.04\%$ of the dynamic range as shown in Chapter 4).

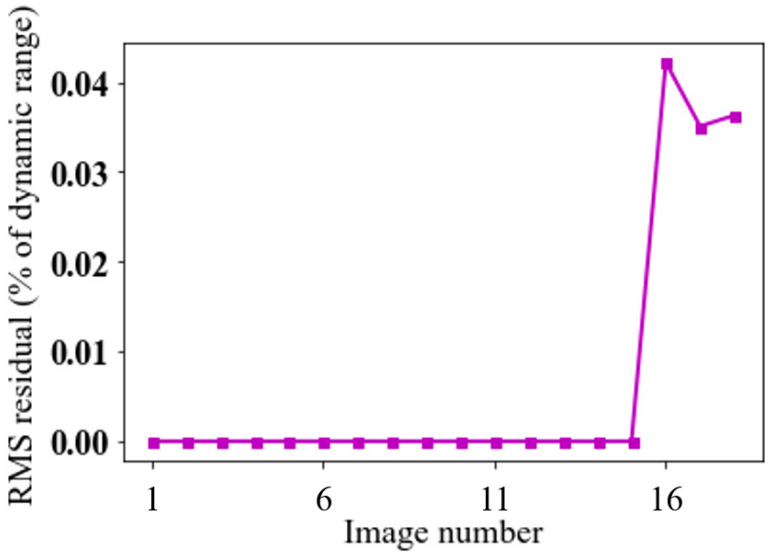

Figure 6.5: RMS residual (% of the dynamic range) as a function of image number between each acquired background and the corresponding estimated background using the background modes.

The proposed background correction was applied to both images used as examples in Figure 6.1. The residual maps for both images are shown in Figure 6.6. The proposed method was efficient even in the case with high spatial frequency variations of pixel intensities contrary to the generic method. With the proposed POD method, only damage sites were visible in both residual maps. One advantage of the POD method was that the

more images were used to create the basis for the brightness correction, the more effective the brightness correction. However, a weakness was that the POD method may not be as efficient as the generic method when only a few images were available to create the basis. This is the case when a new beam is commissioned.

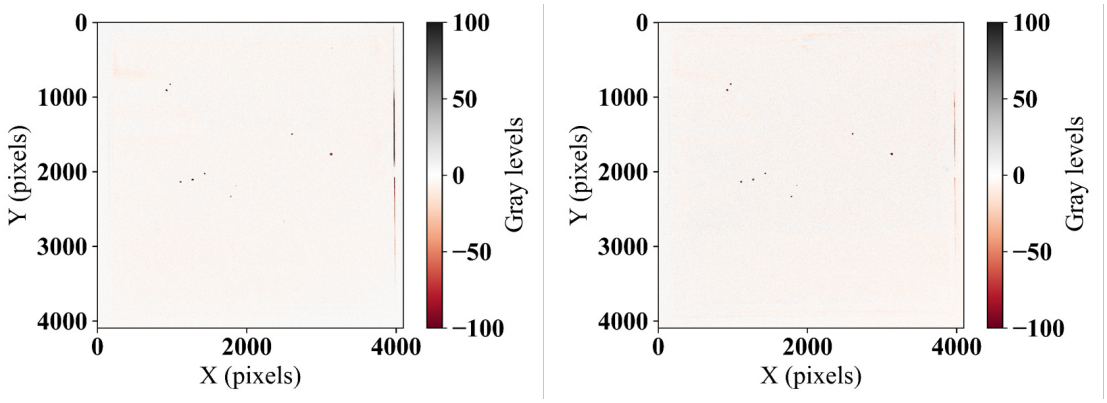

Figure 6.6: Residual maps after image registration and background correction by the POD method for the same vacuum window images as those shown in Figure 6.1. Contrary to the residual map of Figure 6.1(b) with a RMS residual of 0.1% of the dynamic range, the RMS residual after POD correction (b) was 0.06% of the image dynamic range and only damage sites are visible.

6.3.2 Contrast correction

The proposed contrast correction based on LED spatial modes was applied to an image with only one LED switched on. The reference is an image of the same vacuum window with two LEDs switched on. The residual map between both images before contrast correction is shown in Figure 6.7(a). The influence of the switched off LED was clearly visible. When the generic contrast correction was applied to such image, the residual levels were reduced on the whole map (Figure 6.7(b)). However, the result was not sufficient. The final residual map after the proposed contrast correction is shown in Figure 6.7(c). In such map, the residual levels were reduced and more homogeneous than in the residual map of the generic correction.

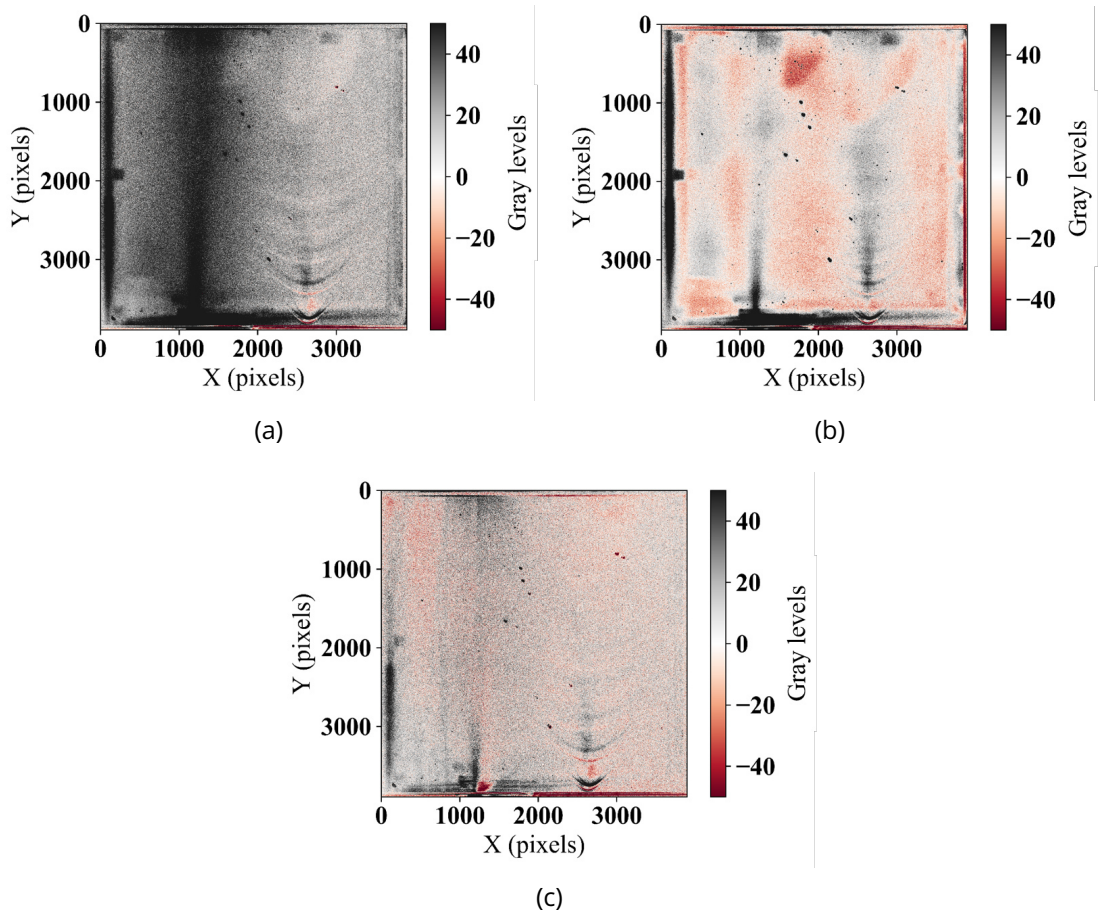

Figure 6.7: Residual maps between an image with 2 LEDs on and another with only 1 LED on (a) without contrast correction, (b) after generic contrast correction, (c) after the proposed correction based on LED spatial modes.

6.3.3 Contrast correction of Chapter 4 images

In order to compare the brightness and contrast corrections based on low-order polynomial fields and on the LED model, the images with subtracted background, of the set used in Chapter 4, were corrected using both methods. The selected image as the reference was 12 for which both LEDs were on. In the image set, one laser shot occurred between each image. Damage sites may have grown between each image when they were in the laser beam area. The bottom LED was off for the first 9 images and on for the last 8 images. The RMS residual was computed in the laser beam area for each image of the set after different correction steps (Figure 6.8). The initial RMS residual values, before any correction,

were between 0.3% and 0.5% of the image dynamic range. After spatial registration, the RMS residual was $\approx 0.3\%$ for images 1 to 9 while it was at $\approx 0.05\%$ for images 10 to 17. An RMS residual of 0.05% was considered at the noise level in Chapter 4. The low and stable residual values for images 10 to 17 indicates that the lighting conditions were similar for these images. The high residual values after spatial registration for images 1 to 9 are due to one LED off (bottom LED for this image set).

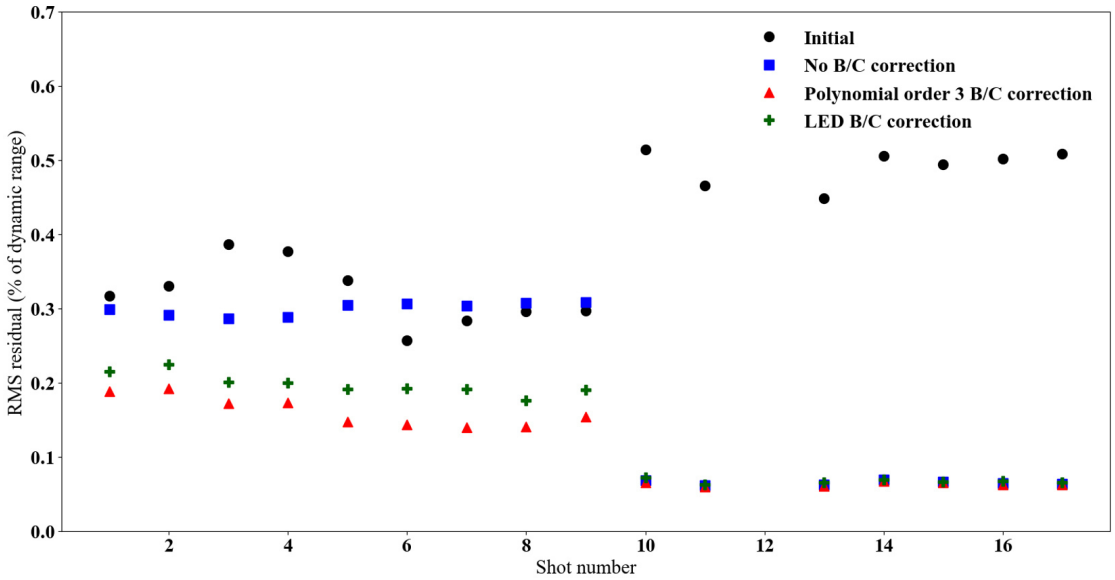

Figure 6.8: RMS residual (% of the dynamic range) as a function of shot number between image 12 with 2 LEDs on and the images after different corrections: no corrections in black, spatial registration in blue, spatial registration with polynomial brightness and contrast correction in red, spatial registration with LED-based contrast correction in green.

The aim was to estimate the adequacy of the proposed methods to mitigate the influence of LED extinction on the estimated diameter of damage sites. Low-order polynomial brightness and contrast corrections, described in Chapter 4, were applied to the 17 images of the set. The RMS residual is plotted as a function of shot number in Figure 6.8. For images 10 to 17, the RMS residuals were equal to those with no brightness and contrast corrections. For images 1 to 9, the RMS residual was lowered to $\approx 0.2\%$, still higher than the noise level. After this generic correction, differences remained between images 1 to 9 compared to the reference one. The spatially registered images of the set were also corrected using the LED-based contrast method. The RMS residual for images 10 to 17

was also the same than the noise level. For images 1 to 9, the RMS residuals were $\approx 0.2\%$, slightly higher than the RMS residuals obtained after polynomial brightness and contrast correction.

To better understand the differences between the images corrected by the polynomial BC and the LED-based contrast methods, profiles of image 1 are plotted before any brightness and contrast correction, after polynomial brightness and contrast correction and after LED-based contrast correction (Figure 6.9). These profiles were compared to the corresponding one of the reference image. In the reference profile, two peaks are observed, corresponding to two LEDs on, with a baseline of ≈ 40 gray levels. The profile of image 1 before BC correction, with a unique peak, indicates that only one LED was on and the baseline was ≈ 25 gray levels. With an efficient gray level correction, the profile of the corrected image should fit the profile of the reference image.

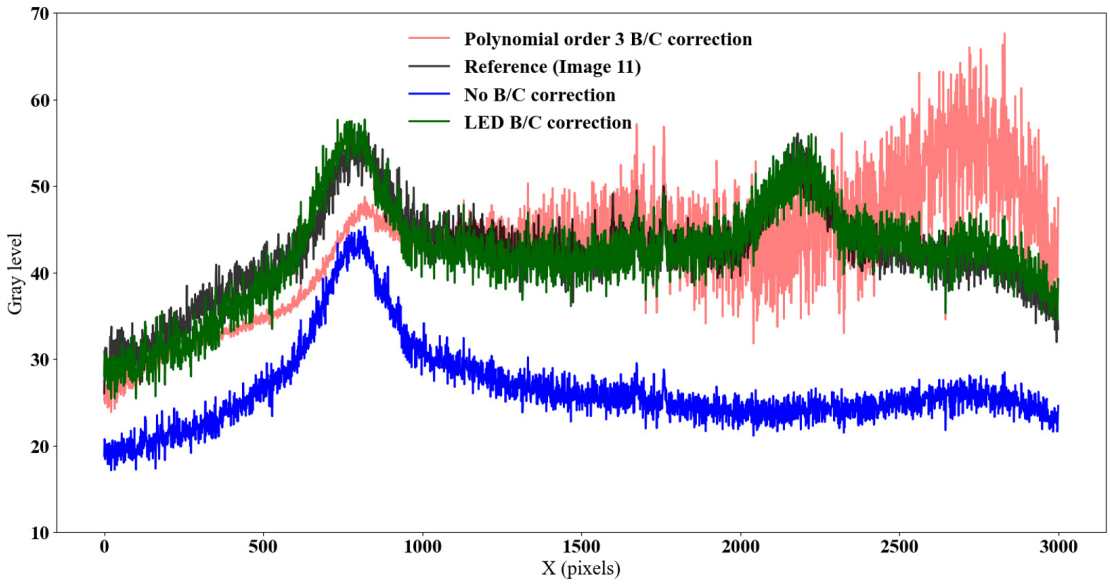

Figure 6.9: Profile comparison of the first image with one LED off after spatial registration in blue, after polynomial BC correction in red and after LED BC correction in green. The reference profile is plotted in black.

After low-order polynomial brightness and contrast correction, the baseline profile of the corrected image was ≈ 40 gray levels. However, the peak between pixels 500 and 1000 was lowered and the other peak between pixels 2000 and 2500 was not reconstructed in the right place. From pixels 1500 to 3000 (resp. 0 to 1000), the corrected profile was noisier (resp. less noisy) than the reference profile. Despite low RMS residuals, the low-order

polynomial brightness and contrast correction did not correctly describe the gray level modification induced by a LED extinction. In case of polynomial brightness and contrast correction, the detection of small damage sites in the over-noisy areas of the images would be complicated. On the contrary, the profile of image 1 generated after LED-based contrast method was consistent with the reference profile, with two peaks and similar noise amplitude.

To compare the influence on the diameter estimation of damage sites using the Total Integrated Signal, the diameters of 3 damage sites (Figure 6.10) were estimated using the pixel intensity method for the 17 images of the set.

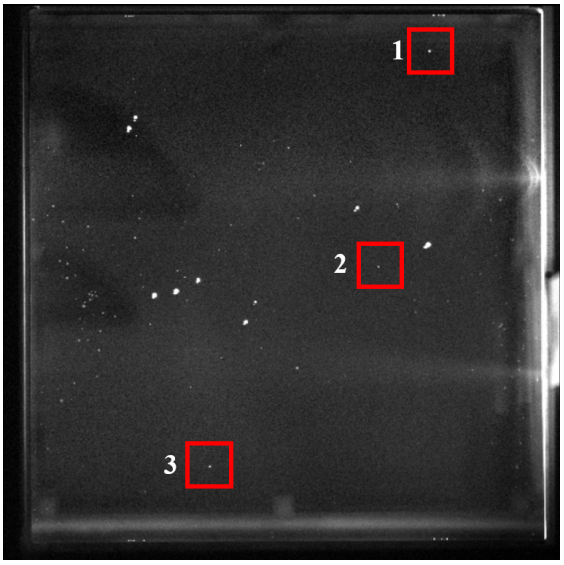

Figure 6.10: Vacuum window image with the three damage sites (in red boxes) whose diameters were measured after polynomial and LED-based corrections.

Damage site 1 (Figure 6.11) was located at the top of the image, near the LED constantly on (Figure 6.10). Since this damage site was outside the laser beam area, its diameter should be constant over the laser shot sequence. From images 11 to 18 (2 LEDs on), the estimated diameter was $\approx 500\,\mu m$ before and after gray level corrections. From images 1 to 10, the diameter was underestimated by $\approx 100\,\mu m$ before gray level correction and overestimated by $\approx 100\,\mu m$ after low-order brightness and contrast corrections. The LED-based correction allowed for a correct estimation of the damage diameter even when one of the LEDs was off.

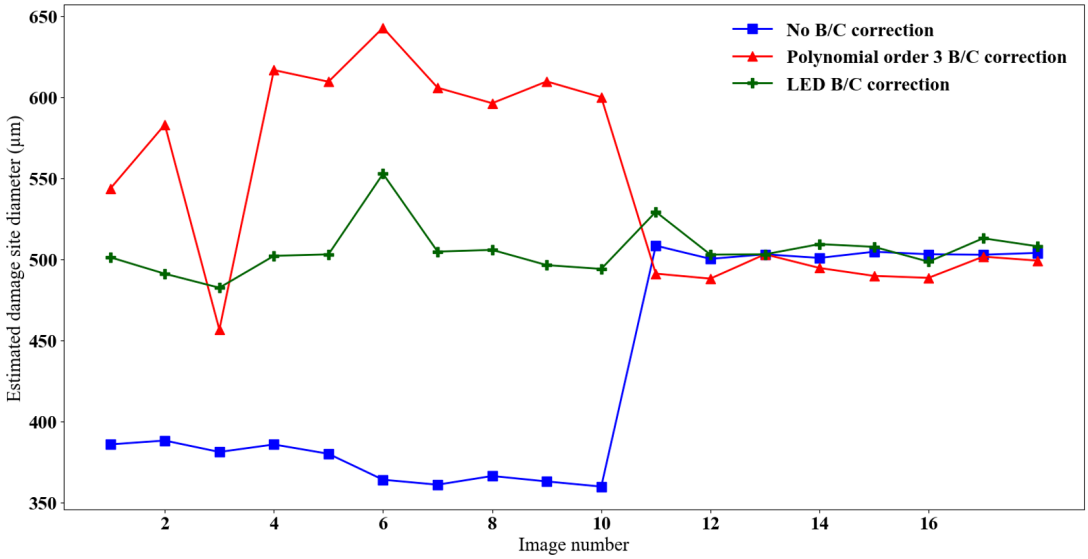

Figure 6.11: Site 1 - Estimated diameter from no BC corrected images in blue, polynomial BC corrected images in red, LED BC corrected images in green. The damage site is outside the laser beam area, close to the constantly lit LED.

Damage site 2 (Figure 6.12) was in the centre of the vacuum window, between the two LEDs (Figure 6.10). Since it was in the laser beam area, this site was susceptible to grow during the laser shot sequence. Without correction, the measured diameter increased from images 1 to 14 with a large gap from images 10 (bottom LED off) to 11 (bottom LED on). The polynomial brightness and contrast correction and the LED-based contrast correction allowed damage growth to be estimated from images 1 to 10 by $\approx 150\,\mu\mathrm{m}$. However, diameters assessed by polynomial corrections were $\approx 50\,\mu\mathrm{m}$ larger to those estimated after LED-based contrast correction. The most realistic diameter estimation seems to be the one provided after the LED-based correction since there was a continuity in the diameter increase from images 1 to 14. On the contrary, a diameter decrease was observed between images 10 and 11.

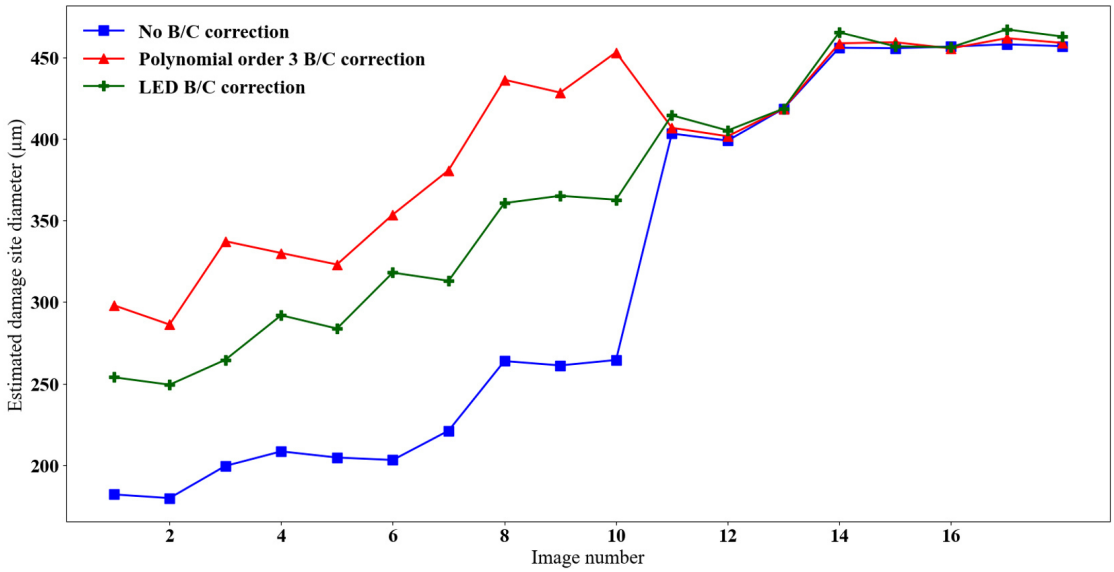

Figure 6.12: Site 2 - Estimated diameter from no BC corrected images in blue, polynomial BC corrected images in red, LED BC corrected images in green. The damage site is in the laser beam area, between the two LEDs.

Damage site 3 (Figure 6.13) was at the bottom of the image, close to the turned off LED at the beginning of the image set and on after (Figure 6.10). Outside the laser beam area, this damage site should not exhibit growth. Before gray level correction, a diameter discontinuity induced the turning on the bottom LED between images 10 and 11 was observed. After low-order polynomial brightness and contrast corrections, the estimated diameters from images 1 to 5 was estimated at the same values as for images 11 to 18. The diameter was overestimated by $\approx 200\,\mu\mathrm{m}$ between images 6 and 10. The LED-based contrast correction provided a different diameter estimation for images 1 to 10. Diameters were underestimated by $\approx 150\,\mu\mathrm{m}$ on these images. The LED-based contrast correction allowed the diameter underestimation to be reduced by $\approx 100\,\mu\mathrm{m}$ with respect to images that were corrected in intensity.

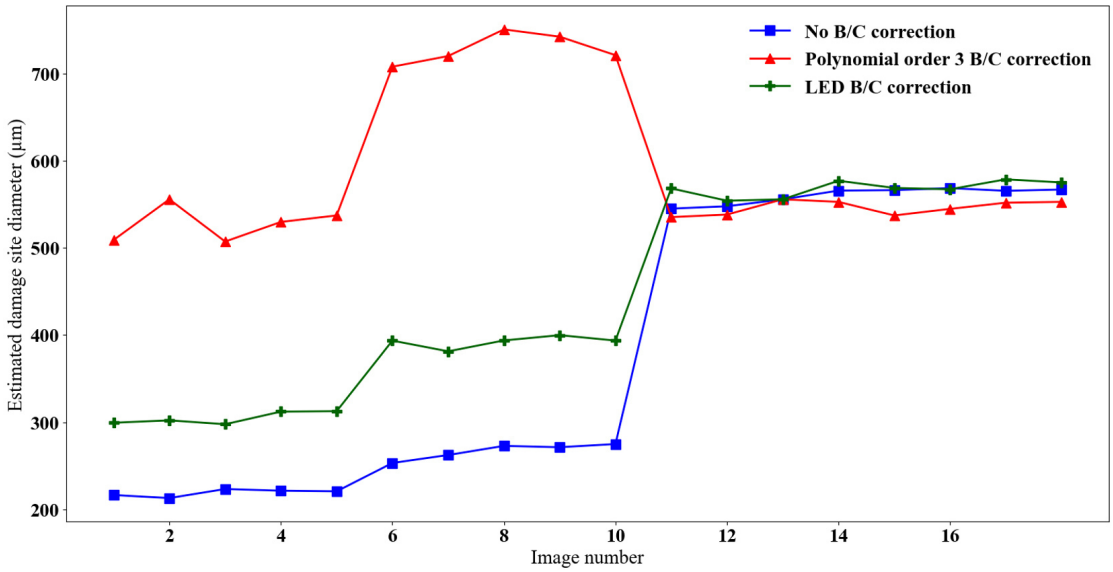

Figure 6.13: Site 3 - Estimated diameter from no BC corrected images in blue, polynomial BC corrected images in red, LED BC corrected images in green. The damage site is outside the laser beam area close to the intermittently lit LED.

The contrast correction based on LED model resulted in more realistic images than the low-order polynomial brightness and contrast correction. The LED-based contrast correction reduced the influence of LED turn-offs and it appeared more efficient than the polynomial brightness and contrast correction to estimate damage diameters in deteriorated lighting conditions. However, the polynomial and LED-based methods were compared on an image set for which true damage diameters were not known. Damage growth was estimated according to the position of the damage sites on the vacuum window (in or out of the laser beam area). It is necessary to perform more validation tests. It could be useful to acquire images of the vacuum window presented in Chapter 2 with different lighting conditions (without laser shot between images): one image with two LEDs on, one with the top LED on and the bottom LED off, one image with the top LED off and the bottom one on. Thus, it would be possible to check that the contrast correction method based on optical modeling may mitigate the influence of LED extinction on damage intensity levels. In case of an insufficient gray level correction for all positions in the vacuum window (as it seemed to be the case for damage site 3), a precise measurement of the angular emission cone of the LED should be planned in order to refine the model used to generate the LED contrast fields. More accurate modeling of the lighting system may reduce the impact of LED turn-offs by using the proposed LED-based contrast correction while waiting for the lighting system modification proposed in Chapter 3. Although LED-based contrast corrections reduced diameter measurement errors, it is recommended to work with images acquired with two functional LEDs. Monitoring the contrast coefficients of the LED correction should allow for early identification of LED failure during image acquisitions on the facility.

6.4 Conclusion

It was observed that the generic brightness and contrast correction did not always give satisfying results, in particular in cases of high spatial frequency brightness variations or when one LED was switched off. A new brightness and contrast correction method was specifically designed to take into account such difficult cases. The brightness correction was based on Proper Orthogonal Decomposition of background images while the contrast correction relied on an optical model of the LED lighting system. The performances of the proposed method were compared to the generic brightness and contrast correction proposed in Chapter 4. It was demonstrated that the POD-based brightness method successfully corrected

the high spatial frequency intensity variations. One of the limitations regarding the POD method relies on the possibility that a new disturbance may appear on an image and that it was not taken into account in the POD basis. An additional learning step would then be required. The model-based contrast correction provided an answer to correct for the influence of the extinction of one LED. Further validation steps are required to determine the validity limits of the contrast correction based on the model of the lighting system, particularly regarding the correction of LED extinction.

References

[1] L. Kegelmeyer, P. Fong, S. Glenn, and J. Liebman, "Local area signal-to-noise ratio (lasnr) algorithm for image segmentation," *Proceedings of SPIE - The International Society for Optical Engineering*, vol. 6696, Oct. 2007. doi: 10.1117/12.732493.

[2] A. Carr *et al.*, "Defect classification using machine learning," in *Laser-Induced Damage in Optical Materials: 2008*, G. J. Exarhos, D. Ristau, M. J. Soileau, and C. J. Stolz, Eds., International Society for Optics and Photonics, vol. 7132, SPIE, 2008, pp. 322–327. doi: 10.1117/12.817418. [Online]. Available: https://doi.org/10.1117/12.817418.

[3] G. M. Abdulla, L. M. Kegelmeyer, Z. M. Liao, and W. Carr, "Effective and efficient optics inspection approach using machine learning algorithms," in *Laser-Induced Damage in Optical Materials: 2010*, G. J. Exarhos, V. E. Gruzdev, J. A. Menapace, D. Ristau, and M. J. Soileau, Eds., International Society for Optics and Photonics, vol. 7842, SPIE, 2010, pp. 386–393. doi: 10.1117/12.867648. [Online]. Available: https://doi.org/10.1117/12.867648.

[4] F. Bo, C. Fengdong, L. Bingguo, and L. Guodong, "Segmentation of small defects in Final Optics Damage Online Inspection images," in *2012 International Conference on Image Analysis and Signal Processing*, Nov. 2012, pp. 1–4. doi: 10.1109/IASP.2012.6425003.

[5] G. Liu *et al.*, "Fast automatic classification of input and exit surface laser-induced damage in large-aperture final optics," in *2018 IEEE 3rd Advanced Information Technology, Electronic and Automation Control Conference (IAEAC)*, 2018, pp. 782–790. doi: 10.1109/IAEAC.2018.8577501.

[6] F. Wei *et al.*, "Automatic classification of true and false laser-induced damage in large aperture optics," *Optical Engineering*, vol. 57, no. 5, pp. 1–11, 2018. doi: 10.1117/1.OE.57.5.053112. [Online]. Available: https://doi.org/10.1117/1.OE.57.5.053112.

[7] G. Hallo, C. Lacombe, J. Néauport, and F. Hild, "Detection and Tracking of Laser Damage Sites on Fused Silica Components by Digital Image Correlation," *Optics and Lasers in Engineering*, vol. 146, p. 106 674, 2021.

[8] A. Conder, J. Chang, L. Kegelmeyer, M. Spaeth, and P. Whitman, "Final optics damage inspection (FODI) for the National Ignition Facility," in *Optics and Photonics for Information Processing IV*, A. A. S. Awwal, K. M. Iftekharuddin, and S. C. Burkhart, Eds., International Society for Optics and Photonics, vol. 7797, SPIE, 2010, pp. 167–178. doi: 10.1117/12.862596. [Online]. Available: https://doi.org/10.1117/12.862596.

[9] W. Tong, "An evaluation of digital image correlation criteria for strain mapping applications," *Strain*, vol. 41, no. 4, pp. 167–175, 2005. doi: https://doi.org/10.1111/j.1475-1305.2005.00227.x. eprint: https://onlinelibrary.wiley.com/doi/pdf/10.1111/j.1475-1305.2005.00227.x. [Online]. Available: https://onlinelibrary.wiley.com/doi/abs/10.1111/j.1475-1305.2005.00227.x.

[10] M. A. Sutton, J.-J. Orteu, and H. W. Schreier, *Image Correlation for Shape, Motion and Deformation Measurements - Basic Concepts, Theory and Applications*. Springer Science, 2009, isbn: 978-0-387-78746-6. doi: 10.1007/978-0-387-78747.

[11] P. Dietrich, S. Heist, M. Landmann, P. Kühmstedt, and G. Notni, "Bicos—an algorithm for fast real-time correspondence search for statistical pattern projection-based active stereo sensors," *Applied Sciences*, vol. 9, p. 3330, Aug. 2019. doi: 10.3390/app9163330.

[12] B. Pan, H. Xie, and Z. Wang, "Equivalence of digital image correlation criteria for pattern matching," *Appl. Opt.*, vol. 49, no. 28, pp. 5501–5509, Oct. 2010. doi: 10.1364/AO.49.005501. [Online]. Available: https://opg.optica.org/ao/abstract.cfm?URI=ao-49-28-5501.

[13] F. Hild and S. Roux, "Digital image correlation," in *Optical Methods for Solid Mechanics. A Full-Field Approach*, P. Rastogi and E. Hack, Eds., Weinheim (Germany): Wiley-VCH, 2012, pp. 183–228.

[14] A. Charbal *et al.*, "Integrated digital image correlation considering gray level and blur variations: application to distortion measurements of ir camera," *Optics and Lasers in Engineering*, vol. 78, pp. 75–85, Mar. 2016. doi: 10.1016/j.optlaseng.2015.09.011.

[15] A. Mendoza, J. Schneider, E. Parra, E. Obert, and S. Roux, "Differentiating 3D textile composites: A novel field of application for Digital Volume Correlation," *Composite Structures*, vol. 208, pp. 735–743, Jan. 2019. doi: 10.1016/j.compstruct.2018.10.008. [Online]. Available: https://hal.archives-ouvertes.fr/hal-02156832.

[16] M. Mendez *et al.*, "Pod-based background removal for particle image velocimetry," *Experimental Thermal and Fluid Science*, vol. 80, pp. 181–192, 2017, issn: 0894-1777. doi: https://doi.org/10.1016/j.expthermflusci.2016.08.021. [Online]. Available: https://www.sciencedirect.com/science/article/pii/S0894177716302266.

[17] Zemax LLC, *Opticstudio*, version 15.5, 2015. [Online]. Available: https://www.zemax.com/pages/opticstudio.

[18] P. Holmes, J. L. Lumley, and G. Berkooz, *Turbulence, Coherent Structures, Dynamical Systems and Symmetry*, ser. Cambridge Monographs on Mechanics. Cambridge University Press, 1996. doi: 10.1017/CBO9780511622700.

Part IV

From gray levels to damage morphology

In Part III, it was demonstrated that, after image corrections (spatial registration and correction of lighting variations) based on DIC principles, the correlation residual is an accurate indicator of damage initiation and growth. In Part II, it was also shown that the estimation of damage diameter using pixel intensities is more accurate than diameter measurement by pixel-counting method. Analysis of pixel intensities after image corrections allows for monitoring damage surface growth at a sub-pixel resolution. Damage growth in surface was detected earlier using pixel intensities than counting the number of pixels (Chapter 5).

The results presented up to this part were focused on surface damage monitoring. In Chapter 7, it is proposed to consider the growth of damage sites in the bulk. A dedicated experiment was performed on MELBA set-up to acquire traditional surface images with high spatial resolution as well as images from the sample side that gives access to damage depth. The aim was to estimate damage depth from the data contained in surface images only (pixel intensities and damage diameters).

7

Estimation of laser-induced damage depth from surface image features

In laser damage experiments, damage initiation and growth are typically monitored by imaging the face of the tested sample, ignoring the bulk morphology of damage sites. The depth of a damage site in fused silica optics is considered to be proportional to its equivalent diameter. However, some damage sites experience phases with constant diameter, and growth in the bulk of the sample, independently from its face. A proportionality relationship with damage diameter does not accurately describe the growth of such sites. In the sequel, an accurate estimator for damage depth is proposed, which is based on a linear combination of surface features such as equivalent diameter and mean gray level in the damaged area. The estimator is obtained through Bayesian ridge regression on damage diameter and gray levels. Such an estimator based on pixel intensity describes damage depth increase while it is not observed solely with diameters.

The results presented in this chapter were obtained during the internship of Yanis Abdelmoumni-Prunes, under my supervision from March to August 2022.

7.1 Introduction

Fused silica optics are prone to laser damage when they are exposed to high-fluence laser beams [1]. Once a damage site has initiated, it grows after each laser shot with an energy greater than a growth threshold [2]. Damage experiments were thus conducted to show that the damage growth probability is dependent on laser fluence, pulse duration, laser wavelength and damage size among other properties [3–6]. To quantify damage growth, images of damage sites are acquired through the face of the tested sample and damage sizes are estimated through pixel-counting on binarized images [3, 7]. Damage sites take the form of highly fractured craters. The depth of a damage site is considered to be a proportion of its equivalent diameter on the face of the sample, namely, a 3^{rd} for the fracture depth, a 5^{th} for the crater depth [8]. However, experimental results have underlined the existence of phases with constant apparent damage size on the face of the sample while damage growth in depth, so-called Veinhard plateaus [9]. The relationship between damage depth and equivalent diameter is thus not always linear, underlying that fused silica crack growth is a stochastic phenomenon.

Since imaging the volume of a damage site is not always possible, an accurate damage depth estimator using only surface images is desirable to precisely study damage growth. The analysis of gray levels in non-binarized surface images has proven to be more accurate than pixel-counting as a means of determining equivalent damage diameter [10] (Chapter 2). It was also shown that, during Veinhard plateaus, gray levels on surface images increased [9]. Besides, gray-level analyse have also been shown to enable for detection of damage growth earlier than pixel-counting methods [11].

It is proposed to provide gray level analysis in conjunction with pixel-counting to obtain a robust damage depth estimator only based on non-binarized images of the surface. A laser damage growth experiment was conducted on four different damage sites on a highly instrumented laser damage testing setup (Section 7.2.1). A traditional surface imaging, as well as an imaging from the side of the sample, make it possible to measure both damage diameter and depth, between each laser shot. Two of these four sites experienced the aforementioned Veinhard plateau phases. A series of corrections was applied to ensure that all the images in a sequence were comparable (Section 7.2.2). Relevant features were extracted from images such as surface diameters, total and mean gray levels (Section 7.2.3). An estimator for damage depth was then inferred through Bayesian ridge regression on the features obtained from surface

images for two of the available sites. The proposed depth estimator was tested on the two remaining damage sites (Section 7.3).

7.2 Materials and methods

Damage growth sequences were conducted on the laser damage set-up MELBA [12]. Both surface and bulk images were acquired during growth experiments with tunable laser parameters. A dedicated sample with polished edge without bevelled corner is required to acquire bulk images. The acquired images were processed to correct for camera motions between acquisitions, gray level variations and focus changes. Damage features were extracted from corrected images such as damage diameter, total gray levels, mean gray levels from images of the surface and damage depth from bulk images. Such features were analysed in order to estimate damage depth only from surface data.

7.2.1 Laser damage set-up

MELBA is a laser damage test set-up designed for precise metrology of laser damage initiation and growth. It delivers a $351\,\mathrm{nm}$ laser beam with up to $9\,\mathrm{mm}$ in diameter and customizable temporal and spatial profiles [13]. For previous laser damage experiments, a fused silica sample was polished on one of its lateral sides [9, 14]. As a complement to the standard surface imaging, a camera was added on the side of the sample to provide pseudo-volume images describing damage sites in the sample bulk (Figure 7.1). The imaging system used to acquire images of the surface was a Leica M420 macroscope, set up to have a pixel size of $6.45\,\mu\mathrm{m}$ in the object plane. Volume imaging was based on a Navitar Zoom 6000 lens system coupled with a CCD camera, with a pixel size of $2.28\,\mu\mathrm{m}$ in the object plane. The sample was lit by a white LED bar on one of its edges during the damage growth sequence. The lighting system was the same for both imaging systems.

Four damage sites were initiated on the silica sample. For image correction purposes, three damage sites (*i.e.,* surface fiducials) were initiated on the surface of the sample near each damage site using the laser beam of the MELBA set-up. Such surface fiducials were visible on surface images but not in volume images. Other damage sites, or bulk fiducials, were initiated in the bulk of the sample using a laser beam with a pulse duration of $0.8\,\mathrm{ps}$ at a wavelength of $1054\,\mathrm{nm}$ [15]. The intra-volume engraving method is similar to the process described in Ref. [16]. The laser beam

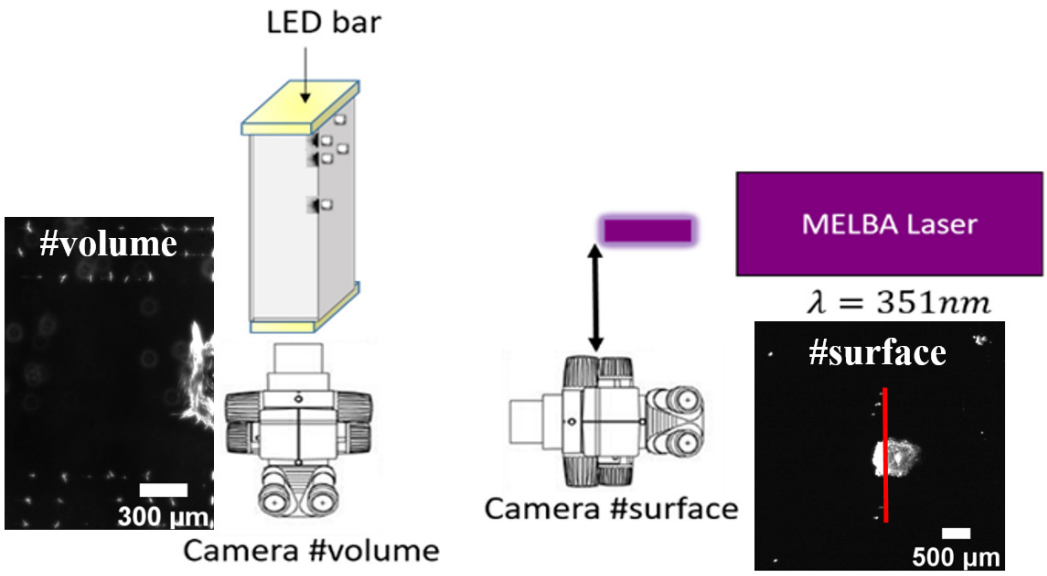

Figure 7.1: MELBA experimental setup used to perform damage growth sequence and to acquire images of the surface and bulk of damage sites. The camera #surface is inserted in front of the sample after each laser shot and removed before next shot. Images of the surface and the bulk of a damage site are acquired after each laser shot. The image plane of the bulk image is represented by the red line in the surface image.

was focused at several depths varying between 0 and $1\,\mathrm{mm}$ below the surface of the sample (Figure 7.2).

The four damage sites were then subjected to a growth sequence consisting of 250 to 450 laser shots with fluences between 1 and $8\,\mathrm{J\,cm^{-2}}$, with both surface and volume images captured between each of them. To avoid growth on surface and bulk fiducials, the spatial shape of the beam was locally shadowed in order not to irradiate the fiducials during the growth sequence. The damage sites were subjected to temporally square laser pulses, with a $5\,\mathrm{ns}$ pulse duration for the first two sites, $10\,\mathrm{ns}$ for the two others. The fluence was regularly modified between every laser shot, in order to ensure slow and progressive damage growth.

7.2.2 Image corrections

Throughout the growth sequence, images were affected by disturbances such as camera motions, spurious light and focus changes. In order to ensure that the images are comparable during the whole sequence, with

differences between them only caused by damage growth, it is needed to correct for all of those changes (Chapter 4). Such corrections were needed to exploit gray levels and to ensure that the damage segmentation process was consistent throughout the sequence. The metric used to evaluate the efficiency of the corrections is the Root Mean Square (RMS) residual [17]. The RMS residual is the normalized quadratic norm of the difference between the reference and the perturbed image over zones of interest, expressed as a percentage of the dynamic range of the reference image. For each sequence, the first image is used as the reference.

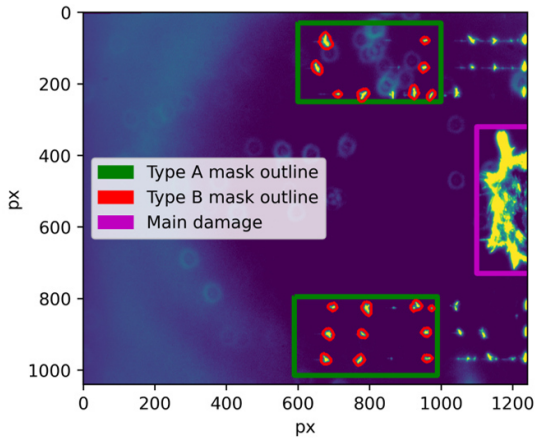

Figure 7.2: Outline of type A (resp. B) fiducial masks in green rectangles (resp. red contours) and main growing damage site for volume image in the magenta rectangle.

The first step of image corrections was to define the fiducial zones that were used as references. Two different fiducial masks were created, both shown for site 1 in Figure 7.2. The first one, type A, is composed of large rectangles containing the bulk fiducials. The second one, type B, was defined through Otsu thresholding to tightly segment fiducials [18]. Type A is used for spatial registration in the same way than in Chapter 5. Type B is dedicated to brightness and contrast corrections. It is assumed that light disturbances affect the fiducial pixels (type B) in the same way as the pixels of damaged sites while it may not be the same for the pixels corresponding to bulk silica (background). Some fiducials were not contained in these masks, as they ended up being absorbed by the main damage site during the growth sequence. Therefore such absorbed fiducials were not suitable as reference markers. For consistency and comparison purposes, all displayed RMS residual curves were calculated on type B fiducial zones, even if the correction itself was based on type A zones.

First, the volume images of one damage site are used to exemplify the proposed corrections, before moving to less complex surface images.

Camera motions between images may arise due to vibrations, or hysteresis in the motorized systems of the cameras. Digital Image Correction (DIC) was used to estimate the displacement field $\boldsymbol{u}$ between reference image I_0 and perturbed image I_n. By decomposing the displacement field on a selected basis (Chapter 4), the cost function

$$\Psi = \int [(I_n(\boldsymbol{x} + \boldsymbol{u}(\boldsymbol{x}) - I_0(\boldsymbol{x})]^2 d\boldsymbol{x} \tag{7.1}$$

was minimized over the type A fiducial mask with a Gauss-Newton method [19].

As shown in Figure 7.3(a), the image registration procedure decreased the RMS residual on fiducial zones, making it less than 3% of dynamic range. However, several jumps in the residual remained, corresponding to discontinuities in the estimated kinematic parameters (Figure 7.3(a)). It is worth noting that such discontinuities occurred only when the system had to be reset, moving the cameras back into place and turning off the LED bar. They were also associated with significant time gaps, during which spurious light may arise, explaining why the residual variations were still visible after correction of camera motions. Changes in the way the

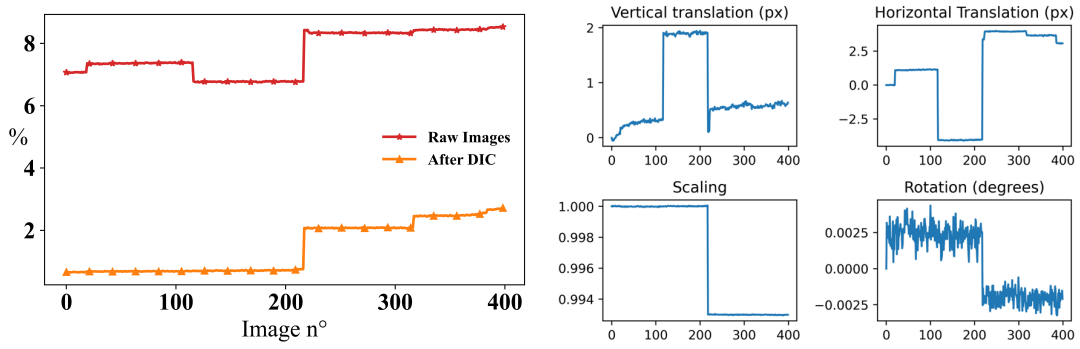

(a) (b)

Figure 7.3: (a) Normalized RMS residual on type B zones before (red) and after displacement correction (orange). (b) Transform parameters estimated during the displacement correction process.

sample was illuminated led to differences in gray levels of the images. To correct such variations, brightness and contrast fields b and c were introduced in the cost function [20]. In order to minimize the cost function $\Psi_1 = \int [(1 + c(\mathbf{x}))(I_n \circ \mathbf{\Phi})(\mathbf{x}) - I_0(\mathbf{x})]^2 d\mathbf{x}$, b and c are decomposed on a

polynomial basis of low degree (2 in the present case). The minimization is thus reduced to solving of a linear system. Here, the summation was performed on the type B fiducial mask, as the camera acquired images of the light scattered by the damage sites. Therefore, it is assumed that fiducials provided a similar response to illumination changes as the main damage site, while that of bulk silica is different. Such difference involved to use tightly segmented fiducials for an accurate estimation of the brightness and contrast fields.

The last correction was related to camera focus and consequently to image sharpness. The Tenengrad function on the segmented fiducials was used to estimate image sharpness [21]. Then images were convolved by a Gaussian kernel whose standard deviation was adjusted to equalize sharpness levels throughout the image sequence. Another effect of such correction was an overall decrease in RMS residual values since the convolution smoothed out acquisition noise. After displacement, brightness, contrast and sharpness corrections, one variation in the RMS residual levels remained, as observed in Figure 7.4, but its amplitude decreased more than five-fold thanks to the image processing pipeline.

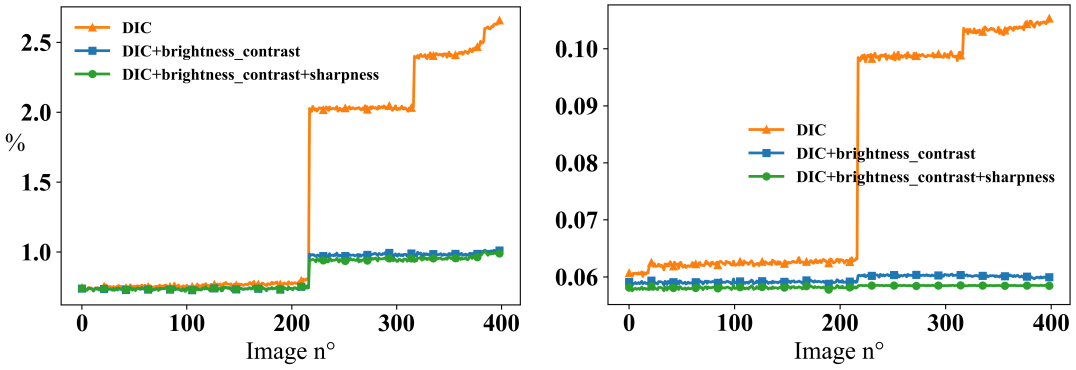

(a) (b)

Figure 7.4: (a) Normalized RMS residual on type B zones after displacement (orange), brightness and contrast (blue) and sharpness (green) correction for volume images. (b) Tenengrad sharpness on type B zones after displacement (orange), brightness and contrast (blue) and sharpness (green) corrections.

The surface images required less complex correction processing than the volume set of images. As shown in on Figure 7.5, after displacement and gray level corrections, no significant residual variations remained. Therefore, no further corrections were applied to surface images.

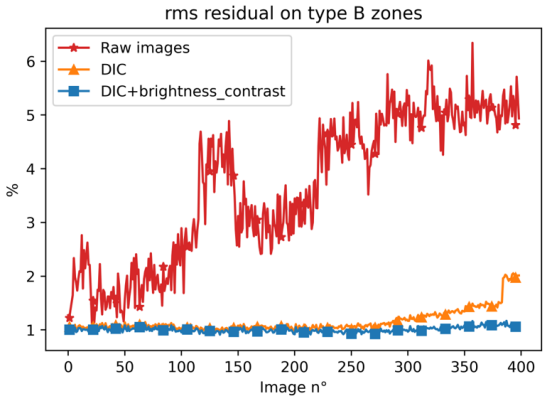

Figure 7.5: Normalized RMS residual on type B zones for surface images before (in red), after displacement (in orange) and after brightness and contrast correction (in blue) for surface images.

7.2.3 Feature extraction

To extract relevant features from both surface and volume images, the first step was to determine the outline of the main damage site in every image. In both types of images, the chosen segmentation method was the same. First, the outline of the damage site and its fractures were intensified through the use of a Sato filter [22]. Originating from medical image analysis, the Sato filter was designed to identify curvilinear structures, and it is thus adapted to heavily-fractured laser damage sites. The output of the filter was then subjected to a global thresholding, which, after contour selection, resulted to the mask containing the main damage site. The specific parameters of the Sato filter and of thresholding were determined empirically, and were the same for every damage site (although they differ between surface and volume images, as their dynamic ranges were different). An example of the proposed segmentation process of a volume image is shown on Figure 7.6.

The obtained mask was used for pixel-counting in surface images, which gave the apparent damage area A, as well as its equivalent diameter d, through

$$d = 2\sqrt{\frac{A}{\pi}}. \tag{7.2}$$

For each surface image, the RMS residual and the mean gray level were extracted from the damage mask. In volume images, the depth of the damage site was estimated with the farthest point to the face of the sample in the damage mask. The values for damage depth, surface and

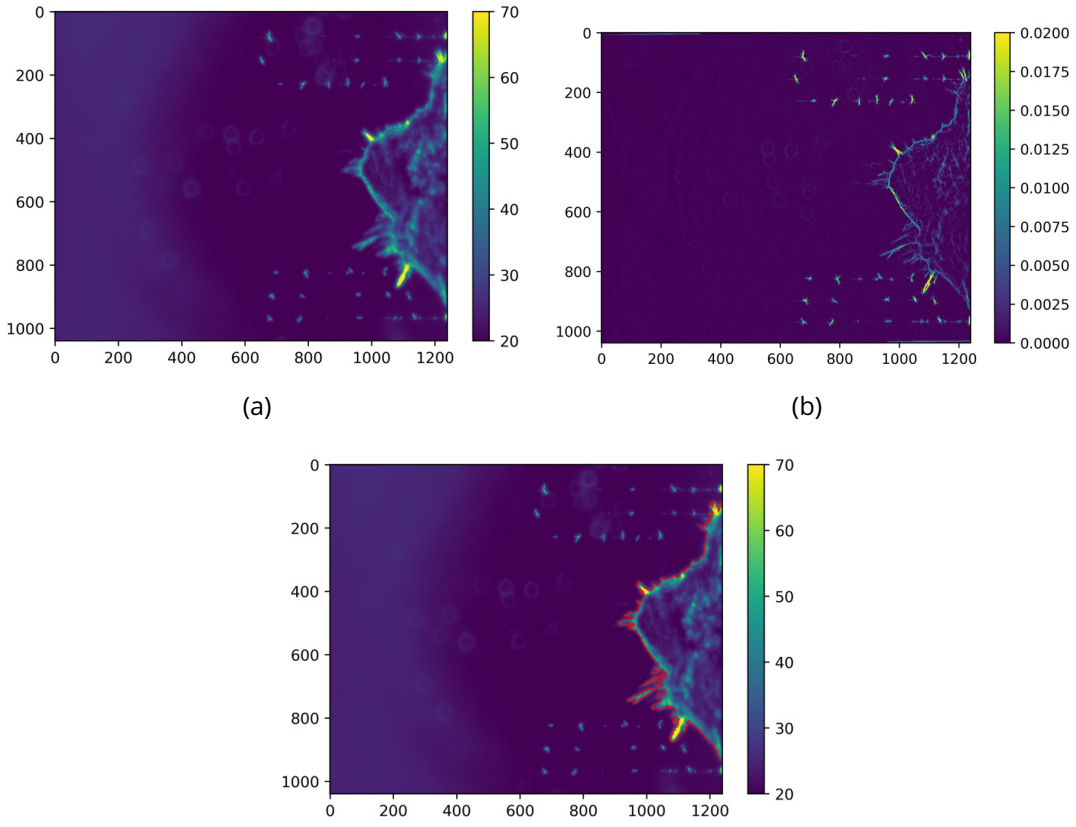

Figure 7.6: Steps of the segmentation process for a volume image: (a) original image, (b) output of Sato filter and (c) resulting contour in red.

equivalent diameter were converted into micrometres to be expressed on the same scale.

A fit method based on Bayesian Ridge Regression [23] was chosen to fit the data, using the mean gray level in the damage site on surface images as a corrective term for the diameter-based depth estimator. The resulting model gave an approximation of damage depth, Δ, as a linear combination of damage diameter, d and mean gray level in the damage area, $\overline{GL}$, with a constant additive parameter γ.

$$\Delta = \alpha d + \beta \overline{GL} + \gamma \tag{7.3}$$

7.3 Results and discussion

The estimator of damage depth based on the damage diameter or using the proposed model (Equation (7.3)) were evaluated according to the R^2 scores reported in Table 1. The R^2 estimator, or Pearson correlation coefficient, is the score that quantifies the quality of a linear regression. A perfect regression involves an R^2 score equal to 1. The R^2 scores were calculated between the true depth measured on the images (in blue in Figure 7.7) and the depth given by the different estimators: third of diameter (in red) or the proposed model trained on different data sets (B in orange and D in green). Sites 3 and 4 are well described by the depth estimator based on third of diameter, with R^2 scores of 0.96 and 0.97. Site 2, having an R^2 score equal to 0.92, experienced phases with plateaus in bulk growth and continued surface growth, which is described by the third of diameter estimator. Depth of site 1 on the other hand cannot be described solely with the damage diameter, as shown by an R^2 score of only 0.46, mainly because of a large Veinhard plateau during the growth sequence. The estimator of damage depth based on the third of diameter is equivalent to the proposed model (Equation (7.3)) with $\alpha = 0.33$ and $\beta = \gamma = 0$. When $\beta = 0$, the influence of damage depth on the gray levels is ignored.

Table 7.1: R^2 score on each site, and relative weight of parameters for different estimators. Grayed out cells indicate the damage sites used in the training set for Bayesian ridge regression. *e.g.,* For training set A, sites 1 and 2 were used to estimate parameter weights.

	R^2 score				Parameter weights		
Training set	Site 1	Site 2	Site 3	Site 4	d (α)	$\overline{GL}$ (β)	γ
A	0.93	0.98	0.92	0.74	0.33	5.04	-72.3
B	0.89	0.97	0.98	0.91	0.32	3.53	-34.0
C	0.87	0.98	0.98	0.92	0.33	3.33	-26.0
D	0.70	0.95	0.98	0.98	0.34	0.78	+3.4
E	0.87	0.98	0.98	0.93	0.32	3.13	-24.0
$\frac{d}{3}$	0.46	0.92	0.96	0.97	0.33	0	0

For any training set used to estimate the model weights, the coefficient α, corresponding to the importance given to the diameter in the depth estimation, is always equal to 0.33. The proposed model can thus be construed as a correction to the base depth estimator (a third of the

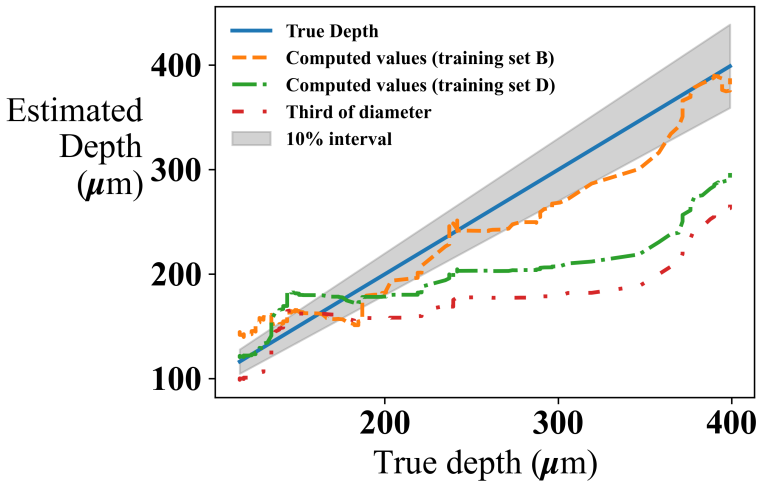

(a)

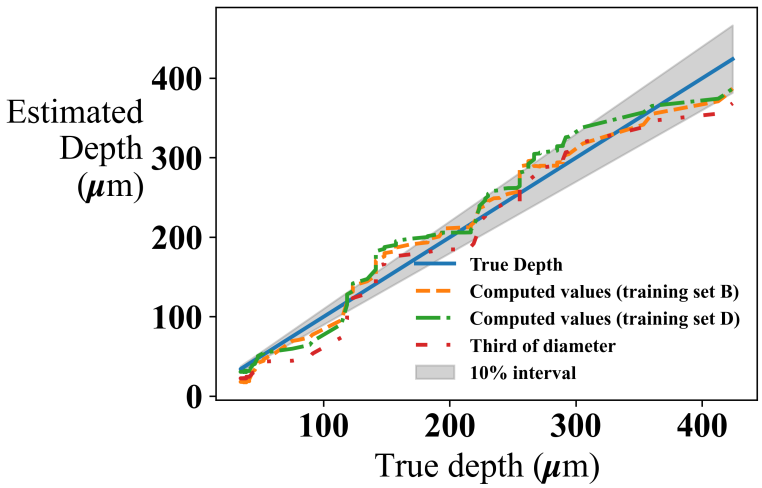

(b)

Figure 7.7: Graph of true damage depth against estimates given by a third of the damage diameter (red), regression based on gray level and diameter on training on set B (orange) and on set D (green) for (a) site 1 and (b) site 4. Diameter and depth increased in a similar way for site 4. For site 1, depth increased while diameter was constant.

damage diameter) with an affine function of mean gray level. The fact that the β parameter, as shown in Table 1, is always strictly positive, denotes a positive correlation between the optical power scattered by a damage site and its depth. This is in line with the conclusions of Ref. [24], where

it was reported that the scattered power was approximately proportional to the square of the pit depth.

For damage sites whose growth follows the third of diameter law, the mean gray level is strictly positive, thus, the correction given by the βGL_m term of Equation (7.3) leads to a systematic overestimation of the damage depth, which needs to be compensated. This result explains why, as observed in Table 1, the higher the β value, the more negative γ. The corrective affine function $\beta GL_m + \gamma$ thus affects the shape of the depth function over successive laser shots, without drastically increasing its values.

The damage sites used for estimating the parameters of the proposed model have an important impact on its efficiency. By choosing to fit the model using only sites 3 and 4 (set D), for which surface and volume growths were highly correlated, the resulting model cannot describe depth of site 1 (R^2 score of 0.67), as its Veinhard plateau involves a decorrelation between surface and volume growth. The relative weights for mean and total gray levels are far smaller than that of the damage diameter, as seen in Table 1, which explains the proximity between the depth estimated with training set D and that with a third of the diameter observed in Figure 7.7. The mean gray level is not used by the model.

Table 1 shows that besides training set E, which uses all the available data, the overall best fits are obtained using training sets B and C. They both combine a damage site well described by the classical depth estimator (site 3), with another one that experienced different growth (site 1 for set B and site 2 for set C). The β parameter took an intermediate value between that obtained with training sets A and D, allowing the resulting model to satisfyingly describe all four sites. This observation highlights the importance of having access to a wide variety of growth regimes and damage morphologies in order to calibrate the proposed model to quantitatively estimate damage depth.

7.4 Conclusion

Laser damage growth experiments described in the present work show that the conventional relationship of proportionality between damage diameter and depth is not accurate for every damage site. Such relationship was enriched by taking into account gray level variations.

Gray levels in surface images are an efficient indicator of damage growth on the surface and in the bulk even in cases when the damage area appears constant through pixel-counting. By only using the damage size

on surface images as a damage growth indicator, laser damage sequence experimenters take the risk of considering a damage site as constant, even though it still grows predominantly in its bulk. The damage growth probabilities may therefore be underestimated. The analysis of gray levels in surface images allows this pitfall to be avoided. It was demonstrated that increasing damage depth with a constant diameter was observable only with surface images by taking into account gray level increases.

It was also proven that after a calibration of the system, it was possible to quantitatively estimate the damage depth only using a linear combination of surface diameter and gray level. However, such calibration requires a damage growing sequence with a wide variety of growth regimes including Veinhard plateaus to be able to describe any damage site. The use of gray level analysis coupled with widely used pixel-counting methods may lead to more accurate damage growth laws.

References

[1] L. Lamaignère, G. Dupuy, A. Bourgeade, A. Benoist, A. Roques, and R. Courchinoux, "Damage growth in fused silica optics at 351 nm: refined modeling of large-beam experiments," *Applied Physics B: Lasers and Optics*, vol. 114, no. 4, pp. 517–526, Mar. 2014. doi: 10.1007/s00340-013-5555-6.

[2] K. Manes, M. Spaeth, J. Adams, and M. Bowers, "Damage mechanisms avoided or managed for nif large optics," *Fusion Science and Technology*, vol. 69, pp. 146–249, Feb. 2016. doi: 10.13182/FST15-139.

[3] R. Courchinoux *et al.*, "Laser-induced damage growth with small and large beams: comparison between laboratory experiments and large-scale laser data," in *Laser-Induced Damage in Optical Materials: 2003*, G. J. Exarhos, A. H. Guenther, N. Kaiser, K. L. Lewis, M. J. Soileau, and C. J. Stolz, Eds., International Society for Optics and Photonics, vol. 5273, SPIE, 2004, pp. 99–106. doi: 10.1117/12.524844. [Online]. Available: https://doi.org/10.1117/12.524844.

[4] R. A. Negres, M. A. Norton, D. A. Cross, and C. W. Carr, "Growth behavior of laser-induced damage on fused silica optics under uv, ns laser irradiation," *Optics Express*, vol. 18, no. 19, pp. 19 966–19 976, Sep. 2010. doi: 10.1364/OE.18.019966. [Online]. Available: http://www.opticsexpress.org/abstract.cfm?URI=oe-18-19-19966.

[5] L. Lamaignere, S. Reyne, M. Loiseau, J.-C. Poncetta, and H. Bercegol, "Effects of wavelengths combination on initiation and growth of laser-induced surface damage in SiO2," in *Laser-Induced Damage in Optical Materials: 2007*, G. J. Exarhos, A. H. Guenther, K. L. Lewis, D. Ristau, M. J. Soileau, and C. J. Stolz, Eds., International Society for Optics and Photonics, vol. 6720, SPIE, 2007, pp. 150–158. doi: 10.1117/12.753057. [Online]. Available: https://doi.org/10.1117/12.753057.

[6] M. A. Norton *et al.*, "Growth of laser-initiated damage in fused silica at 351 nm," in *Laser-Induced Damage in Optical Materials: 2000*, G. J. Exarhos, A. H. Guenther, M. R. Kozlowski, K. L. Lewis, and M. J. Soileau, Eds., International Society for Optics and Photonics, vol. 4347, SPIE, 2001, pp. 468–468. doi: 10.1117/12.425055. [Online]. Available: https://doi.org/10.1117/12.425055.

[7] M. A. Norton, E. E. Donohue, W. G. Hollingsworth, M. D. Feit, A. M. Rubenchik, and R. P. Hackel, "Growth of laser initiated damage in fused silica at 1053 nm," in *Laser-Induced Damage in Optical Materials: 2004*, G. J. Exarhos, A. H. Guenther, N. Kaiser, K. L. Lewis, M. J. Soileau, and C. J. Stolz, Eds., International Society for Optics and Photonics, vol. 5647, SPIE, 2005, pp. 197–205. doi: 10.1117/12.585930. [Online]. Available: https://doi.org/10.1117/12.585930.

[8] M. A. Norton *et al.*, "Growth of laser damage in fused silica: diameter to depth ratio," in *Laser-Induced Damage in Optical Materials: 2007*, G. J. Exarhos, A. H. Guenther, K. L. Lewis, D. Ristau, M. J. Soileau, and C. J. Stolz, Eds., International Society for Optics and Photonics, vol. 6720, SPIE, 2007, pp. 165–174. doi: 10.1117/12.748441. [Online]. Available: https://doi.org/10.1117/12.748441.

[9] M. Veinhard, O. Bonville, R. Courchinoux, R. Parreault, J.-Y. Natoli, and L. Lamaignère, "Parametric study of laser-induced damage growth in fused silica optics with large beams at 351nm. part 2: fractal analysis," *Appl. Opt.*, vol. 59, no. 31, pp. 9652–9659, Nov. 2020. doi: 10.1364/AO.400696. [Online]. Available: http://opg.optica.org/ao/abstract.cfm?URI=ao-59-31-9652.

[10] A. Conder, J. Chang, L. Kegelmeyer, M. Spaeth, and P. Whitman, "Final optics damage inspection (FODI) for the National Ignition Facility," in *Optics and Photonics for Information Processing IV*, A. A. S. Awwal, K. M. Iftekharuddin, and S. C. Burkhart, Eds., International Society for Optics and Photonics, vol. 7797, SPIE, 2010, pp. 167–178. doi: 10.1117/12.862596. [Online]. Available: https://doi.org/10.1117/12.862596.

[11] G. Hallo, C. Lacombe, R. Parreault, *et al.*, "Sub-pixel detection of laser-induced damage and its growth on fused silica optics using registration residuals," *Opt. Express*, vol. 29, no. 22, pp. 35 820–35 836, Nov. 2021. doi: 10.1364/OE.433862. [Online]. Available: http://opg.optica.org/oe/abstract.cfm?URI=oe-29-22-35820.

[12] L. Lamaignère *et al.*, "A powerful tool for comparing different test procedures to measure the probability and density of laser induced damage on optical materials," *Review of Scientific Instruments*, vol. 90, no. 12, 125102, p. 125 102, Dec. 2019. doi: 10.1063/1.5122274.

[13] M. Veinhard, O. Bonville, R. Courchinoux, R. Parreault, J.-Y. Natoli, and L. Lamaignère, "MELBA: a fully customizable laser for damage experiments," in *Laser-Induced Damage in Optical Materials 2017*, G. J. Exarhos, V. E. Gruzdev, J. A. Menapace, D. Ristau, and M. Soileau, Eds., International Society for Optics and Photonics, vol. 10447, SPIE, 2017, pp. 151–157. [Online]. Available: https://doi.org/10.1117/12.2281125.

[14] M. Veinhard *et al.*, "Parametric study of laser-induced damage growth in fused silica optics with large beams at 351nm. Part 1: stochastic approach," *Appl. Opt.*, vol. 59, no. 31, pp. 9643–9651, Nov. 2020. doi: 10.1364/AO.400691. [Online]. Available: http://ao.osa.org/abstract.cfm?URI=ao-59-31-9643.

[15] A. Ollé *et al.*, "Implications of laser beam metrology on laser damage temporal scaling law for dielectric materials in the picosecond regime," *Review of Scientific Instruments*, vol. 90, no. 7, p. 073 001, 2019. doi: 10.1063/1.5094774. eprint: https://doi.org/10.1063/1.5094774. [Online]. Available: https://doi.org/10.1063/1.5094774.

[16] K. Gaudfrin, R. Diaz, G. Beaugrand, S. Bucourt, and R. Kling, "Adaptive optics for intra-volume engraving of glass with ultra-short laser pulses," *International Congress on Applications of Lasers & Electro-Optics*, vol. 2017, no. 1, p. M405, 2017. doi: 10.2351/1.5138168. eprint: https://lia.scitation.org/doi/pdf/10.2351/1.5138168. [Online]. Available: https://lia.scitation.org/doi/abs/10.2351/1.5138168.

[17] F. Hild and S. Roux, "Digital image correlation," in *Optical Methods for Solid Mechanics. A Full-Field Approach*, P. Rastogi and E. Hack, Eds., Weinheim (Germany): Wiley-VCH, 2012, pp. 183–228.

[18] N. Otsu, "A threshold selection method from gray-level histograms," *IEEE Transactions on Systems, Man, and Cybernetics*, vol. 9, no. 1, pp. 62–66, 1979. doi: 10.1109/TSMC.1979.4310076.

[19] J. Neggers, B. Blaysat, J. P. M. Hoefnagels, and M. G. D. Geers, "On image gradients in digital image correlation," *International Journal for Numerical Methods in Biomedical Engineering*, vol. 105, no. 4, pp. 243–260, 2016. doi: 10.1002/nme.4971. [Online]. Available: https://hal.archives-ouvertes.fr/hal-03261191.

[20] V. Sciuti, R. Canto, J. Neggers, and F. Hild, "On the benefits of correcting brightness and contrast in global digital image correlation: monitoring cracks during curing and drying of a refractory castable," *Optics and Lasers in Engineering*, vol. 136, p. 106 316, 2021, issn: 0143-8166. doi: https://doi.org/10.1016/j.optlaseng.2020.106316. [Online]. Available: http://www.sciencedirect.com/science/article/pii/S0143816620305686.

[21] T. Yeo, S. Ong, Jayasooriah, and R. Sinniah, "Autofocusing for tissue microscopy," *Image and Vision Computing*, vol. 11, no. 10, pp. 629–639, 1993, issn: 0262-8856. doi: https://doi.org/10.1016/0262-8856(93)90059-P. [Online]. Available: https://www.sciencedirect.com/science/article/pii/026288569390059P.

[22] Y. Sato *et al.*, "Three-dimensional multi-scale line filter for segmentation and visualization of curvilinear structures in medical images," *Medical Image Analysis*, vol. 2, no. 2, pp. 143–168, 1998, issn: 1361-8415. doi: https://doi.org/10.1016/S1361-8415(98)80009-1. [Online]. Available: https://www.sciencedirect.com/science/article/pii/S1361841598800091.

[23] G. C. McDonald, "Ridge regression," *WIREs Computational Statistics*, vol. 1, no. 1, pp. 93–100, 2009. doi: https://doi.org/10.1002/wics.14. eprint: https://wires.onlinelibrary.wiley.com/doi/pdf/10.1002/wics.14. [Online]. Available: https://wires.onlinelibrary.wiley.com/doi/abs/10.1002/wics.14.

[24] E. Feigenbaum, S. Elhadj, and M. J. Matthews, "Light scattering from laser induced pit ensembles on high power laser optics," *Opt. Express*, vol. 23, no. 8, pp. 10 589–10 597, Apr. 2015. doi: 10.1364/OE.23.010589. [Online]. Available: http://opg.optica.org/oe/abstract.cfm?URI=oe-23-8-10589.

Part V

Conclusion and future work

8

Conclusion and perspectives

The aim of this work was to optimize in-situ detection and monitoring of laser-induced damage initiation and growth on final optics of megajoule class laser facilities such as National Ignition Facility, ShenGuang-III and Laser MegaJoule. In order to limit the impact of damage sites on the operation and laser performances of such facilities, a recycling loop is currently in development for LMJ damaged optics. The effectiveness of this recycling process relies in part on the ability to monitor the growth of laser damage sites with diameters ranging from $10\,\mu\mathrm{m}$ to $750\,\mu\mathrm{m}$. Since the spatial resolution of in-situ acquired images is $\approx 100\,\mu\mathrm{m}$/pixel, sub-pixel resolution is needed for damage growth monitoring.

The work carried out during this thesis had for objectives to:

1. **Measure damage size with sub-pixel resolution** on in-situ images;

2. **Ensure that the diameter measurement is stable over time** by accounting for motions and modifications of lighting and image acquisition systems.

An original calibration process, a new lighting system design and image correction algorithms were explored to reach these objectives. The proposed algorithms were applied to vacuum window images acquired during their operation on the Laser MegaJoule facility and validated with images that were acquired during dedicated laser damage experiments performed on a highly instrumented set-up. The major results are detailed hereafter.

8.1 Major results

Estimation of damage diameters with sub-pixel resolution

It was demonstrated that measuring diameters of damage sites by pixel-counting methods was not sufficient to monitor damage sites from $10\,\mu m$ to $300\,\mu m$ in diameter with in-situ images. The demonstration was based on the analysis of an acquired image of a specific vacuum window with more than 930 damage sites whose diameters were well known. A diameter estimation method based on pixel intensities after an experimental calibration process was proposed for NIF optics. It consisted in measuring in-situ the light intensity emitted by damaged sites for different damage sizes. The diameter estimation by pixel intensities was adapted to the case of images of LMJ vacuum windows. It was experimentally performed by using a damaged vacuum window as a calibration reference.

A new calibration process taking benefit of optical modeling was proposed, which is faster and less time consuming than the experimental method. The procedure was based on modeling the lighting and image acquisition systems and measuring the light scattering signature of laser damage sites. In the case of images without disturbances and after calibration by experiment or modeling, the diameter estimation by the pixel intensity method was compatible with the need for accuracy for damage growth monitoring. However, disturbances regularly occur such as lighting system extinction, image displacement and pixel intensity variation.

Robust damage diameter measurements over time

The issue of accurate comparison of pixel intensity between successive images of the same optical component was addressed by lighting system modifications and image registration algorithms.

First, a new lighting system was designed by a student during its apprenticeship. The aim was to improve the homogeneity of the incident light on the damaged face of a vacuum window and the robustness of the system to electromagnetic interactions between laser beams and the experiment target. Both LEDs were replaced by a unique fiber optic source equipped with a lens. A convex reflector was inserted in the aluminum alloy maintaining frame. The performances of the proposed lighting system were simulated using the model used to numerically calibrate the measured pixel intensities on damage diameters. It was shown that the proposed lighting system improved by a factor 4 the homogeneity of incident light

on the damaged face of a vacuum window. The implementation of such system may improve damage growth monitoring on LMJ vacuum windows.

Second, image processing techniques mainly based on Digital Image Correlation principles were proposed. The aim was to correct as much as possible for image disturbances without any hardware modification. A global and integrated Digital Image Correlation (DIC) approach was proposed and validated on a set of LMJ vacuum window images. The displacement fields, describing similarity transformations (in-plane translations, rotation and scaling), were estimated on stable markers engraved in the four corners of vacuum windows. The sub-pixel resolution of image registration was validated with a dedicated experiment on a highly instrumented laser damage set-up. A generic approach based on low-order polynomial fields was proposed to correct for brightness and contrast variations between successive images of the same vacuum window. However, it was demonstrated that this generic brightness and contrast correction was limited to low spatial frequency intensity variation in brightness. Such generic corrections did not sufficiently correct for LED extinction and occurrence of background features in the images. A more specific brightness and contrast correction process was proposed. The brightness correction was based on Proper Orthogonal Decomposition (POD) of a set of acquired images. The contrast correction fields were estimated by modeling the LED lighting system in order to correct for LED extinction. It is worth noting that one of the limitations of the POD-based method is the representativeness of the image set used to generate the basis of the correction modes. The effectiveness of the contrast correction based on the optical model mainly relied on the accurate and successful spatial registration of the LED modes on the images to be corrected. Such aspects are discussed in the future works.

After displacement, brightness and contrast corrections, residual maps mainly described damage initiation and growth. A simple thresholding technique such as Otsu algorithm applied on residual maps was efficient to detect initiation and growth of damage sites that occured between after each laser shot. The presented works provided an original meeting point between Digital Image Correlation principles and in-situ laser-induced damage growth monitoring on megajoule class laser facilities.

From pixel intensities and damage diameter to damage morphology

Most of the carried out work tackled the problem of in-situ damage monitoring on megajoule class laser facilities. The objective was to extend the field of application of the proposed methods to laser damage metrology performed on dedicated damage set-ups. The analysis of data acquired during a damage growth experiment on a highly instrumented laser damage set-up demonstrated that the growth sequence was observed on pixel intensity variations before damage diameter measurements. An original damage growth experiment was conducted to acquire surface and bulk images after each laser shot. Images of surface and bulk were spatially registered using the algorithm proposed in Chapter 4. It was demonstrated that increasing damage depth without diameter variation was described by pixel intensity increase on surface images. It was shown that damage depth of sites was well described by linear combinations between damage diameter and pixel intensity. Such results pave the way to a simple monitoring of depth variations of damage sites from only surface images of the sample with better accuracy than the commonly used aspect ratio.

8.2 Discussion and future works

It was evidenced that damage growth monitoring over time by pixel intensities was efficient after image registration based on DIC principles and brightness and contrast corrections. The first proposed brightness and contrast correction involved low-order polynomial fields. However, such polynomial description did not describe high spatial frequency variations. To overcome this limit, brightness and contrast correction based on POD and optical modeling of the lighting system were proposed. It was shown that this second correction of pixel intensity was more adapted to vacuum window images than low-order polynomial method. However, it was only validated on a few samples of images. It may be interesting to validate the specific method on other sets of images. It is also important to ensure that the POD modes describe sufficiently the disturbances affecting pixel intensities of the acquired images. It is then necessary to regularly update the POD basis by periodically adding new images to the brightness mode evaluations. Regarding contrast corrections using the optical model of the lighting system, the main issue is to ensure accurate and successful spatial registrations of the LED modes on the images to be corrected. The algorithm proposed to register vacuum window images on the reference

image may be adapted to register the LED modes to the image to be corrected.

After the proposed algorithm has been fully automated and validated on a large number of images, the next step concerns the industrialization of the algorithm and its integration into the LMJ operating tools. It should be useful to work on accelerating the proposed image processing pipeline. The final aim is to process all already acquired images and in real-time the images acquired after each laser shot. Based on the analysis of damage growth from corrected images, it will then be possible to evaluate the impact of each damage site on the life span of the optics. This analysis could be performed by machine learning techniques when the data will be prepared and numerous enough.

The estimation of damage diameters could be more robust and stable over time by modifying the lighting system as proposed in Chapter 3. The modification of the lighting system implies to remove the 176 optical frames, modify each of these frames, install the new lighting system and mount the modified frame on the facility. In order to assess the validity of such mechanical modifications, it would be interesting to compare the cost of lighting system modifications with the induced saving of new optics by the modification. If the operation gain is deemed sufficient, then the lighting system should be modified after experimental validation.

The LMJ focusing gratings are also equipped with an edge illumination (two red LEDs) to make visible damage sites on these optics. The image correction algorithms and calibration process by optical modeling proposed for vacuum window images may be adapted to grating images. However, the gratings do not have fiducials etched in their corners. Such fiducials on vacuum windows were used to spatially register images. It will therefore be necessary to work on the registration of grating images without fiducials. One idea is to use existing damage sites on the gratings as fidicials. In any case, the etching of fiducials on the gratings should be considered.

The observation of vacuum windows and focusing gratings is based on the collection of light scattered from damage sites with edge illumination. Other imaging methods could be studied. What would be the impact of polarization imaging on damage monitoring performance? Would strioscopic imaging reduce the background variations of in-situ damage images? It would be possible to estimate the potential performance gains of different imaging modes experimentally or by optical modeling as it was performed for the light scattering method.

The proposed algorithms may also be adapted to other imaging techniques of damage sites such as bright and dark field images with back

illumination. Such imaging techniques are already available at LMJ to observe the optics of the amplifying and transport sections. Back illumination is based on backlighting of the optics by a non-amplified laser pulse.

In a bright field with back illumination image, a damage site is visible as an interference pattern between the plane wave of the beam and the spherical wave generated by the damage site. To acquire dark field images with back illumination, a stop object is used to transmit only the high spatial frequencies of the bright field image according to the strioscopy (Schlieren imaging) principle.

Dark field with back illumination images are acquired periodically to observe the optics of the LMJ amplifying section. Work is currently in progress to automatically analyze such images and monitor damage of the optics of the amplifying section. Some methods and algorithms presented in the previous chapters, such as spatial registration and brightness and contrast corrections, may be adapted to images of the amplifying section.

The results related to damage depth estimation from surface images, adapted to damage testing set-up equipped with light scattering imaging system providing high spatial resolution images were promising. It would be interesting to study a larger set of damage sites in order to validate and refine the obtained results. Damage growth investigations only focused on damage diameter. With the proposed damage depth estimation method, new damage growth experiments could be performed with an interest in damage depth and diameter, with only a surface imaging system.

The proposed calibration process and algorithms make in-situ damage growth monitoring more precise. This accuracy improvement will allow to fine tune the use of beamblockers. Thus, damaged optics will be sent to the mitigation loop in an optimized way. The work carried out during this thesis should make it possible to reduce the operating cost by reducing the number of new optics required each year on installations such as Laser MegaJoule and potentially National Ignition Facility and ShenGuang-III.

Part VI

Appendices

This part is organised in 4 appendices.

Damage growth experiments using the MELBA set-up were performed at shot per $60\,\mathrm{s}$. In Appendix A, it is proposed to ensure that the representativeness of MELBA compared to LMJ is not altered by the shot frequency of MELBA and thus by thermal effects on damage sites. The aim was to check that the time taken by a damage site to recover its initial temperature after a laser shot was less than the time between two successive shots ($60\,\mathrm{s}$). Thermal measurements on a damage site were performed during and after a laser shot in the UV range and ns pulse duration on the MELBA set-up.

In Appendix B, I describe my experiences in science communication such as my participation to “La Fabrique Defense 2022” forum and the article I wrote for the journal “Chocs Avancées n°16”.

In Appendix C, the article I wrote for the journal “Chocs Focus” is reproduced. It gives an overview of the methods and devices used to in-situ monitor damaged optics in the LMJ facility: from the amplifying section to transport and frequency conversion sections.

Appendix D summarizes the different articles published during my thesis as well as my participation in national and international conferences.

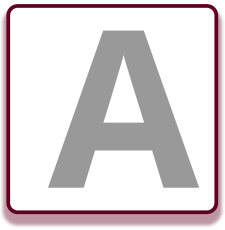

Damage temperature measurements under pulsed laser shots

For fused silica optics, laser-induced damage thresholds vary with the temperature of the sample. Laser damage initiation is associated with a sudden temperature increase of initiation. For damage growth experiments, a damage site was subjected to high energy laser shots at defined frequency. This shot frequency is generally between $0.01\,\mathrm{Hz}$ *and* $10\,\mathrm{Hz}$*. In this appendix, thermal measurements of a damage site, performed during a laser shot (nanosecond pulse duration and ultraviolet wavelength), are presented. It is demonstrated that the temperature of a damage site recovered its initial value over a period of about* $3\,\mathrm{s}$ *after the laser shot. As a consequence, damage growth experiments performed at a frequency less than* $0.3\,\mathrm{Hz}$ *are not affected by thermal variations. For frequencies greater than* $0.3\,\mathrm{Hz}$*, the impact of the damage temperature should be studied in more details.*

A.1 Introduction

When laser damage growth experiments were performed on the MELBA laser set-up, the period between two successive laser shots was about $1\,\mathrm{min}$ [1]. The LMJ optics are exposed to high energy laser beam only every $3\,\mathrm{h}$ [2]. Laser parameters, such as pulse duration, wavelength, fluence and temporal profile, encountered by a damage site on the MELBA set-up are considered representative of those used during LMJ high energy laser shots [1]. Laser damage initiation is due to defects in fused silica optics [3]. Such defects absorb a part of the UV laser energy. Thus, the temperature increase would be more than $5000\,\mathrm{K}$ [3]. It was measured that $100\,\mathrm{ns}$ after a laser pulse (wavelength of $355\,\mathrm{ns}$, pulse duration of $2.7\,\mathrm{ns}$ and fluence of $16\,\mathrm{J\,cm^{-2}}$), the temperature of a damage site in fused silica optics was about $4700\,\mathrm{K}$ [4]. It was shown that laser-induced damage thresholds (LIDT) decreased by heating fused silica samples [5]. When the temperature of fused silica increased from $120\,\mathrm{K}$ to $480\,\mathrm{K}$, the damage threshold decreased from about $30\,\mathrm{J\,cm^{-2}}$ to $20\,\mathrm{J\,cm^{-2}}$. Thermal variations of fused silica have a strong effect on laser damage initiation and they may decrease the damage growth threshold. It is, thus, necessary to check that the thermal transient, of a laser damage site does not alter the damage growth mechanisms observed on MELBA compared to those encountered on the LMJ facility.

Non-contact thermal measurements are used to measure thermal effects on an object without physical contact between the object and the sensor. Non-contact sensors for thermal measurements include radiation thermometers, fiber optics temperature sensors, optical pyrometers and thermal imagers [6]. Optical pyrometers provide only a single value while thermal imagers generate images. An infrared camera acquires an image of the infrared radiance emitted by an object. The higher the temperature of the object, the higher the radiance. The thermal radiation spontaneously emitted by many objects can be approximated as black-body radiation [7]. Since the LMJ final optics are fused silica components, they absorb higher wavelength than $5\,\mu\mathrm{m}$. Hence, IR imagers with spectral range greater than $5\,\mu\mathrm{m}$ are suitable for measuring temperature variations of damage sites after laser shots in fused silica components. As a first approximation, fused silica will be considered as a black body to estimate its temperature variations by infrared measurements.

It is proposed in this appendix to ensure that the representativeness of MELBA compared to LMJ was not altered by thermal effects on damage sites. The time of return to the initial temperature of the damage site

must be less than $1\,\mathrm{min}$. To achieve this objective, the time taken to return to thermal equilibrium of a damage site after a laser shot was measured using a thermal imaging camera. The configuration of the experimental set-up is detailed in Section A.2. The obtained results are presented and discussed in Section A.3.

A.2 Material and method

The experimental set-up (Figure A.1) is divided into three parts: the laser set-up, the visible light imaging system of the damage site, the thermal measurement device.

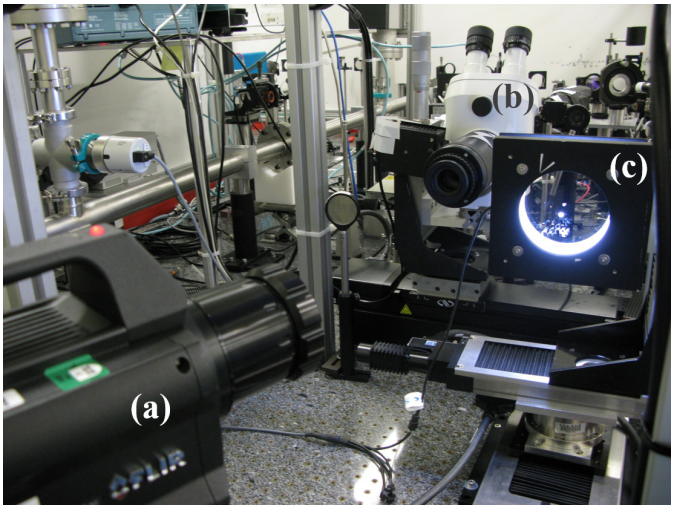

Figure A.1: Laser damage set-up MELBA with (a) a FLIR X6570sc thermal camera, (b) the visible light image acquisition system and (c) the fused silica sample in its support with the lighting system on.

The laser damage set-up MELBA was used to perform the damage growth sequence [8]. The laser beam was about $6\,\mathrm{mm}$ in diameter. This diameter ensured the whole damage site to be covered. The main properties of the laser beam are a pulse duration of $3\,\mathrm{ns}$, $351\,\mathrm{nm}$ wavelength and mean fluences between $2\,\mathrm{J\,cm^{-2}}$ and $10\,\mathrm{J\,cm^{-2}}$.

The damage site was observed after each laser shot using the surface imaging system described in Chapter 5. The spatial resolution in the imaging plane was $6.5\,\mu\mathrm{m}$/pixel.

Variations of temperature were acquired with a thermal imaging camera (FLIR X6570sc) [9]. The acquisition parameters for thermal variations are

given in Table A.1. To measure the temperature decrease of the damage site with sufficient temporal resolution, thermal images were acquired with frequencies of $120\,\mathrm{Hz}$ and $1200\,\mathrm{Hz}$. To obtain the acquisition frequency of $1200\,\mathrm{Hz}$, it was necessary to use the sub-window mode with a definition corresponding to 160x128 pixels. High frequency images ($1200\,\mathrm{Hz}$) were acquired to observe the temperature increase in the first moments after the laser shot while low frequency images ($120\,\mathrm{Hz}$) were used to estimate the time necessary for the damage site to recover its initial temperature. The temperature variations were calibrated using Planck's law of black-body radiation [7].

Table A.1: Parameters of the FLIR X6570sc camera used for the acquisition of thermal variations of a damage site after laser shots.

Parameters	**Values**
Spectral range	$7.7\,\mu\mathrm{m}$ - $9.3\,\mu\mathrm{m}$
Image acquisition frequency	$120\,\mathrm{Hz}$ (or $1200\,\mathrm{Hz}$)
Sensor frame (sub-window mode)	640 x 512 pixels (or 160 x 128 pixels)
Spatial resolution	$25\,\mu\mathrm{m}$/pixel (or $100\,\mu\mathrm{m}$/pixel)
Dynamic range	14 bit
Temperature calibration method	Black body hypothesis

The measurement process consists of several steps:

1. Beginning of the temperature image acquisition sequence;
2. Laser shot on the damage site;
3. End of the temperature image acquisition sequence;
4. Insertion of the visible light imaging system in front of the damage site;
5. Acquisition of a visible image of the damage site;
6. Removal of the visible light imaging system in front of the damage site.

A.3 Result and discussion

Temperature variations were measured over a total duration of $10\,\mathrm{s}$. The damage site was illuminated by the laser beam $4\,\mathrm{s}$ after the beginning

of the acquisition. These $4\,\mathrm{s}$ were described by the first 480 images of the acquisition sequence. A thermal image acquired before the laser shot is shown in Figure A.2(a). The temperature of the damage site at each acquisition time was defined as the maximum value in the corresponding image. The first 480 images (before laser excitation) were used to estimate the initial temperature of the damage site and the confidence interval on this value at $\pm\sigma$: $296.16 \pm 0.02\,\mathrm{K}$.

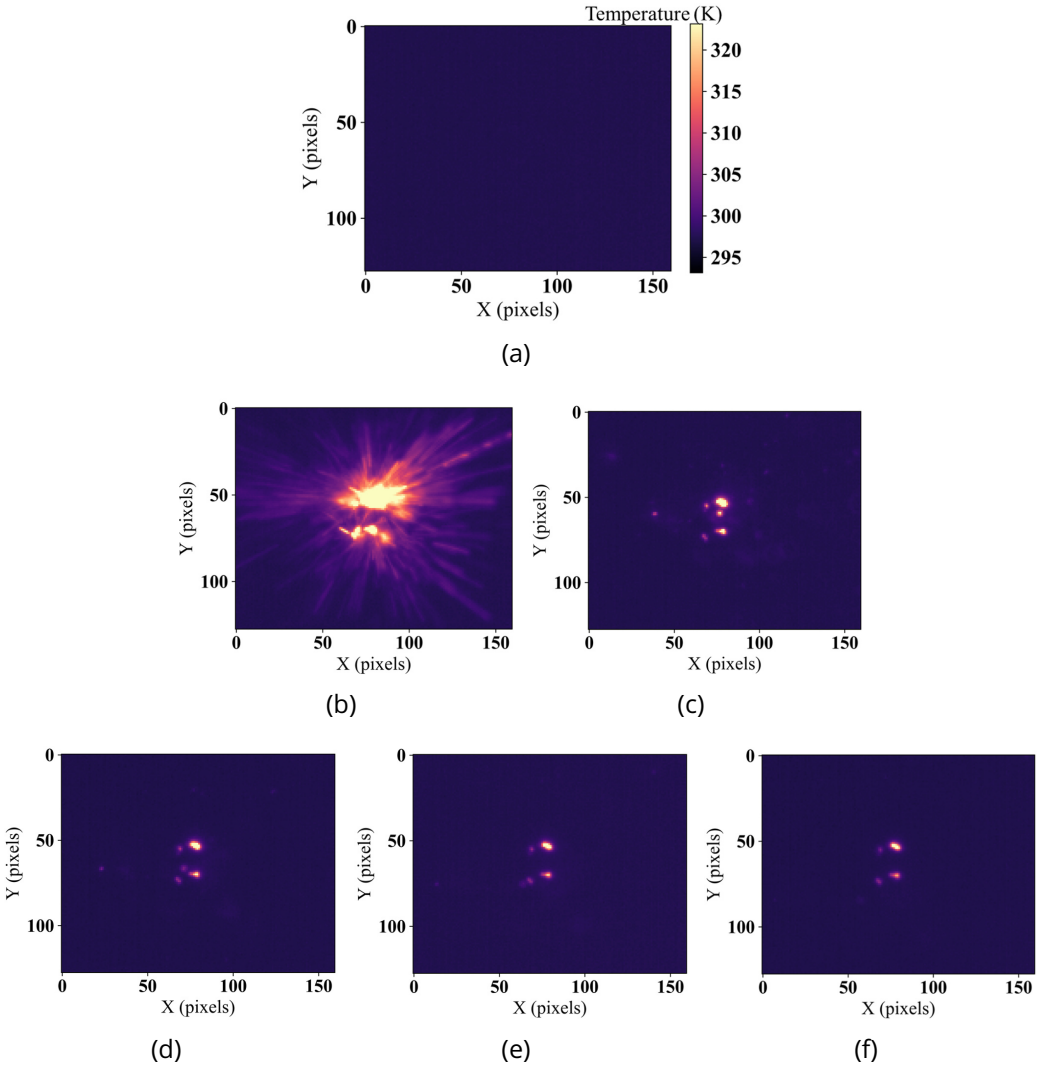

Figure A.2: Successive thermal images of a damage site during a laser shot. The acquisition frequency is $1200\,\mathrm{Hz}$. (a) Before laser shot. (b) First image $0.8\,\mathrm{ms}$ after laser shot. (c-f) Following images ($1.6\,\mathrm{ms}$, $2.4\,\mathrm{ms}$, $3.2\,\mathrm{ms}$ and $4\,\mathrm{ms}$ after laser shot).

The first 5 acquired images (frequency of $1200\,\mathrm{Hz}$) after laser shot are shown in Figure A.2(b-f). In these images, the emitted IR radiance by the damage site is visible in white. In Figure A.2(b), radial rays are observed corresponding to the ejection of hot silica particles as described in Refs. [10, 11]. Moving ejected particles are also visible in the following images. The maximum temperature, reached by the damage site, was measured at about $473\,\mathrm{K}$. This measured temperature was lower than the temperature of $12\,000\,\mathrm{K}$ measured in Ref. [4]. It was due to three main reasons:

- The time between 2 successive thermal acquisitions was $8\,\mathrm{ms}$. The first image was acquired between 0 and $8\,\mathrm{ms}$ after laser excitation while in Ref. [4] the time between two acquisitions was $5\,\mathrm{ns}$ during $0.1\,\mu\mathrm{s}$. The temperature decrease was fast just after the laser excitation, and the maximum measured temperature was not the maximum temperature reached by the damage site.

- The measured temperature was spatially and temporally integrated over the field of view of one pixel ($25\,\mu\mathrm{m}$x$25\,\mu\mathrm{m}$) and a period of $245\,\mu\mathrm{s}$. If the area of maximum temperature was smaller than the field of view of the pixel, the measured maximum temperature was lower than the true maximum value. Regarding the temporal integration, it was measured that the temperature decreased from $12\,000\,\mathrm{K}$ to about $4000\,\mathrm{K}$ over a period of $100\,\mu\mathrm{s}$ [4]. The FLIR camera used on MELBA did not allow to observe such large temperature variation in such a short time.

- The temperature was measured during damage growth of a large damage site (a few millimetres in diameter) while in Ref. [4] the temperature was measured during the initiation of damage sites (10 to $100\,\mu\mathrm{m}$ in diameter).

The variation of maximum temperature of the damage site over time is displayed in Figure A.3. In order to smoothen the measured values, a moving average over $60\,\mathrm{ms}$ was applied to the measured temperatures (in black in Figure A.3). The time taken by the damage site to recover its initial temperature (τ_{eq}) was defined as the first time from which the moving average of the temperature signal stayed within the measurement error of the initial temperature (the blue area). For this damage site, $\tau_{eq} = 3s$. The characteristic time τ_{eq} was much lower than the time between two laser shots on the MELBA set-up. Thus, thermal effects of damage sites have no influence on damage growth experiments performed on MELBA or other set-ups with longer periods between successive laser shots. However,

the thermal evolution of damage sites may have effects for laser set-ups operating at frequencies greater than $0.3\,\mathrm{Hz}$ for numerous laser shots. For an operating frequency of $2\,\mathrm{Hz}$, the initial temperature of the damage site may increase by about $0.1\,\mathrm{K}$ after each laser shot. After 10^4 laser shots, its temperature may be $393\,\mathrm{K}$ if its initial temperature was $293\,\mathrm{K}$ and linear accumulation applied. It would be appropriate to measure the evolution of the temperature of a damage site during a growth experiment at shot frequencies higher than $0.3\,\mathrm{Hz}$. According to Ref. [5], these temperature variations of fused silica may induce a variation of the damage threshold from $30\,\mathrm{J\,cm^{-2}}$ to $27\,\mathrm{J\,cm^{-2}}$, which is not negligible.

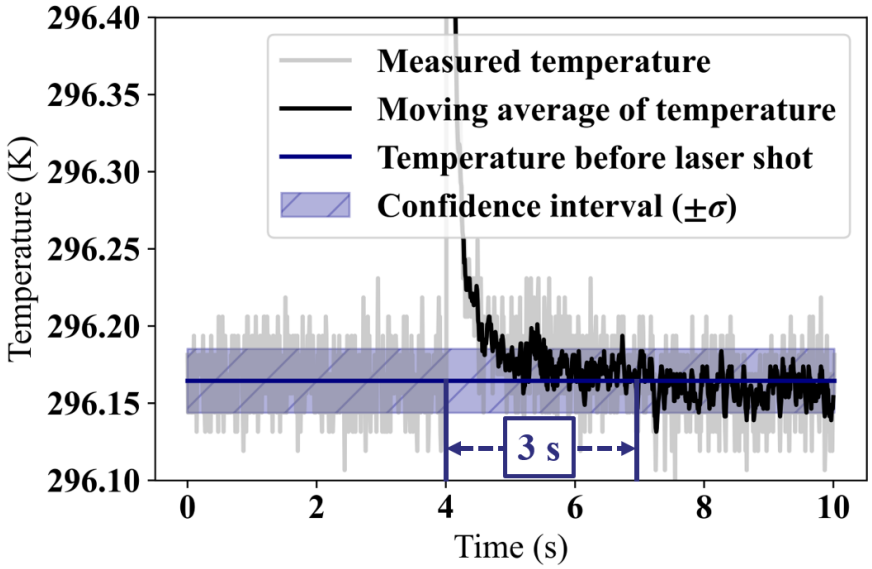

Figure A.3: Measured temperature variation of the studied damage site at a frequency of $120\,\mathrm{Hz}$ versus time in gray and its smoothed values in black. The temperature of the site before the laser shot is plotted in blue with the confidence interval at σ (blue area).

A.4 Conclusion

An experiment was performed on the MELBA set-up to measure the variation of temperature of a damage site exposed to a UV laser pulse at high fluence. An infrared camera allowed such temperature variations to be measured with sufficiently high temporal resolution. It was shown that a growing damage site under UV and ns laser excitation took about $3\,\mathrm{s}$

to recover its initial temperature. Since the operating shot frequency of MELBA set-up was 1 laser shot per $60\,\mathrm{s}$, thermal variations of a damage site after a laser shot had no impact on the results obtained during a damage growth experiment. However, for laser set-ups operating at shot frequency greater than $0.3\,\mathrm{Hz}$, the question is still open.

References

[1] M. Veinhard, O. Bonville, R. Courchinoux, R. Parreault, J.-Y. Natoli, and L. Lamaignère, "MELBA: a fully customizable laser for damage experiments," in *Laser-Induced Damage in Optical Materials 2017*, G. J. Exarhos, V. E. Gruzdev, J. A. Menapace, D. Ristau, and M. Soileau, Eds., International Society for Optics and Photonics, vol. 10447, SPIE, 2017, pp. 151–157. [Online]. Available: https://doi.org/10.1117/12.2281125.

[2] A. Casner *et al.*, "Lmj/petal laser facility: overview and opportunities for laboratory astrophysics," *High Energy Density Physics*, vol. 17, pp. 2–11, 2015, 10th International Conference on High Energy Density Laboratory Astrophysics, issn: 1574-1818. doi: https://doi.org/10.1016/j.hedp.2014.11.009. [Online]. Available: https://www.sciencedirect.com/science/article/pii/S1574181814000871.

[3] C. Bouyer, "Impact du profil temporel sur l'endommagement laser des composants de fin de chaîne en silice du lmj," Thèse de doctorat dirigée par Natoli, Jean-Yves, Ph.D. dissertation, 2022. [Online]. Available: http://www.theses.fr/s308491.

[4] C. W. Carr, H. B. Radousky, A. M. Rubenchik, M. D. Feit, and S. G. Demos, "Localized dynamics during laser-induced damage in optical materials," *Phys. Rev. Lett.*, vol. 92, p. 087 401, 8 Feb. 2004. doi: 10.1103/PhysRevLett.92.087401. [Online]. Available: https://link.aps.org/doi/10.1103/PhysRevLett.92.087401.

[5] K. Mikami, S. Motokoshi, M. Fujita, T. Jitsuno, J. Kawanaka, and R. Yasuhara, "Laser-induced damage thresholds in silica glasses at different temperature," in *Laser-Induced Damage in Optical Materials: 2009*, G. J. Exarhos, V. E. Gruzdev, D. Ristau, M. J. Soileau, and C. J. Stolz, Eds., International Society for Optics and Photonics, vol. 7504, SPIE, 2009, 75041R. doi: 10.1117/12.836350. [Online]. Available: https://doi.org/10.1117/12.836350.

[6] thomasnet.com. “Types of noncontact sensors.” (2022), [Online]. Available: https://www.thomasnet.com/articles/instruments-controls/types-of-noncontact-sensors/ (visited on 10/11/2022).

[7] M. Planck, *The theory of heat radiation*. Blakiston, 1914.

[8] M. Veinhard, O. Bonville, R. Courchinoux, R. Parreault, J.-Y. Natoli, and L. Lamaignère, “Quantification of laser-induced damage growth using fractal analysis,” *Opt. Lett.*, vol. 42, no. 24, pp. 5078–5081, Dec. 2017. doi: 10.1364/OL.42.005078. [Online]. Available: http://ol.osa.org/abstract.cfm?URI=ol-42-24-5078.

[9] FLIR. “Flir r&d/science cameras with mct detectors.” (2022), [Online]. Available: https://flir.netx.net/file/asset/10316/original (visited on 10/11/2022).

[10] S. G. Demos, R. N. Raman, and R. A. Negres, “Time-resolved imaging of processes associated with exit-surface damage growth in fused silica following exposure to nanosecond laser pulses,” *Opt. Express*, vol. 21, no. 4, pp. 4875–4888, Feb. 2013. doi: 10.1364/OE.21.004875. [Online]. Available: https://opg.optica.org/oe/abstract.cfm?URI=oe-21-4-4875.

[11] S. G. Demos, R. A. Negres, R. N. Raman, M. D. Feit, K. R. Manes, and A. M. Rubenchik, “Relaxation dynamics of nanosecond laser superheated material in dielectrics,” *Optica*, vol. 2, no. 8, pp. 765–772, Aug. 2015. doi: 10.1364/OPTICA.2.000765. [Online]. Available: https://opg.optica.org/optica/abstract.cfm?URI=optica-2-8-765.

B

Science education

In this chapter, my different experiences in science communication to audiences inexperienced in the field of laser damage and generally in science are discussed. Firstly, I was a speaker at the forum “La Fabrique Defense 2022”, organised by the French Ministry of Army at the end of January [1]. Secondly, I wrote an article in “Chocs Avancées n°16” to explain in simple words the results of my work for the LMJ facility [2].

B.1 “La Fabrique Defense 2022”

The event “La Fabrique Defense 2022” allowed young European citizens to understand the challenges of defense by meeting companies and organizations involved in European defense. Conferences were organised to promote debates and discussions on topics such as European defense, geopolitics, industry, technology and innovation.

The CEA (“Commissariat à l’Energie Atomique et aux Energies Alternatives”) is one of major research actors in Europe. It is active in the fields of low carbon energies, information, healthcare technologies and defense. In order to present its defense-related activities to the public, the CEA had a stand to:

- Explain the main operating principles of French nuclear weapons through virtual reality demonstrations;
- Present its environmental monitoring activities to verify the strict application of the Comprehensive Nuclear Test Ban Treaty (CTBT);
- Promote its major scientific research facilities such as the Laser Mega-Joule.

I was chosen, among CEA PhD students, to present my research activities for the CEA during a career session. I also participated in the animation

of the CEA stand alongside managers, human resources officers and a communication team (Figure B.1 (a)). During the event, I shared information to master students about the excellent scientific support and the many high-quality experimental facilities that CEA provides for carrying out PhD projects. After my participation in the event, a communication team of CESTA ("Centre d'Etudes Scientifiques et Techniques d'Aquitaine") interviewed me so that I briefly described my work and gave my feelings on this experience (Figure B.1 (b)). Finally, the most difficult aspect for me was not to present in front of a large audience but to speak in front of a camera. This event was also an opportunity for me to speak with

(a) (b)

Figure B.1: (a) The CEA stand at "La Fabrique Defense 2022". (b) Frame of the movie in which I explained my PhD work and my experience in "La Fabrique Defense 2022".

scientists working in companies, such as DGA, Thales and Safran. These discussions considerably contributed to my awareness of the skills acquired during my 3 years of thesis and to prepare the next step of my career as an optronic system engineer at Safran Electronic & Defense.

B.2 "Chocs Avancées"

In parallel to my scientific publications in peer-reviewed journals, I also wrote an article in the journal "Chocs Avancées". In order to provide a vision of the current research work carried out at the "Direction des Applications Miliaires" of CEA, the journal "Chocs Avancées" brings together twenty articles from a selection of the most important publications of the past year in specialized peer-reviewed journals. This journal is intended to be read by non-experts. Writing an article for "Chocs Avancées" therefore required a simplification of the scientific message.

B.2.1 A la poursuite des cratères sur les optiques du Laser Mégajoule

Les faisceaux du Laser Mégajoule sont si puissants qu'ils provoquent des cratères dans ses optiques. Ces cratères, aussi appelés dommages, sont à peine plus larges qu'un cheveu sur des composants de la taille d'un écran d'ordinateur et sont la cause du remplacement de centaines d'optiques par an. Or, comme chaque optique est de très haute qualité et donc très chère, il est souhaitable de détecter les dommages aussi tôt que possible, de les traiter pour réparer l'optique et la réutiliser. Pour détecter les dommages, le CEA – DAM enregistre chaque jour des centaines d'images d'optiques et s'est proposé de mesurer les dommages par l'analyse d'infimes variations d'intensité lumineuse [3] : il parvient ainsi à une détection plus précoce qu'avec la méthode actuelle de mesure du diamètre [4].

Mesurer des objets de l'épaisseur d'un cheveu à dix mètres de distance : impossible ? C'est ce dont a besoin l'un des plus grands lasers de puissance du monde – le Laser Mégajoule (LMJ), situé sur le centre CEA – DAM du Cesta, près de Bordeaux – pour fonctionner de manière nominale et mener à bien les expériences du programme Simulation [5]. En effet, la détection fiable et précoce de l'augmentation de la taille des dommages des optiques est un des prérequis à son bon fonctionnement.

À son apparition, un dommage ressemble à un impact sur un pare-brise, à la différence que son diamètre est de l'ordre de la dizaine de micromètres. L'endommagement est dû à l'interaction entre un des faisceaux du laser et de rares défauts présents à la surface des optiques. À chaque nouvelle exposition au faisceau, le dommage s'amplifie et les fractures qui le constituent représentent des points d'absorption de l'énergie du faisceau. Malgré leur petite taille par rapport à celles des optiques, les dommages dégradent la qualité du faisceau laser. Pour que les performances de celui-ci soient conservées, un composant trop endommagé doit être remplacé.

Pour suivre l'évolution d'un dommage, des images de celui-ci sont prises avec une caméra dont la résolution est néanmoins limitée pour une mesure satisfaisante de sa taille (Figure B.2).

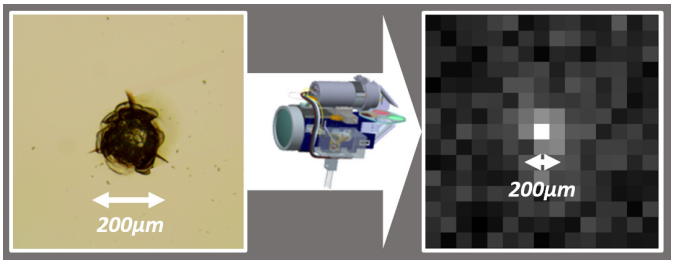

Figure B.2: Image d'endommagement sur une optique du Laser Mégajoule. (a) Image d'un dommage de diamètre 200 µm, mesuré sur une optique transportée en laboratoire. (b) Image d'un dommage de 200 µm fournie par une caméra installée sur le Laser Mégajoule. La dynamique de visualisation s'étend pour cette image de 0 à 200 niveaux de gris. Sur cette image, un seul pixel représente le dommage et ne permet pas de le caractériser de manière satisfaisante.

Une nouvelle approche

Une nouvelle approche est proposée afin de suivre avec une plus grande précision l'augmentation de la taille des dommages [3]. Elle est basée sur l'analyse des variations d'intensité lumineuse dans chaque pixel de l'image enregistrée après le passage d'un faisceau. Pour que cette méthode soit plus efficace et plus fiable in situ que la mesure directe de la taille, il est nécessaire de s'assurer que les variations de luminosité ne sont provoquées que par l'évolution des dommages.

Suite à de petits déplacements de la caméra entre les acquisitions, un système de correction fait correspondre les images successives d'un dommage avec une résolution inférieure au pixel [3, 6]. Une correction en brillance et contraste permet ensuite de s'assurer que la luminosité d'un même pixel est analysable sur l'ensemble des images enregistrées (Figure B.3).

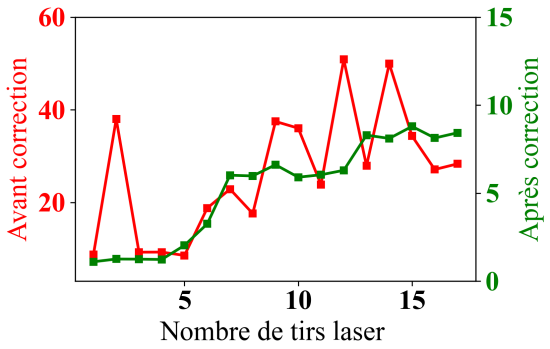

Figure B.3: Évolution du niveau d'intensité des pixels de la caméra, installée sur le Laser Mégajoule, sur une zone de 5 mm encadrant un dommage avant (points rouges) et après (points verts) correction d'une série de dix-sept images successives. Avant correction, les intensités lumineuses sont faussées par de petits déplacements de la caméra et des variations d'éclairement. Au contraire, les intensités lumineuses corrigées décrivent précisément l'augmentation de la taille du dommage.

Comparaison des performances

L'équipe du CEA – DAM a comparé les performances de la mesure directe du diamètre et de celle des intensités lumineuses lors d'expériences réalisées sur le Moyen d'endommagement laser et banc d'analyse (Melba) du centre CEA – DAM du Cesta [4]. L'analyse des intensités conduit à des performances inaccessibles par la mesure du diamètre. Le début de la croissance des dommages est ainsi détecté plus précocement (Figure B.4). Les variations d'intensité lumineuse peuvent donc être utilisées comme un indicateur efficace de la croissance des dommages laser. La recherche des cratères peut alors avoir lieu pour favoriser la bonne réalisation des expériences du programme Simulation.

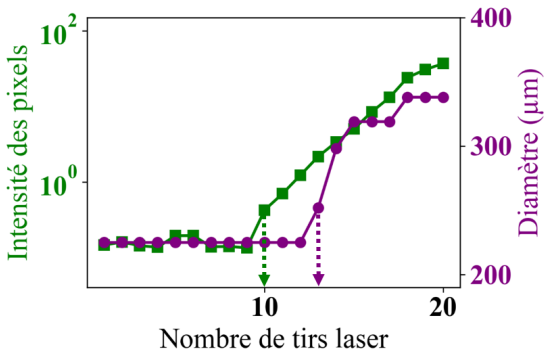

Figure B.4: Évolution du niveau d'intensité des pixels (points verts) et du diamètre mesuré (points violets) lors de la croissance d'un dommage sur l'installation Melba du centre CEA – DAM du Cesta. Bien que les deux séries de données permettent d'observer la croissance, l'intensité des pixels (flèche verte) permet de détecter la croissance du dommage trois passages du faisceau plus tôt qu'en s'appuyant sur la mesure de diamètre (flèche violette). L'aspect plus progressif de l'augmentation d'intensité lumineuse est également plus fidèle à l'évolution de la croissance que les sauts et paliers observés sur la mesure du diamètre.

References

[1] M. des Armées. "La fabrique défense." (2022), [Online]. Available: https://lafabrique.defense.gouv.fr/ (visited on 10/10/2022).

[2] C. DAM. "Chocs avancées." (2022), [Online]. Available: https://www-physique-chimie.cea.fr/science-en-ligne/chocs-avancees.html (visited on 10/10/2022).

[3] G. Hallo, C. Lacombe, J. Néauport, and F. Hild, "Detection and Tracking of Laser Damage Sites on Fused Silica Components by Digital Image Correlation," *Optics and Lasers in Engineering*, vol. 146, p. 106 674, 2021.

[4] G. Hallo, C. Lacombe, R. Parreault, *et al.*, "Sub-pixel detection of laser-induced damage and its growth on fused silica optics using registration residuals," *Opt. Express*, vol. 29, no. 22, pp. 35 820–35 836, Nov. 2021. doi: 10.1364/OE.433862. [Online]. Available: http://opg.optica.org/oe/abstract.cfm?URI=oe-29-22-35820.

[5] C. DAM, *Les 20 ans du programme Simulation : histoire d'un succès!* Commissariat À L'énergie Atomique, Direction Des Applications Militaires, Dl, 2016.

[6] M. A. Sutton, J.-J. Orteu, and H. W. Schreier, *Image Correlation for Shape, Motion and Deformation Measurements - Basic Concepts, Theory and Applications*. Springer Science, 2009, isbn: 978-0-387-78746-6. doi: 10.1007/978-0-387-78747.

C

Contribution to “Chocs Focus”

The journal “Chocs Focus” aims to highlight scientific news of the “Direction des Application Militaire” (DAM) [1]. The publication of an issue is decided following a significant event. In 2022, the Metrology Forum of DAM was the basis of the publication of an issue. With the support of some colleagues, we wrote an article dealing with the metrology of laser-induced damage of LMJ optics, from the amplifying section to transport and frequency conversion sections.

C.1 Endommagement des 7000 optiques du Laser MegaJoule

Le Laser MégaJoule (LMJ), installation phare du programme Simulation, est destiné à réaliser des expériences de fusion avec des conditions de température et de pression typiques du fonctionnement nucléaire des armes [2]. 176 faisceaux laser, dimensionnés pour fournir $1.3\,\mathrm{MJ}$ sur une cible, parcourent près d’une centaine de kilomètres à travers plus de 7000 grands composants optiques. Les énergies laser engagées sont susceptibles d’endommager ces optiques, augmentant ainsi le coût d’exploitation du LMJ et réduisant ses performances. Le CEA cherche donc à maîtriser l’évolution de l’endommagement de ces optiques en associant des techniques d’analyse innovantes à diverses méthodes d’imagerie.

Les grandes optiques du LMJ sont des composants aux fonctions optiques très variées : miroirs, lentilles, cristaux de conversion de fréquence, hublots plans, réseaux... Selon leur orientation par rapport à l’incidence du faisceau laser, elles mesurent entre $40\,\mathrm{cm}$ et $70\,\mathrm{cm}$ de côté. Lors de son passage, le faisceau laser peut induire la formation de dommages de quelques dizaines de microns. Une fois initiés, les dommages croissent à chaque réexposition au faisceau laser. Répartis longitudinalement sur près

de 100km et spatialement sur $1000\,\mathrm{m}^2$ de surface optique, la détection et le suivi de ces dommages est un enjeu majeur pour prévoir au juste besoin l'approvisionnement de nouvelles optiques ou leur restauration. Pour cela, le CEA a développé des moyens d'observation de l'endommagement des grandes optiques sur l'installation LMJ et y associe des outils d'analyse automatiques. Les moyens d'observation reposent sur trois méthodes d'imagerie. Limités en précision par les contraintes d'une telle installation, ces moyens d'observations sont complétés par des bancs de métrologie plus résolus en base arrière, utiles à la validation des méthodes mises en œuvre.

La première méthode est une mesure par diffusion. Les optiques sont éclairées par des LEDs positionnées sur la tranche. Les dommages, présents en surface, collectent et diffusent une partie de la lumière d'éclairement. Une caméra image l'optique ainsi éclairée, les dommages apparaissent comme des points brillants sur une image à fond noir (Figure C.1 (c)). Cette méthode est utilisée pour deux des dernières optiques traversées par le faisceau laser à $351\,\mathrm{nm}$ et dont le suivi est primordial. La caméra d'observation est positionnée au centre de la chambre d'expériences et, par le biais de séquences machines automatiques, image chacune des 352 optiques concernées à une distance d'environ $\approx 8\,\mathrm{m}$. Pour dépasser la limite imposée par la dimension d'un pixel sur les images ($\approx 100\,\mu\mathrm{m}$), la taille des dommages est estimée à partir des intensités mesurées, étalonnée grâce à un composant optique spécifique composé d'une matrice de plus de 900 dommages. La deuxième méthode est une mesure par strioscopie. Elle consiste à extraire du faisceau d'éclairement les hautes fréquences spatiales, caractéristiques des dommages, par un filtrage dans un plan de focalisation du faisceau, en scannant longitudinalement différents plans optiques (Figure C.1 (a)). Ce mode de mesure est uniquement possible pour les optiques de la section amplificatrice, équipée d'un système de filtrage et masquage adapté. Le traitement actuel de localisation de l'optique endommagée se base sur une évaluation du plan de meilleur focus sur les éléments détectés. Fournissant une localisation longitudinale approximative de l'ordre de $2\,\mathrm{m}$, de nouveaux traitements 3D visent à calculer le plan de l'optique à partir des modifications des formes de l'endommagement sur l'ensemble de la séquence d'images acquise.

La troisième méthode est une mesure par diffraction. L'onde plane du faisceau d'éclairement qui traverse les optiques interfère avec les ondes sphériques générées par les dommages. Les images d'interférences sont acquises par une caméra. Des algorithmes de traitement et de propagation d'ondes, en cours de développement, visent à estimer le défaut de

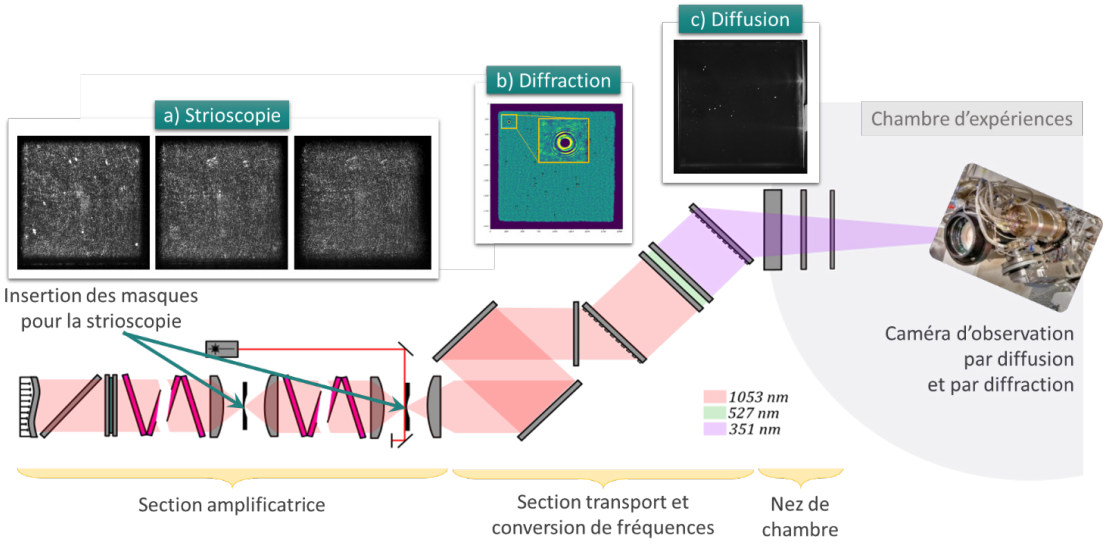

Figure C.1: Représentation schématique des différentes sections traversées par un faisceau laser du LMJ. Exemples d'images obtenues par (a) la mesure en mode strioscopique, (b) la mesure de diffraction avec un zoom sur une figure de diffraction et (c) la mesure de diffusion.

phase et la taille de l'objet à partir des figures d'interférence acquises (Figure C.1 (b)). Cette méthode de mesure peut être utilisée pour une grande majorité des optiques du LMJ à la fois dans la section amplificatrice, la section transport et la section conversion de fréquences. L'efficacité de cette technique a récemment pu être démontrée avec le détection et la localisation d'un dommage sur un miroir de transport. Pour valider ces algorithmes, les optiques extraites de l'installation pour maintenance sont finement observées sur les bancs de métrologie pour compléter les essais réalisés en laboratoire. Pour suivre efficacement la croissance des dommages tir à tir, un algorithme basé sur les principes de la Corrélation d'Images Numériques (CIN) corrige les perturbations affectant les images (déplacements de la caméra, variations d'intensité de l'éclairement) [3]. Mis en œuvre sur les images de diffusion, le CEA prévoit de généraliser cette méthode.

Malgré des images peu résolues spatialement et fortement perturbées, les travaux menés par le CEA sur le suivi de l'endommagement des optiques du LMJ devraient permettre à terme d'optimiser les maintenances et approvisionnements d'optiques neuves. L'exploitation du LMJ serait alors facilitée tout en garantissant les performances laser indispensables à la réussite des expériences de fusion du programme Simulation.

References

[1] C. DAM. "Chocs focus." (2022), [Online]. Available: https://www-physique-chimie.cea.fr/science-en-ligne/chocs-focus.html (visited on 10/10/2022).

[2] ——, *Les 20 ans du programme Simulation : histoire d'un succès!* Commissariat À L'énergie Atomique, Direction Des Applications Militaires, Dl, 2016.

[3] G. Hallo, C. Lacombe, R. Parreault, *et al.*, "Sub-pixel detection of laser-induced damage and its growth on fused silica optics using registration residuals," *Opt. Express*, vol. 29, no. 22, pp. 35 820–35 836, Nov. 2021. doi: 10.1364/OE.433862. [Online]. Available: http://opg.optica.org/oe/abstract.cfm?URI=oe-29-22-35820.

D

Published contributions

Articles

1. **G. Hallo**, C. Lacombe, J. Neauport and F. Hild. "Detection and tracking of laser damage sites on fused silica components by digital image correlation", *Optics and Lasers in Engineering*, vol. 146, 106674, 2021

2. **G. Hallo**, C. Lacombe, R. Parreault, N. Roquin, T. Donval, L. Lamaignere, J. Neauport and F. Hild, "Sub-pixel detection of laser-induced damage and its growth on fused silica optics using registration residuals", *Optics Epxress*, vol. 29, no. 22, pp. 35820-35836, 2021

3. I. Ben-Soltane, **G. Hallo**, C. Lacombe, N. Bonod and J. Neauport, "Estimating and monitoring laser-induced damage size on glass windows with a deep-learning based pipeline", Journal of the Optical Society of America A, 1881-1892, 2022

Conference Proceedings

1. C. Lacombe, **G. Hallo**, M. Sozet, P. Fourtillan, R. Diaz, S. Vermersch and J. Neauport. Dealing with LMJ final optics damage: post-processing and models. In Laser-induced Damage in Optical Materials 2020 11514, 16-21

2. **G. Hallo**, C. Lacombe, J. Neauport and F. Hild. Detection and tracking of lser damage on LMJ vacuum windows by digital image correlation. in Dimensional Optical Metrology and Inspection for Practical Applications X 2021 11732, 87-95

3. **G. Hallo**, C. Lacombe, R. Parreault, N. Roquin, T. Donval, L. Lamaignere, J. Neauport and F. Hild. How to provide reliable metrology of online laser-induced damage on large fused silica optics using digital image correlation? in Optical Fabrication, Testing, and Metrology VII 2021 11873, 31-37

4. C. Lacombe, **G. Hallo**, M. Sozet, P. Fourtillan and J. Neauport. Beam blockers on the Laser MegaJoule. in Laser-Induced Damage in Optical Materials 2021 11910, 1191019

Other contributions

1. **G. Hallo**, C. Lacombe, J. Neauport, L. Lamaignere and F. Hild, "A la poursuite des cratères sur les optiques du Laser MégaJoule", revue *Chocs Avancées*, **16**, p. 52-53, 2022

2. **G. Hallo**, F. Gaudfrin, C. Lacombe, V. Beau, J. Neauport and F. Hild, "Endommagement des 7000 optiques du Laser MegaJoule", revue *Chocs Focus*, *num*, p. page-page, 2022

List of Figures

List of Tables

université PARIS-SACLAY

ÉCOLE DOCTORALE
Sciences mécaniques et énergétiques, matériaux et géosciences (SMEMAG)

Titre : Optimisation des capacités de détection et de suivi de la croissance de l'endommagement laser pour l'installation Laser MegaJoule.
Mots clés : Laser MegaJoule, Endommagement laser, Contrôle de l'endommagement, Corrélation d'images numériques (CIN), Diffusion lumineuse, Traitement d'images.

Résumé : Les 176 faisceaux du Laser MegaJoule (LMJ) délivreront chacun, à terme, $7.5\,\mathrm{kJ}$ d'énergie à une longueur d'onde de $351\,\mathrm{nm}$ sur une durée d'impulsion de quelques nanosecondes. Dans ces conditions, les optiques en silice sont sensibles à l'endommagement laser. Les 176 hublots de chambre, en silice, de $34\,\mathrm{mm}$ d'épaisseur et de $40\,\mathrm{cm}$ de côté, assurent l'étanchéité au vide de la chambre d'expériences tout en permettant aux faisceaux laser d'atteindre la cible. Un système d'imagerie est utilisé pour acquérir quotidiennement des images in-situ des hublots. Cependant, la résolution spatiale des images est supérieure au diamètre des dommages dont la croissance est à contrôler. Le but de cette thèse est d'optimiser les capacités de détection et de suivi de la croissance de l'endommagement des hublots du LMJ. Cette optimisation est organisée selon 3 axes. Premièrement, une méthode d'estimation du diamètre des dommages à partir des niveaux de gris des images est introduite par la modélisation du système d'acquisition et le dépouillement d'une expérience d'étalonnage. Deuxièmement, un algorithme de corrections des images basé sur la corrélation d'images numériques a été développé pour corriger les perturbations des acquisitions et permettre le suivi in-situ de la croissance des dommages. Troisièmement, nous démontrons que l'analyse des niveaux de gris et du diamètre d'un dommage permet d'acquérir une information supplémentaire : sa croissance en profondeur, habituellement accessible par des méthodes plus complexes.

Title: Optimization of laser damage detection and growth monitoring capabilities: application to the Laser MegaJoule facility.
Keywords: Laser MegaJoule, Laser-induced damage, Damage monitoring, Digital Image Correlation (DIC), Light scattering, Image processing.

Abstract: The 176 beams of the Laser MegaJoule (LMJ) facility are designed to deliver each one $7.5\,\mathrm{kJ}$ of laser energy at a wavelength of $351\,\mathrm{nm}$ over a pulse duration of few nanoseconds. Under these conditions, fused silica optics are particularly susceptible to laser damage. The 176 vacuum windows, critical fused silica components of the LMJ, with a thickness of $34\,\mathrm{mm}$ and a side length of $40\,\mathrm{cm}$, ensure the vacuum tightness of the experiment chamber while allowing the laser beams to reach the target. An imaging system is used to acquire daily in-situ images of vacuum windows. However, the spatial resolution of the images is greater than the diameter of damage sites whose growth must be monitored. The aim of this thesis is to optimize the in-situ detection and monitoring capabilities of damage growth on the LMJ final optics. This optimization is organized in 3 parts. First, a method to estimate the diameter of damage sites from the gray levels of the images is introduced. Second, an image correction algorithm based on digital image correlation principles has been developed to correct for image disturbances and thus to in-situ monitor damage growth. Third, we demonstrate that the analysis of the gray levels and the diameter of a damage site allows an additional information to be extracted, namely, damage growth in depth, usually accessible by more complex methods.